N84-28990

NASA Technical Memorandum 83622

Oxygen Diffusion in $\alpha-Al_2O_3$

James D. Cawley
Lewis Research Center
Cleveland, Ohio

and

John W. Halloran and Alfred R. Cooper
Case Western Reserve University
Cleveland, Ohio

June 1984

NASA

TABLE OF CONTENTS

Page

CHAPTER

1 INTRODUCTION 1

2 LITERATURE SURVEY 4

2.1 Mathematics of Self-diffusion Measurements 4

2.2 Self-diffusion Studies 10

2.3 Defect Energy Calculations 27

2.4 Defect Structure of α-Al_2O_3 31

2.4.1 Defect Diffusion in doped α-Al_2O_3 31

2.4.2 Density Measurements 33

2.4.3 Spectroscopic Investigations 34

2.4.3.1 Undoped α-Al_2O_3 34

2.4.3.2 Defect Clustering 36

2.4.3.3 Nickel Doping 36

2.4.4 Electrical Conductivity Measurements 37

2.4.5 Sintering Studies 42

2.4.6 Creep Studies 43

2.4.7 Deformation Work 44

2.4.8 Summary 45

3 EXPERIMENTAL PROCEDURE 47

3.1 Sample Preparation and Characterization 47

3.1.1 Single Crystal Samples 47

3.1.2 Polycrystalline Samples 58

3.2 Exchange Apparatus 62

Page

3.3 Exchange Procedure 69

3.4 Analysis of Samples 70

3.4.1 Proton Activation 70

3.4.2 Rutherford Backscattering (RBS) 78

3.4.3 Secondary Ion Mass Spectrometry (SIMS) 81

4 RESULTS 92

4.1 Proton Activation 92

4.1.1 Standards 92

4.1.2 Channeling 104

4.1.3 Nuclear Reaction 116

4.1.3.1 Qualitative Interpretation 116

4.1.3.2 Fits to Diffusion Equations 133

4.2 Secondary Ion Mass Spectrometry 141

4.2.1 Oxygen-18 Profiles in Single Crystals at P_{O_2} = 1 atm 141

4.2.2 Oxygen-18 Profiles in Single Crystals at $P_{O_2} = 10^{-15}$ atm 155

4.2.3 Oxygen-18 Profiles in Polycrystals at P_{O_2} = 1 atm 155

4.2.4 Attempt to Profile Polycrystals at low P_{O_2} 166

4.2.5 Contamination of Single Crystals 166

4.2.6 Contamination of Polycrystals 170

Page

5 DISCUSSION 194

5.1 Analysis Techniques 194

5.2 Oxygen Diffusion 196

5.2.1 Thermodynamics of Point Defect Clustering 197

5.2.1.1 General Background 198

5.2.1.2 Clustering in α-Al_2O_3 201

5.2.1.3 Cluster Mobilities 237

5.2.2 Impurity Insensitivity of Oxygen Self-diffusion 244

5.2.3 P_{O_2} Dependence 258

5.2.4 Non-Fickian Tracer Profiles 260

6 CONCLUSIONS 266

7 SUGGESTIONS FOR FUTURE WORK 267

REFERENCES 268

Appendix A - The Thermal Oxidation of Silicon 275

Appendix B - The Thermal Oxidation of Silicon Carbide 326

Appendix C - Solutions to the Diffusion Equation Including Convection 337

CHAPTER I

INTRODUCTION

Diffusion is a fundamental process and alumina is both a widely occurring and widely used ceramic. Interest in oxygen diffusion in α-Al_2O_3 naturally follows. Such processes as sintering, creep, electrical conductivity, and oxidation of metals may all involve the mass transport of oxygen. The motivation for this work stems from the latter, in particular the oxidation of NiCrAl alloys.

These alloys exhibit good oxidation resistance due to an α-Al_2O_3 scale which forms on their surface and across which material must be transported for further oxidation to take place. It is believed that the growth of the oxide arises primarily due to an inward diffusion of oxygen from the gas across the scale to the metal, with outward diffusion of aluminum along short circuit paths playing a secondary role(1).

The oxide scale tends to spall. This has been attributed to growth of oxide within the existing oxide occurring when inward oxygen and outward aluminum fluxes coexist. Small additions of oxygen-active elements such as zirconium and yttrium reduce or eliminate this problem(1-4). The postulate has been that these materials segregate to the short circuit paths and inhibit outward aluminum diffusion.

The oxygen which diffuses across the scale sees a complex environment. The scales are polycrystalline and the grain size varies across the scale. One side of the scale is exposed to an oxidizing atmosphere and the other, which is in contact with the metal, is in a strongly reducing environment. This scale, while primarily Al_2O_3, will pick up impurities as it grows. Concentration gradients will likely occur.

In order to get basic knowledge about this problem, it was the intent of this work to study oxygen diffusion in single crystals of α-Al_2O_3 singly doped with Cr, Ni, Y, and Zr, in both a 1 atm O_2 and in a CO/CO_2 atmospheres of low P_{O_2}. These dopants were chosen because they are likely contaminants in the scales.

Chromium would not be expected to produce defects since it is isovalent and the difference in ionic radii between chromium and aluminum is small. Yttrium is also isovalent, however it has an ionic radii much larger than that of aluminum and it has been suggested that this strain can cause yttrium to act as a donor[5]. However, as will be discussed, the current author questions the experimental evidence.

Nickel is divalent with small misfit and is expected to behave as an acceptor. Since a nickel ion on an aluminum site is a negative defect and the crystal must retain electroneutrality, the incorporation of nickel will necessitate an increase in the concentration of positive defects. The positive defect on the anion sublattice is an oxygen vacancy.

Zirconium is quadrivalent with large misfit and is expected to behave as a donor. Zirconium on an aluminum site is a positive defect. The concentration of oxygen interstitials which are negative defects would be expected to increase with Zr-doping.

A study of crystals whose behavior is governed by these dopants, then, provides information about the mechanism of oxygen diffusion in, and the defect structure of, α-Al_2O_3.

CHAPTER II

LITERATURE SURVEY

In this section the literature on self-diffusion and the defect structure in alumina will be reviewed. Properties such as electrical conductivity, sintering, creep, and deformation are related to diffusion through the defect structure. Therefore, it is appropriate to also review the studies of these properties.

2.1 MATHEMATICS OF SELF-DIFFUSION MEASUREMENTS

At temperatures above absolute zero, atoms in a solid are in constant motion about their lattice sites. When an atom obtains enough energy it may jump to a neighboring site. Such a process is termed diffusion. The random motion of atoms in the absence of a concentration gradient is termed self-diffusion.

The study of self-diffusion is most often accomplished by introducing a tracer to the system, that is atoms which are similar to those under study yet in some way identifiable. Most often an isotope with a small natural abundance is used. The tracer is allowed to make contact with a sample of material at a given temperature for a given period of time. After which, the tracer concentration profile is determined. A tracer diffusion coefficient may be determined knowing the initial profile, the final profile, and the appropriate solution to the diffusion equation. The relationship

between the tracer diffusion coefficient and that of the species of interest is dependent on their similarity. In the case of isotopes, the difference in diffusion coefficients is related to the isotope mass difference[6] by:

$$\frac{D_1}{D_2} - 1 = f_1 \left[\left(\frac{M_2}{M_1} \right)^{1/2} - 1 \right] \qquad (2.1\text{-}1)$$

Where D_1 is the isotope diffusion coefficient, M_1 is the isotope mass, and f_1 is the isotope correlation coefficient. The value of f_1 depends on the crystal structure and mechanism of diffusion. When the isotope oxygen-18 is used to study oxygen diffusion, the difference, neglecting correlation, is roughly 6 percent.

In a gas exchange experiment, an atmosphere of O_2 enriched with tracer was brought in contact with the sample at a given temperature. The initial profile in the sample is only the natural abundance, 0.204 percent, which can be subtracted out. The final profile is then compared with a concentration profile predicted by a solution to the diffusion equation.

Fick's First Law, in one dimension, may be written as:

$$J_i = -D_i \cdot \rho \frac{\partial c_i}{\partial x} \qquad (2.1\text{-}2)$$

where J_i is the flux density (kg/m^2s) of the ith species, D_i is the diffusion coefficient (m^2/s), and ρ is the density (kg/m^3). With conservation of mass, and constant density, it may be shown[7] that:

$$\frac{\partial c_i}{\partial t} = \frac{\partial}{\partial x} D_i \frac{\partial c_i}{\partial x} \qquad (2.1\text{-}3)$$

With the assumption that D_i is independent of position this becomes:

$$\frac{\partial c_i}{\partial t} = D_i \frac{\partial^2 c_i}{\partial x^2} \qquad (2.1\text{-}4)$$

Solutions to this equation, using the appropriate boundary conditions, which give the tracer concentration as a function of position, x, and time of anneal, t, may be obtained.

For diffusion into a semi-infinite slab from a gaseous source of tracer, which is well-mixed and infinite, the following three cases are considered.

(i) The surface is maintained in equilibrium with a gas containing a constant concentration of tracer. The boundary conditions in this case are:

$$c(x,t) = c_\infty \quad \text{for} \quad t \le 0 \quad 0 \le x \le \infty$$

$$c(x,t) = c_0 \quad \text{for} \quad t > 0 \quad x = 0$$

$$c(x,t) = c_\infty \quad \text{as} \quad x \to \infty$$

The solution to equation (2.1-4) for these conditions is[7]:

$$c(x,t) - c_\infty = (c_0 - c_\infty)\ \mathrm{erfc}(\theta) \qquad (2.1\text{-}5)$$

where $\theta = x/2\sqrt{Dt}$.

(ii) The surface does not instantaneously equilibriate with the gas containing a constant concentration of tracer. The boundary conditions for this case are:

$$c(x,t) = c_\infty \qquad \text{for} \quad t \le 0 \quad 0 \le x < \infty$$

$$-D \left.\frac{\partial C}{\partial x}\right|_{x=0} = K[c_g - c(0,t)] \quad \text{for} \quad t > 0$$

$$c(x,t) = c_\infty \qquad \text{as} \quad x \to \infty$$

where K is the first order surface exchange coefficient, C_g is the concentration of tracer in the gas, and $C(0,t)$ is the concentration of tracer in the solid at the surface. The solution to equation (2.1-4) for this case[7] is:

$$\frac{c(\theta,\phi) - c_\infty}{c_g - c_\infty} = [\text{erfc}(\theta) - \exp(\phi^2 + 2\theta\phi)\text{erfc}(\theta + \phi)] \qquad (2.1\text{-}6)$$

where $\phi = K\left(\frac{t}{D}\right)^{1/2}$

It has been shown that for $\phi > 6$ the rate of surface exchange may be considered infinite[8].

(iii) The surface does not instantaneously equilibriate and the concentration of tracer in the gas is allowed to vary with time in a manner described by:

$$C_g(t) = A_2 t + A_1 t^{1/2} + A_o$$

The solution to equation (2.1-4) is[9]:

$$C(\theta,\phi) - C_\infty = \sum_{n=0}^{2} (-1)^{n+1} \frac{A_n t^{n/2} - C_\infty \partial_{no}}{\phi_n} \cdot \qquad (2.1\text{-}7)$$

$$\Gamma\left(1 + \frac{n}{2}\right) \{\exp[\phi(2\theta + \phi)]\ \text{erfc}\ (\theta + \phi) - \sum_{r=0}^{n} (-2\phi)^r i^r\ \text{erfc}\ (\theta)\}$$

where Γ is the tabulated gamma function, $i^r\text{erfc}$ is the rth integral of the complementary error function, and ∂_{no} is the Kronecker delta (1 for n = o and 0 otherwise).

Defects must be present in the lattice for diffusion to take place. Diffusion mechanisms are usually thought of in terms of point defects, either vacancies or interstitials, although defect complexes may play a role.

An atom on a lattice site adjacent to a vacancy may move to the vacancy's site. The vacancy may be thought of as moving in the opposite direction of the mass flow.

An atom in an interstitial site may move directly to another interstitial site or it may move to a normally occupied site and knock the lattice atom to an interstitial site.

The tracer diffusion coefficient can be related to the defect diffusion coefficient by:

$$D = f c_d D_d \tag{2.1-8}$$

where D is the tracer coefficient, f is the correlation factor (1 for interstitials, <1 for interstitialcy and vacancy), c_d is the fractional concentration of defects, and D_d is the defect diffusion coefficient.

From random walk considerations it can be shown[10] that:

$$D_d = \frac{1}{6} \bar{a}^2 \Gamma_d \tag{2.1-9}$$

where $\bar{a}^2$ is the mean square of the jump distance and Γ_d is the jump frequency.

Since jumping is an activated process, the defect jump frequency depends on temperature, as described by:

$$\Gamma_d = \nu \exp \frac{-\Delta G_m}{RT} \tag{2.1-10}$$

where ν is the vibrational frequency and ΔG_m is the activation energy for defect migration.

For the case of thermally generated defects, termed intrinsic, the relation for the concentration of defects to temperature is:

$$c_d = \exp(\frac{-\Delta G_f}{RT}) \qquad (2.1\text{-}11)$$

From equations (2.1-8) to (2.1-11):

$$D = \frac{1}{6} f\bar{a}^2 \ \nu(\exp \frac{-\Delta G_m}{RT})\exp(\frac{-\Delta G_f}{RT}) \qquad (2.1\text{-}12)$$

Since $\Delta G = \Delta H - T\Delta S$, this may be rewritten as:

$$D = \frac{1}{6} f\bar{a}^2 \ \nu \exp (\frac{(\Delta S_f + \Delta S_m)}{R})\exp (\frac{-(\Delta H_f + \Delta H_m)}{RT}) \qquad (2.1\text{-}13)$$

For the case of defects produced by the presence of an aliovalent impurity, termed extrinsic, where there is no appreciable temperature dependence on defect concentration, the expression for defect concentration is:

$$c_d = bc_f \qquad (2.1\text{-}14)$$

where b is a number dependent on the charge of the impurity atoms and c_f is the concentration of the impurity atoms. The value of b is independent of temperature if the defects produced by the impurity are the majority defects contributing to diffusion. However when the diffusion is by a minority species and the impurity creates a majority defect, b will contain a reaction coefficient and have a temperature dependence.

From equations (2.1-8) to (2.1-10) and (2.1-14):

$$D = \frac{1}{6} f\bar{a}^2 \nu b c_f \exp\left(-\frac{\Delta G_m}{RT}\right) \quad (2.1\text{-}15)$$

which may be rewritten as:

$$D = \frac{1}{6} f\bar{a}^2 \nu b c_f \exp\left(\frac{\Delta S_m}{R}\right) \exp\left(-\frac{\Delta H_m}{RT}\right) \quad (2.1\text{-}16)$$

Experimental diffusion coefficients can be represented by an Arrhenius type equation:

$$D = D_o \exp\left(\frac{-Q}{RT}\right) \quad (2.1\text{-}17)$$

where D_o is the pre-exponential term (m^2/s) and Q is the activation energy (kJ/mol). Comparison of equations (2.1-13), (2.1-16), and (2.1-17) shows the different quantities measured when the material behaves intrinsically and extrinsically.

	Intrinsic	Extrinsic
D_o	$\frac{1}{6} f\bar{a}^2 \nu \exp\left(\frac{\Delta S_f + \Delta S_m}{R}\right)$	$\frac{1}{6} f\bar{a}^2 \nu b c_f \exp\left(\frac{\Delta S_m}{R}\right)$
Q	$\Delta H_f + \Delta H_m$	ΔH_m

2.2 SELF-DIFFUSION STUDIES

There have been four studies conducted, since 1960, on the self-diffusion of oxygen in alumina and one study of aluminum self-diffusion in alumina.

The first was that of Oishi and Kingery[11]. In this work a finite amount of α-Al_2O_3, in the form of either spheres (0.30 in. diameter) or crushed Verneuil grown rods (200 to 300 mesh) was annealed,

in an atmosphere enriched in oxygen-18 at the temperature range 1450° to 1750° C. The powder was then reduced, the oxygen converted to CO_2, and the ratio of CO_2^{18}/CO_2^{16} was determined by mass spectrometry.

An Arrhenius plot of $\log_{10}(D)$ versus 1/T showed a break in slope at 1650° C. The data at temperatures higher than this were fit with:

$$D = 1.9\times10^{-1} \exp\left(\frac{-636\ \mathrm{kJ/mol}}{RT}\right)\ m^2/s \qquad (2.2\text{-}1)$$

The data below this temperature displayed much more scatter and were fit by:

$$D = 6.3\times10^{-12} \exp\left(\frac{-241\ \mathrm{kJ/mol}}{RT}\right)\ m^2/s \qquad (2.2\text{-}2)$$

This behavior was ascribed to an intrinsic-extrinsic transition. However, when samples in the low temperature region were preannealed before the diffusion anneal, the measured diffusion coefficients fell on the extrapolation of the high temperature data.

In Oishi and Kingery's investigation, it was assumed that the exchange between the gas and the solid was sufficiently fast that the process was diffusion controlled. Since what was measured was the total amount of tracer, either gained by the sample (in most cases) or lost by the atmosphere, the presence of a surface exchange effect would cause an underestimation of D. It was not until late in the study that the effect of preannealing the specimens prior to exchange was investigated. The fast transport of oxygen to the interior of the material, by dislocations, again undetectable due to the measurement of only total amounts of tracer, would lead to over-

estimations of the values of D. This was determined in later work to be the cause of 'extrinsic' break.

The second and third studies of oxygen self-diffusion occurred concurrently, in 1978 one by Reed and Weunsch[12,13] and the other study by Reddy and Cooper[15,16] in 1980.

In the work of Reed and Weunsch, diffusion of tracer into a semi-infinite slab was investigated. The source of tracer was an O-18 enriched polycrystalline Al_2O_3 layer on a single crystal slab. This was generated by successive deposition of Al metal and oxidation in an O-18 enriched atmosphere.

The diffusion coefficients that were determined could be described by

$$D = 6.4\times10^{1} \exp\left(\frac{-787\ \text{kJ/mol}}{RT}\right)\ m^2/s \qquad (2.2\text{-}3)$$

This is about a factor of fifteen below that of Oishi and Kingery.

One-half the single crystal slabs were preannealed in air, prior to thick film deposition, at 1650° C for four hours. The other half of the slabs were used in the as-polished state. The diffusion anneal took place with a pair of samples, one preannealed and one not, bound together with the tracer sources in contact. A schematic of the configuration is shown in figure 1. The concentration versus depth profile of O-18 was then determined with an Ion Probe (SIMS) and a diffusion coefficient was determined.

Reed and Weunsch state that those samples which had been preannealed showed Fickian profiles and those which had not been preannealed showed an anomolously high enrichment in the near surface

region. This was attributed to fast transport in the region damaged during polishing.

Examination of Reed's thesis, however, reveals that the thick film solution to the diffusion equation, which Reed employed in his analysis, does not describe the experimental situation.

The thick film solution requires that the diffusion coefficient not be a function of position. Referring to figure 1 it can be seen that this is not the case. The work of Oishi and Kingery showed that diffusion of oxygen in Al_2O_3 is enhanced in the presence of grain boundaries. Hence the diffusion coefficient in the labelled polycrystal is different than in the single crystal. Further, Reddy showed that the damage produced by polishing Al_2O_3 also enchances diffusion. Therefore, the diffusion coefficient is different in the as-polished and preannealed single crystals.

Both of these enhancements will have time dependencies. The work of Monahan and Halloran[14] suggests that the single crystal will consume the polycrystal, and Reed demonstrated that the polishing damage can be annealed out.

A clear experimental observation that the thick film solution has been violated is a flux of tracer across $x = 0$, in this case the sample surfaces correspond to $x = 0$. Such a flux was observed in the work of Reed and Weunsch. Equal amounts of tracer were deposited on the samples that were simultaneously annealed. However, after annealling the as-polished samples contained substantially greater amounts of tracer than did the preannealed samples, up to 1.5 times.

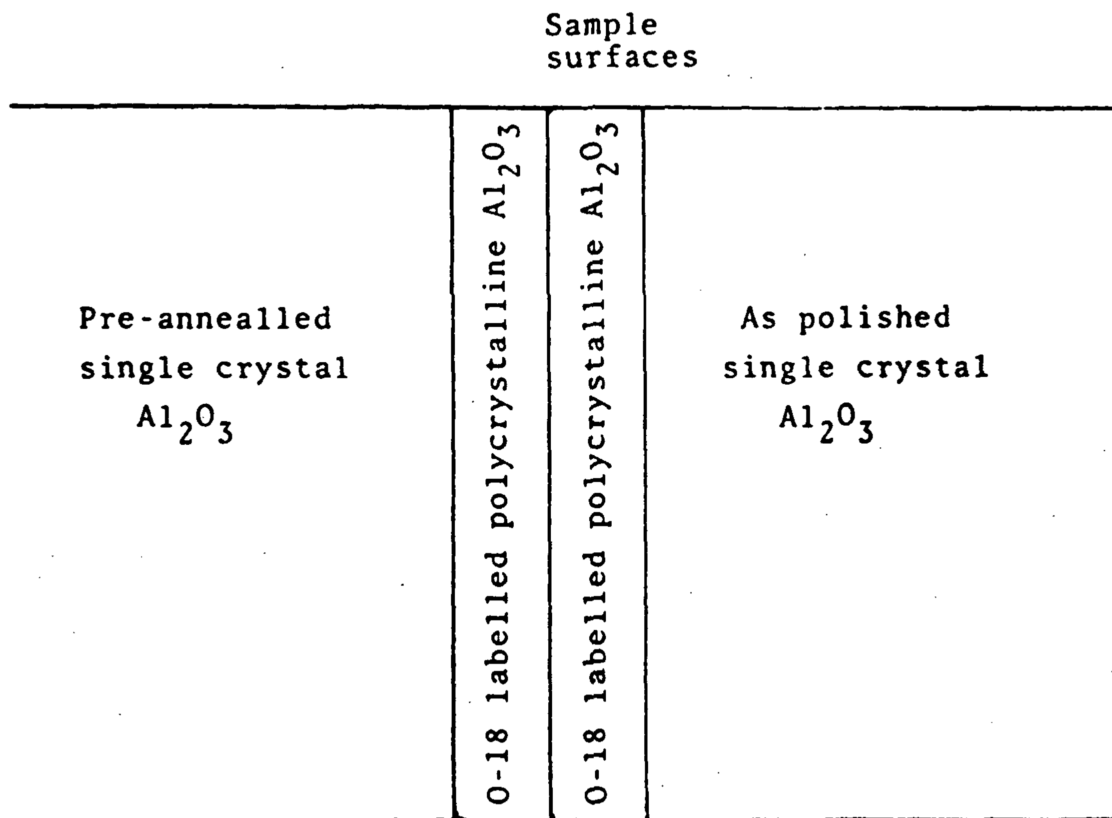

Figure 1. - Schematic of the sample configuration employed by Reed.

Figures 2 to 5, were made by tracing the figures in Reed's thesis and arranging them so that the diffusion couples in this experiment are shown. It can be seen that the profiles are not symmetric. Other aspects worth noting include the fact that there is no discontinuity between the samples which indicates a good couple; the degree of skewness seems to increase with increasing temperature of the experiment; the areas under the initial and final profiles are very nearly the same.

It is also puzzling that the as-polished samples which contained the most tracer (suggesting higher effective diffusion coefficients) also had the steepest concentration gradients, (suggesting lower diffusion coefficients).

In addition, Reed and Weunsch allowed the initial concentration to be an adjustable parameter during the fitting procedure. It is invalid to assume different values of c_o for the as-polished and preannealled samples that were bound together during the experiment. Figure 6 shows profiles predicted with the reported values of both the as-polished and preannealled diffusion coefficients, using the thick film solution, compared with Reed's experimental data. The lack of fit is apparent, however, it should be pointed out this profile was the most skewed.

Finally, Reddy analyzed Reeds preannealed samples by proton activation. He determined diffusion coefficients which were in reasonable agreement with those determined by Reed. However in order to obtain fits to the profiles, Reddy found it necessary to assume that the sample contained more tracer than Reed reported depositing

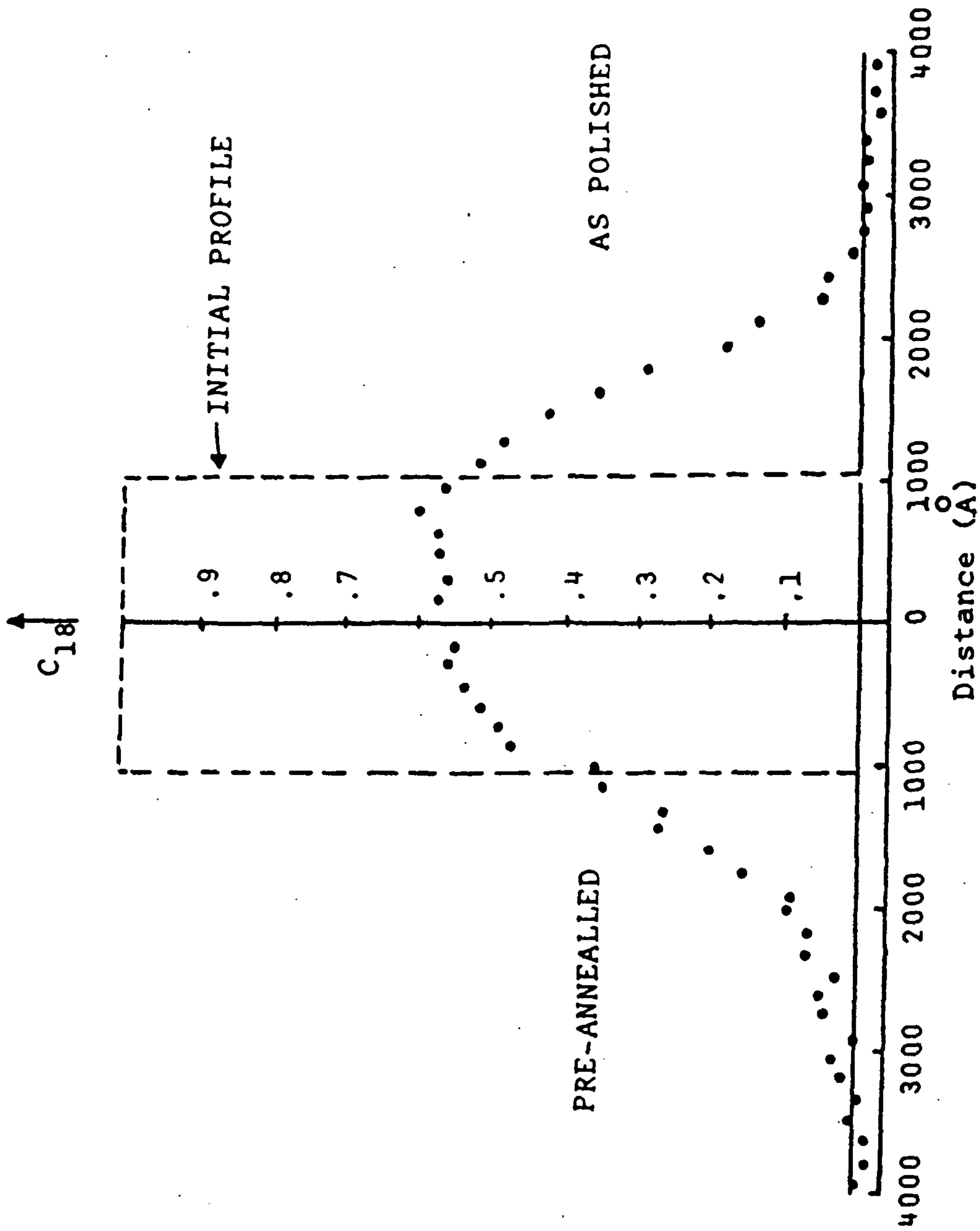

Figure 2. - Reed's diffusion couple at 1584° C for 257 hr.

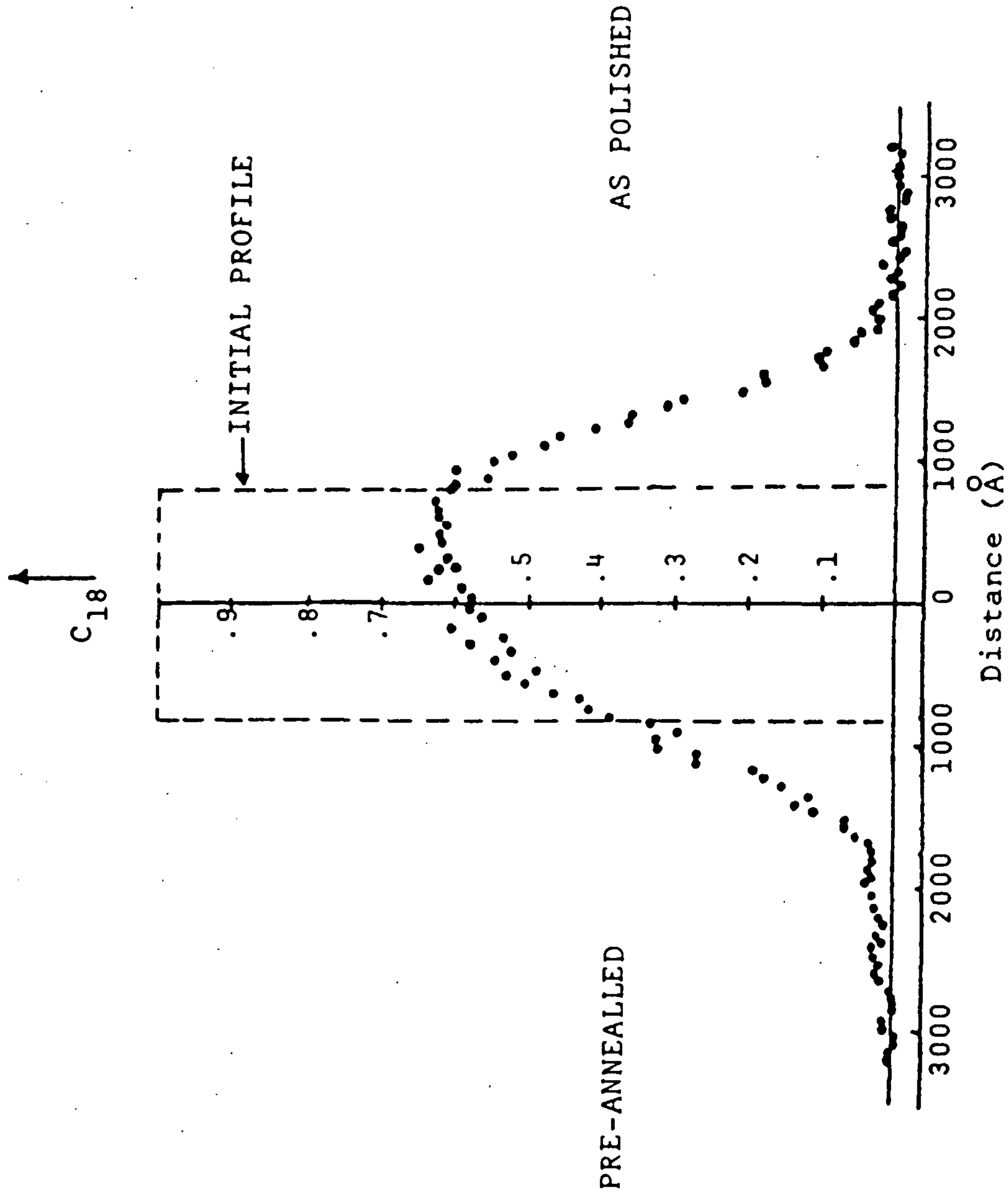

Figure 3. - Reed's diffusion couple at 1676° C for 74 hr.

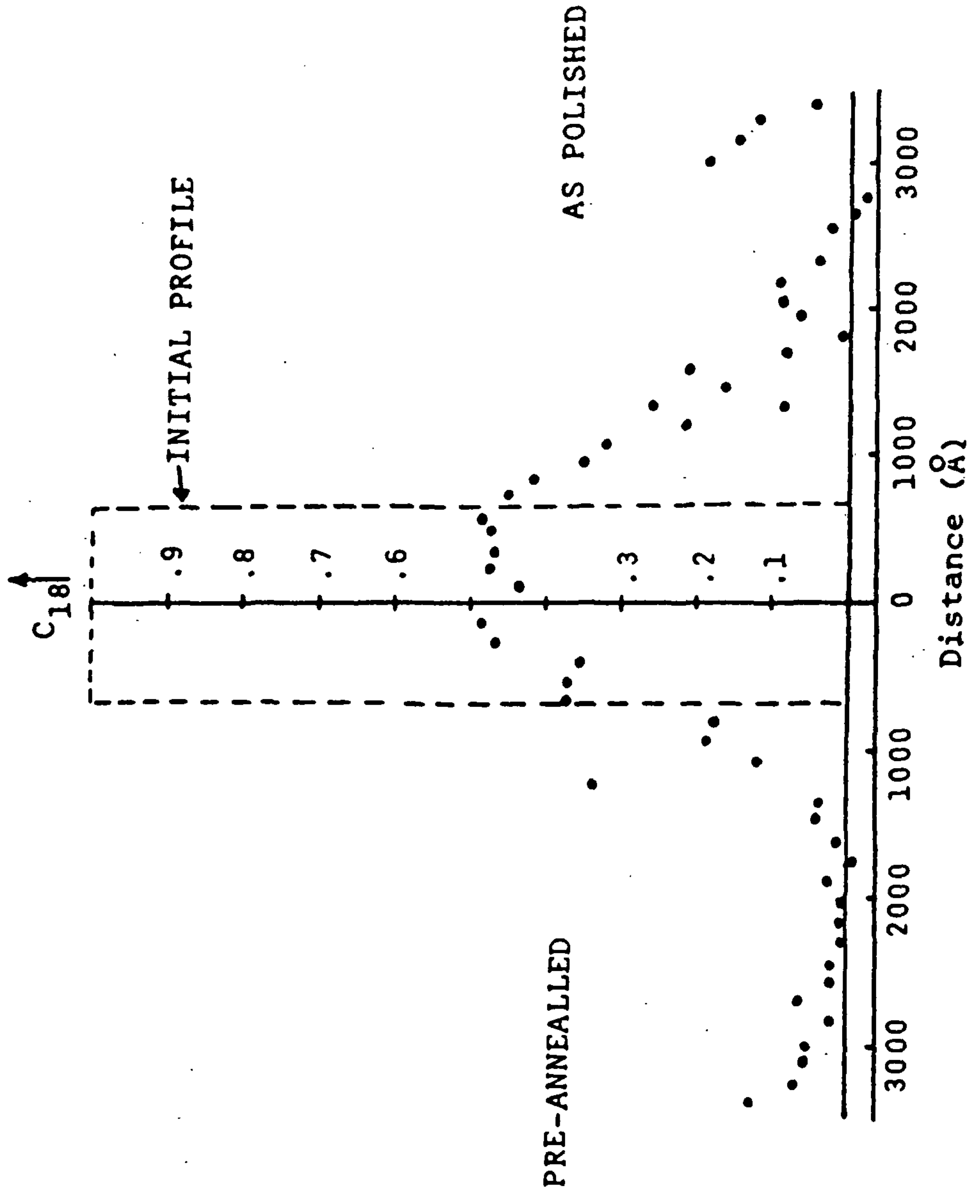

Figure 4. - Reed's diffusion couple at 1742° C for 2.0 hr.

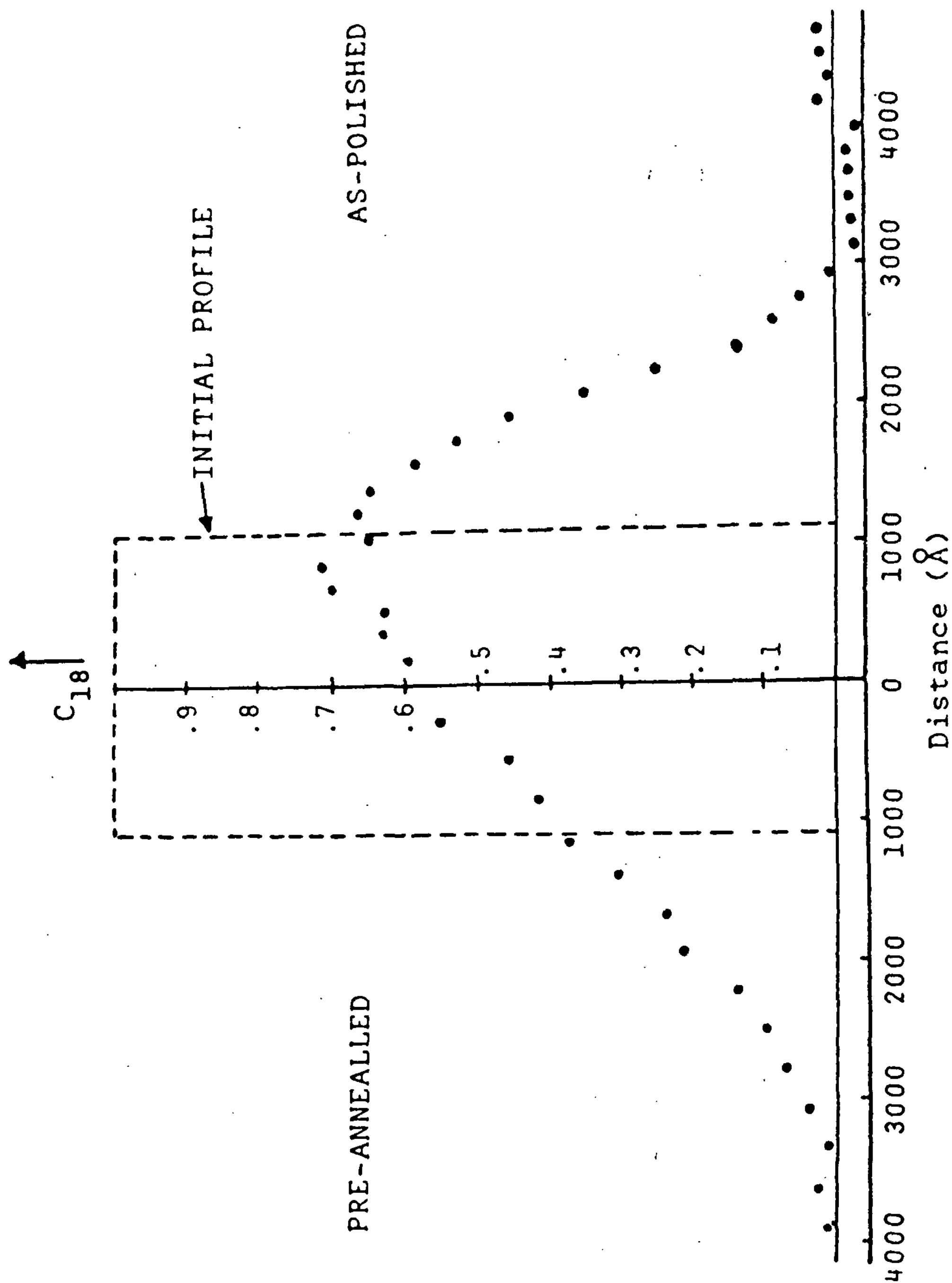

Figure 5. - Reed's diffusion couple at 1839° C for 1.1 hr.

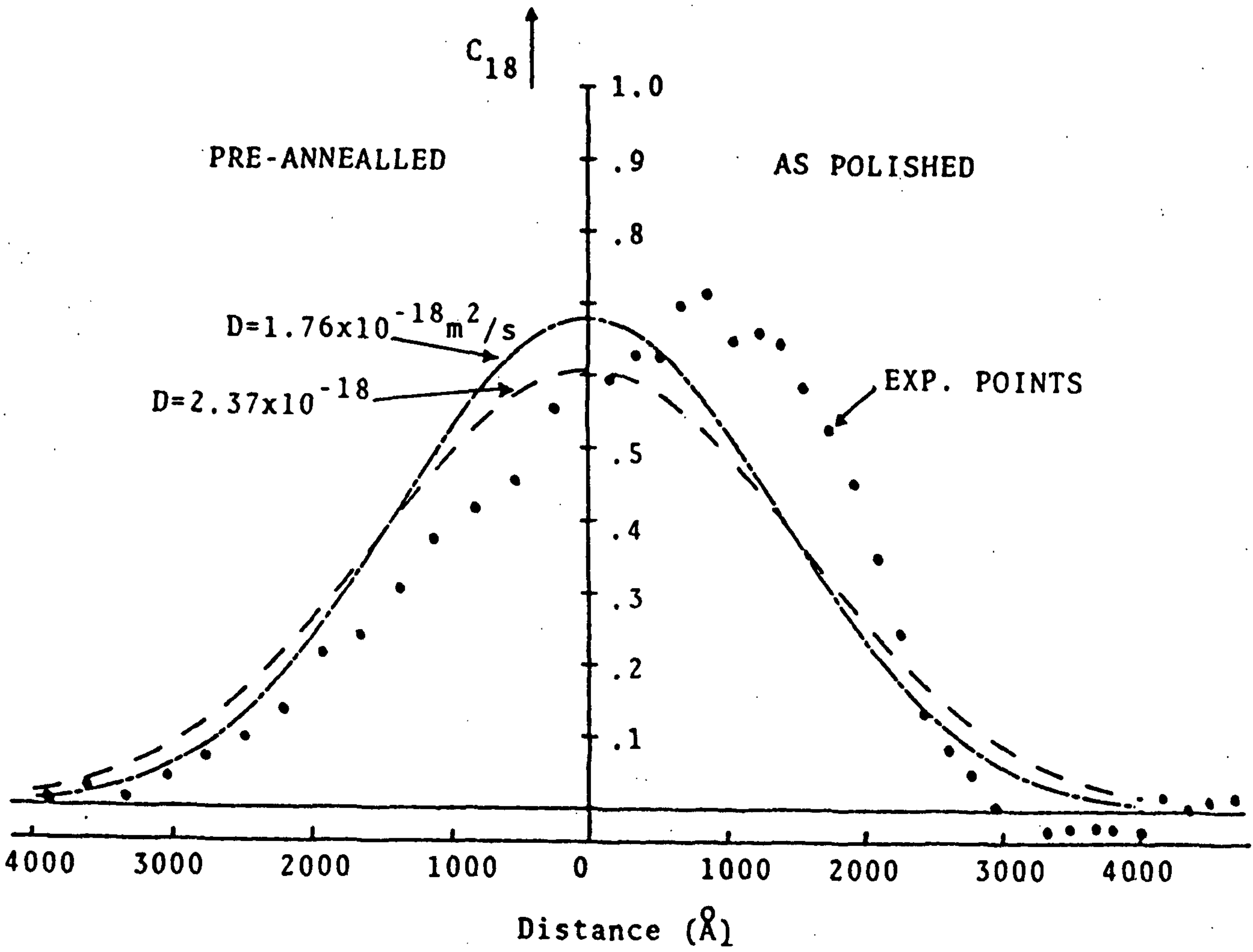

Figure 6. – Comparison of the reported values of the diffusion coefficient with Reed's experimental data at 1839° C.

on the sample. Note that this is the opposite of the finding of Reed; that tracer left the preannealed samples during the anneals.

In summary, this determination of diffusion coefficients seems to contain major flaws and it would be useful to have a second solid state experiment, to see if there is a true discrepency with the gas exchange results.

In addition, these exchanges were carried out at 10^{-5} atm total pressure in the furance, both Reed and Reddy pointed out that defect chemistry may be a function of P_{O_2} and therefore it is difficult to compare these results with those carried out at 1 atmosphere.

In the study of Reddy and Cooper, semi-infinite slabs of Al_2O_3 were annealed in an O-18 enriched atmosphere. The profile of O-18 versus depth was determined by the Single Spectrum Proton Activation technique (see Chapter 3). After deconvolation with a solution to Fick's Second Law which took into account a surface exchange reaction, this data was fit by:

$$D = 2.66 \times 10^{-2} \exp\left(\frac{-615\ \mathrm{kJ/mol}}{RT}\right)\ m^2/s \qquad (2.2\text{-}4)$$

This was in good agreement with the high temperature data of Oishi and Kingery.

In addition to Fickian profiles, when samples of as-received material were exchanged, deeply penetrating "tails" of low concentration were observed. It was stated that these "tails" could be reduced or eliminated by preannealing the samples in air.

As mentioned, Reddy analyzed Reed's five preannealed samples and determined diffusion coefficients by Proton Activation which corresponded well with the profiles determined by Ion Probe, indicating that the difference in D did not result from the technique used. Reddy also exchanged a slab of Reed's crystal in the apparatus at C.W.R.U. and found the resulting profile to be in agreement with the rest of his (Reddy's) work. Reddy offered an explanation of the discrepancy under the following assumptions:

(i) The Al_2O_3 in each case was pure

(ii) The P_{O_2} in Reed's setup was between 10^{-5} and 10^{-6},

(iii) No clustering, and

(iv) The mechanism of diffusion is interstitial. In pure Al_2O_3 interstitial oxygen has an oxygen partial pressure dependence resulting from the reaction:

$$\frac{1}{2} O_2(g) \rightarrow O_i'' + 2h^{\cdot} \qquad (2.2\text{-}5)$$

then, the equilibrium constant for this reaction is:

$$k_i = \frac{[O_i''][h^{\cdot}]^2}{P_{O_2}^{1/2}} \qquad (2.2\text{-}6)$$

therefore:

$$[O_i''] \propto P_{O_2}^{1/2} \qquad (2.2\text{-}7)$$

Since the concentration of oxygen interstitials depends positively on P_{O_2}, any transport by interstitials would decrease with decreasing P_{O_2}.

In addition to his investigations of undoped Al_2O_3, Reddy investigated two types of doped samples; one with a divalent impurity Mg, and one with a quadrivalent impurity Ti. The Mg-doped sample showed diffusion very similar to the undoped material. This was attributed to the evaporation of Mg from the near surface region, or the formation of second phase particles, where the profiles are determined. The Ti-doped material yielded values for the diffusion coefficient which were lower than those obtained with the undoped material by a factor of five.

Ti-doping is expected to enter the material by one of the following reactions:

$$3TiO_2 \rightarrow 3Ti^{\cdot}_{Al} + V'''_{Al} + 6O^{x}_{O} \qquad (2.2\text{-}8)$$

or:

$$2TiO_2 \rightarrow 2Ti^{\cdot}_{Al} + O''_{i} + 3O^{x}_{O} \qquad (2.2\text{-}9)$$

Either case would cause the concentration of oxygen vacancies to tend to decrease and the concentration of oxygen interstitials to increase. The fact that the diffusion coefficient decreased in the situation where the concentration of oxygen interstitials increased, was interpreted as evidence that oxygen diffusion does not take place by interstitial mechanism. This is inconsistent with the Reddy's explanation of Reed's data. It should be noted that the level of doping was high, 800 ppm. The reduction of D by a factor of five is surprisingly low.

The most recent work on alumina has been done by Oishi, Ando, and Matsuhiro[17]; and Oishi, Ando, and Kubota[18]. This work involved two procedures.

The first was a comparison of oxygen diffusion, in a very high purity Al_2O_3, prepared by chemical vapor deposition (CVD), with that in the relatively impure Verneuil of Oishi and Kingery. The samples were prepared using Oishi and Kingery's method of crushing the material and measuring the total amount of tracer absorbed. These results correlated very well in both the high and low temperature regions with those of Oishi and Kingery. This lack of dependence on impurity content was explained as having the secondary defects produced in crushing (e.g., dislocations) as having carried most of the tracer.

The second procedure employed semi-infinite slabs of Al_2O_3. There were preannealed for thirty minutes in natural oxygen at the temperature of the diffusion anneal. Two types of samples were used. Verneuil material, with impurities: 100Ti, 90Fe, 40Ca, 20Si, <10Mn, <10Mg, <10Ni, <10Na, <10Cu, and <10V ppm; and CVD material with total impurity content reported to be <0.1 ppm.

It was shown that the behavior had no dependence on composition and could be described by:

$$D = 1.12\times10^{-1} \exp\left(\frac{-649 \text{ kJ/mol}}{RT}\right) \text{ m}^2/\text{s} \qquad (2.2\text{-}10)$$

This was interpreted as evidence for intrinsic behavior. Other explanations include the possibilities that the samples were not as

clean as suggested or that the surface was contaminated by furnace atmosphere during the exchange.

Oishi, Ando, and Kubota also investigated the effect of preannealing. Samples which were preannealed at 1730° C in air showed enhanced diffusion whereas those samples preannealed at 1900° C in vacuo do not. This was attributed to the formation of dislocation networks or subgrain boundaries, from polygonization.

A summary of oxygen self-diffusion data from the four studies outlined above is presented in figure 7.

While aluminum self-diffusion is not directly related to oxygen self-diffusion, both are dependent on the defect structure of the material. Since anion and cation defect populations are related through Schottky and Frenkel products, the study of aluminum self-diffusion by Paladino and Kingery is of interest[19].

Diffusion couples were constructed by hot pressing two polycrystals together; one of which was enriched with a radioactive tracer, Al^{26}, which decays to $Mg^{26} + \beta^{+}$. The γ-rays resulting from the annihilation reaction $\beta^{+} + B^{-} \rightarrow 0.511$ MeV γ-ray were detected. The couples were annealed in air and the profile of tracer was subsequently determined by sectioning.

The diffusion behavior could be described by:

$$D = 2.8\times10^{-3} \exp\left(\frac{-477\ \text{kJ/mol}}{RT}\right)\ m^2/s \qquad (2.2\text{-}11)$$

While this was interpreted as intrinsic, the impurity analysis showed Mg, Ca, Fe, Mn, and Si all present in concentrations <100 ppm. Also,

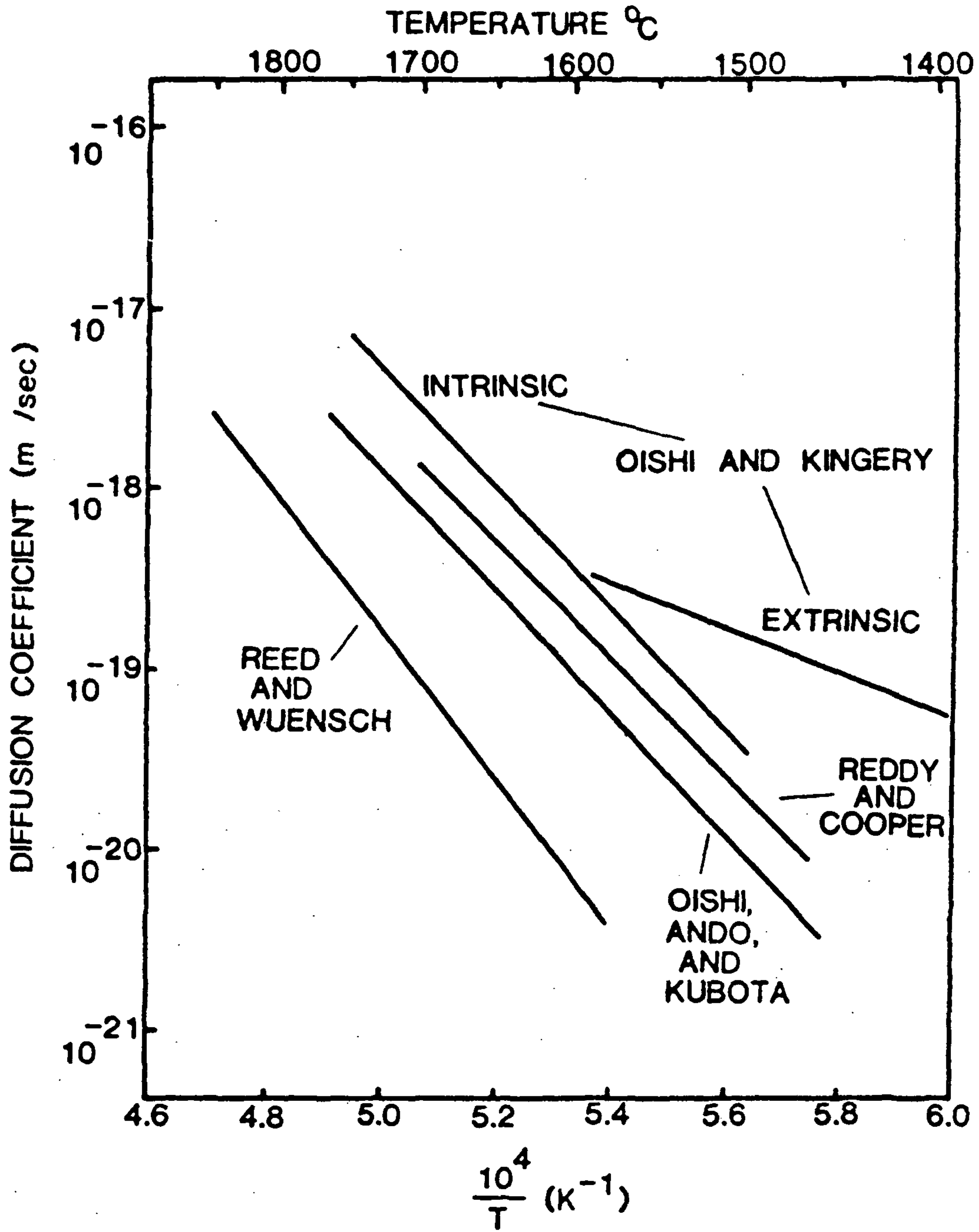

Figure 7. - Summary of oxygen self diffusion studies.

the concentration of Mg increases with time as the tracer disintegrates, therefore, it seems doubtful that this is truly intrinsic.

2.3 DEFECT ENERGY CALCULATIONS

There have been two sets of calculations, that of Dienes et al.,[20] and recently, that of Catlow, James, Mackrodt, and Stewart[21]. A summary of the results of the calculations is presented in table 1.

Both sets of calculations were made with a shell model-Mott Littleton approach. This included the assumption that the material under consideration was completely ionic. The calculations of Dienes et al., and the Hades II calculations of Catlow et al., assume dielectric isotropy, which is not appropriate for Al_2O_3 because all the ions do not sit in cubic symmetry. The Hades II and Hades III calculations of Catlow et al., use a larger number of atoms resulting in better convergence properties. Therefore it is felt that the calculations of Hades III are the current best estimates.

The Hades III calculations were made with both an empirical interionic potential derived from fits to available data on cohesive energy, lattice parameters, dielectric and elastic constants, and with nonempirical interionic potentials obtained by the method of Mackrodt and Stewart. The nonempirical approach allows potentials for redox and doping to be calculated in the same manner as those of the lattice.

TABLE 1. - DEFECT ENERGIES IN α-Al_2O_3 (kJ/defect)

Defect type	Empirical Potential		Nonempirical Potential	
	Hades II	Hades III	Hades III	Dienes et al.
Schottky Quintuplet	453	403	496	550
Anion Frenkel Pair	392	366	798	675
Cation Frenkel Pair	644	504	679	956

The choice of potential greatly affects the energies calculated for the defects and hence the type of disorder predicted to dominate. The calculation with the empirical potential suggests anion Frenkel will predominate, whereas the calculation with the nonempirical potential suggests Schottky disorder.

The empirical potential has the advantage of being derived from real crystals. However the interatomic forces at small distances, such as encountered with an interstitial, are not well determined by the experimental values (of cohesive energy, lattice parameters, and dielectric and elastic constants) used to determine the potential.

Calculations on doping were also performed. The results, with the nonempirical potential, for Ti-doping indicate that it is energetically more favorable for the compensating defect to be a cation vacancy, enthalpy of solution = 341 kJ/Ti, rather than an oxygen interstitial, 726 kJ/Ti. However, when the empirical potential was used it was not possible to select one mode of compensation over another.

In the calculations for Mg-doping, the results (with both types of potentials) show three mechanisms with nearly the same energy penalty. These are shown table 2.

Although Reddy explained the lack of effect of Mg-doping on the basis of evaporation, it is interesting to note that the type of disorder predicted to have the lowest energy is Mg substitutional on an Al site compensated for by Mg interstitials. In this situation it is not necessary to produce defects on the anion sublattice and oxygen diffusion could be unaffected.

Calculations done on the energy reduction gained by clustering of defects shows that the defect formation energies will involve a large stabilizing term from clustering and this will probably determine the type of disorder present. This is a new result. Virtually all previous work on Al_2O_3 has been interpreted on the basis of unassociated defects.

For example, it is predicted with these calculations, that even as little as 1 ppm Ti-doping, clustering will dominate up to 1500 K.

The defect clusters investigated by Catlow et al., show clustering tends to favor compensation by vacancies for both divalent and quadrivalent impurities, see table 3, since the amount of energy available from clustering is larger for those clusters involving vacancies, though as mentioned the choice of potential makes a large difference in the Ti case.

TABLE 2. - CALCULATED ENTHALPIES OF SOLUTION OF Mg IN α-Al_2O_3

Mode of Mg incorporation	ΔH_s, kJ/mg
$2MgO \rightarrow 2Mg_{Al}' + V_o^{\cdot\cdot} + 2O_o^x$	303
$3MgO \rightarrow 2Mg_{Al}' + Mg_i^{\cdot\cdot} + 3O_o^x$	292
$3MgO + Al_{Al}^x \rightarrow 3Mg_{Al}' + Al_i^{\cdot\cdot\cdot} + 3O_o^x$	346
$3MgO \rightarrow 3Mg_i^{\cdot\cdot} + 2V_{Al}''' + 3O_o^x$	558
$MgO \rightarrow Mg_i^{\cdot\cdot} + O_i''$	1348

TABLE 3. - BINDING ENERGIES OF CLUSTER IN α-Al_2O_3

Cluster	Energy, kJ/cluster
$2Ti_{Al}O_i$	-293
$3Ti_{Al}V_{Al}$	-503
$2Mg_{Al}V_o$	-246
Mg_iMg_{Al}	-234

2.4 DEFECT STRUCTURE OF α-Al_2O_3

2.4.1 Defect Diffusion in doped α-Al_2O_3

The diffusion of point defects has been studies by the movement of color boundaries in doped Al_2O_3.

In 1969, Jones, Coble, and Mogab[22] investigated the movement of the color boundary in Ti-doped, 5000 ppm, material. The presence of Ti^{+3} in Al_2O_3 produced a pink-violet color, whereas oxidized Ti^{+4} is optically inactive leaving the material colorless. Crystals which had been reduced by annealing in hydrogen were heated in air. After given intervals of time the samples were removed and the progression of the boundary into the sample was determined. It was stated that the defect with the highest diffusivity would be rate controlling. It was found that the movement of the boundary could be described by:

$$D = 4.3\times10^{-2} \exp\left(\frac{-335\ \text{kJ/mol}}{RT}\right)\ m^2/s \qquad (2.4\text{-}1)$$

It was suggested that this diffusivity was that of the point defect causing the oxidation.

Hower, Akul'Onok et al.,[23] who studied the same system in 1978 pointed out that the diffusivity of the boundary is related to the defect diffusivity by:

$$D_{boundary} = 2\,\frac{N_o}{C_o}\,D_{defect} \qquad (2.4\text{-}2)$$

where N_o is the equilibrium defect concentration and C_o is the initial concentration of impurity. They suggest the high dopant level, 5000 ppm, would make N_o/C_o a small enough number to signifi-

cantly change the deduced value of D; however, the activation energy term should remain very similar.

Akul'Onok et al., reduced the Ti by vacuum annealing and found good agreement with the value of D from Jones' H_2 reduced crystals. This indicates that the diffusion of hydrogen was not rate controlling.

Akul'Onok et al., also studied the effect of P_{O_2} on color boundary motion by annealing crystals in mixtures of He-O_2. A dependence of $P_{O_2}^{0.178}$ was found which most closely resembled that predicted if triply ionized aluminum vacancies were assumed to be the diffusing species. Supporting evidence for the rate limiting step involving a negatively charged defect was given in the form of an observed shift in color toward a positive electrode when the oxidation anneal was carried out under an electric field. This indicates the $V_{Al}^{'''}$ were compensated by holes, but that they are not bound into a complex.

The diffusion coefficient for aluminum vacancies, estimated from color boundary motion, at 1500° C is:

$\sim 4\times10^{-9}\ m^2/s$

compared with Paladino and Kingery's self-diffusion coefficient of aluminum at 1500° C is:

$1\times10^{-6}\ m^2/s$

The difference suggests that the self-diffusion of aluminum takes place by a mechanism involving a considerably less mobile defect. If aluminum diffuses by a vacancy mechanism, then:

$$D_{Al} = [V_{Al}]D_{V_{Al}} \qquad (2.4\text{-}3)$$

therefore:

$$[V_{Al}] = \frac{D_{Al}}{D_{V_{Al}}} \qquad (2.4\text{-}4)$$

using the values of Akul'Onok:

$$\frac{D_{Al}}{D_{V_{Al}}} = \frac{10^{-16}}{4\times10^{-9}} = 2.5\times10^{-8} \qquad (2.4\text{-}5)$$

This would correspond to a defect concentration of 0.025 ppm which is considerably less than the aliovalent impurity concentration, a puzzling result.

Cox[24] observed the motion of a color boundary in Mg-doped Al_2O_3 and found it proceeded much faster than the boundary in Ti material. It was stated that the rate of boundary motion in Mg-doped Al_2O_3 at 1000 K was equivalent to the rate in Ti-doped Al_2O_3 at 2000 K. He used this as an argument for an interstitial cation rather than an anion vacancy based on indications that the mobility of the former is greater than that of the latter. However, Mohapatra and Kroger have suggested that what was more likely observed is the diffusion of the hydrogen used in the reduction of the crystal.

2.4.2 Density Measurements

Rasmussen and Kingery[25] investigated the effect of the addition of dopants on the density and lattice parameters of Al_2O_3. The dopants employed were Ca, Mg, Cr, Ti, V, and Si.

The density measurements indicated that the donor dopants of Si and Ti were compensated by aluminum vacancies. There was also evidence for the solubility limits. In the case of Si-doping, regardless of the concentration of Si in the starting powder from which the crystals were grown (250, 500, 750, and 1000 ppm), the resulting crystal contained <250 ppm. In the Ti-doped material a second phase was observed in the samples with >500 ppm dopant.

In the crystals doped with the acceptors Ca and Mg, a second phase was present in all samples. The effect of the second phase on the density measurements was much greater than that arising from the production of defects. This made it difficult to draw any conclusions on the incorporation mechanism. What it does suggest is that the solubility limit for these ions is low, <400 ppm.

The Cr-doped samples show density change consistent with no defect production and the one sample containing vanadium indicated that it was also incorporated as an isovalent ion, V^{+3}.

2.4.3 Spectroscopic Investigations

Discussion in this section will be limited to results on defects in undoped Al_2O_3, defect clustering in acceptor doped Al_2O_3, and Al_2O_3 co-doped with acceptors and donors (since in practice all samples contain both), and nickel-doped Al_2O_3 (since this is our acceptor).

2.4.3.1 Undoped α-Al_2O_3

Lee and Crawford[26] found that when undoped alumina was heated to 2000° C in a strongly reducing environment the material became colored, with the principle absorption at 6.1 eV. This was attri-

buted to an F-Center, an oxygen vacancy associated with two electrons, on the basis of the observed symmetry.

The absorption of 6.1 eV. was unaffected by postcoloration anneals up to 1300° C and that an anneal of one-half hour at 1400° C was insufficient to remove much color. This was contrasted to the ease with which coloration produced by neutron irradiation can be annealed out.

The difference in rate of color center removal by annealing may be used as an argument for Schottky defects predominating in undoped alumina. It is considered that the majority of defects produced by neutron irradiation are Frenkel pairs. The neutron knocks an ion from its lattice position into an interstitial site. In annealing out such Frenkel defects the relevant diffusion distance governing the kinetics is that between the interstitial and the vacancy which can recombine. The Frenkel reactions for Al_2O_3 are:

$$V_o^{\cdot\cdot} + O_i^{''} \rightarrow O_o^{x} \qquad (2.4\text{-}6)$$

$$V_{Al} + Al_i^{\cdot\cdot\cdot} \rightarrow Al_{Al}^{x} \qquad (2.4\text{-}7)$$

However, in the case of Schottky disorder, the vacancies must travel to a sink, et., dislocations or the crystal surface. The Schottky reaction for Al_2O_3 is:

$$2V_{Al}^{'''} + 3V_o^{\cdot\cdot} \rightarrow \text{Null} \qquad (2.4\text{-}8)$$

In this case the distance across which the defect must migrate is related to the dislocation density and the sample thickness. This

is presumably a much greater distance than for Frenkels, leading to the increased resistance to the defect removal through annealing.

It should be noted that there is some question as to the purity of the material since no results of a chemical analysis are given.

2.4.3.2 Defect Clustering

The EPR spectra of Al_2O_3 and Al_2O_3 doped with iron have been studied by Bauer and Whitmore[27]. The material was doped with 15, 30, and 230 ppm Fe. In order to account for the observed g-values, the symmetry of the centers, and the dependence of the absorption on Fe content, the investigators found it necessary to invoke clusters of defects containing the cation impurities.

In a study of Fe-doped, Ti-doped, and Fe-Ti co-doped Al_2O_3, Eigenmann and Gunthard[28] used Verneuil grown material doped with Fe at 75 ppm, Ti at 350-600 ppm, Fe-Ti at 250 to 1000 ppm Fe, and 50 to 350 ppm Ti.

It was reported that the ESR and optical spectra of the Fe-Ti co-doped material could not be accounted for by the summation of the spectra from the singly doped materials. This is evidence for cluster formation, in this case, Fe-Ti ion pairs.

2.4.3.3 Nickel Doping

In the spectroscopic studies of Ni-doped Al_2O_3 the valence state of the nickel has been unclear. McClure[29] observed that heating a Ni-doped crystal in a vacuum to 1600° C for fifteen minutes (Verneuil grown with 0.2 mol percent Ni in the starting material) removed the coloration associated with Ni^{+3} but that the coloration associated with Ni^{+2} did not appear. Also observed was that upon heating the

crystal to 1600° C in an oxidizing environment, the Ni^{+3} color was restored.

In another study of Ni-doped Al_2O_3, Marshall, Kikuchi, and Reinberg[30] also observed the color change upon heating the sample in a vacuum to 1800° C for two hours; but no change in the EPR spectra was observed. It was also noted in this study that two Verneuil grown crystals with quite different amounts of nickel oxide in the starting material, 0.4 percent and 4.0 perccent, showing identical EPR spectra with only a slight difference in intensity. This suggests that the solubility of nickel in alumina $\leq$0.4 percent.

Muller and Gunthard[31] were able to reduce Ni-doped Al_2O_3 with hydrogen at 800° C and found the EPR spectra changed. The amount of hydrogen uptake was measured and found to be 1.0 ± 0.7 H/Ni. It was also observed that H_2 was present in the crystals stemming from the Verneuil process.

In summary, the spectroscopic studies of nickel-doped alumina have produced interesting yet inconsistent results and it remains to be explained why the nickel is apparently not reduced in vacuum.

2.4.4 Electrical Conductivity Measurements

The conductivity in alumina is very small and is therefore difficult to measure. In 1965, Peters, Fienstein, and Peltzer[32] found that the conductivity measured by their equipment was the same value whether or not the sample was in place. This was attributed to conduction through air.

Kitazawa and Coble[33] measured the conductivity of undoped alumina in the temperature range of 900° to 1700° C, being careful

to choose sample configurations so as to block the external circuits through the gas phase and along the surface. The resulting conductivity versus temperature plot shows two linear regions with different activation energies: 238 kJ below 1300° to 1400° C and 335 kJ above 1400° C.

It was also observed that conductivity was electronic at high temperatures (>1600° C) being n-type at low P_{O_2} and p-type at high P_{O_2}, and ionic at lower temperatures. On the basis of the subsequent work of Kroger et al., it seems more likely that the observed conductivity was mixed ionic-electric in all temperature ranges.

Kroger and his co-workers have conducted numerous studies on the conductivity of both undoped and doped alumina. It is appropriate to review these studies in chronological order stating the findings of each and offering comments. In none of these studies is a break observed in conductivity versus 1/T, however, these measurements are confined to the high temperature region (>1300° C) of Kitzawa and Coble.

In 1975, Dutt, Hurrell and Kroger[34] studied cobalt-doped alumina (impurity levels in ppm 31 Co, 4.6 Cr, <8 Fe, 52 Si, 1.3 Mg, and 5.0 Ca in ppm) using optical absorption, ESR, electrical conductivity, and EMF measurements. The presence of cobalt was found to increase the conductivity. When the cobalt is divalent it is a negative defect Co'_{Al} and the concentration of positive defects $V_O^{\cdot\cdot}$, $Al_i^{\cdot\cdot\cdot}$, and $h^{\cdot}$ must increase to compensate. Based on a comparison of aluminum and oxygen self-diffusion in alumina it is postulated that the defect responsible for the ionic conductivity is $Al_i^{\cdot\cdot\cdot}$.

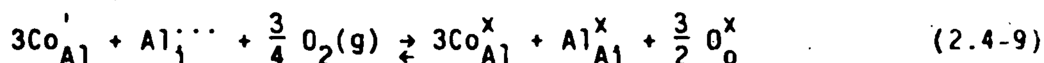

$$3Co'_{Al} + Al_i^{\cdot\cdot\cdot} + \frac{3}{4}\,O_2(g) \rightleftarrows 3Co^x_{Al} + Al^x_{Al} + \frac{3}{2}\,O^x_o \qquad (2.4\text{-}9)$$

To reconcile discrepancies between theoretical predictions and experimental data it had to be assumed that an unknown donor was present, that this donor was fixed valence, and that the donor level was above the cobalt level in the bandgap. While this is possible, the presence of the donor was not experimentally verified. The only donor which showed up in the spectro-chemical analysis was silicon and this was thought to be an artifact.

Dutt and Kroger[35], also in 1975, interpreted the data of Pappis and Kingery on conductivity in alumina and came to the conclusion that aluminum interstitials were the ionic charge carries and holes were the electronic charge carries. The measurements of Pappis and Kingery were made in an improperly guarded cell. A correction factor based on the work of Dutt and Kroger on Co-doped alumina, in a different setup, was applied to these measurements, which casts some doubt on the reliability of the analysis.

In 1977, Mohapatra and Kroger[36] investigated Mg-doped Al_2O_3. It was not clear however that the sample was Mg-doped as the spectrochemical analysis showed other impurities of significant concentrations: 5 Cr, 10 Mg, 5 Fe, 5 Si, 1 Co, 1 Ca, 2 Na ppm. It was also stated that between 12 to 90 percent of the total conductivity measured was due to surface and gas phase conduction. The authors were

unable to conclude whether aluminum interstitials or oxygen vacancies were the defect responsible for ionic conduction.

In 1977, Mohapatra and Kroger[37] also studied Ti-doped alumina. Analysis of this material indicated a well-doped crystal, 430 ppm Ti, 6.2 Ca, 1.2 Mg, and 26 Si. The authors suggest that clusters of $(3Ti_{Al}V_{Al})^x$ may form but they assume, without evidence, that the clusters have disassociated at the temperature of measurement, 1600° C. Further, they conclude that aluminum vacancies are the ionic charge carries and electrons the electronic charge carries, although it is pointed out that a model based on oxygen interstitials is only slightly less satisfactory.

In 1978 Mohapatra and Kroger[38] reviewed the data available at the time and compared it with the defect energy calculations of Dienes et al. The point is made, by the authors, that to get information on the defect structure in Al_2O_3 from conductivity, self-diffusion, creep, and sintering involves testing models against P_{O_2} dependencies.

$$X = B\,(P_{O_2})^r\ [\text{dopant}]^s \qquad (2.4\text{-}10)$$

where X is the property of interest and B is a proportionality constant. The exponents r and s are often very similar for different models. There is often a large uncertainty in the experimentally determined values of these processes in alumina. This is contributed to by the fact that conductivity is low, self-diffusion rates are low, etc. This makes it difficult to distinguish between models.

The authors then go on to interpret the available data as indicating a predominance of Schottky disorder, despite mentioning arguments by others that there is evidence for Frenkel predominance.

In 1979, Mohapatra, Tiku, and Kroger[39] addressed the question of finding Al_2O_3 pure enough to show behavior not dominated by impurities. One sample used, grown on a molybdenum die, displayed acceptor dominated behavior despite the fact that the spectrochemical analysis showed only marginal traces of acceptors 1.3 Mg, 0.7 Cu, 2.8 ppm Ca, and a sizeable donor concentration, 53 ppm Si, with the 41 ppm Mo assumed isovalent with Al. A second sample grown by the Czochralski method initially showed donor doped behavior which changed to acceptor dominated after annealing is oxygen. The donor behavior was attributed to hydrogen incorporated into the material during growth. In the interpretation of this data, arguments are, again, found for both Schottky and Frenkel defects as the majority species.

In 1980, Tiku and Kroger[41] further investigated the presence of hydrogen in alumina and its action as a donor. Despite the fact that data points garnered by extrapolation are plotted in several figures and that linear behavior is sometimes tested with only two measurements, there seems to be convincing evidence for hydrogen acting as a donor. This is in accordance with the observation that hydrogen may reduce impurities. Efforts to deduce the dominant type of native disorder using this information were unsuccessful.

Also in 1982, El-Aiat and Kroger[42] investigated yttrium as a possible donor, due to misfit strain, in alumina. The material

used was obtained from the same source as that used in the present work. The crystal we obtained, as will be shown later, had all of the yttrium segregated to its surface and had bulk impurity levels virtually identical to that of our undoped crystal. This raises a question as to whether or not the donor doped behavior of the crystal in El-Alat's work is truly due to the presence of yttrium. It is also stated that the crystal used as an undoped standard contains "cloudy areas" and behaves as if it were acceptor doped.

Other points of the paper which tend to diminish its credibility are the fact that the transference numbers are derived from the slope of a curve determined by just three points and the fact that the yttrium-doped crystal has a conductivity which is time dependent after a temperature change. It does not seem there is enough evidence at present to conclusively indicate that yttrium does in fact act as a donor.

A conclusion based on the electrical conductivity data in terms of unasssociated point defects seems to be very difficult. In light of the new defect calculations it may be that clustering is of major importance and will have to be taken into account. Such a review and reinterpretation will not be attempted here.

2.4.5 Sintering Studies

The sintering behavior of Al_2O_3 has been widely studied. In this section only a few points relevent to the present study will be brought out.

The role of both acceptors and donors has been investigated. Rao and Cutler[43] studied the effect of Fe and Ti doping. Bagley,

Cutler, and Johnson[44] also studied the effect of Ti doping. Brook[45] further interpreted their data. The conclusions arrived at were based on Frenkel defects with cation diffusion being the rate controlling step, with the compensating defects being aluminum interstitials for iron and aluminum vacancies for titanium.

Mistler and Coble[46] using the single crystal and polycrystal oxygen diffusion data of Oishi and Kingery and the aluminum diffusion of Paladino and Kingery, under the assumption that aluminum diffusion is not enhanced by grain boundaries, calculated that with a grain size below 5 μm, the diffusion of aluminum would be rate controlling.

Delaunay, Huntz, and Lacombe[47] conducted an investigation into the effect of yttrium on sintering of Al_2O_3. The particle size of the Al_2O_3 was 50Å, which is well below the Mistler critical size. It was found that the addition of yttrium increased the observed sintering rate, with additions of up to 1 percent. By inference, the addition of yttrium increases the diffusion of aluminum rather than impedes it, as was suggested by Golightly et al.

2.4.6 Creep Studies

Creep studies can give information about the rate controlling step. In Al_2O_3 this is generally believed to be lattice diffusion of aluminum, although Lessing and Gordon have shown that with large grain size in a heavily acceptor doped material, grain boundary diffusion of oxygen may become limiting.

Studies of acceptor, Fe, and donor, Ti, doped material have been carried out by Hollenberg and Gordon[48]; Lessing and Gordon[49]; Hou, Tiku, Wand, and Kroger[50]; and El-Aiat, Hou, Tiku, Wand, and

diffusion control, with the exception mentioned above. The defect in Fe-doped material was felt to be Al_i and in Ti-doped material to be V_{Al}. Gordon and co-workers felt this to be evidence for Frenkel disorder while Kroger and co-workers were able to show that this was not the only situation which would satisfactorily explain the results.

Kroger and co-workers[50 and 51] also measured the conductivity of the materials used in the creep studies. The results indicated that while there was grain boundary contribution to electronic conduction, no contribution was evident in the ionic conduction. This was interpreted as evidence for grain boundary diffusion by a neutral oxygen species, O_i^x.

2.4.7 Deformation Work

Pletka, Mitchell, and Heuer[52] studied the hardening of sapphire with isovalent and an aliovalent impurity. The hardening achieved from the solid solution of isovalent impurities Cr^{3+}, Ti^{3+}, was due to the development of a strain field resulting from the differences in ionic radii. The much greater effect, an order of magnitude, of Ti^{4+} was explained using a model of defect clusters. The proposed cluster consisted of a cation vacancy surrounded by three quadravalent impurities.

Later work by Phillips, Mitchell, and Heuer on the growth of dislocation arrays during the precipitation of rutile in Ti-doped sapphire (star sapphire) led to the conclusion that the compensating defect for the Ti was an oxygen interstitial rather than an aluminum vacancy.

Currently, Lagerlof and Heuer[54] are investigating the annihilation of dislocation loops in cylinders of Al_2O_3 which are deformed, generating a large population of dislocations. The radii of small loops are observed by TEM as a function of annealing time. Based on measurements of the radii of these loops, and the assumption that self-diffusion of oxygen is rate controlling, an oxygen self-diffusion coefficient can be calculated (see fig. 8). The calculated diffusion coefficients for undoped Al_2O_3 agree very well with the extrapolation of the data of Oishi, Ando, and Kubota. However, in Mg-doped Al_2O_3 the calculated diffusion coefficients are much higher, a factor of 50, than in the undoped case and in Ti-doped Al_2O_3 the calculated diffusion coefficients are lower, a factor of 5, then in the undoped case. This dopant dependence is in contrast to the impurity independence of Oishi, Ando, and Kubota.

2.4.8 Summary

The determination of the defect chemistry in terms of unassociated point defects has been generally unsuccessful. There is growing evidence that clustering of defects is important even with low defect concentrations and at high temperature.

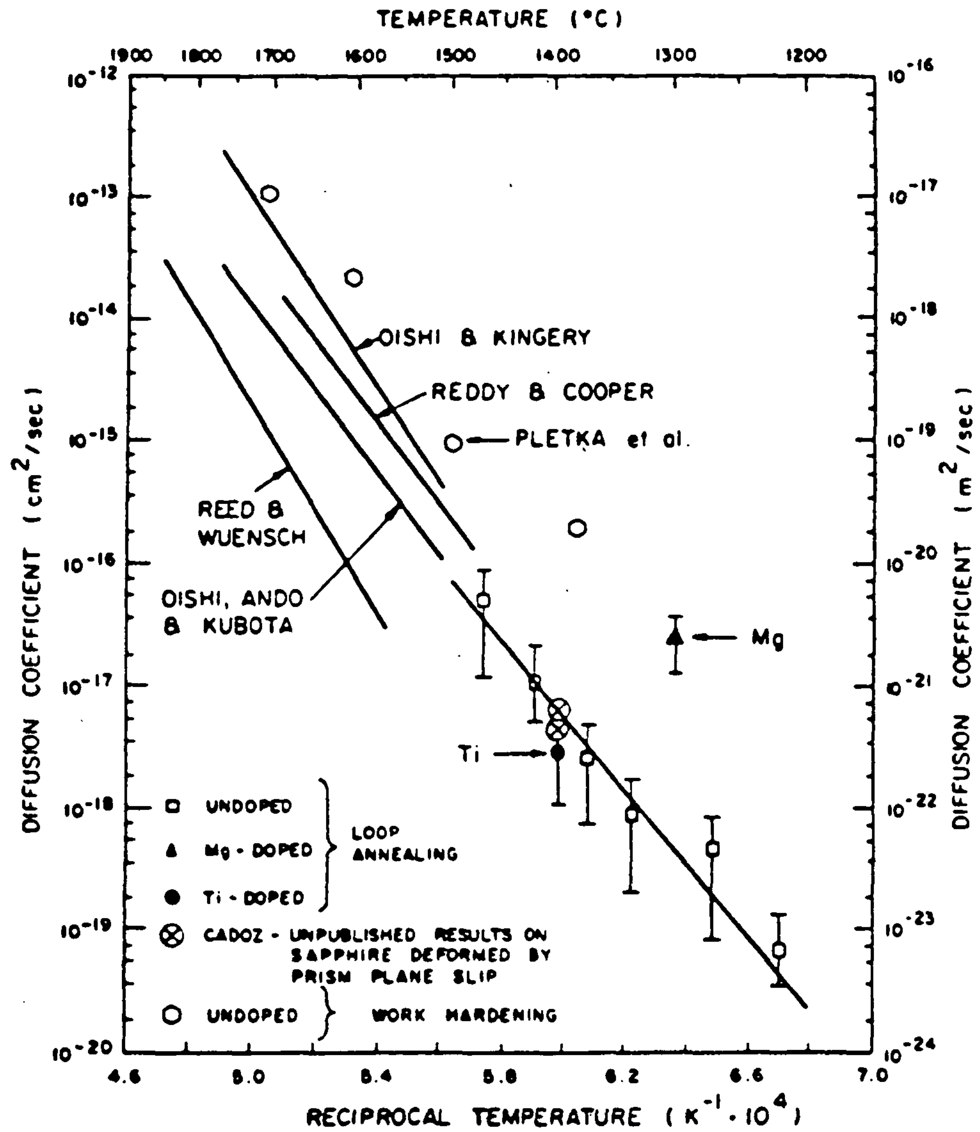

Figure 8. - Diffusion coefficients determined from dislocation loop annihilation. (figure taken from Reference 54).

CHAPTER III

EXPERIMENTAL PROCEDURE

3.1 SAMPLE PREPARATION AND CHARACTERIZATION

3.3.1 Single Crystal Samples

Single crystals were obtained through NASA Lewis Research Center[1]. These crystals were grown in France by La Pierre Synthetique Biakowski International.

The crystals were grown by the Verneuil process. It was the intent of the study to have five crystals of different composition, an undoped crystal and four singly doped crystals; one with yttrium, one with chromium, one with nickel, and one with zirconium. The starting material for the doped crystals was reported to have contained 100 ppm of the desired impurity. The undoped crystal appeared clear and well-formed, that is, with a smooth surface and an even shape. The chromium-doped crystal had a uniform red color and was also well formed. The nickel-doped crystal appeared green-yellow, however, it had a deeper coloration toward the center of the boule than at the edges. It was also a well-formed crystal. Both the yttrium-doped and the zirconium-doped crystal showed what appeared to be precipitates on the surface of the boule. These precipitates were a brown color in the case of the yttrium-doping and a white color in the case of the zirconium-doping (see figs. 9 and 10).

---

[1]Courtesy of Dr. J. Smialek, NASA Lewis

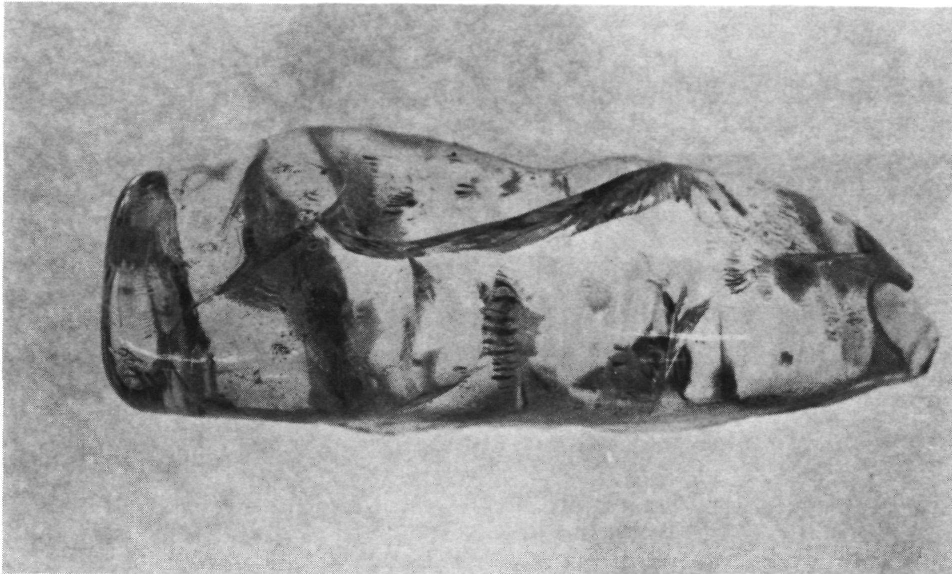

Figure 9. - Photograph showing precipitates on the Y-doped boule.

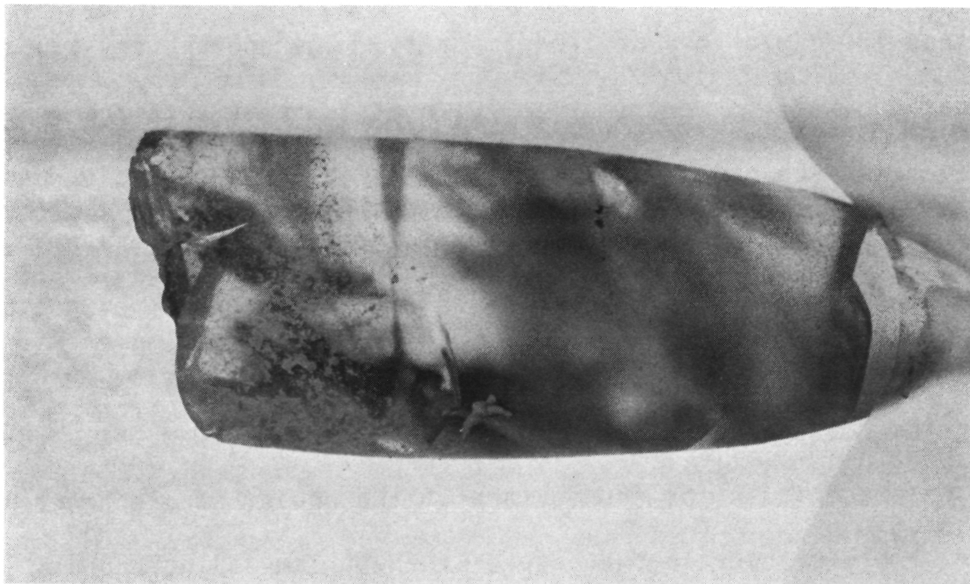

Figure 10. - Photograph showing precipitates on the Zr-doped boule.

While the zirconium-doped crystal appeared to be evenly shaped, the yttrium-doped crystal had an irregular shape with three large-scale facets having formed along the length of the boule. Both crystals contained numerous cracks in their interiors.

Two types of samples were submitted to Coors Spectrochemical Laboratories for analysis. The results are shown in table 4.

TABLE 4. - ANALYSIS OF SINGLE CRYSTALS[a] (ppm)

	Sample	Ca	Cr[b]	Fe	Mg	Ni[b]	Si	Na	Y[b]	Zr[b]	Total
Undoped	C1	5.6	---	16	23	--	27	4.5	---	---	76.1
	N8/4	6.0	---	14	30	--	34	5.6	---	---	89.6
	N8/2	10.0	---	14	26	--	42	7.0	---	---	99.0
Y-doped	C2	5.8	---	14	27	--	37	5.6	<10	---	89.4
	N10/3	6.0	---	11	18	--	28	5.2	150	---	236.2
	N10/1	4.0	---	14	17	--	52	6.2	18	---	111.2
Zr-doped	C3	9.4	---	10	30	--	57	5.2	---	<10	121.6
	N13/4	8.5	---	16	17	--	28	7.0	---	410	486.5
	N13/2	6.0	---	15	21	--	50	6.3	---	86	
Ni-doped	C4	4.6	---	11	15	15	33	4.2	---	---	82.8
	N9/4	5.4	---	9	16	30	32	5.0	---	---	97.4
	N9/2	17.0	---	18	17	22	37	5.2	---	---	116.2
Cr-doped	C3	6.0	118	24	20	--	33	5.2	---	---	206.2
	N7/2	17.0	114	22	17	--	42	16.2	---	---	228.2
	N7/3	8.5	110	22	15	--	47	6.2	---	---	208.7

[a]Coors Spectrochemical Laboratory.
[b]Dopant.

The samples with the prefix 'N' consisted of a full slice of the boule, and those with the prefix 'C' were slices of the boule from which the outer edge, or the "skin," had been ground off with a diamond lap (45 μm). In the case of the undoped, Cr-doped, and Ni-doped samples, there is little difference between the two types. The

analysis of the undoped crystal reveals a level of background impurities around 100 ppm. The Cr-doped crystal had a similar amount of background impurities with the intended level of dopant, 100 ppm, almost precisely being obtained. The Ni-doped crystal, while appearing colored to the eye, did not have a sufficient amount of nickel such that its presence would dominate the crystal behavior. There is as much magnesium and twice as much silicon. In both the case of Y-doped and Zr-doped samples there is a striking difference between the two types. The "surface removed" type had no dopant detected and showed background impurities similar to the undoped crystal. The "full slice" types showed the presence of the dopant in concentrations which varied dramatically between samples by a factor of between five and eight. This indicates that the dopant is rejected to the surface of the boule during crystal growth. This was later confirmed by SIMS analysis, the surface precipitates on each boule found rich in the dopant, (figs. 11 and 12).

A 'single precipitate' was removed from the surface and analyzed with an SEM[2]. Prior to analysis the sample was polished with 6, 3, and 1 μm diamond paste followed with a Syton etch. The polish was done at a slight angle to reveal the boule/precipitate interface. Figure 13 shows low magnification micrographs of the precipitate. It can be seen that the microstructure is complex but very ordered, similar to that of eutectic phase. Also visible are isolated islands of the eutectic phase and a long "stringer," which may be responsible

---

[2]NASA Lewis' AMRAY 1200

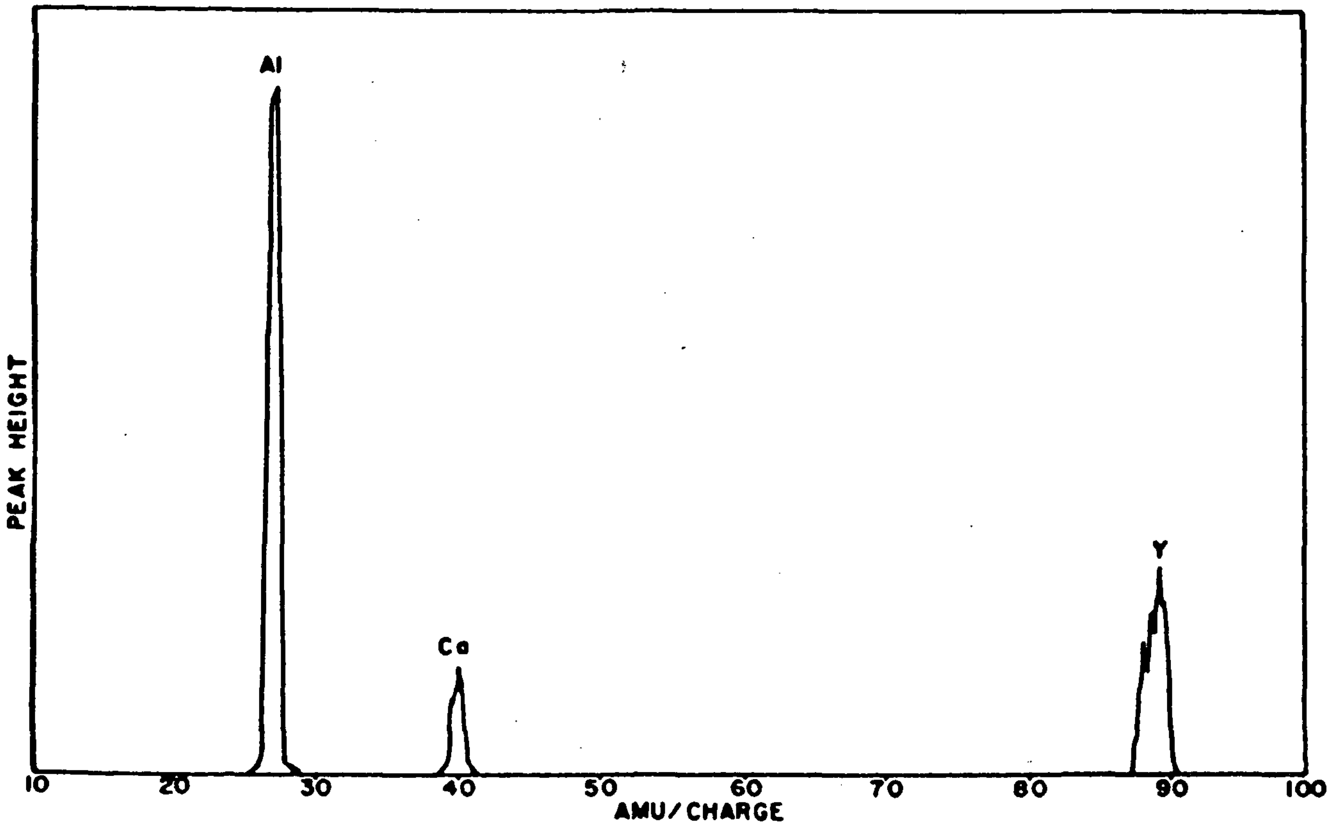

Figure 11. - Mass scan of precipitates on the Y-doped boule.

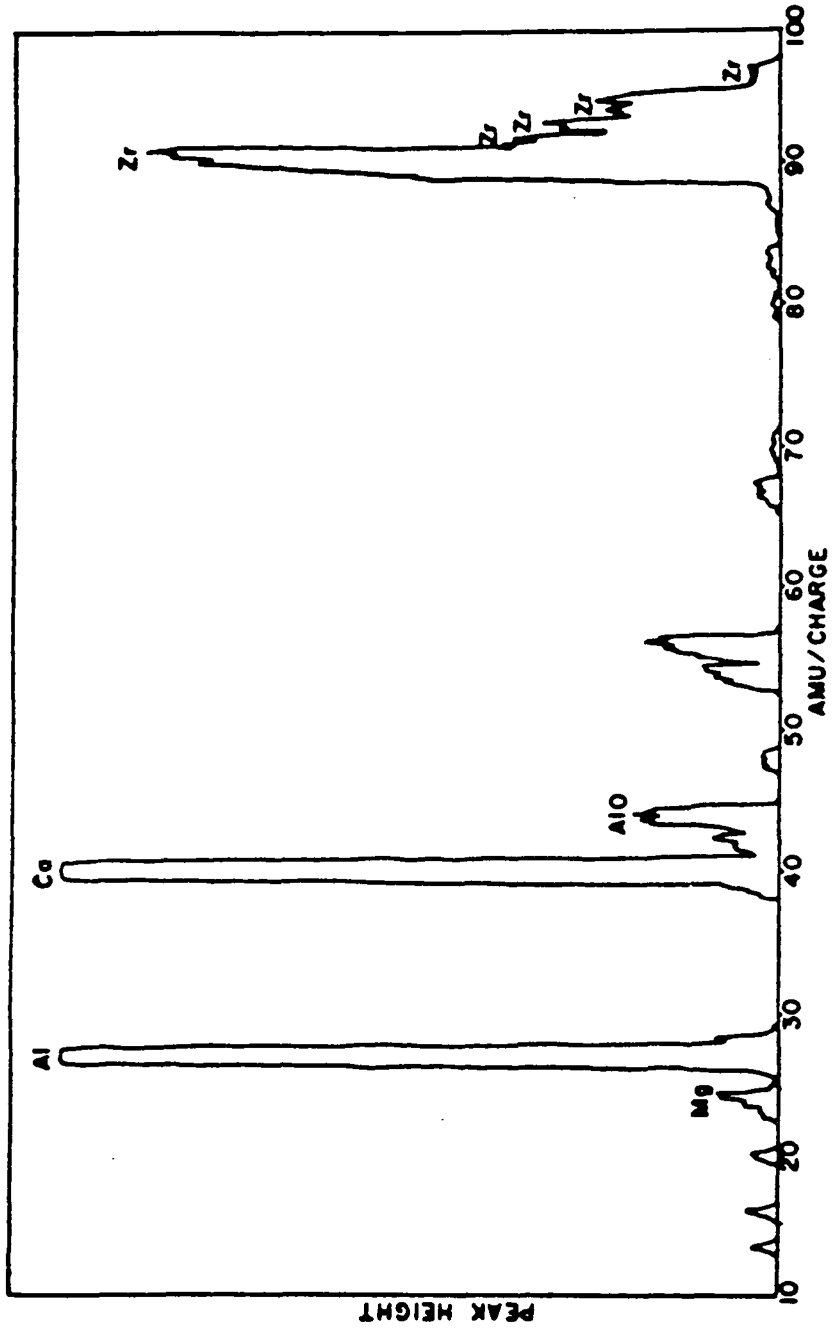

Figure 12. - Mass scan of precipitates on the Zr-doped boule.

a

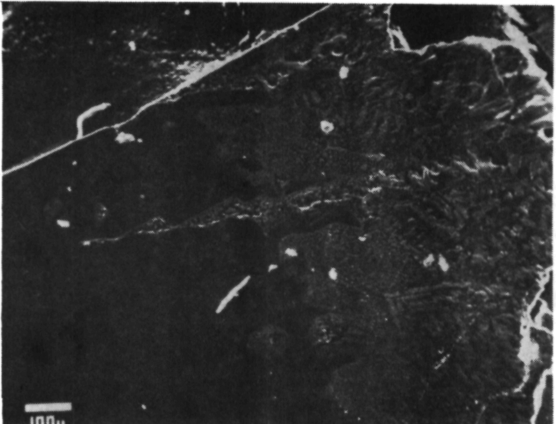

c

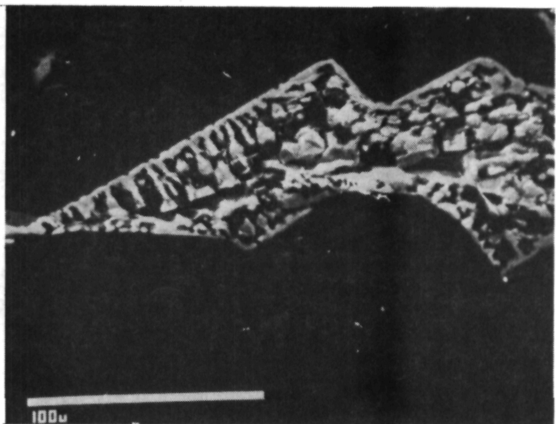

b

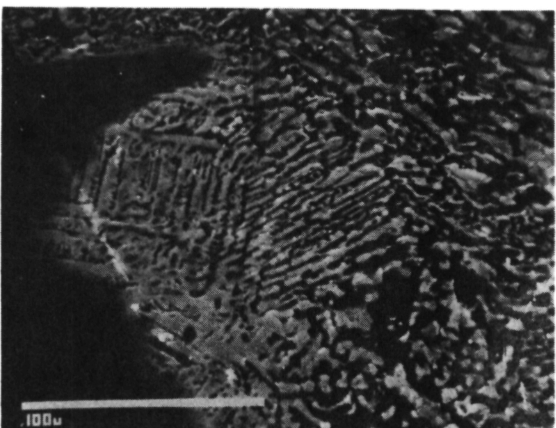

Figure 13. - Low magnification optical micrographs of precipitate from Y-doped boule. a) SEM micrograph of sapphire and precipitate showing eutectic type microstructure, b) close-up of sapphire precipitate interface, c) close-up of "stringer" showing facets.

for the internal cracking in the boule. It is interesting that the facets on the "stringer" form an angle which appears to be the same as the large scale facets on the boule. Evidently there is an epitaxy problem in the growth of this phase, though no serious investigation into it was made.

A region of rather coarse microstructure was investigated with EDAX. An EDAX spectrum is shown in figure 14. All the peaks could be accounted for by Al, Y, Ca, and Au. The Au was deposited to dissipate charge in the microscope. The other three were also present in the SIMS. A micrograph and element maps for this area are shown in figure 15.

It is clear that the phase which appears white in the micrograph is enriched in yttrium while the dark phase is enriched in aluminum and has a very low yttrium content. The calcium does not have a significant correlation to the apparent microstructure and is treated as a trace impurity[3].

The implication of this is that during crystal growth the dopant is continuously rejected to the melt until the local concentration becomes sufficient to form this eutectic mixture on solidification. The fact that spectroscopic samples taken from a crack free interior

---

[3]Samples of this boule were given to Bob McCune (at Ford Motor Co.) and his analysis found this boule to contain more Ca than the boule of intentionally Ca-doped sapphire purchased from the same manufacturer. In addition he found an axial gradient, first grown end ~15 ppm last grown >300 ppm.

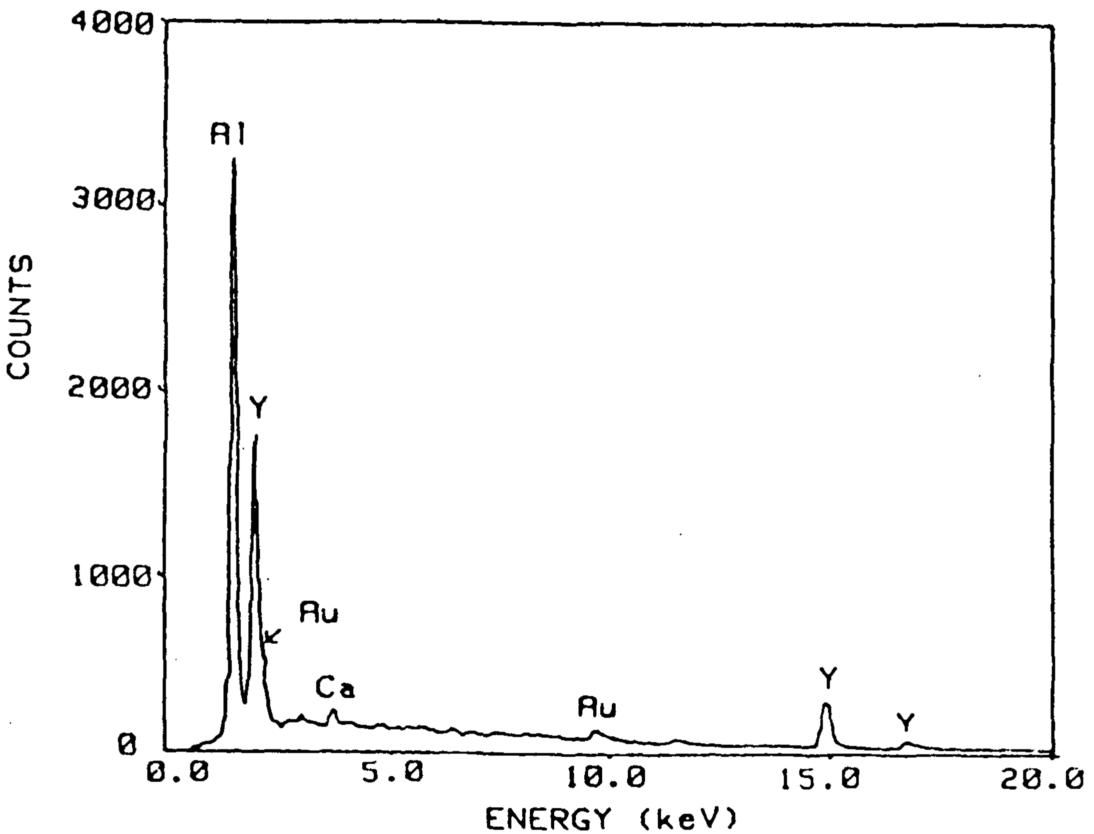

Figure 14. - EDAX spectrum of precipitate from Y-doped boule showing the presence of Al, Ca, and Y. The Au was deposited to prevent charging.

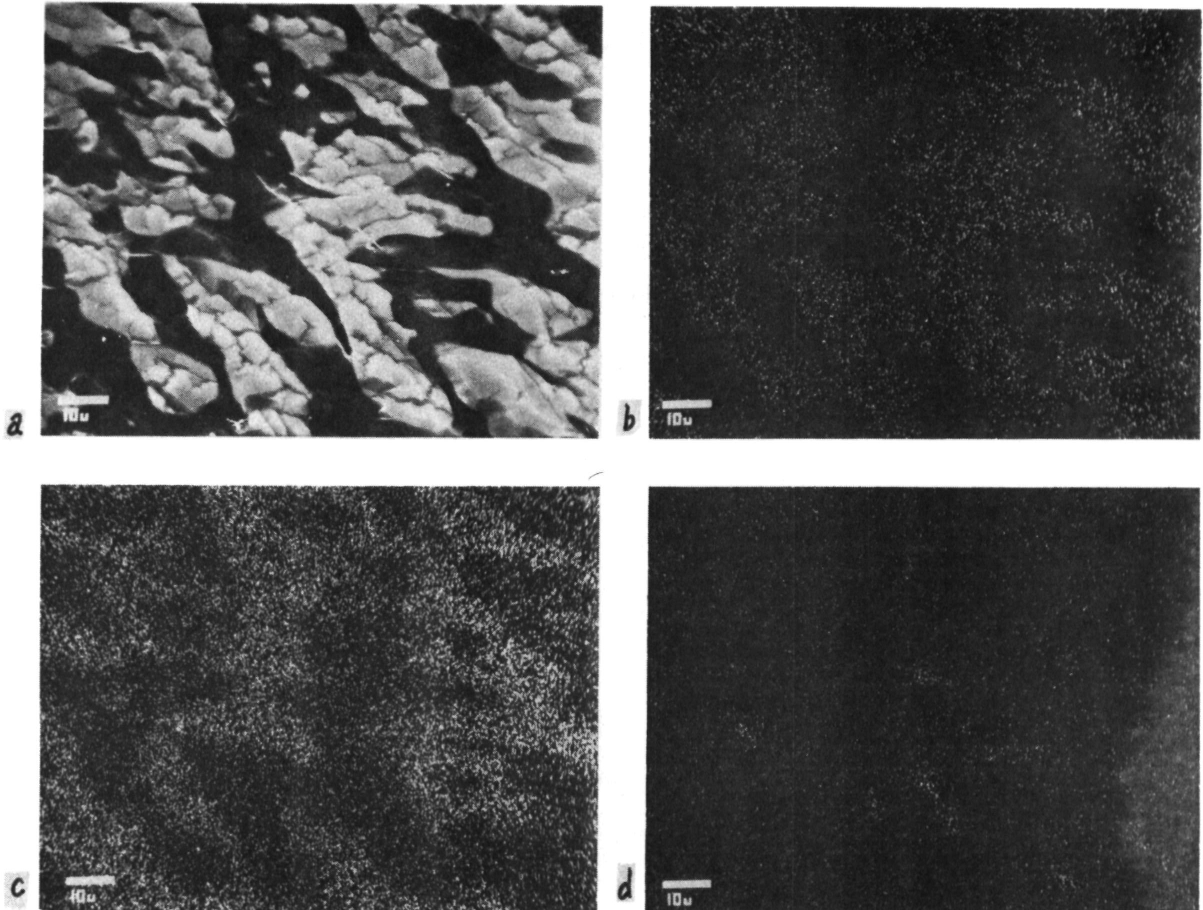

Figure 15. - Element maps of precipitate from Y-doped boule. a)SEM micrograph of precipitate microstructure, b) EDAX map of Yttrium, c) EDAX map of Aluminimum, d) EDAX map of Calcium.

region (presumably with no "stringers" or inclusions) did not contain detectable amounts of yttrium suggests the solubility of yttrium in sapphire is less than the 10 ppm detectability limit. The eutectic phase formed in this system would be expected to be YAG, however it has been found that when molten YAG is quenched a different phase YAP[55] is formed, which has the perovskite structure. What is clear is that samples from this boule contain, at best, levels of yttrium which are small compared to the background impurities.

While the Zr-doped crystal was not examined in detail, similar behavior is expected.

The net result is that we have three crystals with virtually indistinguishable impurity levels which will be termed undoped no. 1, undoped no. 2, and undoped no. 3; a crystal with its dopant, nickel, representing ~20 percent of the total impurity content which will be termed Ni-doped; and a crystal with the isovalent dopant chromium representing ~50 percent of the total impurity content which will be termed Cr-doped. Such a set of samples is wholly unable to provide the investigator with the information sought regarding the influence of Cr, Ni, Y, and Zr content on the self-diffusion of Al_2O_3. It is unfortunate then, that the spectrochemical analyses[4] which were obtained at the beginning of this investigation proved to be incorrect and that the results presented here were not obtained until the single crystal diffusion anneals and proton activation had been completed.

---

[4] Herron Testing Labs, Cleveland, OH.

The boules were oriented by the Laue back reflection and sliced perpendicular to the c-axis. These samples were polished on a brass lap with successive grades of diamond paste suspended on Beuhler Texmet paper. Some rounding of the sample occurred during polishing. It was observed, by fortunate coincidence[5], near the end of this work that using Buehler AB Selected Silk allowed one to take a rough ground sample directly from the wafering machine to 3 μm diamond paste. This resulted in an enormous savings in time (approx 1 hr vs two days using 30 and 15 μm diamond discs and successive 6, 3, and 1 μm diamond pastes). The sample was also much flatter by the time a scratch free surface was obtained.

All samples were preannealed in air, at the temperature to which they would be exposed during the diffusion anneal. This was done in order to remove polishing damage and equilibriate the sample. The samples which were given diffusion anneals at 1300° and 1350° C were preannealed at 1600° C for 10 days eradication of polishing damage at 1350° C would have required a prohibitively long time.

3.1.2 <u>Polycrystalline Samples</u>

Polycrystalline samples were prepared[6] from Al_2O_3 powders which were supplied to us through NASA-Lewis from Biakowski. These consisted of five basic compositions, undoped, Cr-doped, Ni-doped,

---

[5]On the advice of R. J. Schut.

[6]The assistance of F. W. Dynys in the operation of the C.W.R.U. hot press is gratefully acknowledged.

Y-doped, and Zr-doped. The doped powders were of three levels, 200, 500, and 1000 ppm.

The powders were hot pressed at C.W.R.U. using a GCA/Vacuum Industries hot press. The billets were formed in a graphite die, 3 in. diameter, at a temperature of 1500° C, under a pressure of 4000 psi, for a duration of 1 hr.

The spectrochemical analyses on the resulting material showed that the anticipated level of dopant was very nearly attained, with background impurities ~250 ppm, (see table 5).

TABLE 5. - IMPURITY LEVELS IN HOT PRESSED SAMPLES[b] (ppm)

Sample	Ca	Cr[a]	Cu	Ga	Fe	Mg	Ni[a]	Si	Zr[a]	Na	Y[a]	C	S
Undoped	30	---	--	30	3	56	--	88	----	38	----	31	-
Cr-doped	30	210	--	30	7	56	---	54	----	42	----	32	21
Cr-500	30	510	-	30	19	48	---	54	----	50	----	62	20
Cr-1000	30	970	--	30	24	48	---	56	----	38	----	16	11
Ni-200	30	---	20	30	3	45	200	58	----	44	----	13	21
Ni-500	30	---	30	30	3	56	460	65	----	42	----	7	18
Ni-1000	30	---	20	30	4	52	960	70	----	59	----	7	10
Y-200	30	---	-	30	5	48	--	70	----	51	190	30	24
Y-500	30	---	--	30	2	52	---	88	----	53	480	4	--
Y-1000	30	---	--	30	5	56	---	54	----	53	1000	34	26
Zr-200	30	---	--	30	2	56	--	74	195	39	----	14	18
Zr-500	30	---	--	30	6	59	---	70	480	38	----	4	6
Zr-1000	30	---	--	30	4	64	---	56	1010	48	----	33	18

[a]Dopant.
[b]Coors Spectrochemical Laboratory.

In the Ni-500 ppm material, normally a green color, a substantial number of "white spots" ~1 mm in diameter appeared throughout the volume. Under an optical microscope these "white spots" (see figs. 16 and 17) appeared as a core of very dense material surrounded by a halo of quite porous material. The origin of these

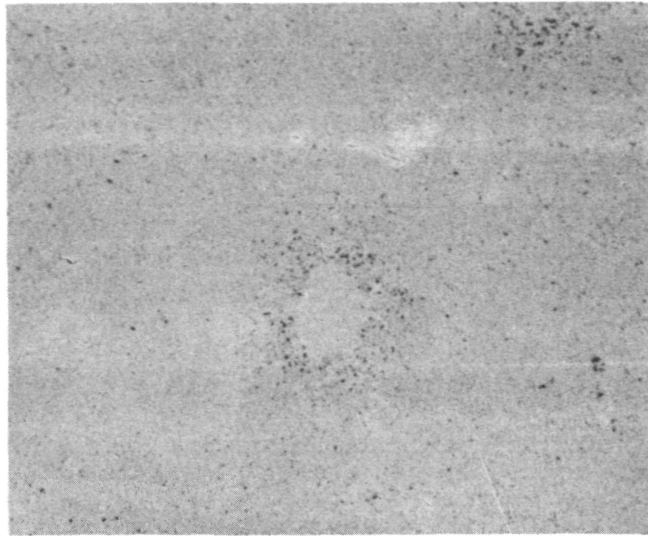

Figure 16. - Optical micrograph of "white spot" in Ni-500 ppm sample (40X).

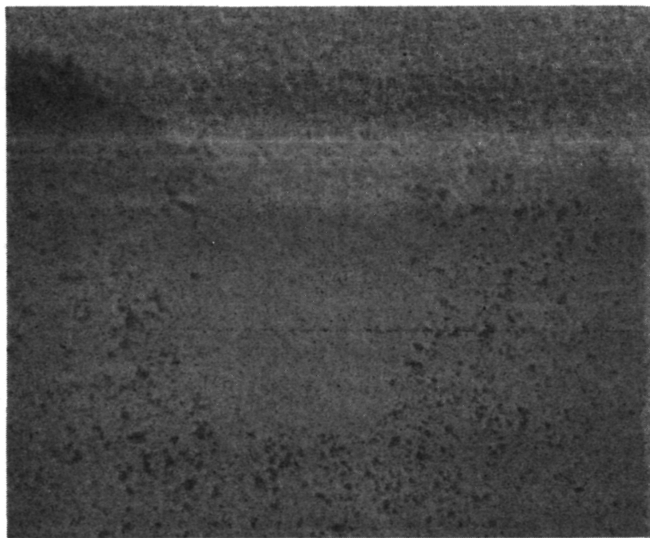

Figure 17. - Optical micrograph of "white spot" in Ni-500 ppm sample (160X).

spots is unknown. X-ray diffraction of samples with and without spots were the same. EDAX showed an enrichment of iron in the white spot compared to the matrix, however, the iron content of the Ni-500 ppm was not different from the other samples (see table 1). If iron is the cause, there is no reason why "white spots" should form in one material and not the others.

One set of samples of each composition were subjected to a grain growth anneal at 1850° C for 1 hr. The samples were buried in powder, of the same composition, in a McDanel 998 crucible. It was observed that the undoped samples which had been in contact with the crucible were discolored, picking up the yellow tinge characteristic of McDanel 998. The resulting grain sizes were >0.1 mm for all samples except the Ni-doped sample which had grain sizes <0.02 mm. Attempts to polish these samples were unsuccessful. This was attributed to micro-cracking upon cooling due to thermal stresses generated between the large grains.

A second set was subjected to a more modest anneal of 1630° C for 10 hr. These samples polished readily. The near surface densities and grain sizes for these samples are given in table 6. It should be noted that the density reported in table 6 is not the bulk density, all samples registered densities greater than 99 percent by Archimedes' principle. Due to the very small penetration distance of the tracer, the bulk density is not the measure of interest, rather the density in the near surface (<1 mm).

TABLE 6. - PERCENT THEORETICAL DENSITY AND GRAIN SIZE OF HOT PRESSED Al_2O_3

Sample	Percent TD	Grain size, μm
Undoped	97.00	5 - 10
Cr-200	98.00	5 - 15
Cr-500	97.00	10 - 20
Cr-1000	99.98	10 - 30
Ni-200	96.00	10
Ni-500	99.00	5
Ni-1000	96.00	5
Y-200	97.00	50 - 150
Y-500	99.98	20 - 60
Y-1000	95.00	10
Zr-200	99.95	10 - 60
Zr-500	95.00	10
Zr-1000	97.00	10

The reported densities were determined by comparing optical micrographs with computer generated standards. The reduction of the density near the surface is doubtless contributed to by the pullout of grains during polishing.

Examples of the microstructures are shown in figures 18 to 22.

3.2 EXCHANGE APPARATUS

A schematic of the apparatus in which the exchanges were performed is shown in figure 23. It is essentially the apparatus used by Reddy[16] with some modifications. The geometry of the shelves was changed to permit a greater number of samples to be exchanged side by side. The addition of a carbon reservoir allowed for a low P_{O_2} to be obtained by the reaction:

Figure 18. - Optical micrograph of undoped hot pressed Al_2O_3 sample annealed at 1630° C for 10 hr. (160X).

200 ppm

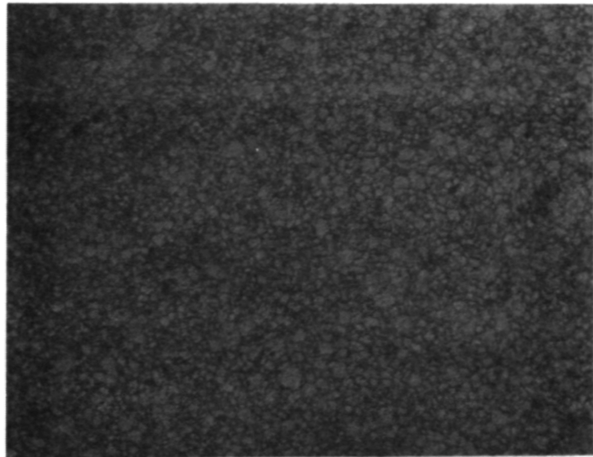

500 ppm

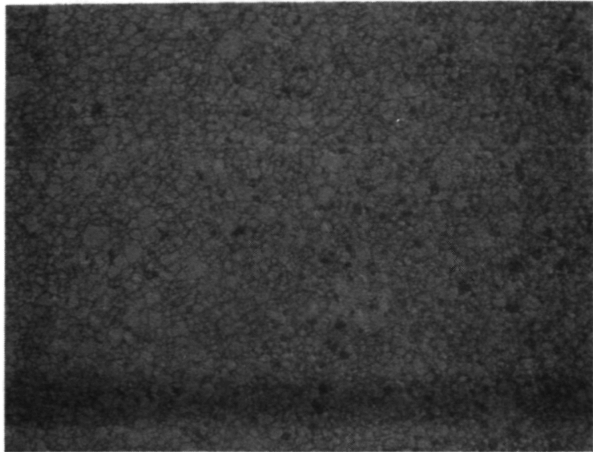

1000 ppm

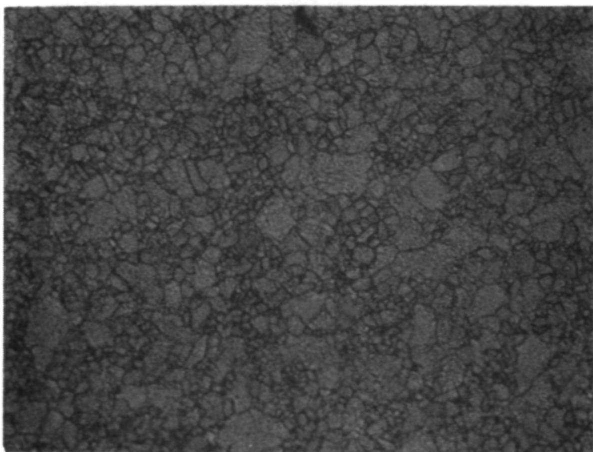

Figure 19. - Optical micrographs of Cr-doped Al_2O_3 annealed at 1630° C for 10 hr (160X).

200 ppm

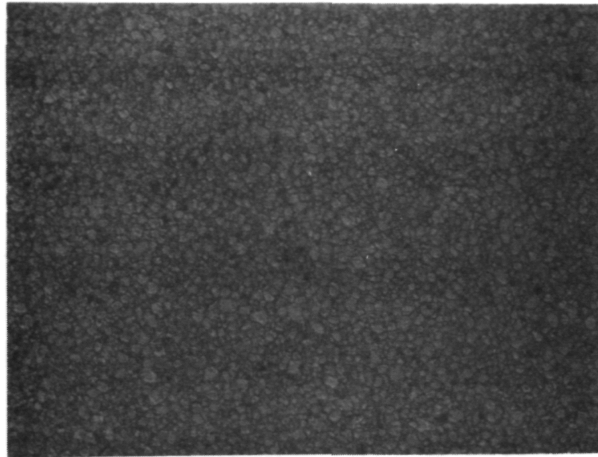

500 ppm

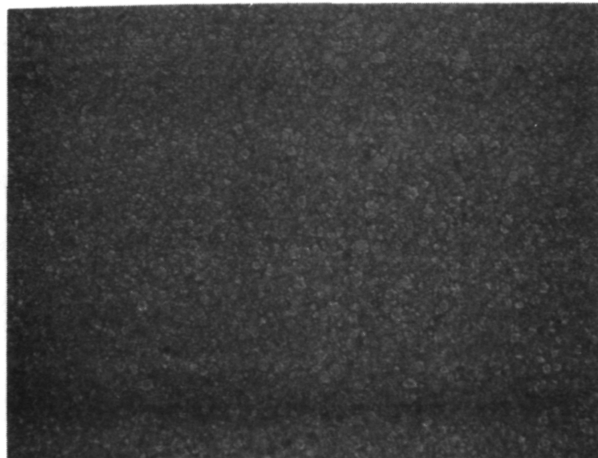

1000 ppm

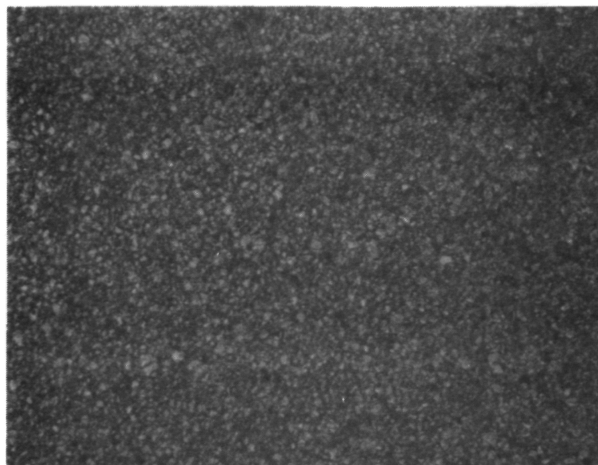

Figure 20. - Optical micrographs of Ni-doped Al_2O_3 annealed at 1630° C for 10 hr (160X).

200 ppm

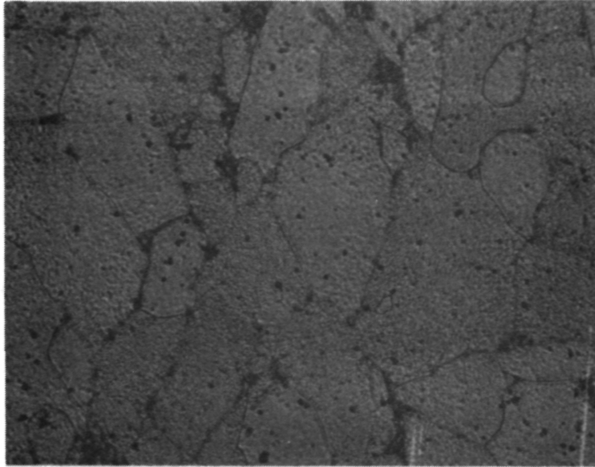

500 ppm

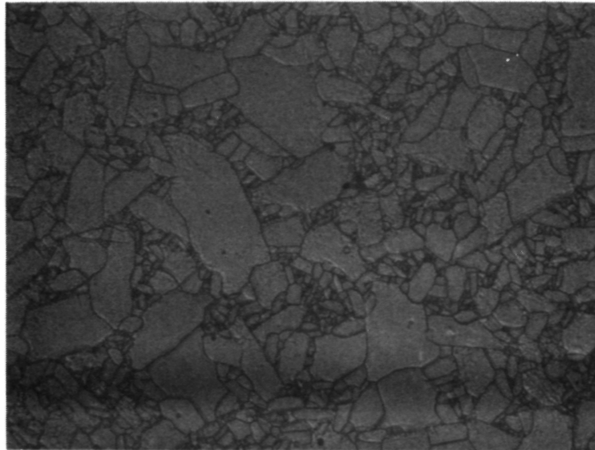

1000 ppm

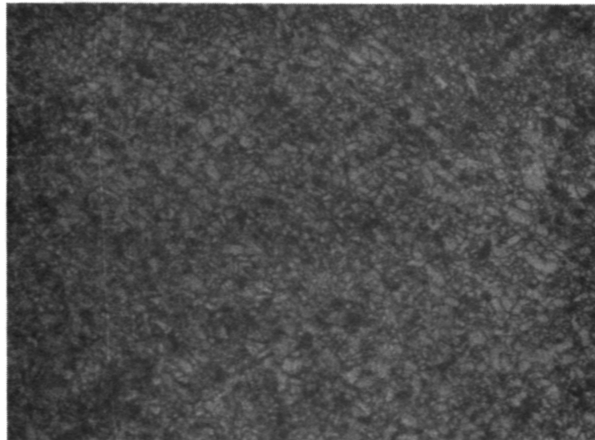

Figure 21. - Optical micrographs of Y-doped Al_2O_3 annealed at 1630° C for 10 hr (160X).

200 ppm

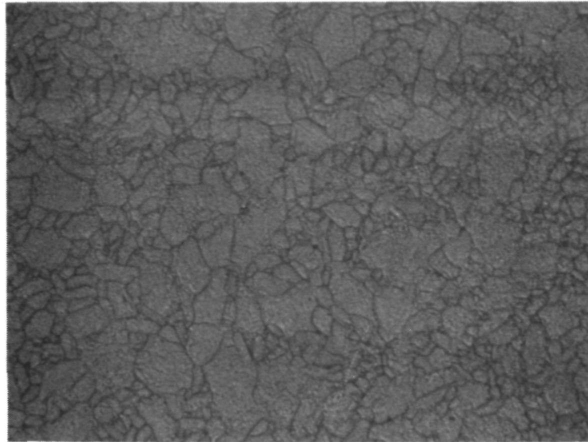

500 ppm

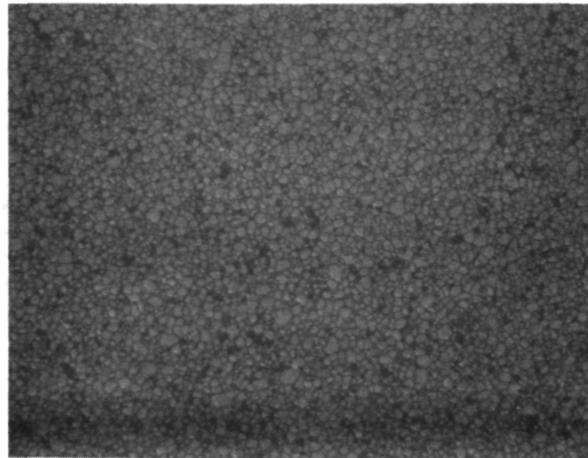

1000 ppm

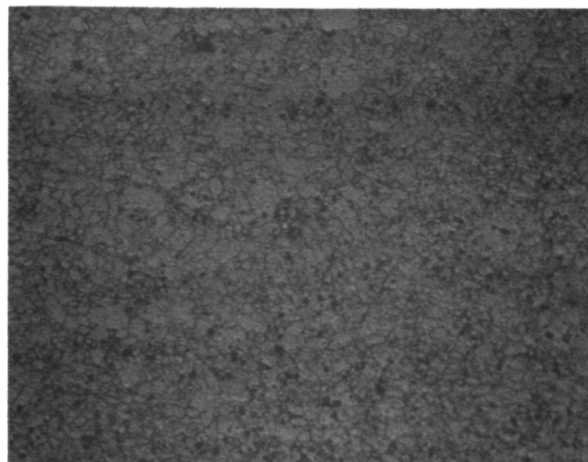

Figure 22. - Optical micrographs of Zr-doped Al_2O_3 annealed at 1630° C for 10 hr (160X).

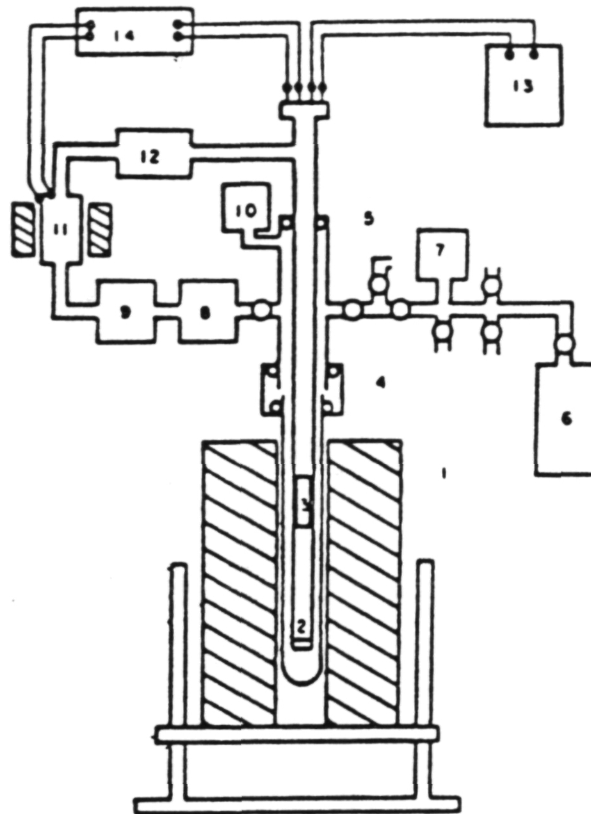

1. FURNACE
2. SAMPLE SHELF
3. CARBON RESERVOIR
4. O-RING SEALS
5. GAS SAMPLE OUTLET
6. ZEOLITE O-18 STORAGE
7. THERMOCOUPLE VACUUM GAUGE
8. FLOW METER
9. DRIERITE
10. PRESSURE/VACUUM GAUGE
11. ZrO_2 CELL
12. PUMP
13. MILLIVOLT METER

Figure 23. - Schematic of the exchange apparatus.

$$3C + 2O_2 \rightarrow CO_2 + 2CO \quad (3.2\text{-}1)$$

The pump was added to circulate the gas and a ZrO_2 cell was placed in the system to monitor the P_{O_2}.

3.3 EXCHANGE PROCEDURE

The exchange for the 1 atm oxygen experiments was conducted in a manner similar to that employed by Reddy. The samples were placed on the shelf, the chamber was then evacuated, and the temperature was raised to ~1000° C, typically within thirty minutes. The tracer atmosphere was then allowed in, to a pressure slightly higher than that of the ambient in order to reduce contamination by air if a leak was present. The temperature was then raised to that desired for the diffusion anneal, typically in less than ten minutes. The temperature was controlled at ±5° C for the duration of the anneal, 24 hours, shortest; 80 days, longest.

In the bulk of the experiments, gas samples were taken periodically to record the change in tracer concentration as a function of time. At the end of the anneal the furnace was shut off and the tracer atmosphere reclaimed to the zeolite storage pump.

One exchange was carried out at low P_{O_2}. In this case the procedure was identical to the one just described, except that a reservoir of carbon was placed in the hot zone of the furnace. The configuration was such that the pump caused the gas to flow down the inner tube over the carbon and across the samples. It was then recirculated up through the outer tube.

Although the ZrO_2 cell suffered a loss of continuity during the experiment, by monitoring the pressure change as the gas equilibriated with the carbon, the calculated P_{O_2} was verified.

3.4 ANALYSIS OF THE SAMPLES

After the samples had undergone the diffusion anneal, the concentration of oxygen-18 versus depth information was obtained by two methods, Single Spectrum Proton Activation and Secondary Ion Mass Spectrometry (SIMS). Comprehensive treatments of both procedures are available[8, 9, 13, 55]. Only the basic concepts and items relating to our particular experiments will be discussed here.

3.4.1 Proton Activation

This technique is based on the nuclear reaction $^{18}O(p,\alpha)^{15}N$. In this reaction a proton striking an oxygen-18 nucleus causes an alpha particle to be ejected, yielding a nitrogen-15 nucleus.

This work was carried out at the Universite de Paris VII. The geometry of the setup is illustrated in figure 24. The samples were irradiated with a monoenergetic beam of 750 KeV protons. The 3 MeV alpha particles which resulted were detected with Ortec surface barrier detectors and energy discriminated with a Multichannel Analyzer, or a dedicated computer. The energy of an alpha particle is related to the depth at which the reaction occurred and the intensity of a alpha particles of a particular energy is related to the concentration of oxygen-18. Ideally, the relationship of alpha energy to depth is a unique function. This relation involves the

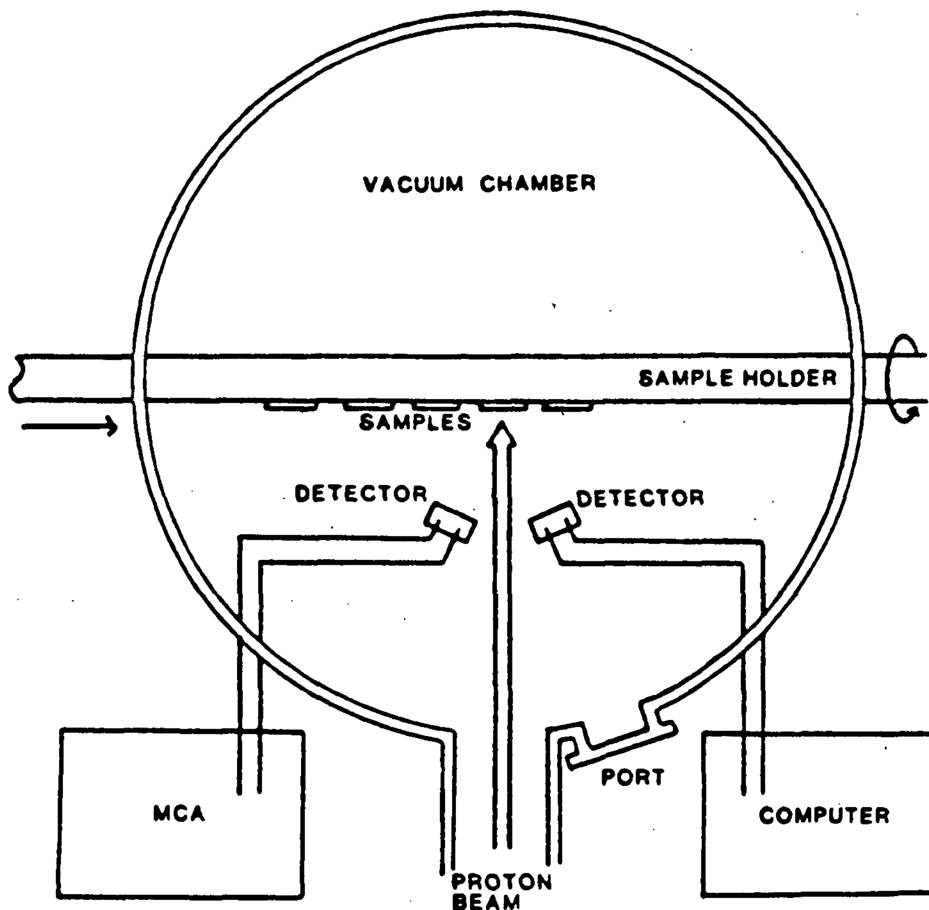

Figure 24. - Geometry of the chamber used in Proton Activation.

rate at which incoming protons and outgoing alpha particles lose energy. This is given by the stopping powers which are tabulated[57 to 59].

The stopping power is a function of the particle energy. Over the energy ranges encountered in single spectrum proton activation both the proton and alpha particles stopping powers could be accurately described by linear functions.

The stopping power for protons in Al_2O_3, S_p, over the proton energy range, E_p, 750 to 500 KeV follows the relation

$$S_p = B_p + M_p \cdot E_p \quad (\text{keV}/\mu\text{m}) \tag{3.4-1}$$

with

$B_p = 161.637$

$M_p = -9.512 \times 10^{-2}$

and the stopping power for alphas, $S\alpha$, over the alpha energy range, E_α, 3369 to 2500 keV follows

$$S_\alpha = B_\alpha + M_\alpha \cdot E_\alpha \tag{3.4-2}$$

with

$B_\alpha = 582.710$

$M_\alpha = -7.363 \times 10^{-2}$

During a nuclear reaction relativistic energy is conserved. If the assumption is made that the O-18 nucleus is at rest then[60]

$$m_{^{18}O}c^2 + m_p c^2 + Ep = m_{^{15}N}c^2 + E_{^{15}N} + m_\alpha c^2 + E_\alpha \tag{3.4-3}$$

where m is the rest mass, c is the speed of light, and E is the kinetic energy. The energy balance, Q, may be written

$$Q = (m_{^{18}O} + m_p - m_{^{15}N} - m_\alpha)\, c^2 = E_{^{15}N} + E_\alpha - E_p = \Delta mc^2 = \Delta E \quad (3.4\text{-}4)$$

If the value of Q is positive, kinetic energy is gained and the reaction is termed exoergic whereas when the value of Q is negative, kinetic energy is lost and the reaction termed endoergic.

The $^{18}O(p,\alpha)^{15}N$ reaction is exoergic with $Q = 3.98$ MeV. Over the energy range used for proton activation the alpha energy is linearly related to the proton energy by(61)

$$E_\alpha = B_{nr} + M_{nr}\, Ep \quad (3.4\text{-}5)$$

with

$$B_{nr} = 3002.724$$

$$M_{nr} = 0.482$$

Given the above, as well as:

(1) A detected alpha particle energy, E_α^d, which is equal to the alpha energy at the sample surface, $E_\alpha\ (x = 0)$.

(2) A known incident proton energy, in our case 750 keV, which is equal to $E_p\ (x = 0)$. The relationship between the detected alpha energy and the depth at which the reaction took place, x_r, can be illustrated as follows. The geometry of the chamber is such that the angle between the incoming protons and the outgoing alpha particles is 165°. The alphas, therefore, travel a distance x_r cos(15); The energy of the alpha at x_r can be calculated with:

$$E_\alpha(x_r) = E_\alpha\ (x = 0) + S_\alpha\ \frac{x_r}{\cos(15)} \quad (3.4\text{-}6)$$

Since S_α is a linear function of energy, the effective stopping power, $\bar{S}_\alpha$, between $x = 0$ and $x = x_r$ is

$$\bar{S}_\alpha = B_\alpha + \frac{m_\alpha}{2} (E_\alpha (x = 0) + E_\alpha (x = x_r)) \quad (3.4\text{-}7)$$

Substitution of equation (3.5-5) into (3.5-4) and rearranging yields

$$E_\alpha(x_r) = E_\alpha (x = 0) \frac{2 \cos(15) + M_\alpha x_r}{2 \cos(15) - M_\alpha x_r} + \frac{2 B_\alpha x_r}{(2 \cos(15) - M_\alpha x_r)} \quad (3.4\text{-}8)$$

The energy of the proton, $E_p (x = x_r)$, which under went the reaction to produce this detected alpha, is related to $E_\alpha (x = x_r)$ by equation (3.5-3). It is also related to the incident proton energy by

$$E_p(x_r) = E_p (x = 0) - S_p x_r \quad (3.4\text{-}9)$$

By analogus substitution to that for alphas, this may be rewritten as

$$E_p(x_r) = E_p (x = 0) \cdot \frac{2 - M_p x_r}{2 + M_p x_r} - \frac{2 B_p x_r}{2 + M_p x_r} \quad (3.4\text{-}10)$$

By combining equations (3.5-6), (3.5-3), and (3.5-8), and rearranging the following may be obtained

$$E_\alpha (x = 0) = \frac{2 \cos(15) - M_\alpha x_r}{2 \cos(15) + M_\alpha x_r} \cdot B_{nr} + E_p (x = 0) \cdot M_{nr} \frac{2 - M_p x_r}{2 + M_p x_r}$$

$$- \frac{2 M_{nr} B_p x_r}{2 + M_p x_r} - \frac{2 B_\alpha x_r}{2 \cos(15) + M_\alpha} \quad (3.4\text{-}11)$$

This equation contains as the only variables $E_\alpha (x = 0)$ and x_r. It is a complicated expression, however, as the plot in figure 25

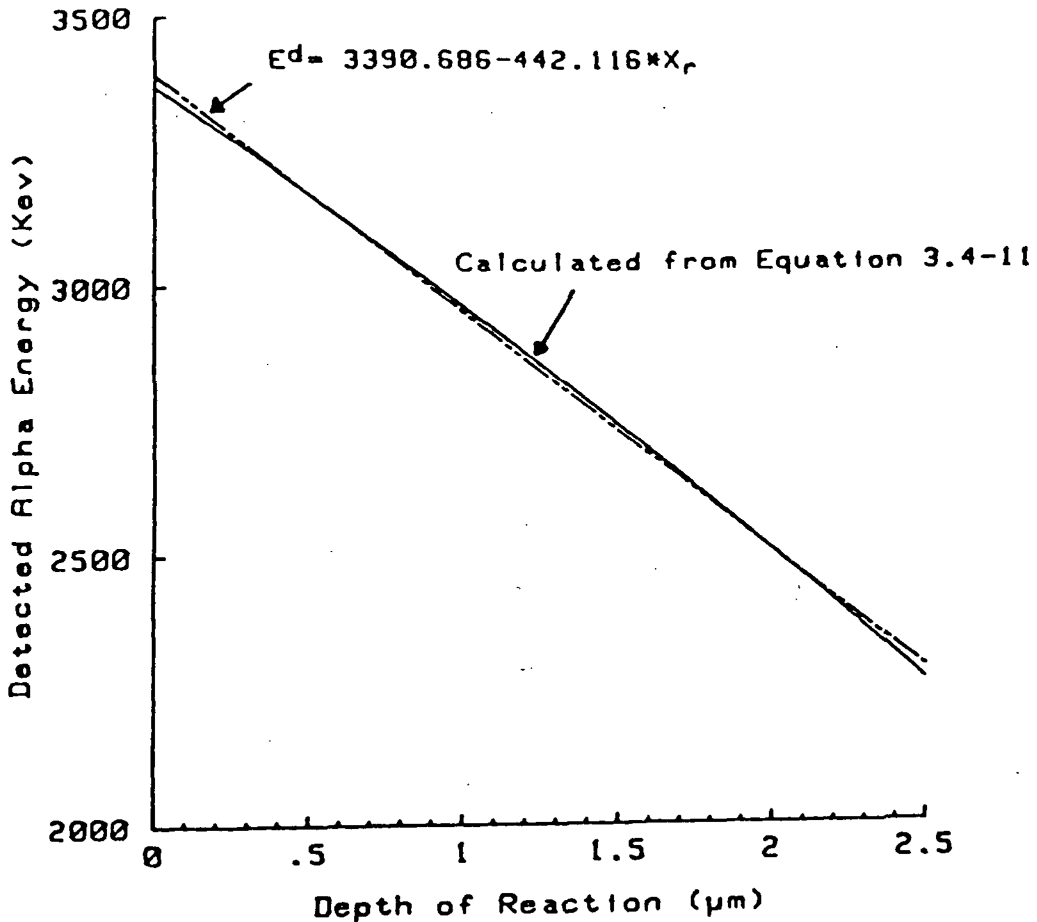

Figure 25. - Plot of the energy of the detected alpha particle versus the depth at which the proton activation took place. Also shown is a linear regression of the depth energy relationship.

shows, the depth energy relationship varies by only a small degree from a linear relationship when the appropriate values of the constants are substituted in. A second order approximation was used in the spectra fitting routine.

The number of counts in each channel is related to the concentration of tracer by:

$$N_i = c(x_i)\ L\ell\sigma(x_i)\Delta x_i \Delta\Omega \tag{3.4-12}$$

where

n_i = the number of counts in the ith channel

$c(x_i)$ = the fractional concentration of tracer at a depth corresponding to the channel, x_i

L = volume fraction of oxygen

ℓ = number of protons

$\sigma(x_i)$ = the cross section of the reaction for a proton at depth, x_i

Δx_i = the width in distance of the ith channel

$\Delta\Omega$ = solid angle of observation

Note L is a material constant and ℓ, $\sigma(x_i)$, Δx_i, and $\Delta\Omega$ are experimental parameters.

The number of protons was determined by measuring the charge imparted to the sample chamber. A typical charge was 50 μcb corresponding to 3.1×10^4 protons.

The cross-section is dependent on the incident proton energy chosen and is illustrated in figure 28.

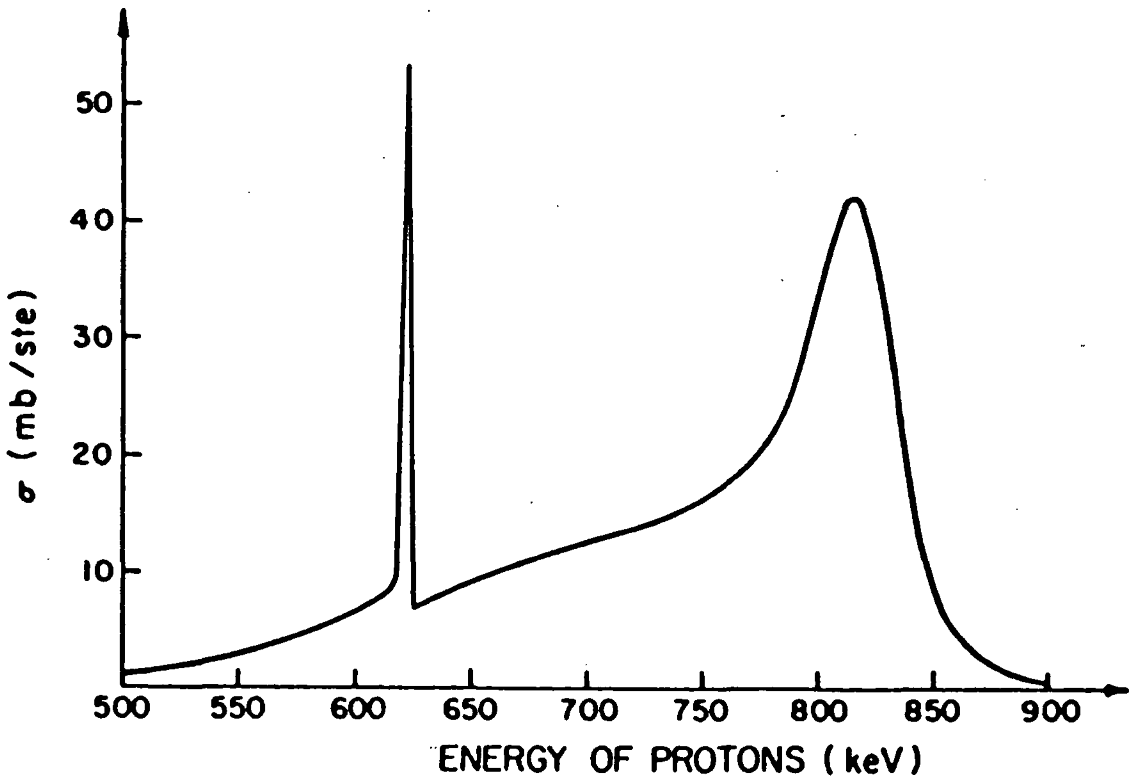

Figure 26. - Differential cross section of $^{18}O(p,\alpha)^{15}N$ reaction at a scattering angle of 165°.

The width of the channel was selected electronically to correspond to ~13 keV which is ~0.03 μm in distance.

The solid angle is dependent on the dimensions of the detector and its distance from the sample. In our case, $\Delta\Omega \sim 0.4$ Steradians.

This discussion has been for an ideal case. In reality the monoenergetic particles decay into wider distributions as they pass through the material. The stopping powers give the average energy lost. The imprecision in the detector and the electronics also give rise to uncertainties in the detected energies. Both of these effects can be accounted for by a spreading function. This function is experimentally determined and found to be very nearly gaussian. It is this spreading function which determines depth resolution.

An example of a proton activation spectrum is shown in figure 27.

3.4.2 Rutherford Backscattering (RBS)

Many of the protons which strike the nuclei do not cause a reaction to take place and simply undergo an elastic collision. These Rutherford backscattered protons were detected simultaneously with the proton activation spectra. This was done to ensure that the proton beam was not being channeled. Channeling affects the proton activation spectra in two ways.

First, channeled particles lose energy at a lower rate than those which see the lattice in a random way. This makes the energy depth relationship ambiguous. Two alphas with the same detected energy may have been generated at different depths, one from a channeled proton and from an unchanneled proton.

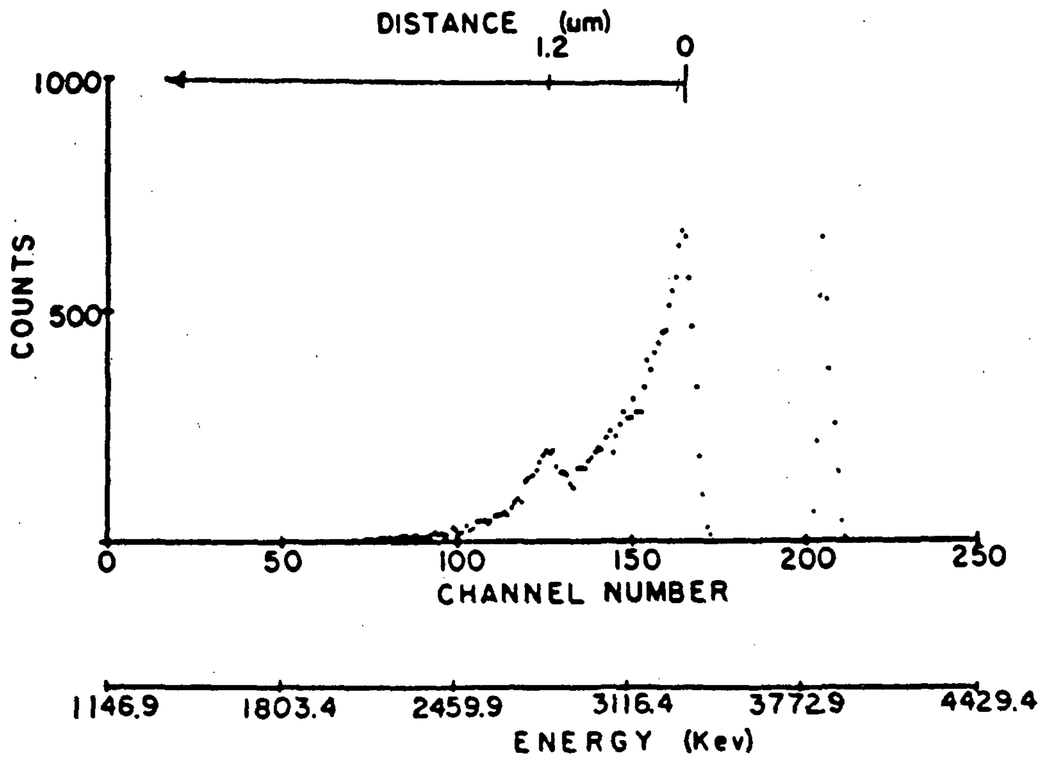

Figure 27. - Example of a proton activation spectrum.

Secondly, channeled protons have a much lower possibility of reacting with the nuclei. This changes the relationship between alpha intensity and concentration of tracer.

The RBS spectra proved to be a good indicator of channeling and were used as a guide to selectively reject spectra.

The energy relationship of a backscattered particle is:

$$E_{RBS}(x_r) = K_m E_1(x_r) \qquad (3.4\text{-}13)$$

where $E_{RBS}(x_r)$ is the energy of the backscattered particle; $E_1(x_r)$ is the energy of the particle prior to backscattering; and, K_m is the backscattering kinematic factor dependent on the mass and charge of the particle, and, the mass of the struck nucleus and the scattering angle.

The kinematic factor may be calculated using the following relation[62]

$$K_m = \left[\frac{m_1 \cos\theta + (m_2^2 - m_1^2 \sin^2\theta)^{1/2}}{m_1 + m_2}\right]^2 \qquad (3.4\text{-}14)$$

where m_1 is the mass of the particle, M_2 is the mass of the struck nucleus and, θ is the laboratory scattering angle.

The energy of a detected RBS particle, E_{dRBS}, also depends on the depth at which the RBS event took place. This may be written

$$E_{dRBS} = K_m(E_o - S_1 x_r) - \frac{S_2 x_r}{\cos(15)} \qquad (3.4\text{-}15)$$

where X_r is the depth of the RBS event, E_o is the incident particle energy, and, S_1 and S_2 are the stopping powers for the particle traveling into and out of the material, respectively.

3.4.3 Secondary Ion Mass Spectrometry (SIMS)

In SIMS the sample is bombarded with a primary ion beam, either Ar^+ or O^- was used in our case. As the ion is implanted it transfers its momentum to matrix atoms. Near the surface sputtering may occur. The sputtered fragments may be elemental or compound and may be positively charged, negatively charged, or neutral. Fragments from alumina may include O, Al, O_2, Al_2, AlO, AlO_2, Al_2O, etc. The fragments are then separated according to AMU/Charge by mass spectrometry.

The bulk of this work was done at the Pennsylvania State University MRL (referred to as PSU) using a Gatan SIMS. In this case the primary beam was Ar^+, typcially 7 keV. Due to the insulating properties of alumina, it was necessary to compensate the positive charge of the primary beam by spraying electrons on the sample. These electrons also cause some desorption of light elements such as oxygen from the near surface region. This Electron Stimulated Desorption (ESD) gives rise to a background intensity for both oxygen-16 and oxygen-18. The background was found to be constant, for single crystal samples, and could be subtracted out.

The primary beam was rastered in order to give a large flat bottomed crater (see fig. 28). The detector was electronically gated to receive information from only the center third of the crater. A quadrapole mass spectrometer was used on this machine.

Additional work was done at the University of Illinois at Urbana MRL (referred to as UIU). In this case no electron beam was available, so the use of a negative primary beam was required.

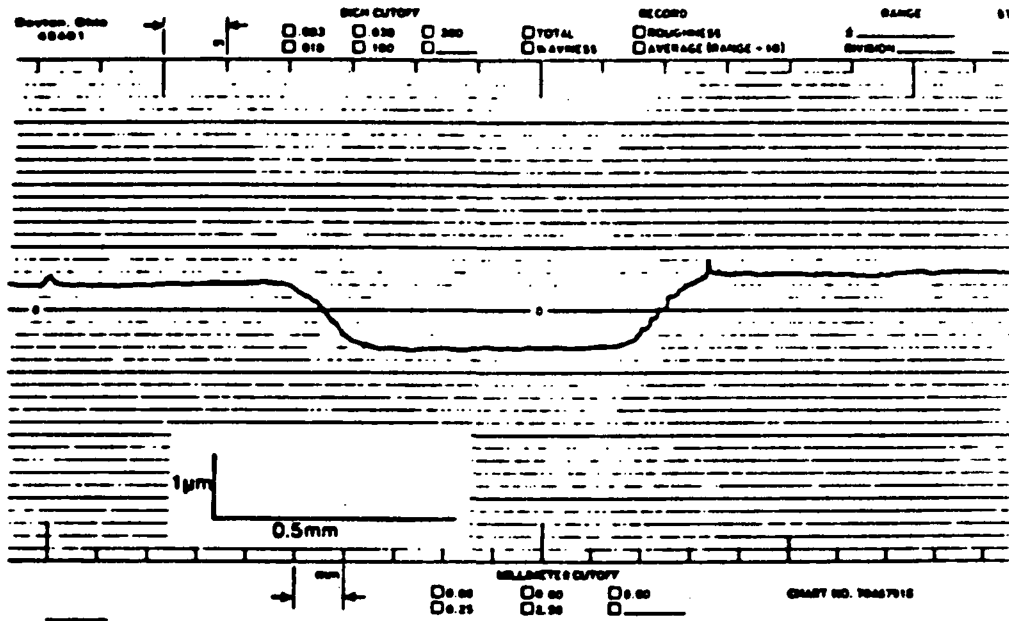

Cross section of SIMS crater

Figure 28. - Profilometer trace of a crater sputtered with the PSU Gatan SIMS.

Unfortunately, the only ion available on the machine was O^-, which complicates the interpretation of the spectra. The beam was rastered and a double focusing mass spectrometer was used to separate the masses.

The output from both machines was directly transferred to computers. This allowed monitoring more than one mass charge as a function of sputtering time. Typical raw data for the two machines is shown in figures 29 and 30. The conversion of the PSU data concentration profile is straightforward. The fractional concentration of oxygen-18 tracer, c_{18}, at a given value of sputter time, t_s, for the case of the Ar^+ primary beam is:

$$c_{18}(t_s) = \frac{\dot{h}_{18}(t_s)}{\dot{h}_{18}(t_s) + \dot{h}_{16}(t_s)} \qquad (3.4\text{-}16)$$

where $\dot{h}_{18}(t_s)$ is the counting rate of mass-18 at time t_s, and $\dot{h}_{16}(t_s)$ is the counting rate of mass-16 at time t_s.

In order to convert sputter time to sputter depth, the total depth of the crater, measured with a profilometer was divided by the total time under the beam to give the sputter rate, $\dot{\gamma}$; such that $x_s = \dot{\gamma} t_s$.

In the case of the O^- primary beam, at UIU, the simple ratio does not hold because of dilution from the beam. The true concentration of oxygen-18 is given by:

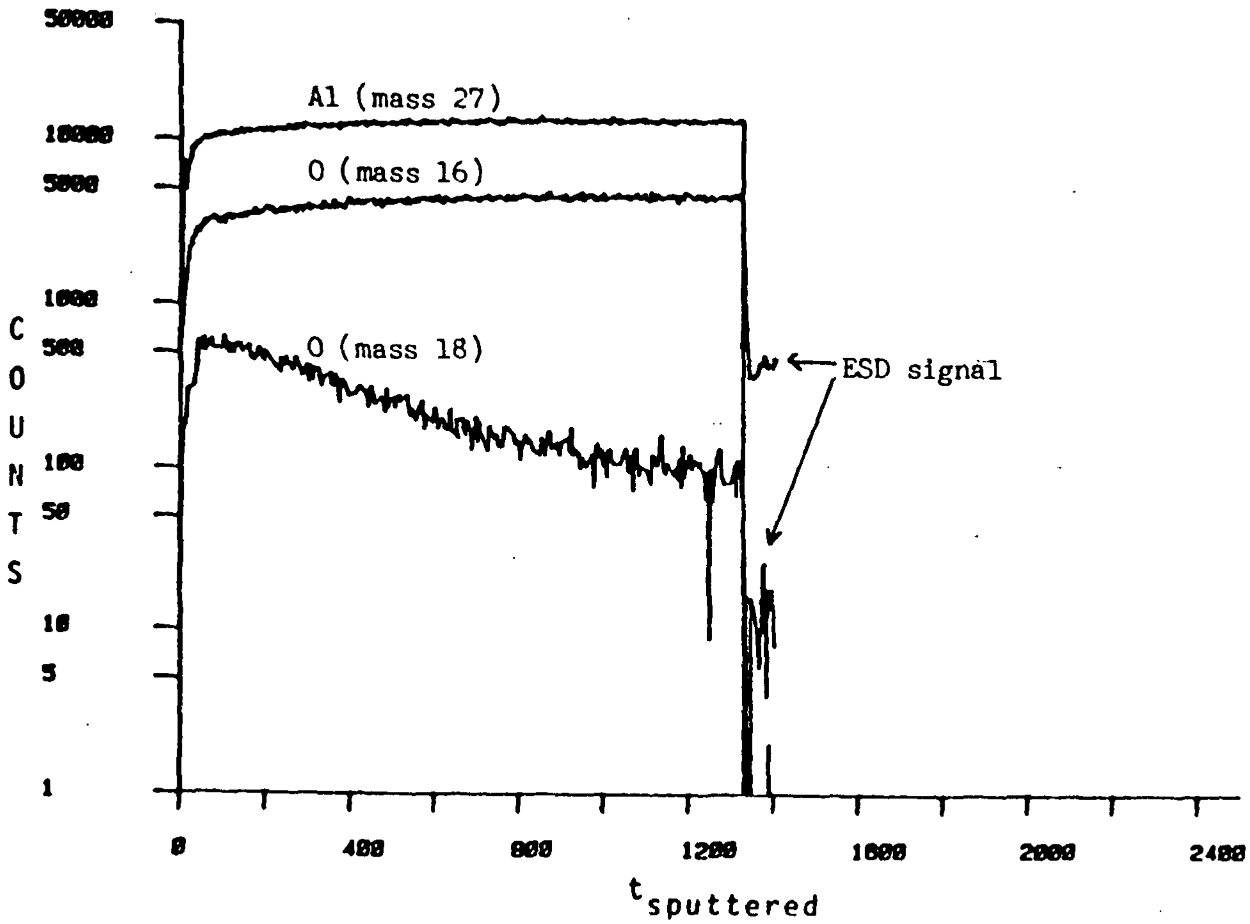

Figure 29. - Example of the output of the PSU Gatan SIMS during depth profiling.

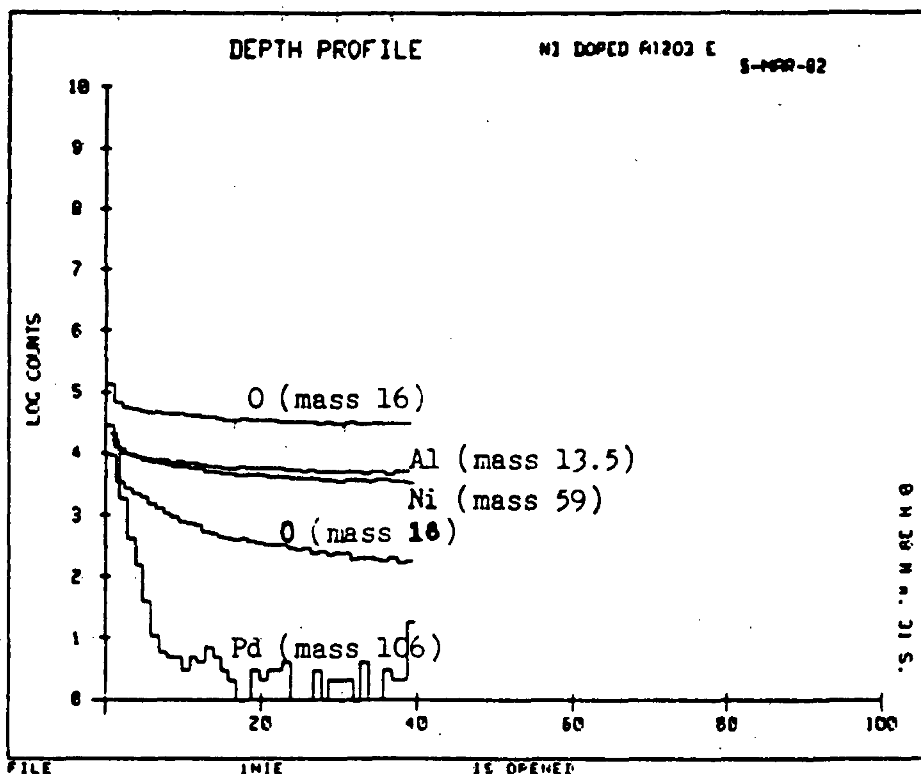

MEASUREMENT CONDITIONS

SAMPLE REFERENCE: NI DOPED Al203 E DATE: 5-MAR-82
PRIMARY POLARITY: - SECONDARY POLARITY: +
PRIMARY CURRENT: 3.39E-07 Amps.
PRIMARY VOLTAGE: 9.7 Kv.
RASTER: 500 Microns
IMAGE FIELD: 150 Microns

Figure 30. - Example of the output of the UIU SIMS during depth profiling.

$$c_{18}(t_s) = \frac{\dot{h}_{18}(t_s)}{\dot{h}_{18}(t_s) + \dot{h}_{16}(t_s) - \dot{h}_{16}(\text{beam})} \qquad (3.4\text{-}17)$$

In order to determine the contribution from the beam, a sample analyzed with the Ar^+ primary beam was reanalyzed with the O^- beam. There were some differences in the data collection. The PSU machine counted for 1 second intervals and plotted counting rate versus sputter time, whereas, the machine at the University of Illinois counted for ten second intervals and plotted the number of counts versus channel.

Determination of the sputtering rates allowed by the PSU data to be normalized to that of UIU. A plot of the two spectra is shown in figure 31. Apparent in this plot is a surface peak in the UIU data not found in the PSU data. Also, the lower values of UIU ratio arise from the primary oxygen dilution. The magnitude of the dilution from the beam can be determined at each point and is plotted in figure 32. As seen in this plot, the dilution from the beam makes up 80 percent of the total oxygen-16 counting rate and it is not constant. Therefore, an attempt was made to normalize the UIU data to the PSU data by using the aluminum signals as the reference. Two assumptions were made (the notation used is; the symbol h refers to the counting rate or counts, the subscript refers to the mass/charge being counted, and the superscript refers to the location of the instrument).

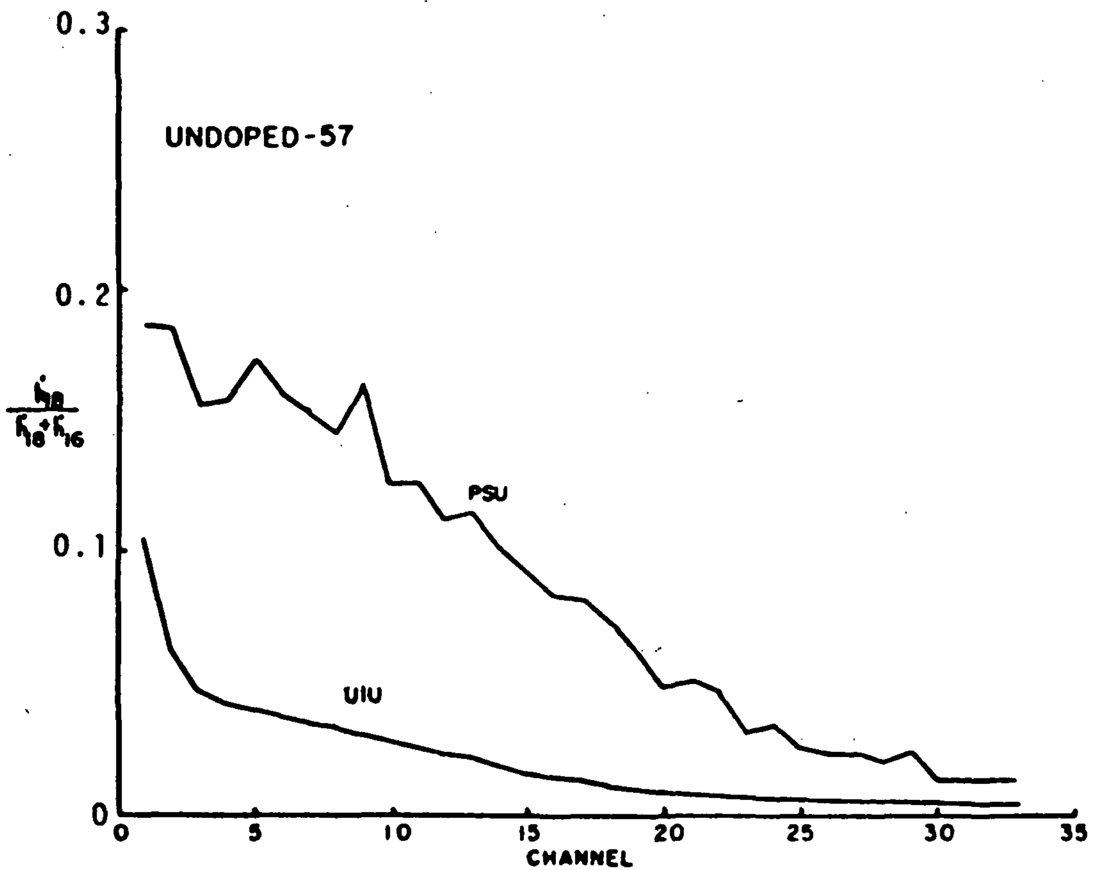

Figure 31. - UIU and PSU depth profiles on UD57 plotted on a normalized scale.

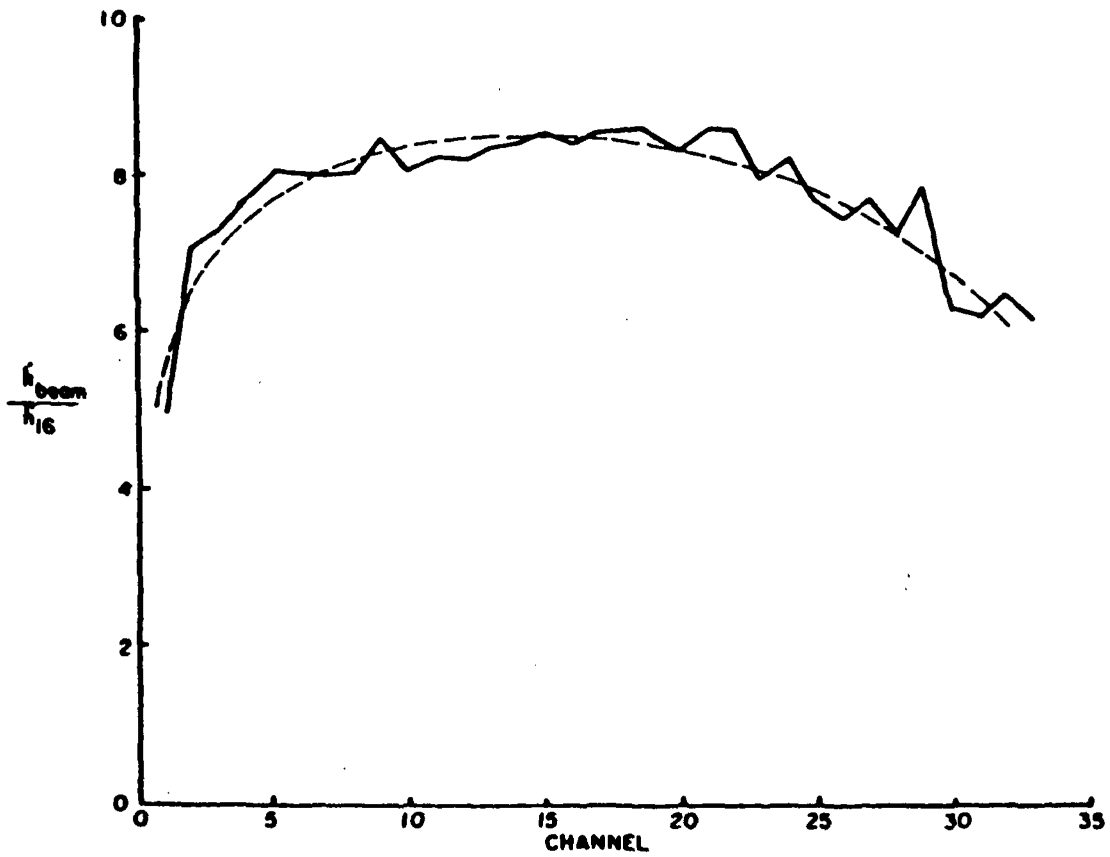

Figure 32.- The fraction of the O-16 signal due to the primary beam dilution, on the UIU SIMS.

(i) the oxygen-18 signal divided by the aluminum signal was a constant for both machines. These ratios would then be proportional, that is:

$$\frac{h_{18}^{UIU}/h_{13.5}^{UIU}}{h_{18}^{PSU}/h_{27}^{PSU}} = \text{a constant} = 5.3 \text{ (see fig. 33)} \tag{3.4-18}$$

(ii) the total oxygen over aluminum signal for PSU is constant, that is:

$$\frac{h_{18}^{PSU}/(h_{18}^{PSU} + h_{16}^{PSU})}{h_{18}^{PSU}/h_{27}^{PSU}} = \text{a constant} = 11.9 \text{ (see fig. 34)} \tag{3.4-19}$$

Notice these are not perfect assumptions. Using these assumptions:

$$C_{18}(t_s) = \frac{h_{18}^{UIU}}{h_{13.5}^{UIU}} \; \frac{h_{18}^{PSU}/h_{27}^{PSU}}{h_{18}^{UIU}/h_{13.5}^{UIU}} \; \frac{h_{18}^{PSU}/(h_{18}^{PSU} + h_{16}^{PSU})}{h_{18}^{PSU}/h_{27}^{PSU}} \tag{3.4-20}$$

which, when values are substituted in, becomes

$$C_{18}(t_s) = \frac{11.9}{5.3} \; \frac{h_{18}^{UIU}}{h_{13.5}^{UIU}} \tag{3.4-21}$$

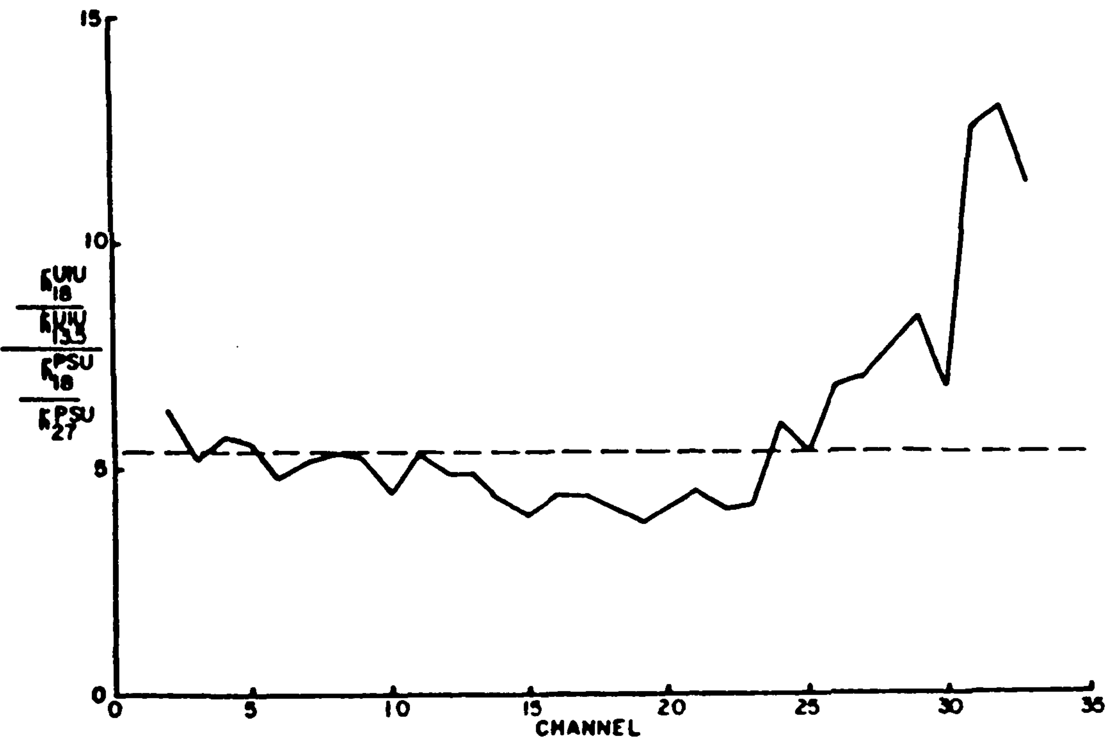

Figure 33. - The ratio of tracer signals, normalized to aluminum, between PSU and UIU.

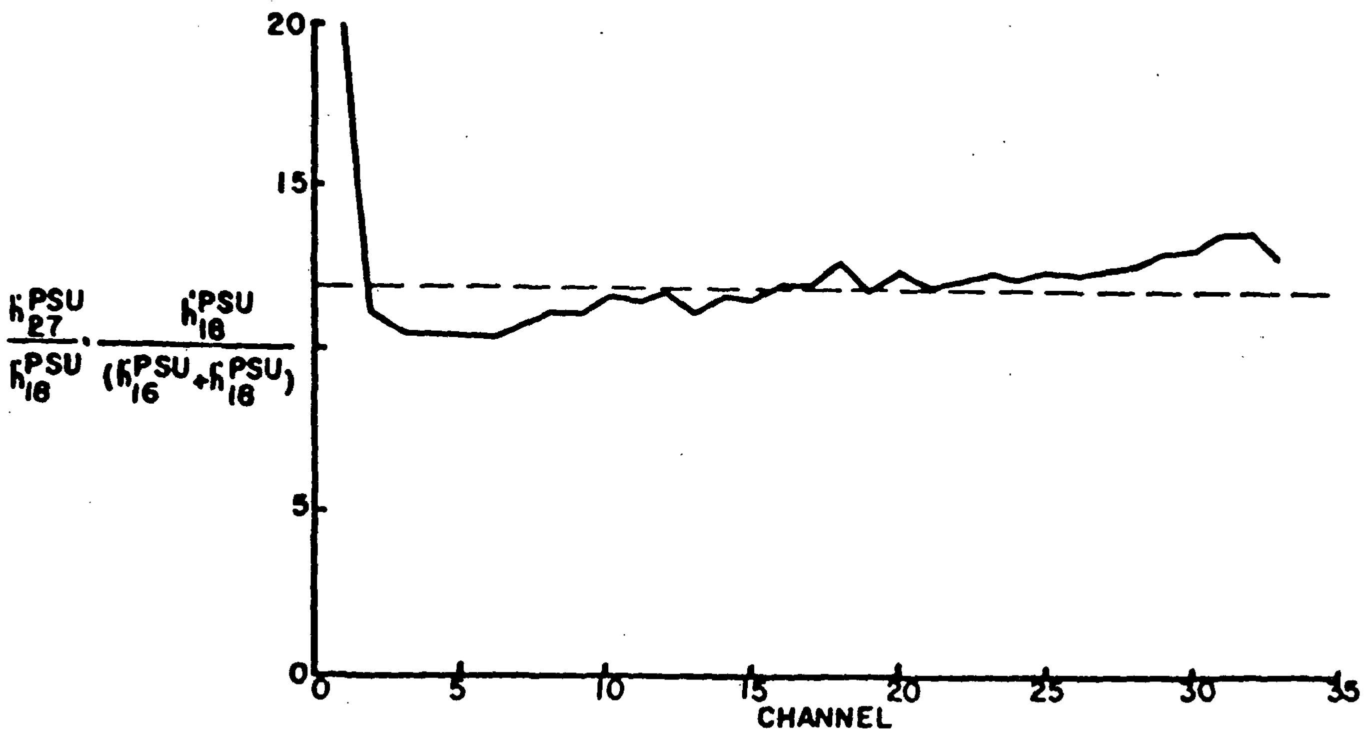

Figure 34. - Total oxygen to aluminum ratio for PSU SIMS.

CHAPTER IV

RESULTS

4.1 PROTON ACTIVATION

4.1.1 Standards

In order to obtain experimental values for spectrum fitting parameters, four types of standards were utilized:

(i) Electronic test pulses which were generated and run through the electronics to the amplifier on the detector and back to the MCA.

(ii) Two oxide films of uniform oxygen-18 concentration. A thin film, 10 nm, of Al_2O_3 on anodically oxidized aluminum; and a thick film, 600 nm, of SiO_2 on thermally oxidized silicon in a water bearing atmosphere.

(iii) Metallic samples of niobium and tantalum.

(iv) A sample of the undoped no. 1 boule containing only the natural abundance of oxygen-18.

As previously mentioned, the proton activation spectra was spread due to the imperfect nature of the electronics and the detector. In order to assess the magnitude and source of the spreading, the proton activation spectrum for the thin film of $Al_2O_3^{18}$ and an electronic test pulse were analyzed. The actual spectrum is shown in figure 35. The data points are indicated with crosses and the curves drawn through them are Gaussian Functions. In the case of the electronic test pulse, the standard deviation was 12.4 KeV (~30 nm);

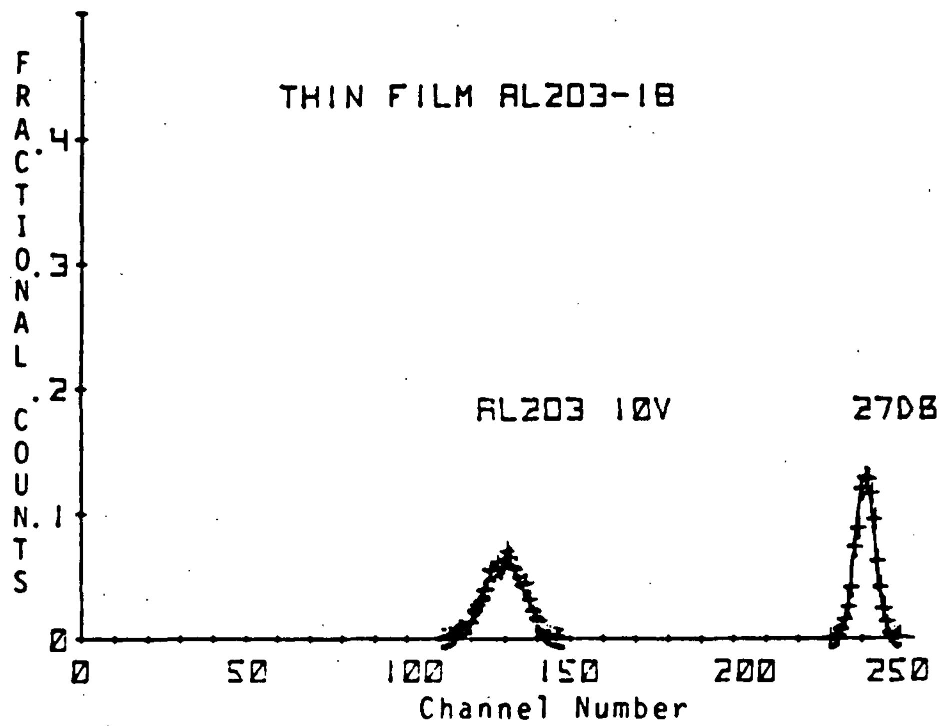

Figure 35. - Proton activation spectrum on a 10 nm thick film of Al_2O_3 18 and an electronic test pulse.

and in the case of the $Al_2O_3^{18}$ the standard deviation was 25 KeV. The electronics appear to contribute to nearly half of the spreading.

It was also necessary to calibrate the MCA in terms of the energy of each channel. Three physical calibration points were used. RBS spectra were obtained, on the metallic samples of niobium and tantalum, using alpha particles with an incident energy of 1850 KeV. This gave points near the low end of the energy range of interest. A point at the high end was obtained through proton activation of the thick film of SiO_2^{18}. These spectra are shown in figures 36 to 38 and the surface channels are indicated. Since these are surfaces only the kinematic scattering factor needs to be known for the RBS and the reaction kinetics for the proton activation, there is no ambiguity introduced by stopping powers.

A set of electronic test pulses, (see fig. 39) which were generated by passing a constant pulse through an amplifier set over a range of decibels, was calibrated using the physical values of the expression

$$-db = 20 \log_{10} \frac{V_{output}}{V_{input}}$$

A set of such pulses was run at the beginning and close of each day of analysis, by referring to the calibrated set changes in the setting were followed.

The MCA was found to deviate significantly from linearity and a second order polynomial was always used, a typical channel vs energy plot is shown in figure 40.

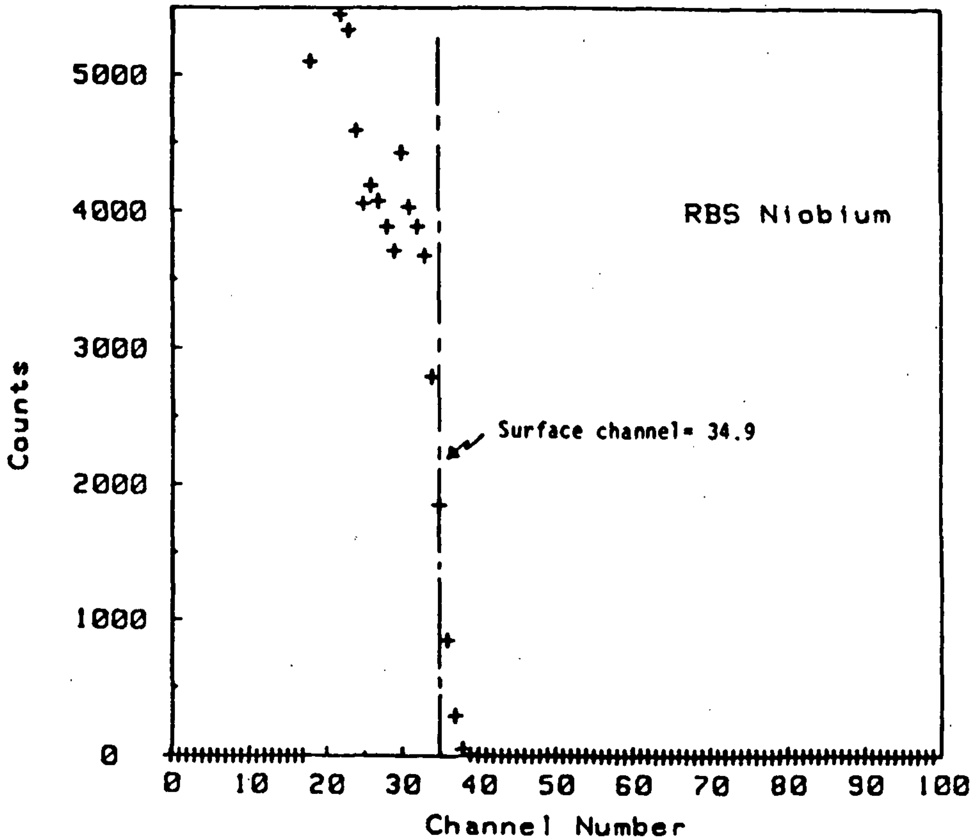

Figure 36. - Physical calibration point no. 1. Rutherford backscattering spectra on Niobium, E_{surf} = 1561.6 keV.

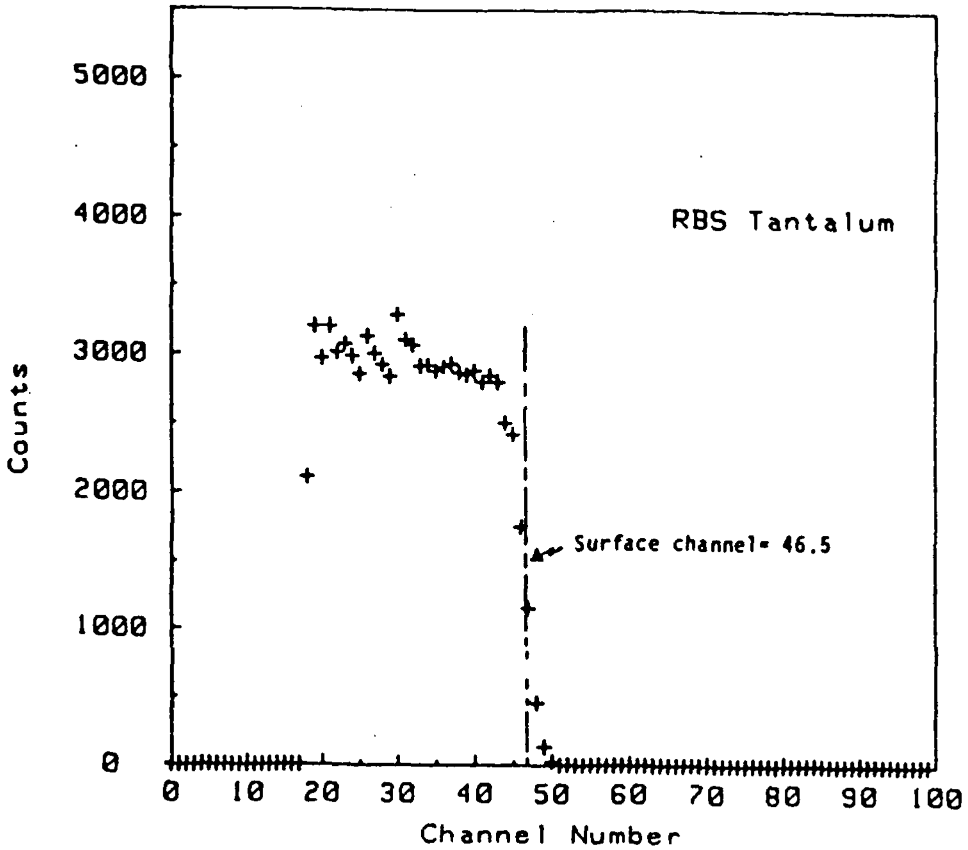

Figure 37. - Physical calibration point no. 2. Rutherford backscattering spectra on Tantalum, E_{surf} = 1695.9 keV.

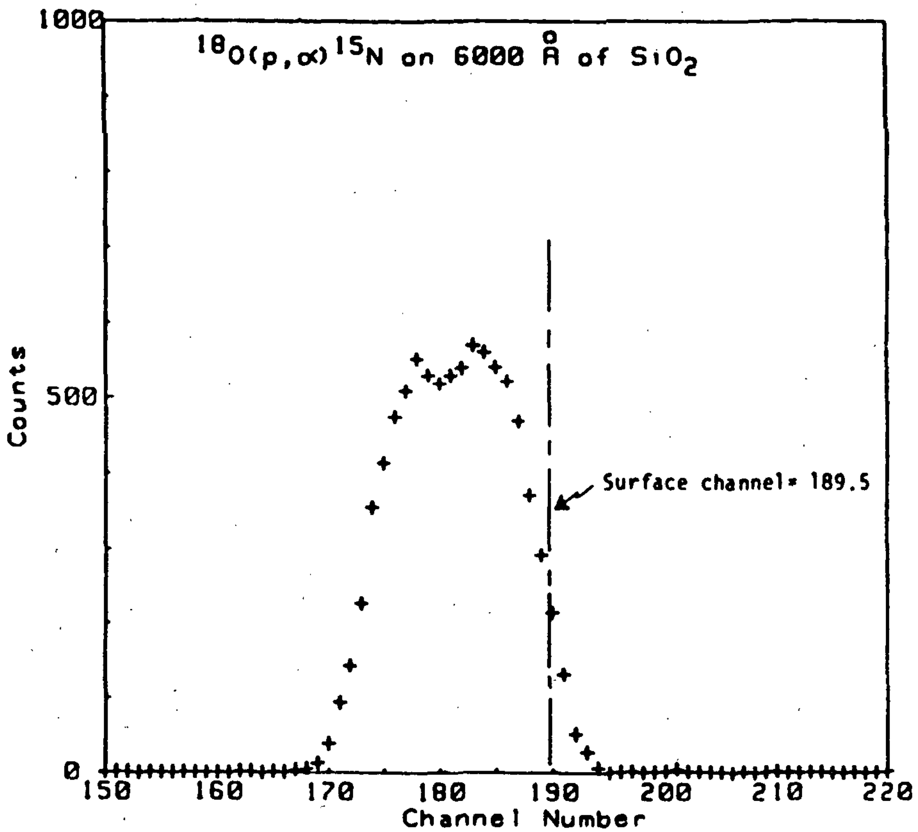

Figure 38. - Physical calibration point no. 3. Proton activation on a 6000 A thick slab of O-18 enriched SiO_2, E_{surf} = 3369 keV.

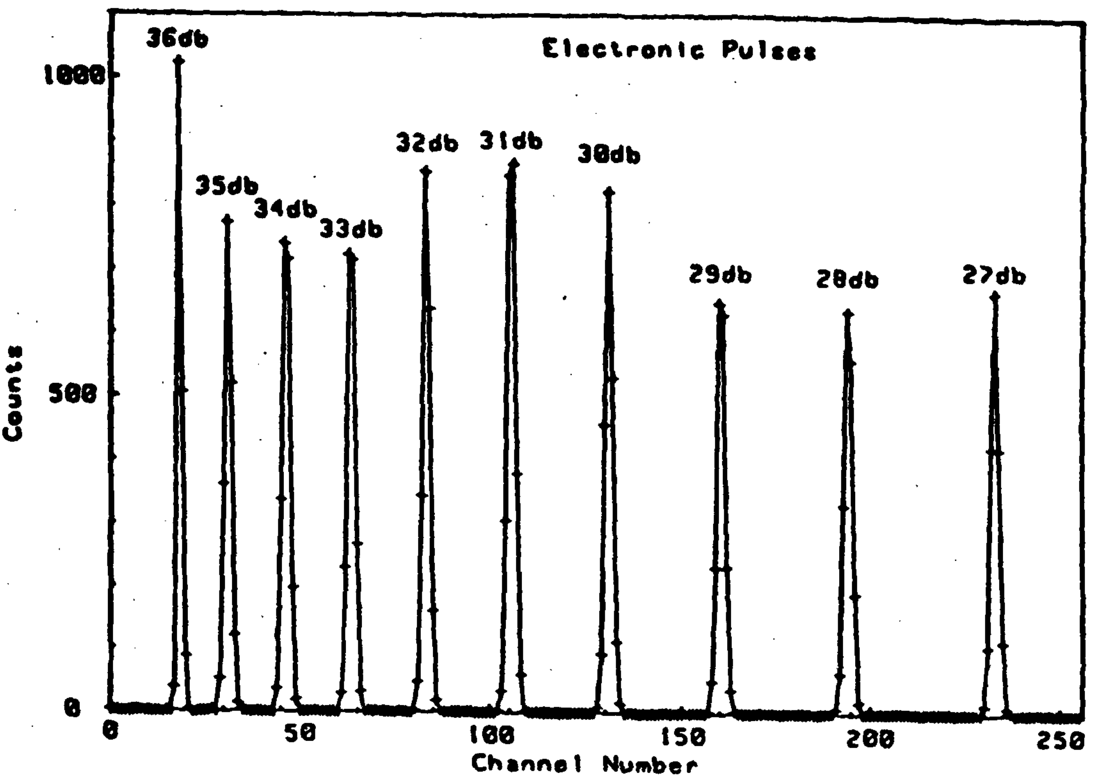

Figure 39. - Electronic pulses used for calibrating the energy of the channels in the MCA.

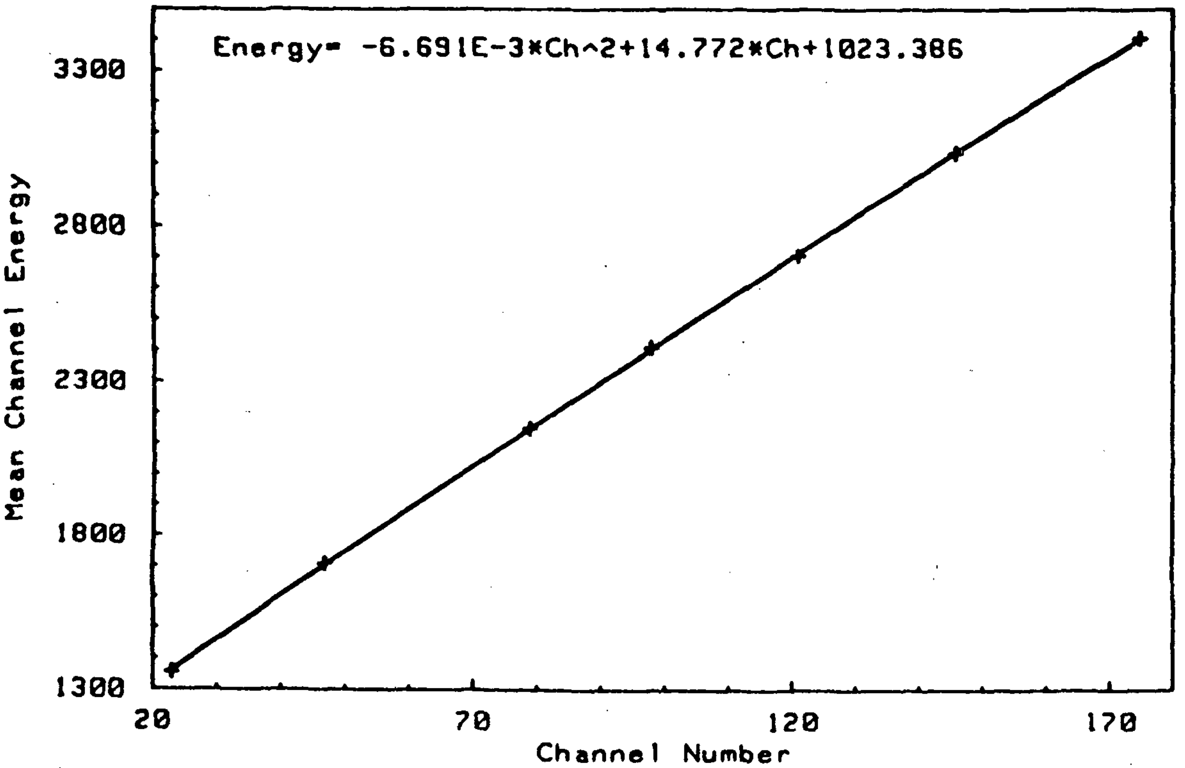

Figure 40. - Typical relationship of energy versus channel number for the MCA. The points are from the electronic test pulses and the curve is a second order polynomial fit.

Using these values and the tabulated stopping powers, assuming the elemental values could be added to give molecular values, an attempt was made to fit the proton activation spectrum for the natural abundance. The result is shown in figure 41. It is lacking in three separate ways. The location of the resonance is off, the resonance is too sharp, and the overall number of predicted counts is low compared to the experimental points.

The mislocation of the resonance is felt to arise from errors in the tabulated stopping powers (quoted errors are 10 to 20 percent) and additional error introduced by assuming additivity. Based on the fact that the energy-depth relationship is very nearly linear the decision was made to multiply this relationship by a factor sufficient to bring the predicted and experimental resonances coincident. The result was a difference of 13 percent.

The increased width of the experimental resonance was attributed to straggling[(63)]. This arises from the statistical fluctuations in the number of nuclear collisions which take place per unit distance. This may be approximated by a Gaussian function whose standard deviation is proportional to the square root of the distance travelled. The resonance was fit using a value of 4 $KeV/\mu m^{1/2}$.

The overall low counting rate was attributed to the use of the data of Amsel et al.[1] for the reaction cross section. This data and the approximation used in the fitting program are shown in figures 42 and 43. In previous work Yinnon[(63)] found these values

---

[1]Kindly supplied by L. D. Major.

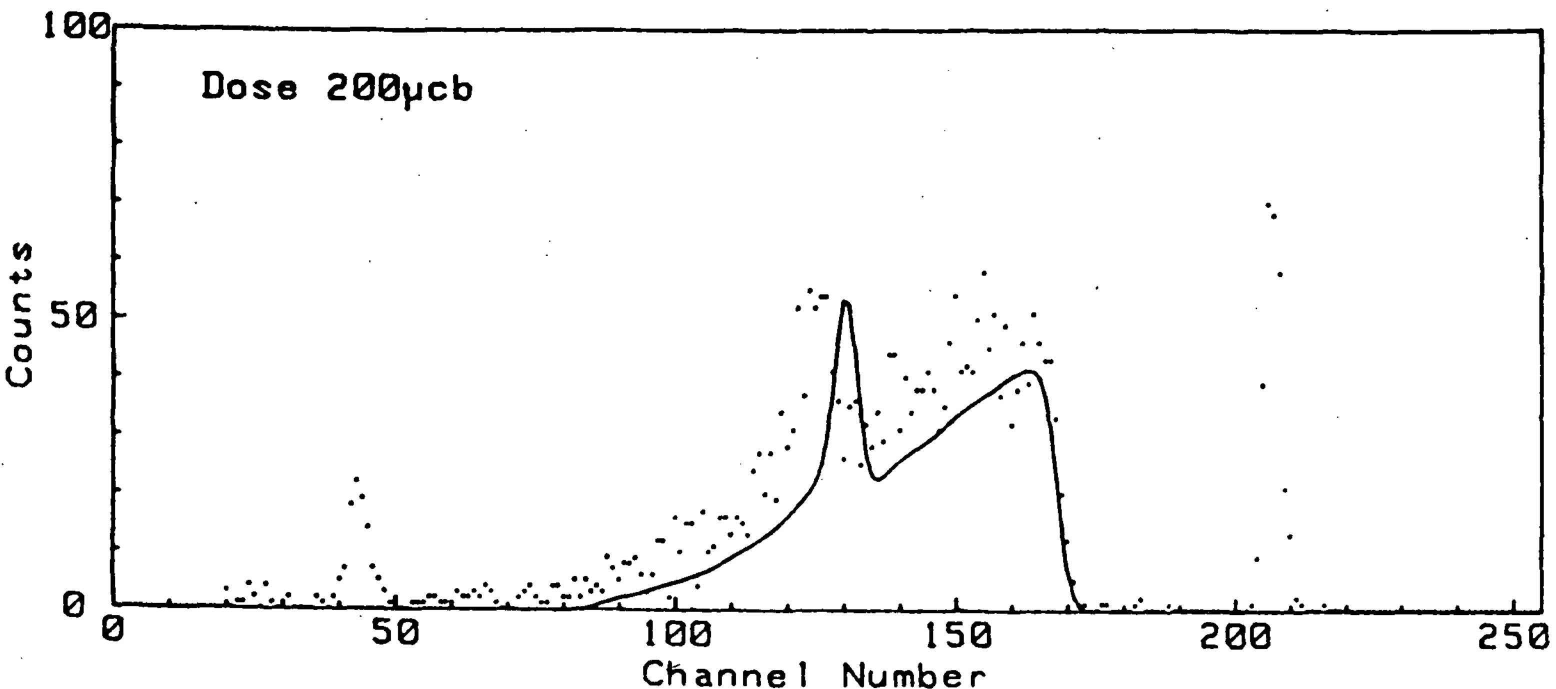

Figure 41. - A predicted proton activation spectrum for the natural abundance of O-18; i) using the tabulated stopping powers, ii) using the approximation of Amsel's data for the cross section, iii) neglecting straggling, compared with experimental points.

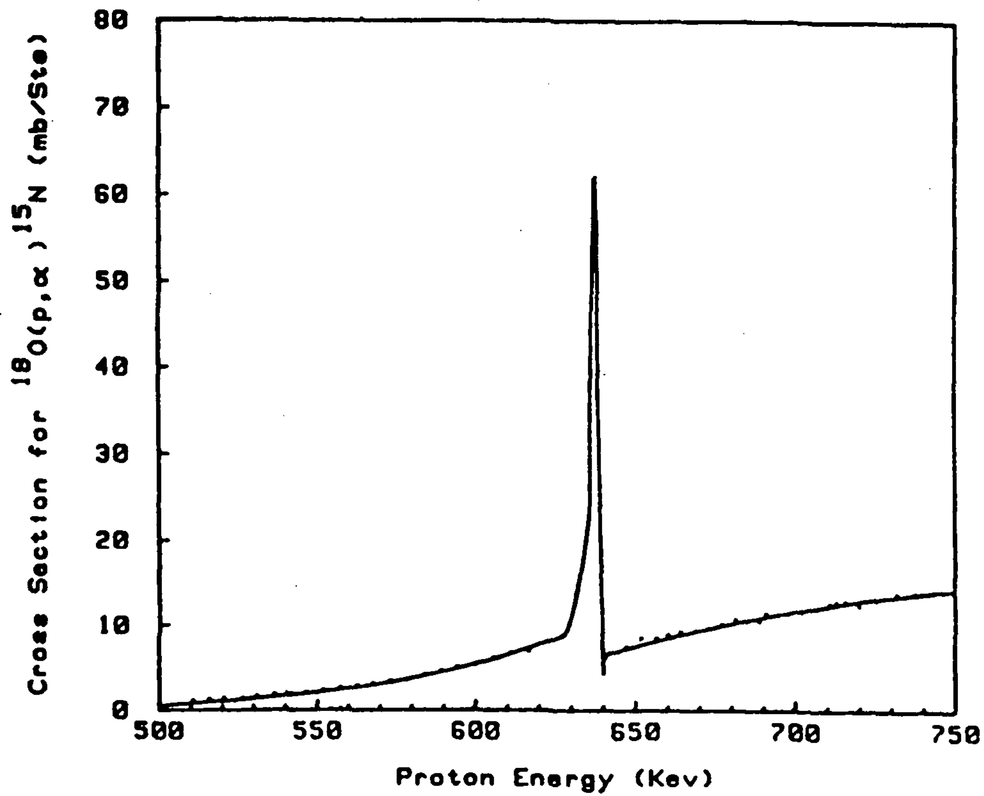

Figure 42. - Cross section for the nuclear reaction $^{18}O(p,\alpha)^{15}N$. The points are the experimental data of Amsel and the solid curve is the approximation used in fitting spectra.

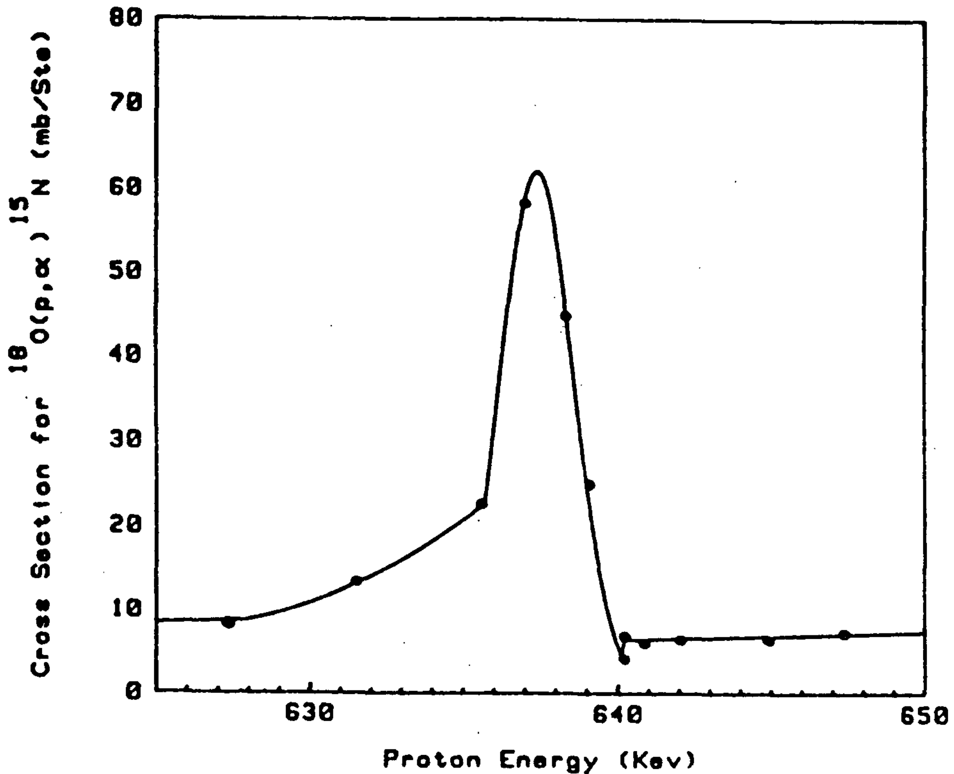

Figure 43. - Close-up of the resonance in the cross section for the nuclear reaction $^{18}O(p,\alpha)^{15}N$, showing the quality of the Gaussian approximation.

had to be multiplied by a factor of 1.2 in order to obtain a satisfactory fit for a spectrum from a sample of Ta_2O_5 enriched to 98 percent oxygen-18. In this work a multiplication of the Amsel data by a factor of 1.29 gave a good fit.

A fit of the natural abundance with these corrections is shown in figure 44. The corrections were used in all subsequent fits of concentration profiles. It is clear that an internal landmark in the form of the resonance is quite useful.

4.1.2 Channeling

The channeling of protons by Al_2O_3 was investigated primarily to assure it would not occur because of its deleterious effect on the information in a proton activation spectrum.

Two types of channeling experiments were performed. First, the axial channeling positions were determined. In this experiment the samples were placed in a goniometric chamber. In the chamber it is possible to translate the sample and/or rotate it around 3 axes.

The alignment was performed using a beam of 1.5 MeV alpha particles rather than 750 KeV protons because greater mass separation is obtained.

Rutherford backscattering spectra taken in both a "random" direction and when the crystal is oriented such that the beam travels down the c-axis, are shown in figure 45. The term random arises because, due to the thermal vibrations of the lattice atoms and the probabilistic nature of the electron positions, the location of an unchanneled particle, after a small number of collisions, can only be described statisticly.

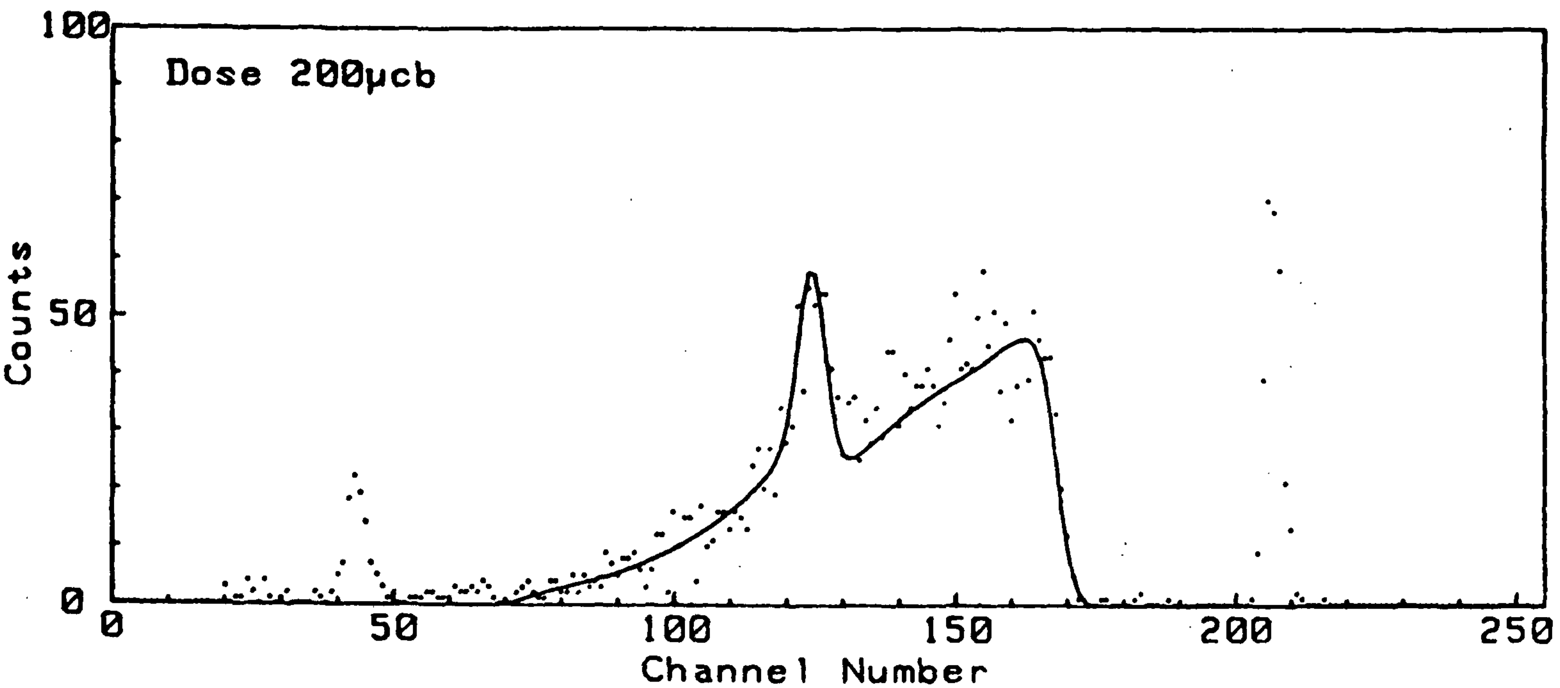

Figure 44. - A predicted proton activation spectrum for the natural abundance of O-18; i) using an arbitrary reduction in the depth energy relation of 13 percent, ii) using an arbitrary multiplication of Amsel's data for the cross section by a factor of 1.29, iii) using a straggling coefficient of 4 keV/um$^{1/2}$, compared to the experimental points.

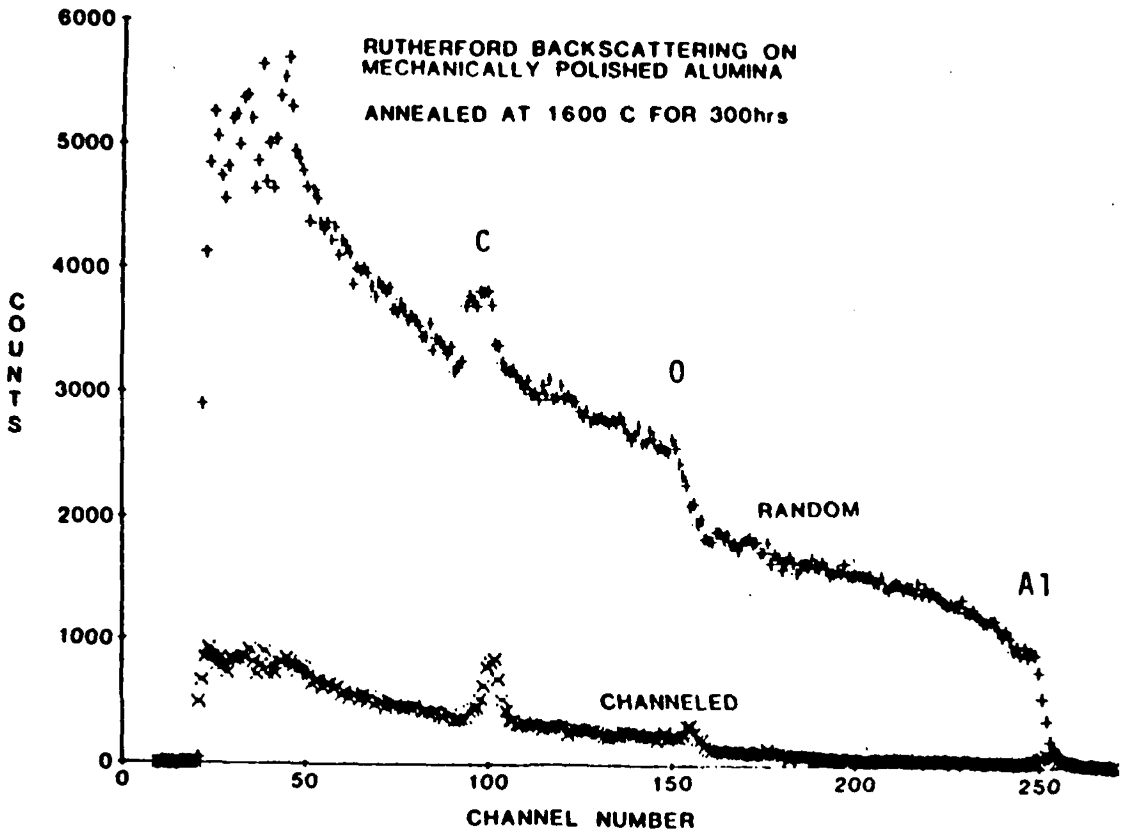

Figure 45. - Rutherford backscattering spectra on an annealed α-Al_2O_3 sample, in and out of axial channeling conditions.

It can be seen that in the channeling orientation the counting rate for collisions with the lattice is markedly reduced both in the Al and O plateaus. The counting rate for the amorphous carbon layer evaporated on the sample to dissipate charge is, of course, not affected by orientation.

A second sample from the same boule which had been polished but not subjected to any anneal, was treated in the same way. The RBS spectra for random and c-axis orientation are shown in figure 46. A comparison of figure 45 with figure 46 shows that the counting rates in the channeled spectra for the unannealed sample are considerably higher than for that of the annealed sample. Note, also, that the counting rate decreases, indicating an increase in channeling, until channel 210, corresponding to a depth of 0.25 μm. This is certainly due to the damaged layer near the surface of the sample which was generated during the mechanical polishing. The absence of this behavior in the annealed sample is experimental evidence that this damage can be removed by annealing.

A second, polished and annealed, sample was investigated by transmission electron microscopy (TEM). The sample was back thinned to reveal the region which had been subjected to the polishing. An area of 1×10^{-4} cm^2 was investigated and no evidence of damage was seen, e.g., dislocations, figure 47. A material with a dislocation density of 10^6 $lines/cm^2$ it would be expected to find on the order of 100 lines within this area. This serves to confirm the RBS data. This result is not new. Both Hockey[63] and Reed[13], found that

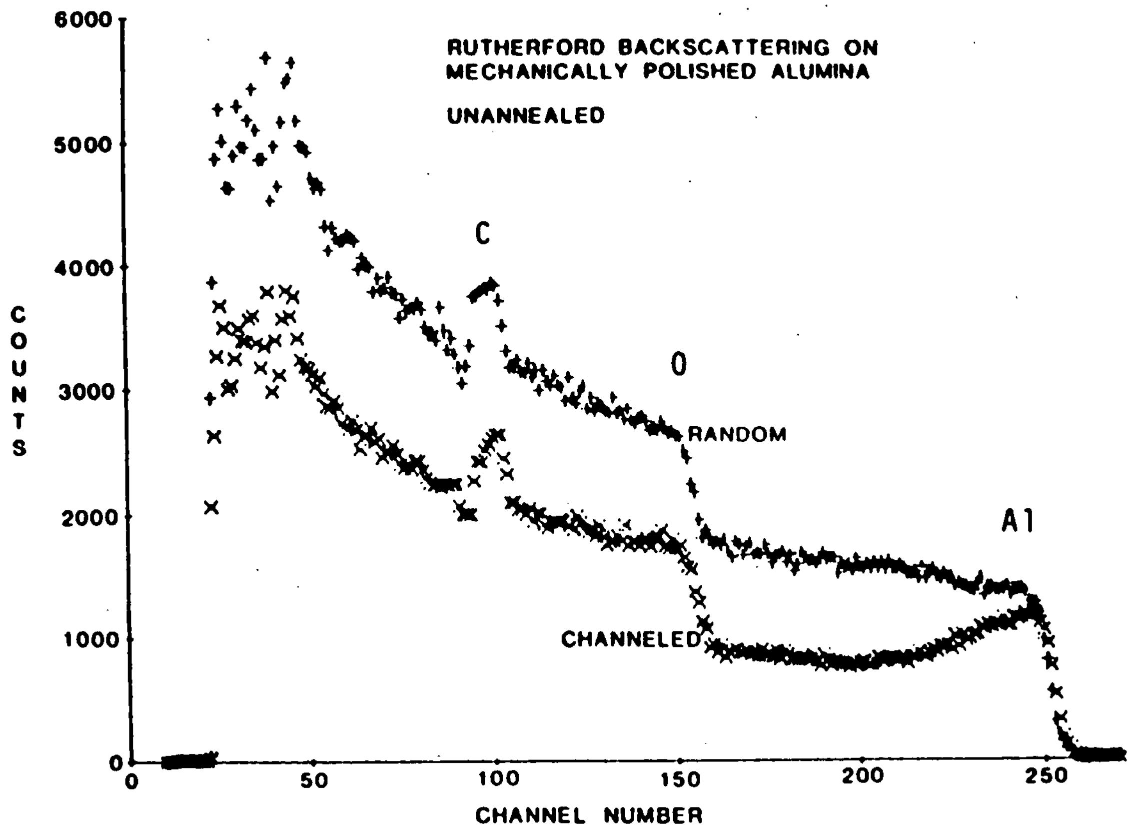

Figure 46. - Rutherford backscattering spectra on an unannealed α-Al_2O_3 sample, in and out of axial channeling conditions.

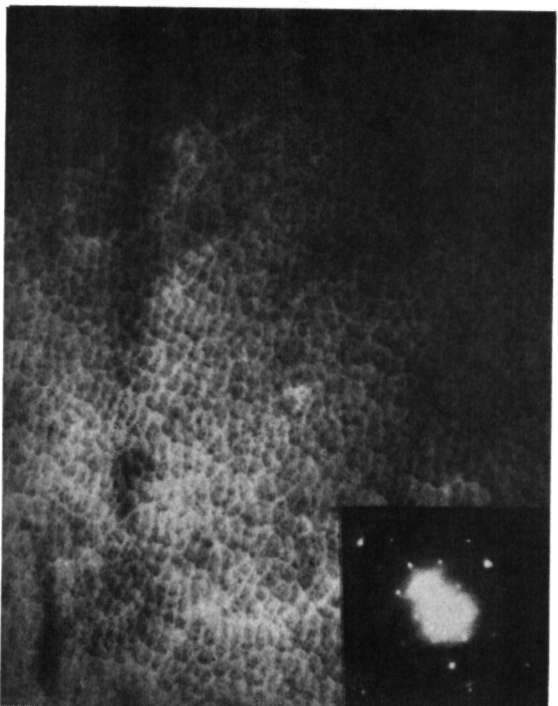

Figure 47. - TEM micrograph of the near surface region in mechanically polished and annealed α-Al_2O_3.

the damage produced by abrasion, in Al_2O_3, could be removed through annealing.

A third set of spectra were taken from a different location on the sample which had been annealed at 1600° C for 300 hr. These are shown in figure 48. It can be seen that there are counts at higher energies than those arising from aluminum at the surface. There is both a plateau, which is depressed when the crystal is aligned in a channeling orientation, and a sharp peak, which is unaffected by channeling. The energy of the peak corresponds to 1.5 MeV alphas scattered from nuclei ~ 39 to 40 Amu which corresponds to K and Ca. The fact that the peak remains unaltered when the sample is in a channeling orientation suggests that these cations are located in an amorphous (at least not epitaxial) phase on the sample surface, and the plateau is consistent with diffusion of these cations into the sapphire. The counting rate for the heavy impurities would be expected to behave during channeling like that of Al when the impurities occupy Al sites.

This suggests that the sample was contaminated at some point during the exchange procedure. It is also indicated that the contamination is not uniform across the sample. Later work established that the samples were indeed contaminated in the form of a Ca, K, Al, Si glass on the sample surface.

The relative concentrations of the heavy impurity may be estimated from the plateau heights in figure 48. The only variable between the leading edges of the two plateaus is the cross sections for the two species. The ratio of cross sections can be calculated

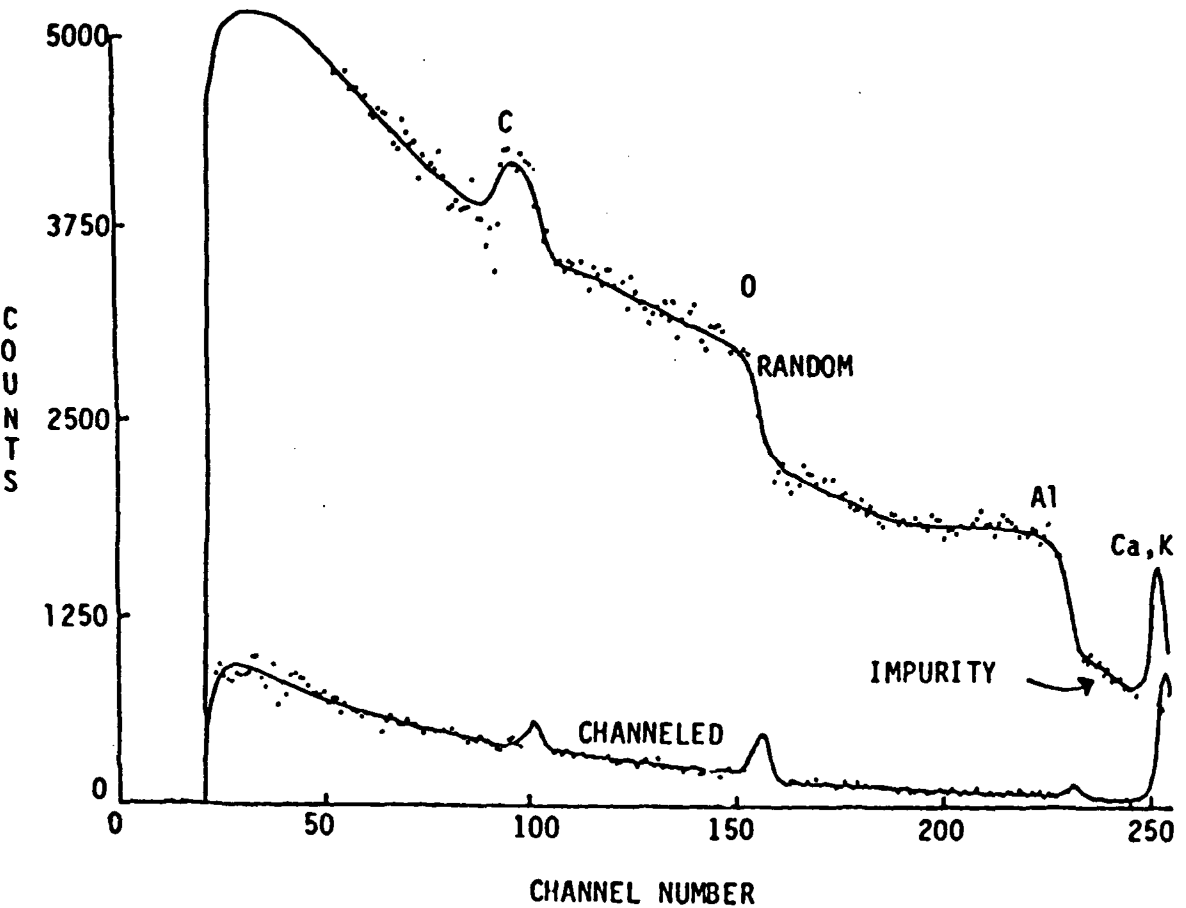

Figure 48. - Rutherford backscattering spectrum on α-Al_2O_3 annealed at 1600° C, containing a heavy impurity.

from the expression[64]

$$\sigma = \left(\frac{Z_1 Z_2 e^2}{2\ E\ \sin(\theta)}\right)^2 \frac{\left\{\cos\theta + \left[1 + \left(\frac{M_1}{M_2}\sin(\theta)\right)^2\right]^{1/2}\right\}^2}{\left[1 - \left(\frac{M_1}{M_2}\sin(\theta)\right)^2\right]^{1/2}} \qquad (4.1\text{-}1)$$

where σ is the differential cross section, E is the particle energy, Z_1 and M_1 are the atomic number and mass of the particle and Z_2 and M_2 are the atomic number and mass of the struck nucleus, while θ is the laboratory scattering angle.

When the appropriate values are substituted the ratio of impurity to aluminum cross sections, R_c, is very nearly equal to the ratio of masses

$$R_c = \frac{m_I}{m_{AL}} \approx \frac{40}{27} = 1.5$$

Extrapolating the impurity plateau to the surface, and measuring the heights in figure 48 allows the impurity concentration, c_I, to be estimated by

$$C_I = \frac{H_I}{1.5\ H_{Al} + H_I} = \frac{4\ (\text{arb. units})}{(1.5)\cdot(5) + 4} = 35 \text{ percent}$$

This is a very high concentration. It is such a high level that it is surprising that the material still has Al_2O_3 channeling behavior, although McCune[66] has observed Ca concentrations of 10 percent in the near surface region arising from the segregation of a dopant level (~100 ppm) bulk concentrations. This sample was the only one in which this very high level of impurities was observed. Concentra-

tions up to a percent, however, would not produce a counting rate sufficient for detection.

The second type of channeling experiment employed an incident beam of 750 keV protons and two detectors. One detector was located on either side of the sample making the same angle to the beam. Each detector was connected to a separate set of electronics, one was used to collect a RBS spectra and the other was used to collect a proton activation spectra. In this way the effect of channeling orientation on each could be studied.

To check for planar channeling, the sample was oriented to 5° away from the c-axis. The sample was rotated about the beam in three degree steps. The geometry is schematically illustrated in figure 49. At each step the sample was bombarded with the proton beam spectra both RBS and $^{18}O(p,\alpha)^{15}N$ were taken. The integral of the aluminum plateau of the RBS spectra and of the entire $^{18}O(p,\alpha)^{15}N$ spectra are plotted as a function of the angle of rotation in figure 50. Two points should be noted here. The first is that when the beam is nearly parallel to a principle crystallographic axis (11.0), (10.0), or (01.0), the counting rate for the proton activation spectrum is less than half of what it is in a random position. In between these major drops there appear smaller decreases ~5 to 10 percent. Secondly, the RBS Al plateau is much more sensitive to the channeling and can be used as a guide for acceptance or rejection of a set of spectra.

For the normal course of spectra accumulation in the chamber (shown in fig. 24), both the RBS and the proton activation spectra

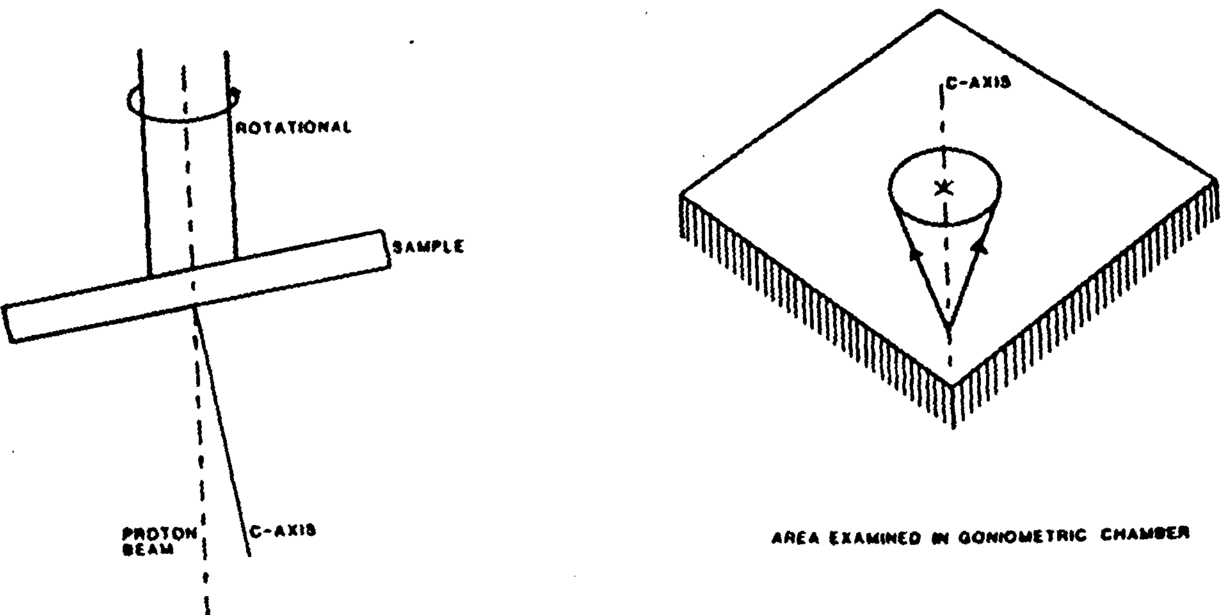

Figure 49. - Schematic of the geometry for a rotational scan.

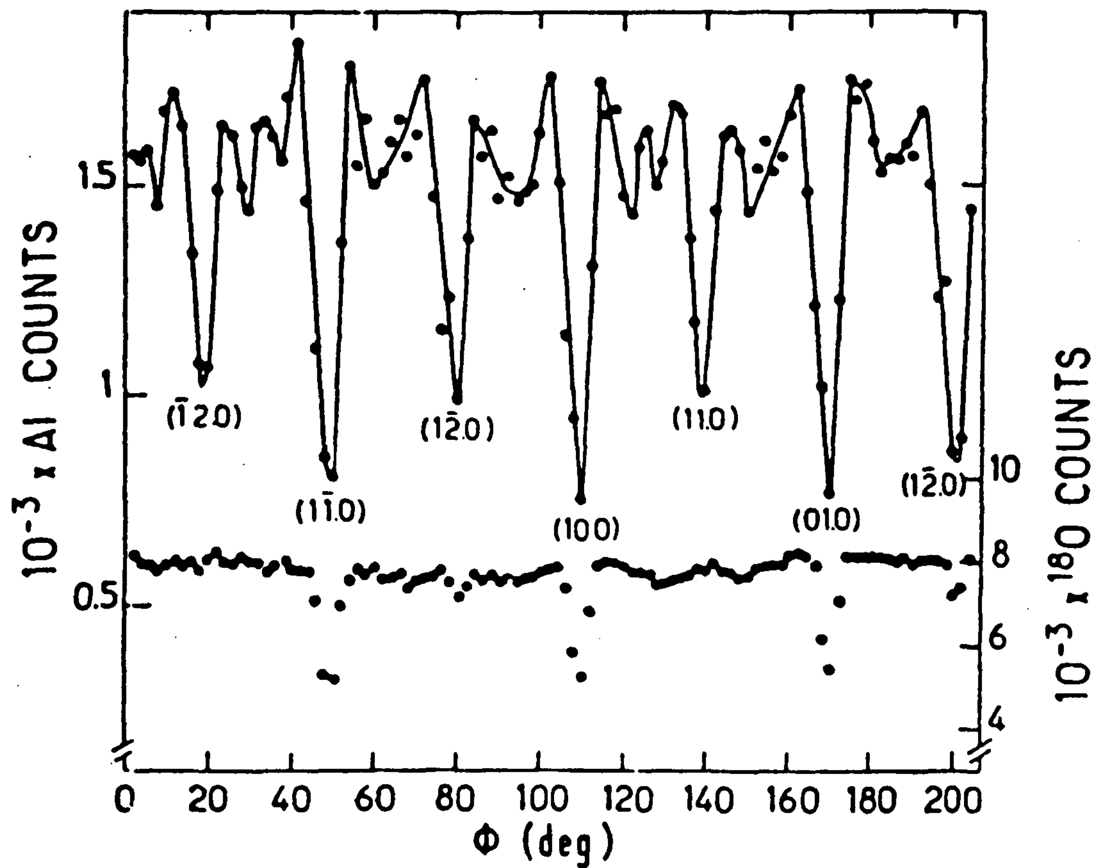

Figure 50. - Results of the rotational scan showing the presence of planar channeling in Al_2O_3.

were accumulated. If the RBS indicated channeling, the run was aborted, the sample rotated a few degrees and rerun. Channeling did appear periodically during analyses, and those spectra aborted. The RBS on Al was not a perfect indicator however, due to the differences between the crystal structure of the aluminum and oxygen sublattices.

Orientation effects occurred in the RBS Al plateau which were not carried over into proton activation spectra. The two sets of figures 51, 52 and 53, 54, show simultaneously recorded RBS and proton activation spectra. Note that although the RBS Al plateau has either a depressed, random, or enhanced counting rate, depending on orientation, the proton activation spectra for each set may be superimposed. For this reason a number of spectra were taken on each sample to ensure that "random" information was obtained.

An example of the effect of being in a random orientation, planar channeling, and axial channeling is shown in figure 55. The effect on the counting rates and the position of the resonance can be seen.

4.1.3 Nuclear Reaction

4.1.3.1 Qualitative Interpretation

The samples analyzed by proton activation were prepared and exchanged in groups. One sample from each of the five boules and usually a duplicate of one were exchanged sitting side by side on the same shelf. In some cases several shelves were loaded at different points in the thermal gradient, to simultaneously exchange at different temperatures. The spectra for the three undoped boules exchanged

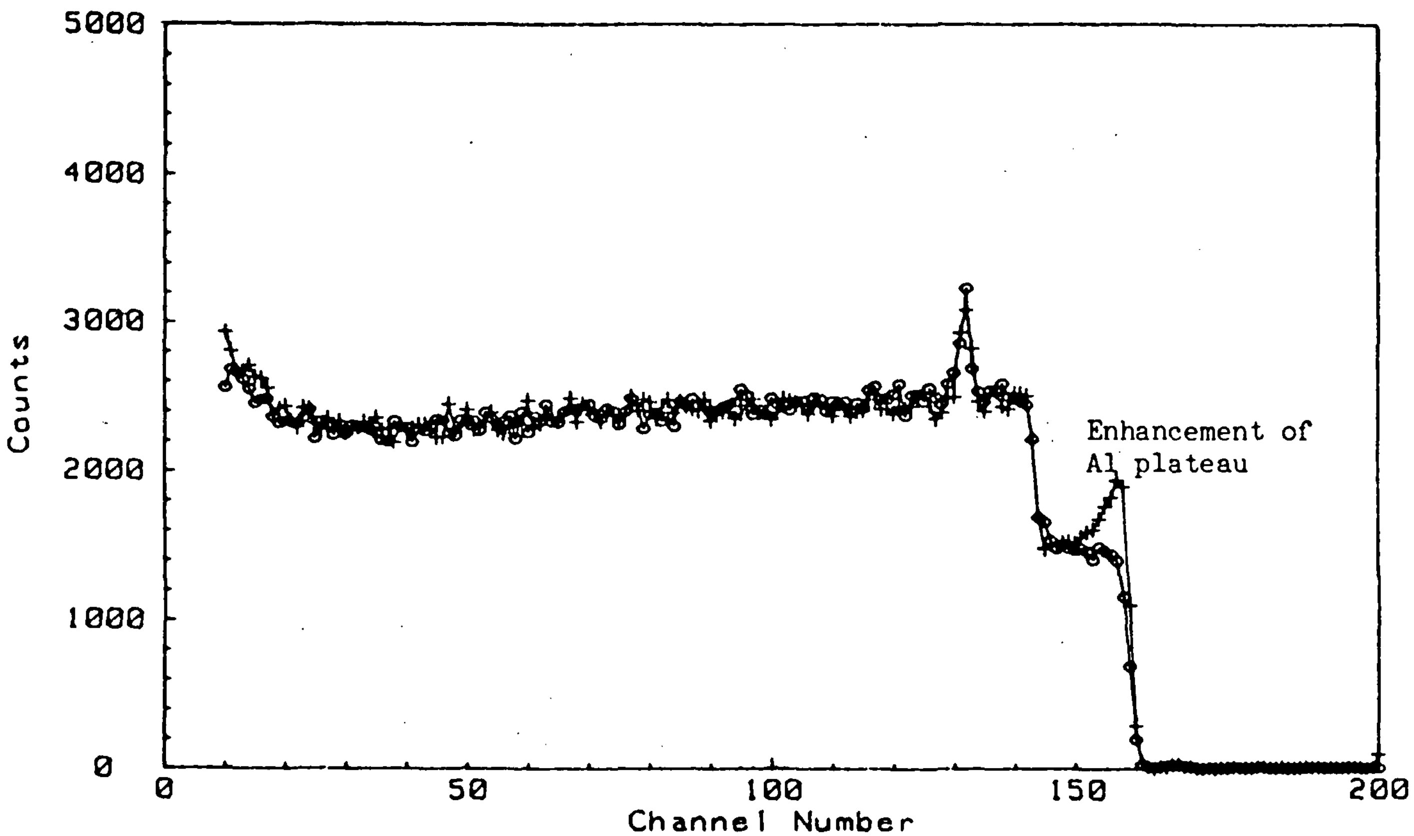

Figure 51. - RBS spectra taken on Ni-12 at two rotation angles, 0 and -4°. The Al plateau displays an enhanced counting rate at -4° of rotation.

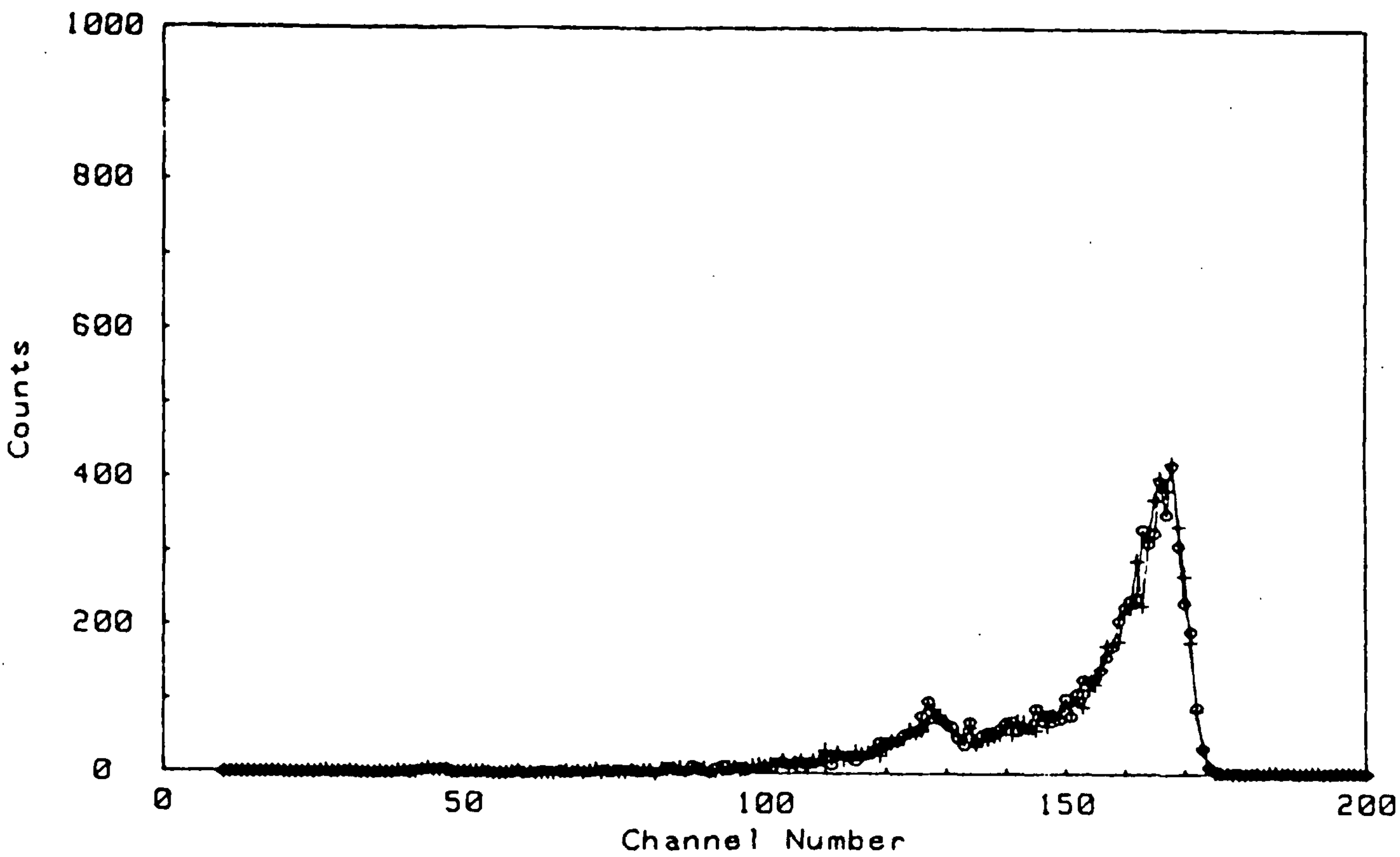

Figure 52. - A comparison of proton activation spectra taken on Ni-12 corresponding to the RBS spectra in figure 51.

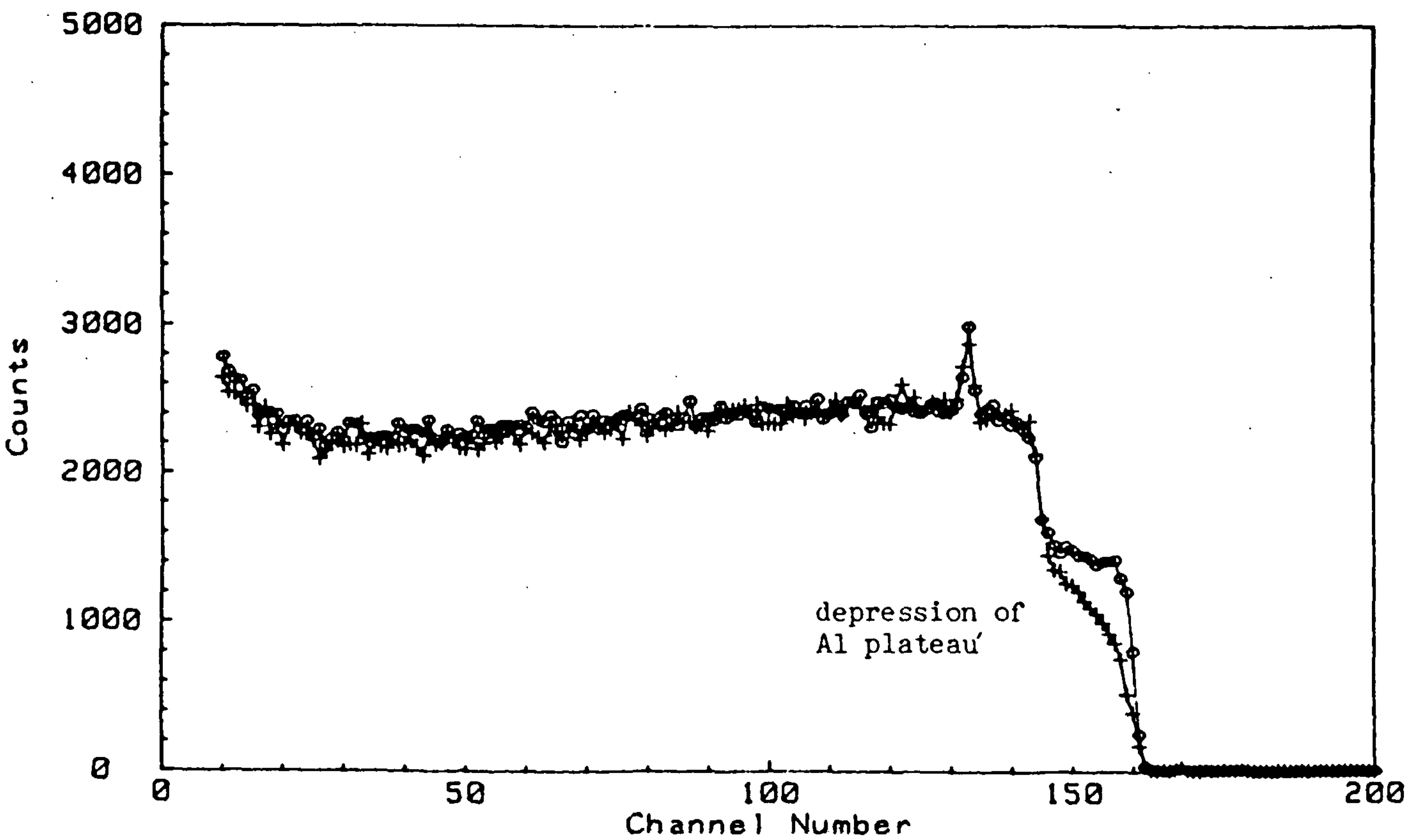

Figure 53. - RBS spectra taken on UD-6 at two angles of rotation, 0 and +4°. The Al plateau displays a depressed counting rate at 0° of rotation.

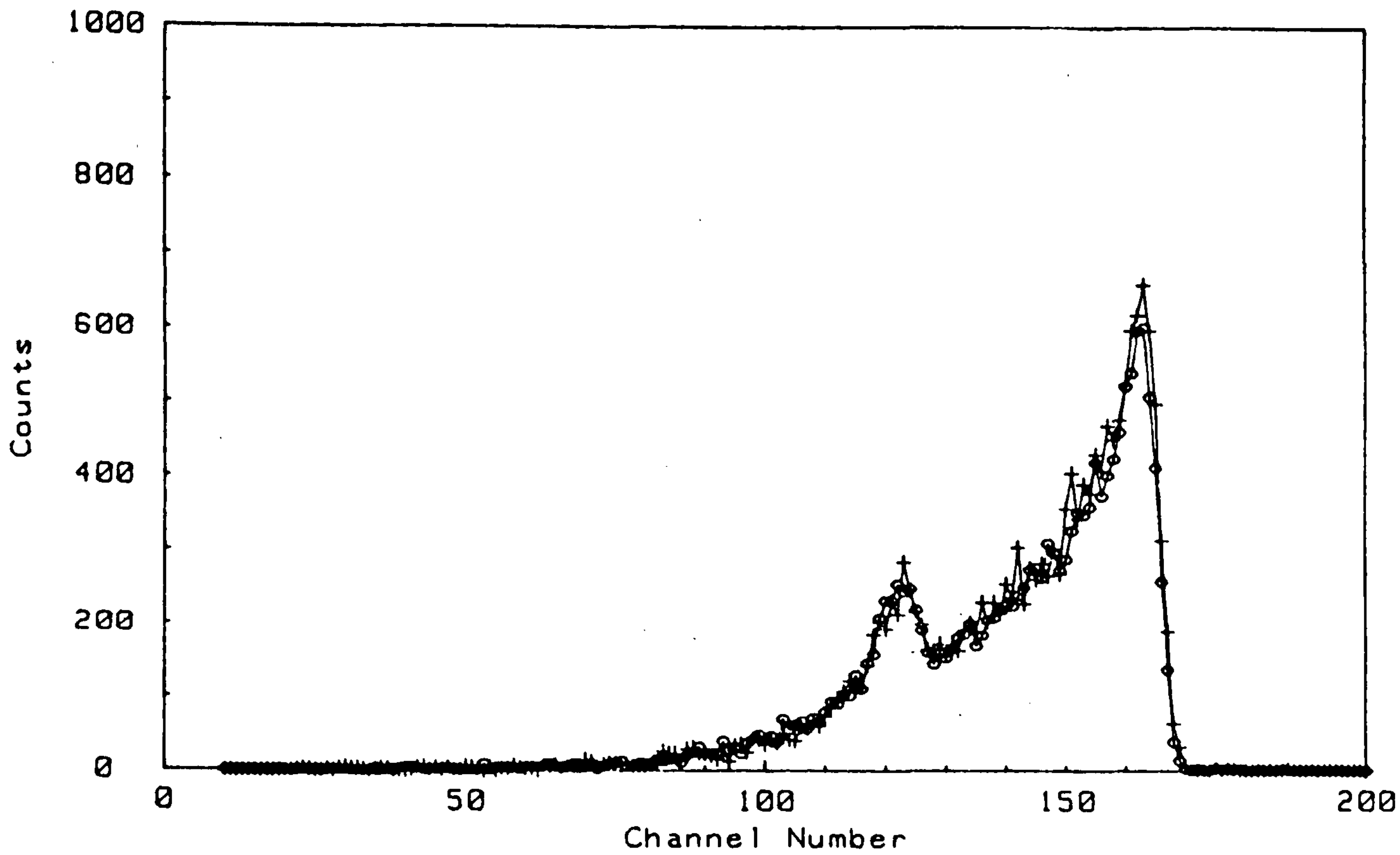

Figure 54. - A comparison of proton activation spectra taken on UD-6 corresponding to the RBS spectra in figure 53.

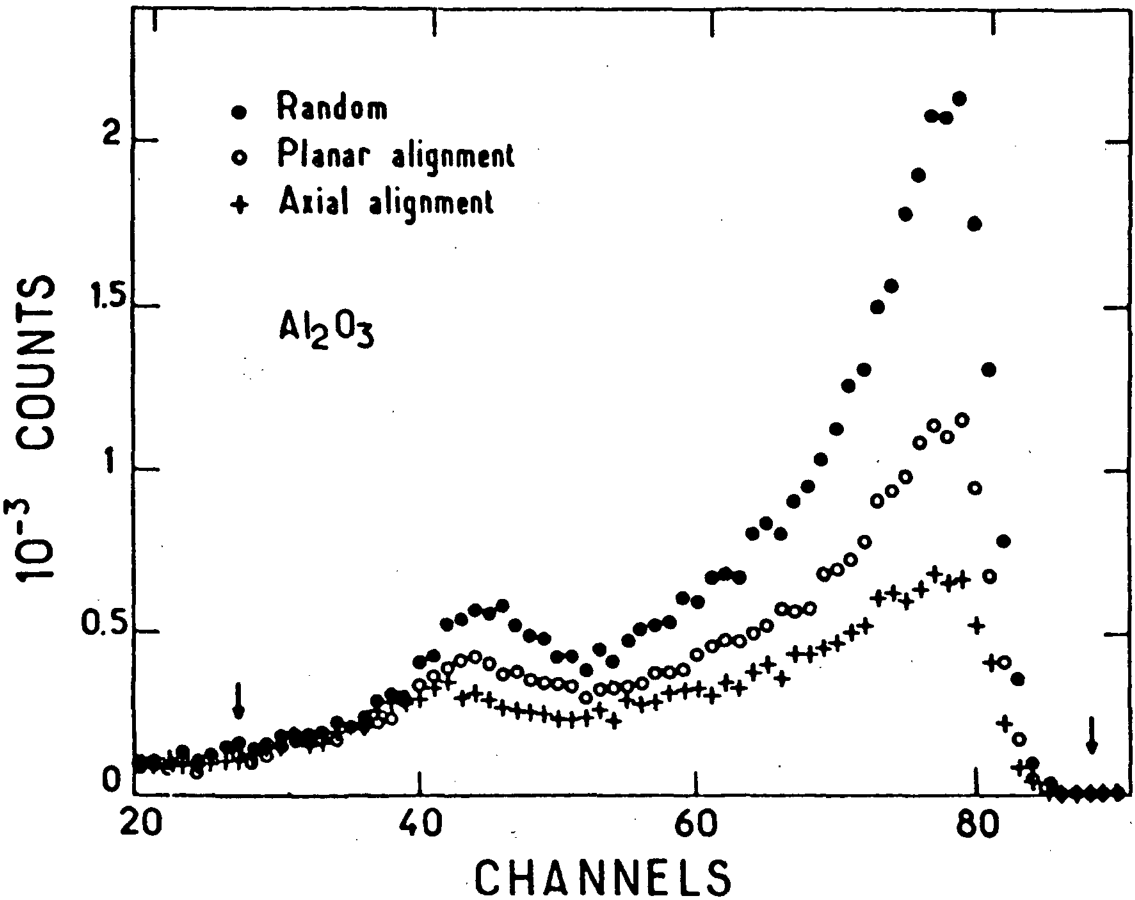

Figure 55. - The effect of axial and planar channeling on a proton activation spectrum.

at 1458° C, is shown in figure 56. Because of the similarity of them only one undoped spectrum was plotted on the rest of the plots.

Several spectra were taken on each sample. An example of two spectra taken one after the other on the same sample, with a four degree rotation of the sample between collection, is shown in figure 57. The agreement between them is quite good but there is some data scatter at the peak.

An example of two samples from the same boule, exchanged together, is shown in figure 58. Again, the spectra look very similar although in this case the "tail" of Ni61 appears to be a little higher than that of Ni60.

Figures 59 to 62 show spectra for samples of the three compositions plotted for four exchanges at temperatures ranging from 1415° to 1677° C. The most striking feature of each plot is the sameness of each profile. There is a small amount of scatter but it is no larger than that between spectra on the same sample or between samples from the same boule.

Another feature of these spectra is the deeply penetrating "tail" of low concentration. "Tails" of this type were observed by Reddy and Cooper. They claimed to be able to remove these "tails" by preannealing their samples in air. Our samples were subjected to such preannealing treatments, however the "tails" persist. There is some difference between the "tail" magnitudes but it does not appear to be systematic. For example, in figure 60, the Ni-doped sample has a larger "tail" than the undoped sample, yet in figure 59, the situation is reversed.

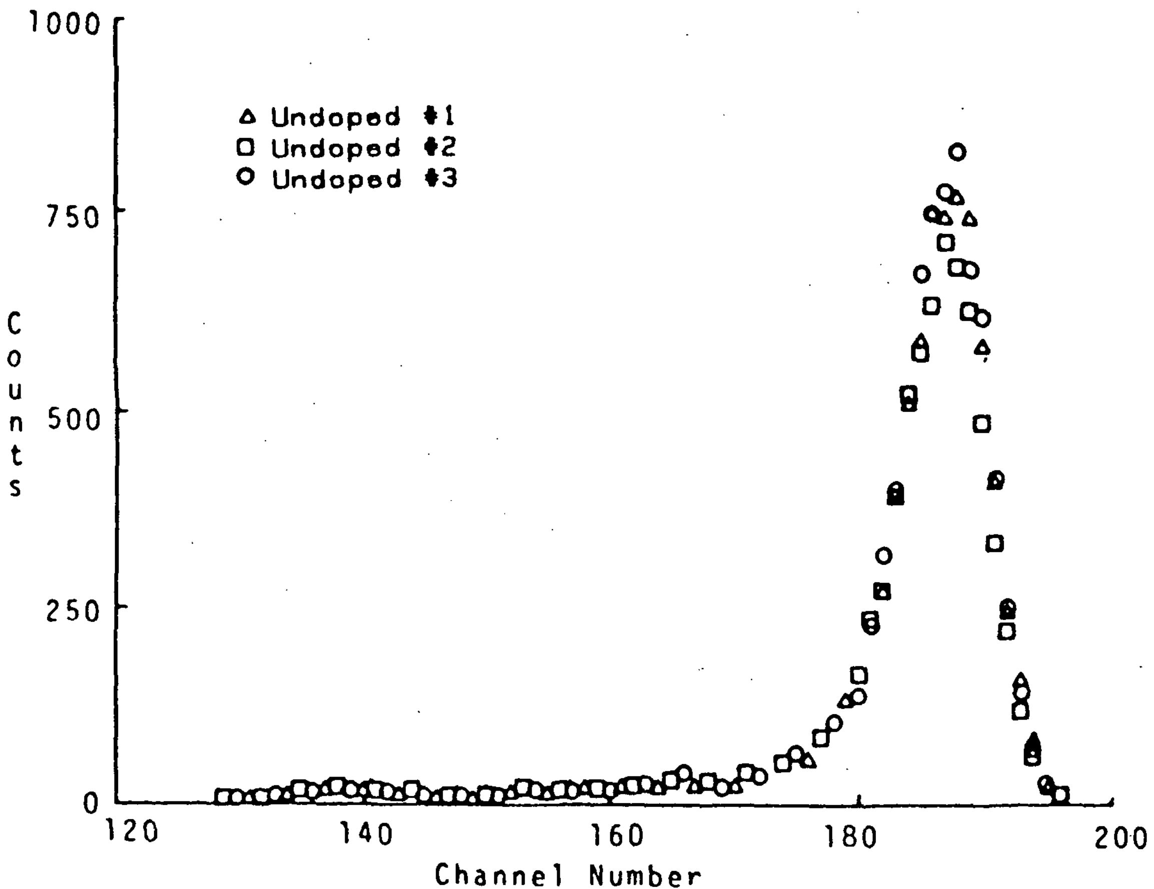

Figure 56. - Proton activation spectra for samples from the three undoped boules, exchanged at 1458° C for 404 hr.

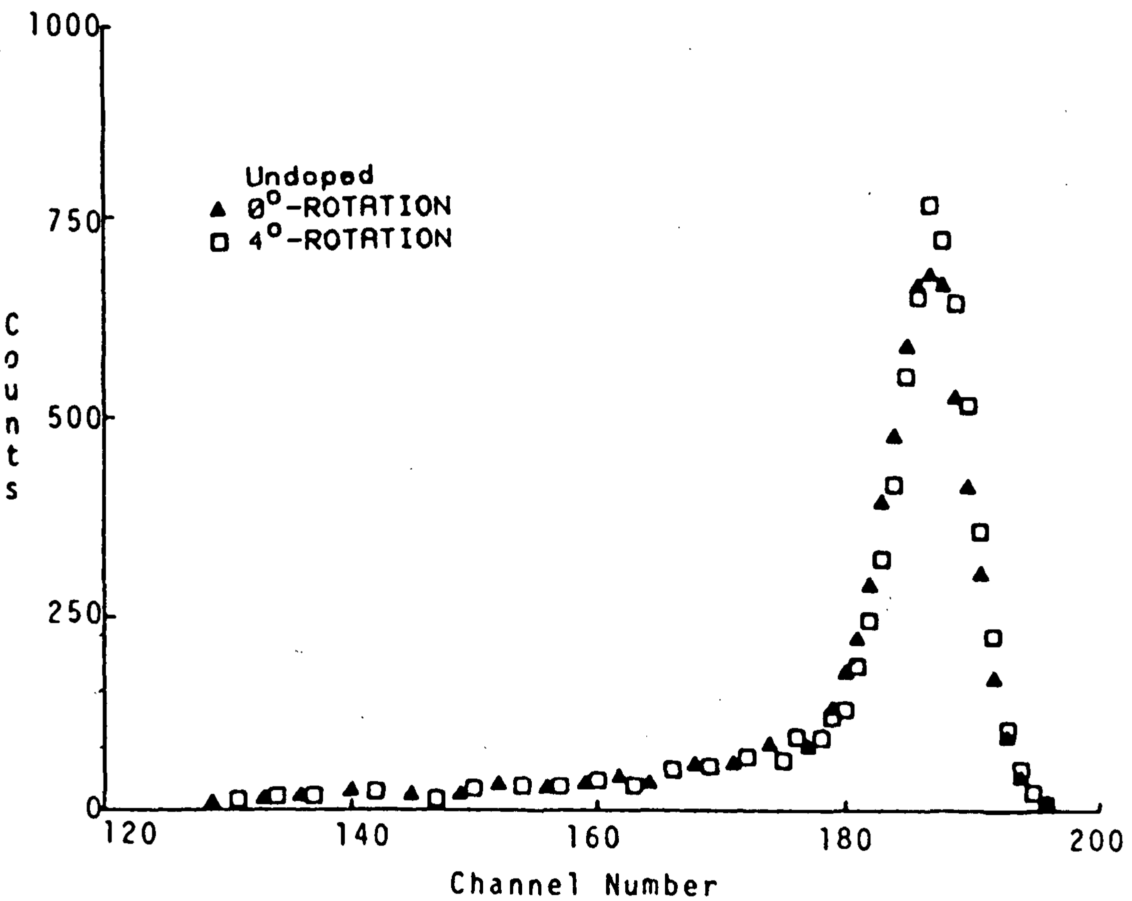

Figure 57. - Two proton activation spectra taken on the same sample exchanged at 1458° C for 404 hr.

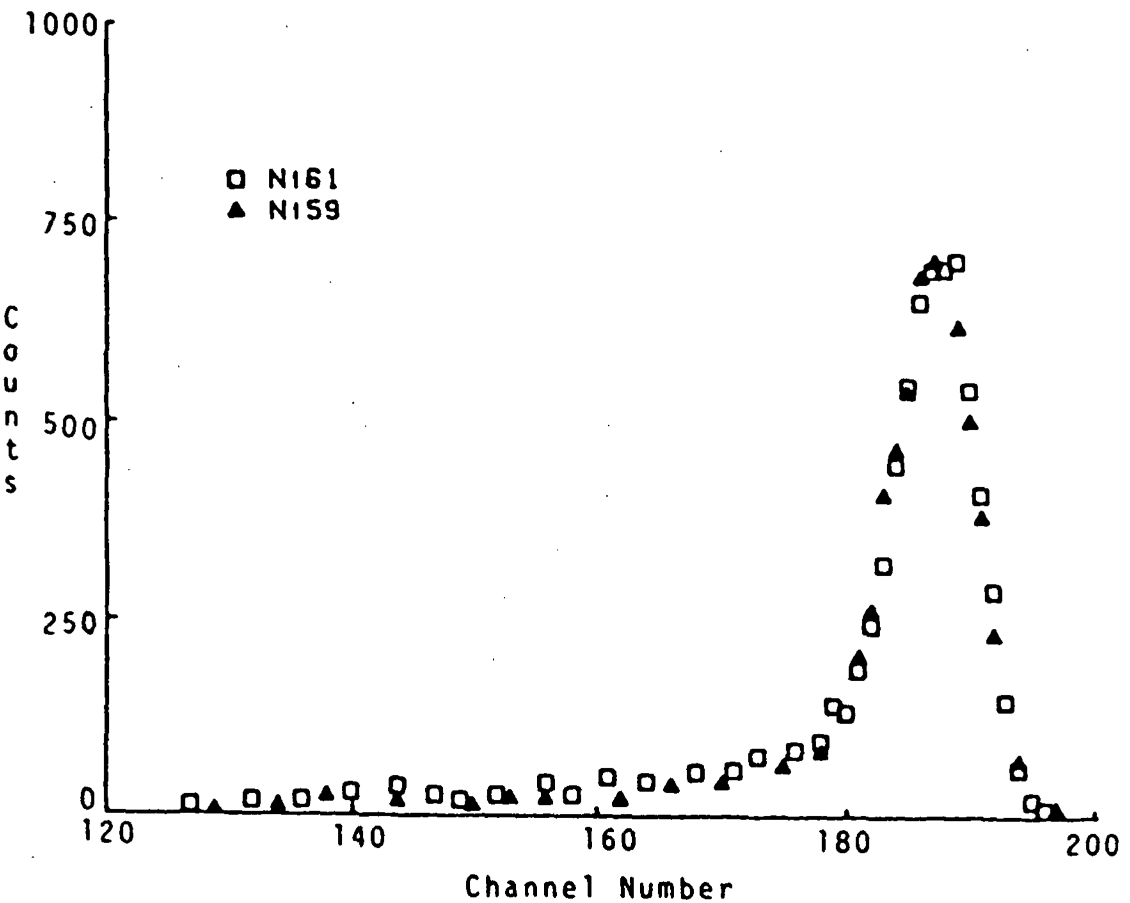

Figure 58. - Proton activation spectra taken on two separate samples from the same boule, exchanged together at 1458° C for 404 hr.

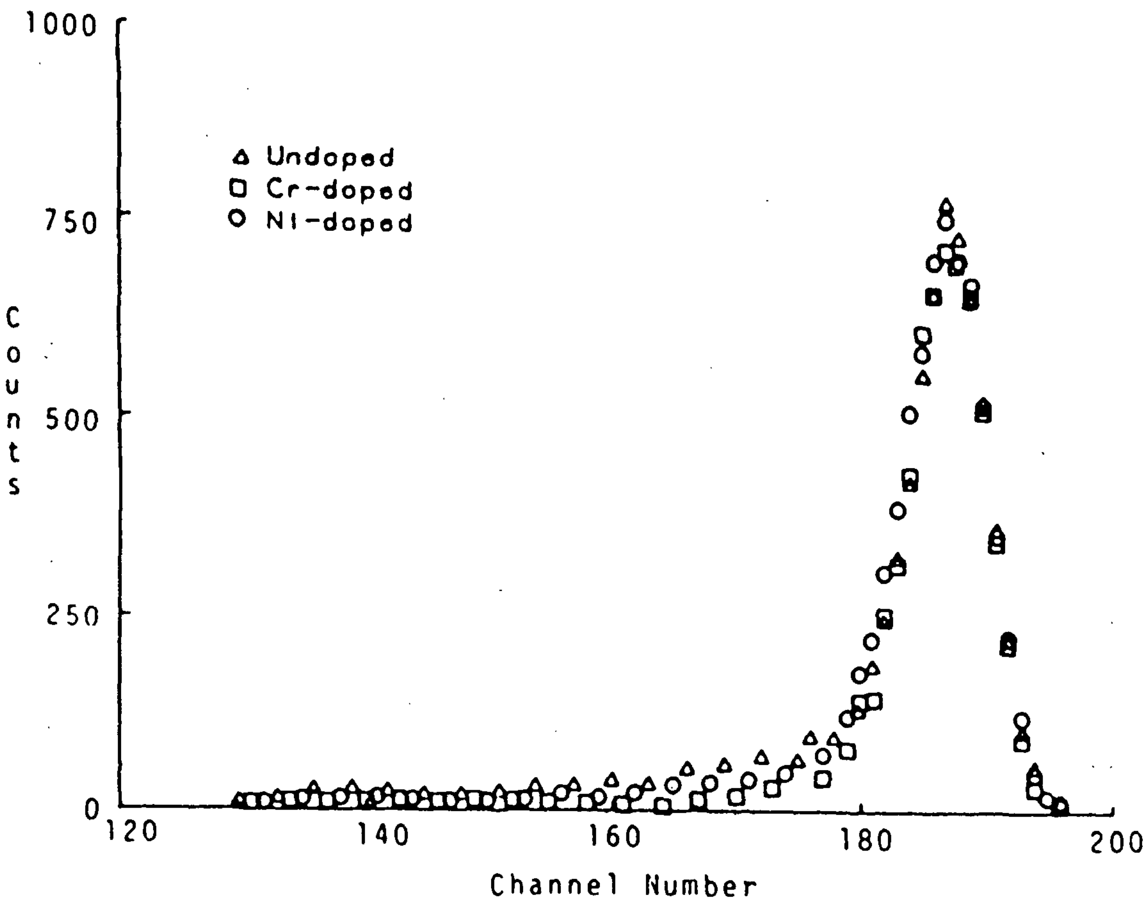

Figure 59. - Proton activation spectra taken on an undoped sample, a Cr-doped sample, and a Ni-doped sample all exchanged together at 1415° C for 404 hr.

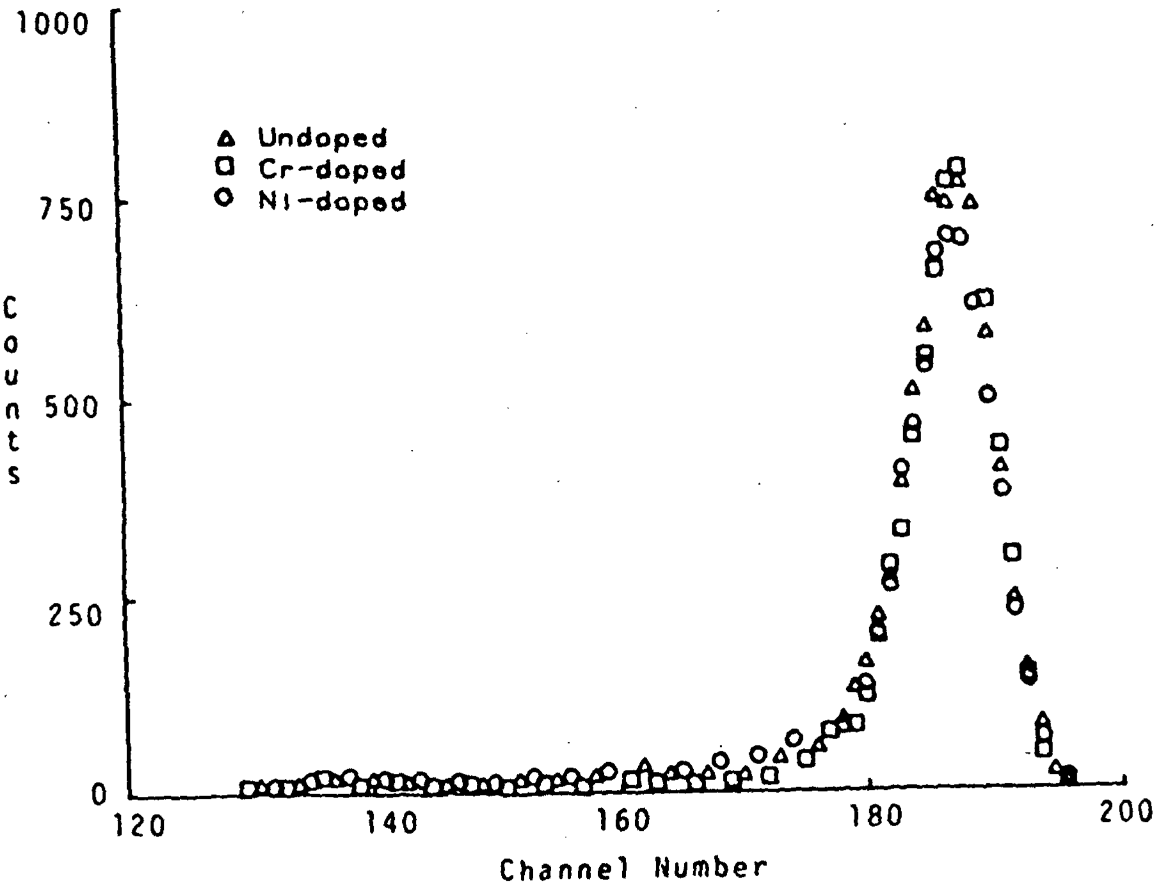

Figure 60. – Proton activation spectra taken on an undoped sample, a Cr-doped sample, and a Ni-doped sample all exchanged together at 1458° C for 404 hr.

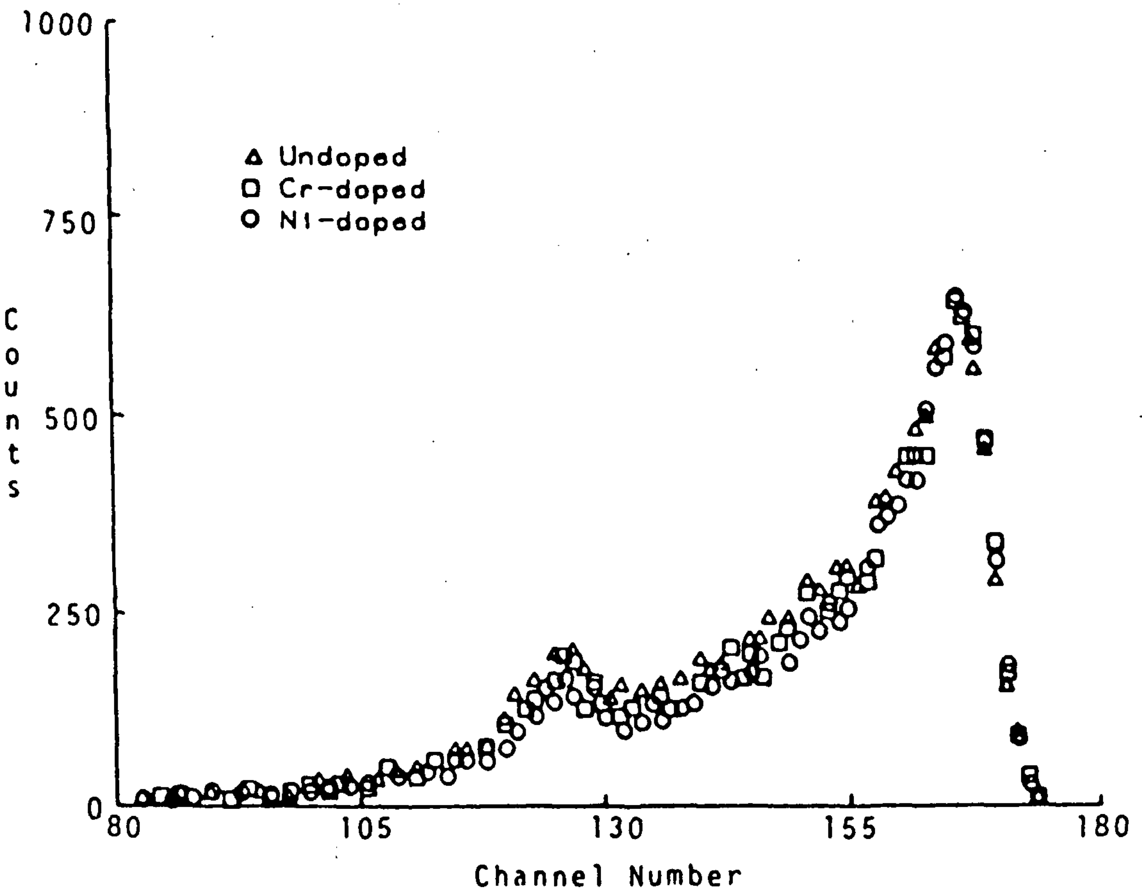

Figure 61. - Proton activation spectra taken on an undoped sample, a Cr-doped sample, and a Ni-doped sample all exchanged together at 1634° C for 98 hr.

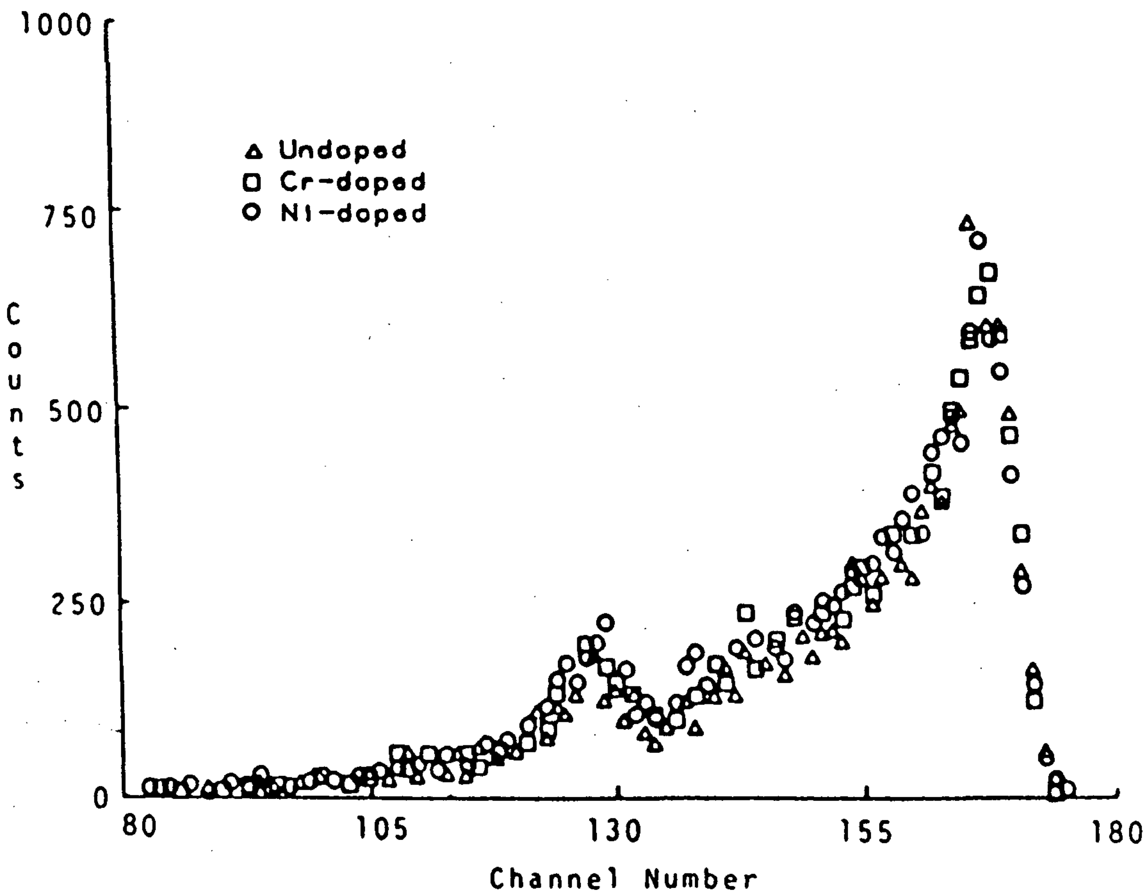

Figure 62. - Proton activation spectra taken on an undoped sample, a Cr-doped sample, and a Ni-doped sample all exchanged together at 1677° C for 23 hr.

A third feature is that all the experiments up through 1550° C have tracer penetration depths which are small compared to the resolution of the analysis. That is the concentration profiles may contain structure that cannot be seen.

It was also noted that the spectra of Cr had apparent counts of an energy higher than that corresponding to the surface of the sample, unless a very low beam current was used. If the charging from the proton beam was not being dissipated by the carbon film, it would continue to build until it reaches the breakdown strength of the sample. Such an arcing condition could affect the spectra[67]. The distortion could be accounted for electrical breakdown if the ruby were significantly more resistant than the other samples, however the reported values for conductivity of ruby are very near that of sapphire[58], or if carbon layer was different and not conductive when deposited on ruby. The latter does not seem likely. There was no visually observable difference in the carbon layer between samples and all the samples were coated together, and the samples remained at room temperature. The detector is sensitive to light however, and it seems possible that the distortions of the spectra (see figures 63 and 64) which involve a shift of counts to higher energy, might occur if the detector were to count a large number of 2 to 3 eV photons and an alpha simultaneously. While all samples fluoresced a violet color, the Cr-doped sample had a much more intense bright red color, typical of ruby.

The experiment necessary to prove this assumption, would be to place an opaque piece of aluminized mylar between the sample and the

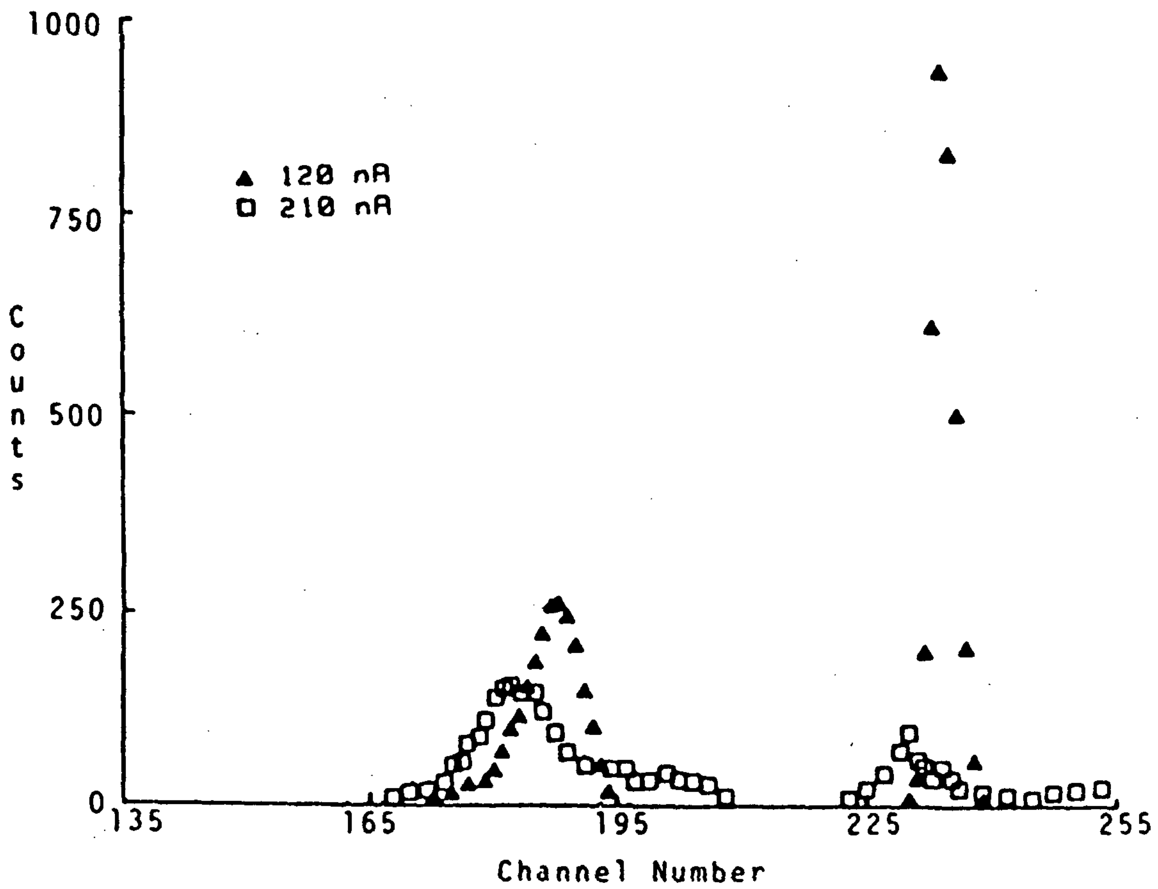

Figure 63. - Proton activation spectra taken on Cr-doped sample with a beam current of 210 nA and 120 nA.

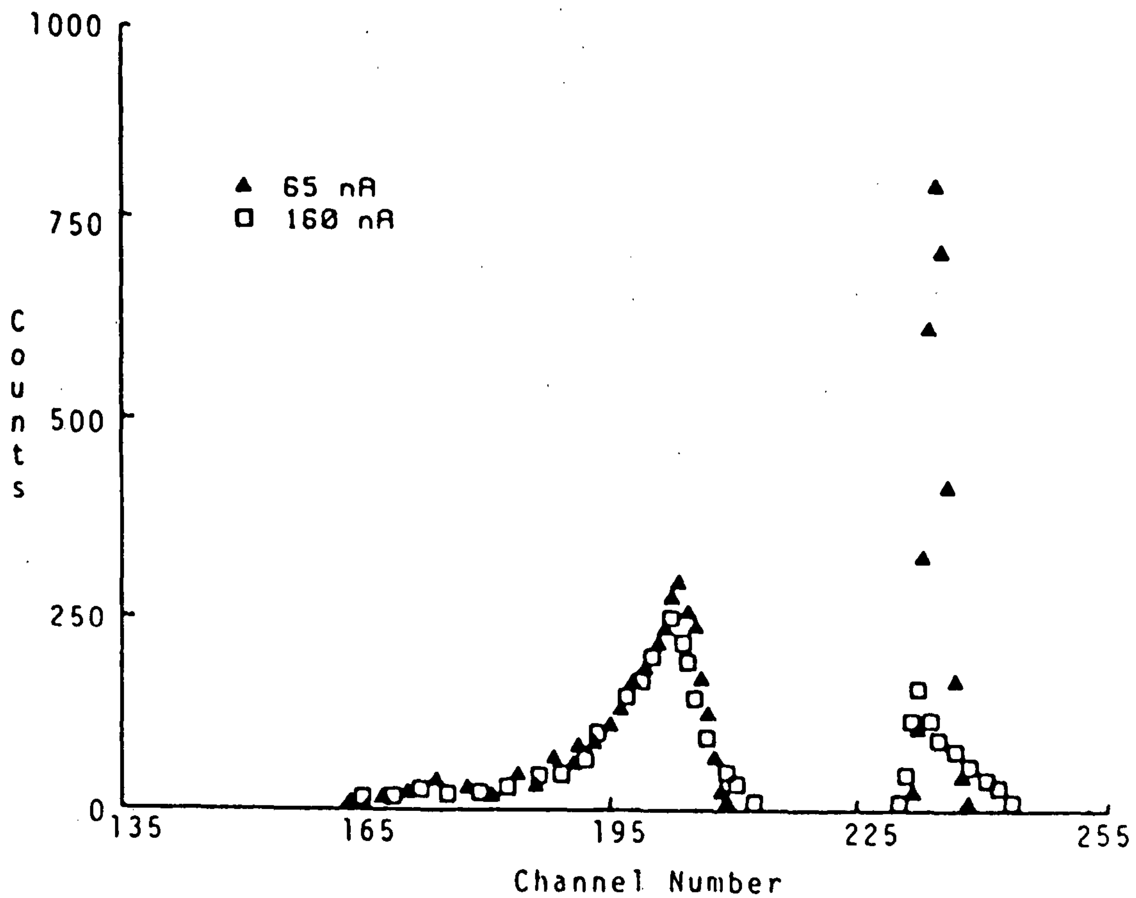

Figure 64. - Proton activation spectra taken on Cr-doped sample with a beam current of 160 nA and 65 nA.

detector, however, it was not possible to return to Paris to attempt the experiment.

If indeed the fluoresence of the ruby causes the spectra to be altered, then it is also possible that the fluorescence of the other samples might cause this shift of counts to higher energies. It must be emphasized that this is speculation supported by no experimental evidence.

These concerns and the logistics of traveling to France to analyze samples prompted the switch to SIMS for the remaining sample analysis.

4.1.3.2 Fits to Diffusion Equations

Many of our spectra were shallow compared to the depth resolution of the analysis technique. However, reasonable fits could be obtained. Fits, calculated using equation (2.1-7), for three temperatures (1457° C, 1550° C, and 1677° C) are shown in figures 65 to 67. It can be seen in these figures that the magnitude of the tail (another way to say this is; the extent of deviation from the predicted profile at large depths) increases with increasing temperature.

A fit of the tail for the specimen exchanged at 1677° C is shown in figure 68.

It was also found that the value of the surface exchange coefficient, K, was sensitive to fluctuations in counting rate between spectra while the value of the diffusion coefficient was not. The spectrum shown in figure 69 was taken consecutive to that shown in figure 67. The spectrum in figure 67 was best eye fit assuming the

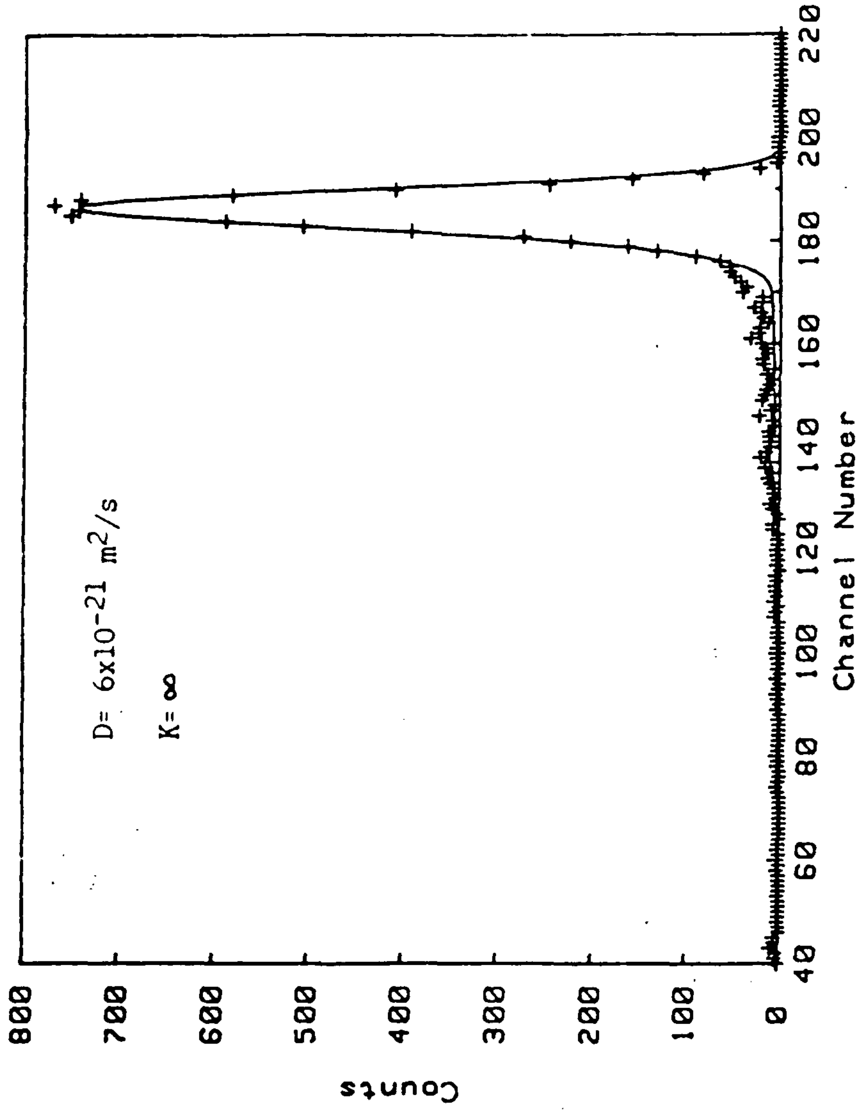

Figure 65. - Proton activation spectrum from a sample, UD-57, exchanged at 1458° C for 404 hr.

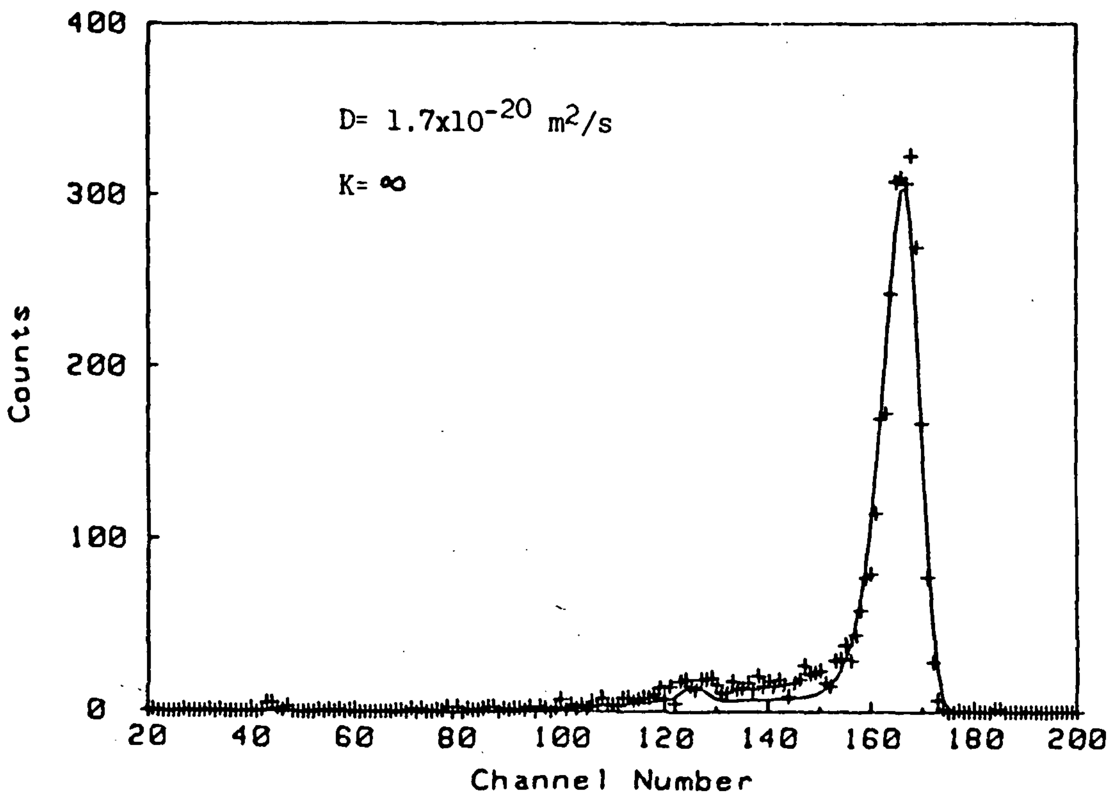

Figure 66. - Proton activation spectrum from a sample, UD3-30, exchanged at 1550° C for 283 hr.

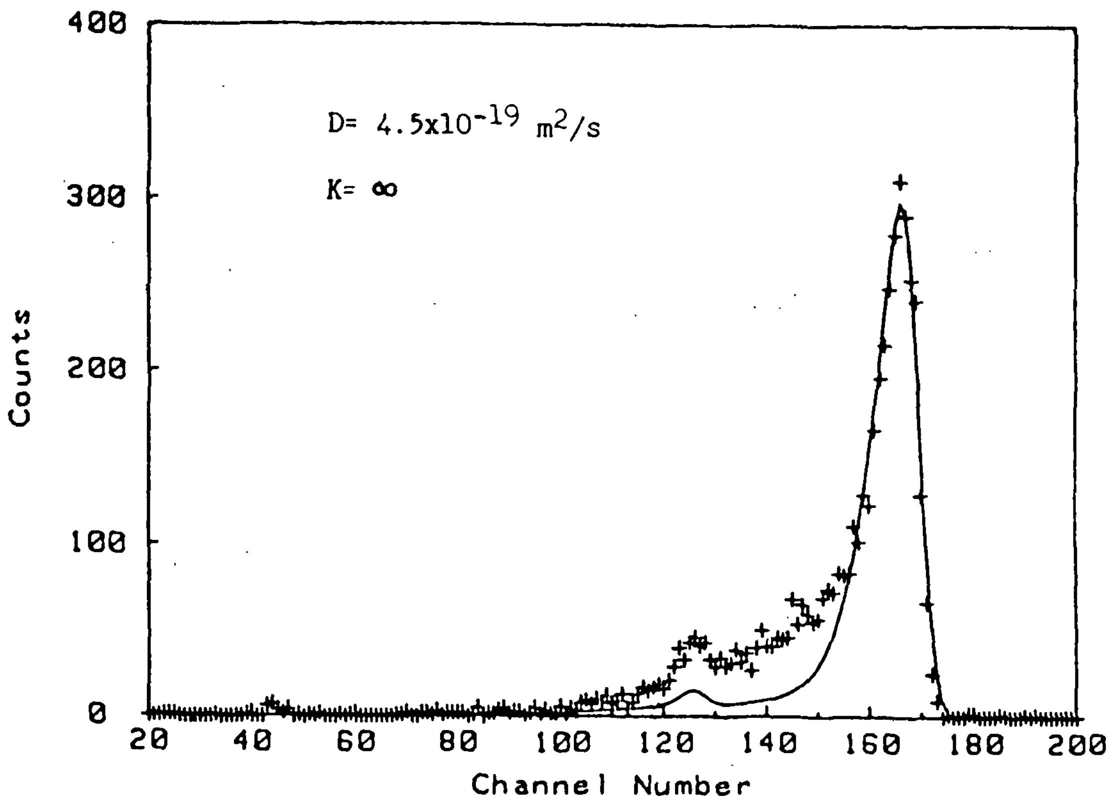

Figure 67. - Proton activation spectrum, with a near surface fit, from sample UD-69 exchanged at 1677° C for 23.3 hr.

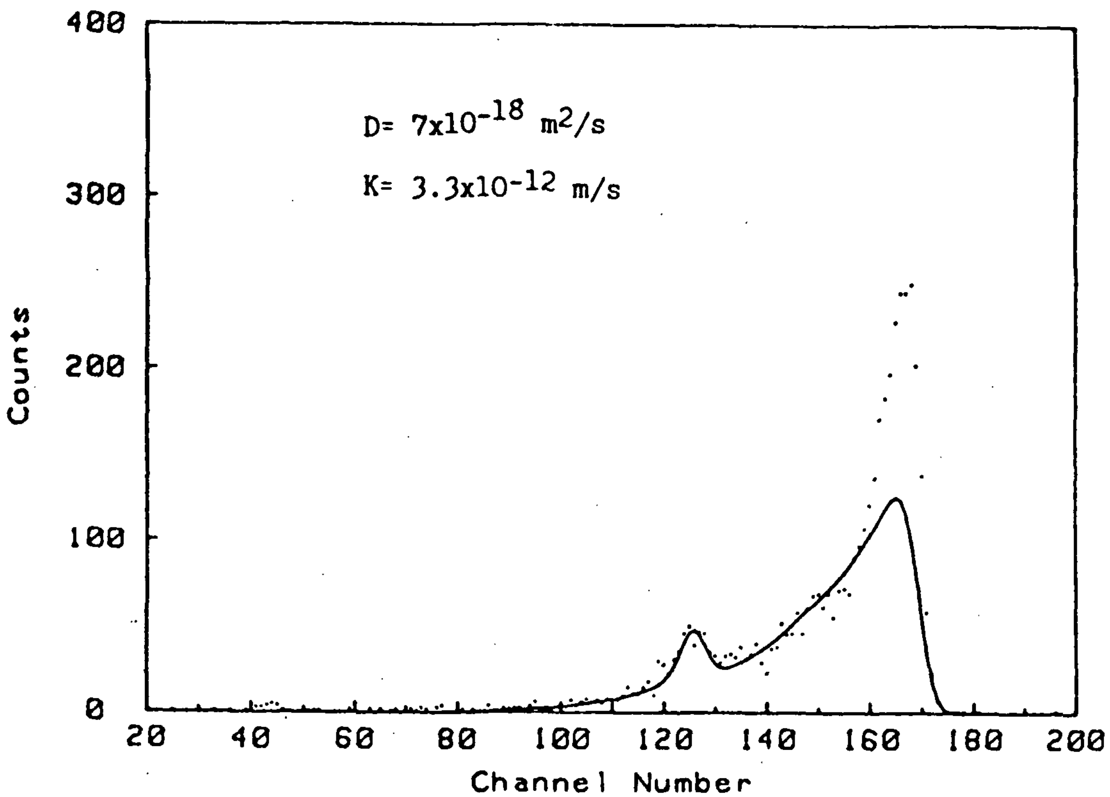

Figure 68. - Proton activation spectrum, with a deep fit, from sample UD-69 exchanged at 1677° C for 23.3 hr.

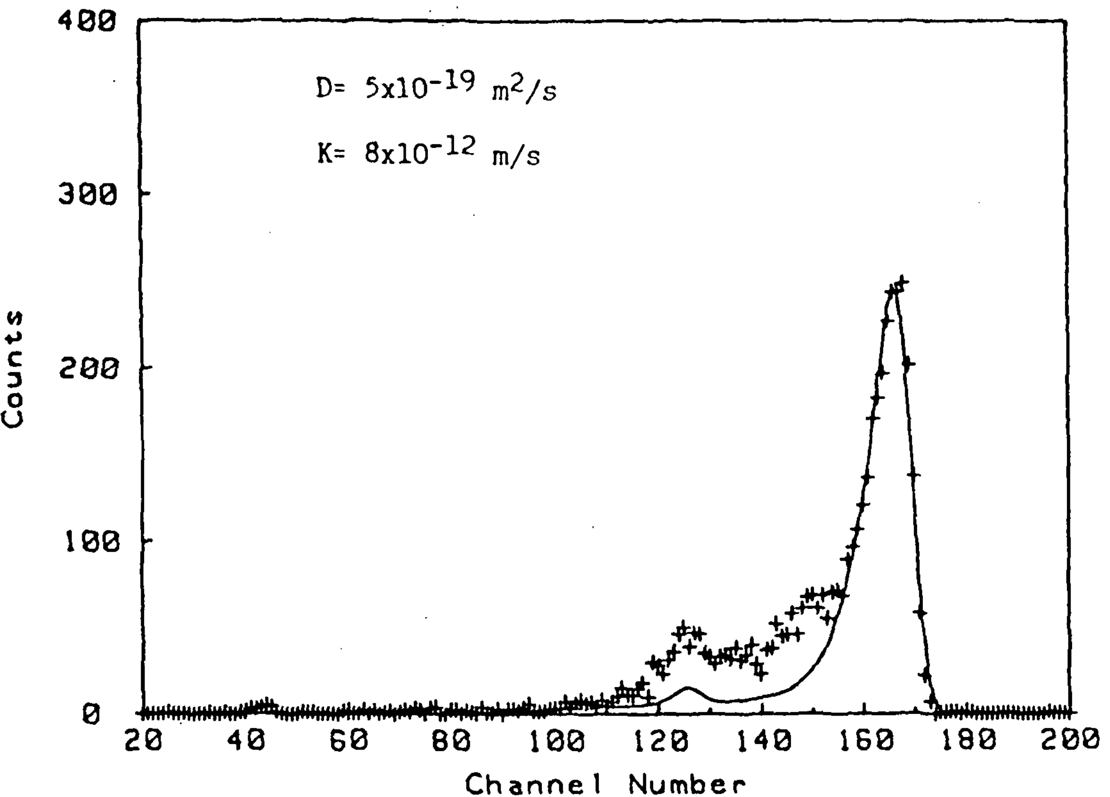

Figure 69. - Proton activation spectrum, with a near surface fit, from sample UD-69 exchanged at 1677° C for 23.3 hr. The value of the value for the surface exchange coefficient is very sensitive to data scatter while the value for the diffusion coefficient is not.

surface reaction was rapid enough to play no role, i.e., $K = \infty$, with a value of $D = 4.5\times10^{-19}$ m^2/s while the spectrum in figure 69 was best fit by assuming $K = 8\times10^{-12}$ m/s and $D = 5.0\times10^{-19}$ m^2/s. In the later case $K\,(\frac{t}{D})^{1/2} = 3.3$, which suggests that the surface reaction plays a significant role. Note, however, that the diffusion coefficients vary by only ~10 percent. Also, the spectra in general were less different than this example pair, and the variation in determined diffusion coefficient accordingly smaller.

There are three possible causes for the inability to fit the spectra. These are:

(i) a non-Fickian profile

(ii) an error in the computer calculated spectrum causing it to underpredict the concentration at larger depths, and

(iii) an artifact from the proton activation experiment

The computer program was extensively checked and found to be correct. Also, latter work with SIMS found that profiles from these same samples confirmed the existance of the tails and their relative magnitudes. This observation by two very different methods of analysis greatly diminishes the probability that they are an artifact.

A summary of the samples analyzed by proton activation is given in table 7.

TABLE 7. - SUMMARY OF SAMPLES ANALYZED BY PROTON ACTIVATION

Sample	T_{diff}(°C)	t_{diff}(s)	T_{pre}(°C)	t_{pre}(s)	D(m^2/s)	K(m/s)	$K \frac{t}{D}^{1/2}$
UD57	1458	1,454,400	1400	1,814,400	$6x10^{-21}$	∞	∞
UD30	1550	1,020,600	1515	608,400	$1.7x10^{-20}$	∞	∞
UD69 Fit1	1677	83,880	1684	72,720	$4.5x10^{-19}$	∞	∞
UD69 Fit2	1677	83,880	1684	72,720	$5.0x10^{-19}$	8x10-6	3.3

4.2 SECONDARY ION MASS SPECTROMETRY

4.2.1 Oxygen-18 Profiles in Single Crystals at P_{O_2} = 1 atm.

SIMS has a much better depth resolution, ~10 Å, than does proton activation. It was warranted to recheck the earlier observation that all the samples exchanged together have identical tracer profiles. Shown in figure 70 is a plot of the concentration of tracer as a function of depth for two samples analyzed at Penn. State, which were exchanged at the same time, one undoped and other Ni-doped. The two curves are indistinguishable. This held true for every case that was examined, although this was a limited number of samples.

The second finding of the SIMS analysis was that, as with proton activation, the tracer profile could be divided into two regions. A near surface profile, which could be fit with a solution to the diffusion equation, and a deeply penetrating tail. Data from the Penn. State SIMS work and fits, for the temperature range 1300° to 1677° C, are shown in figures 71 through 76.

As in proton activation, deep penetrating "tails" appear to varying degrees in the profiles. Again, they do not appear to be systematic. The samples UD-A and UD-B were preannealed together and exchanged, on different shelves, during the same run. Sample UD-A shows a pronounced "tail" and UD-B does not.

The data from the University of Illinois SIMS work, despite utilizing the imperfect normalizing coefficients, were able to be fit quite well. This data (over the temperature range of 1330° to 1458° C) and the fits are shown in figures 77 to 79. The "tails"

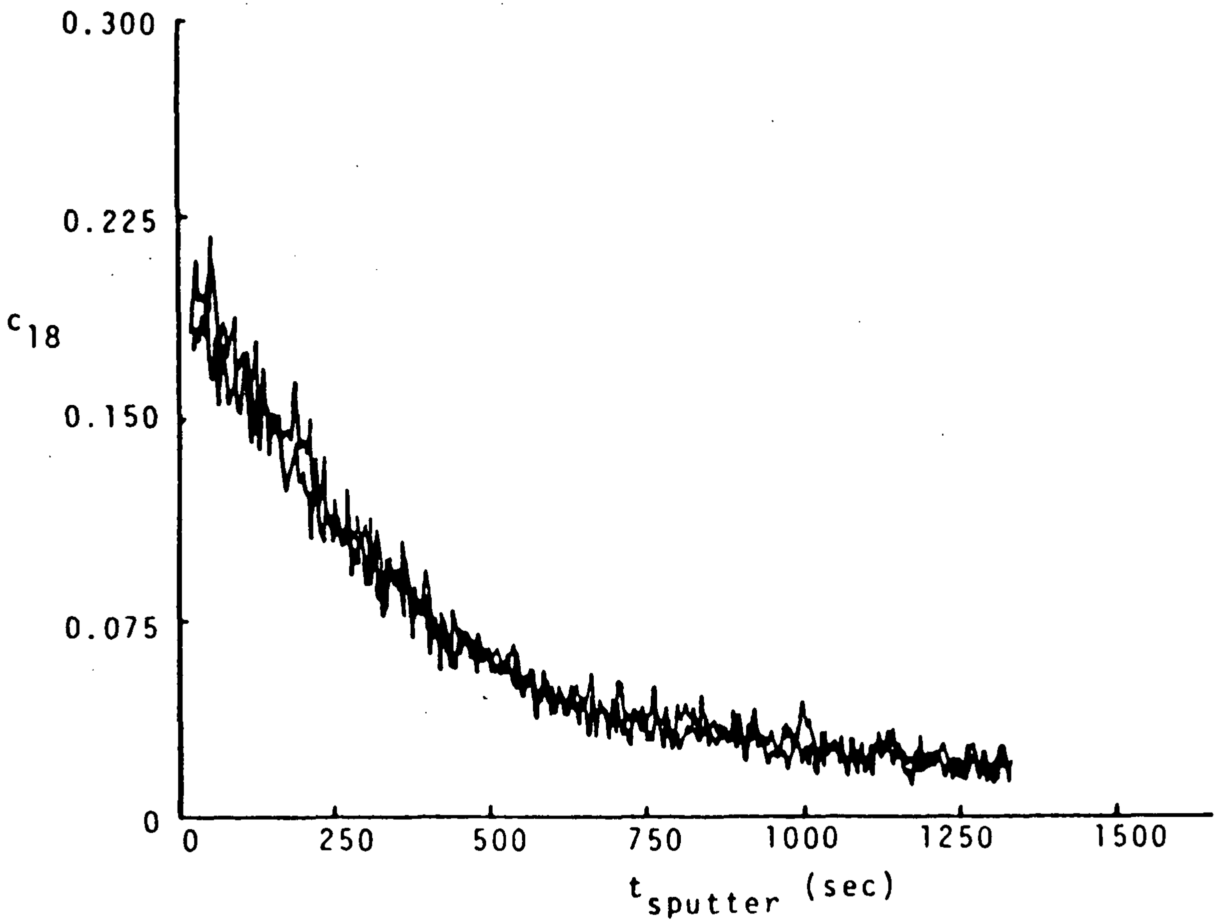

Figure 70. - PSU SIMS profiles on an undoped sample and a Ni-doped sample exhanged at 1435° C for 1920 hr.

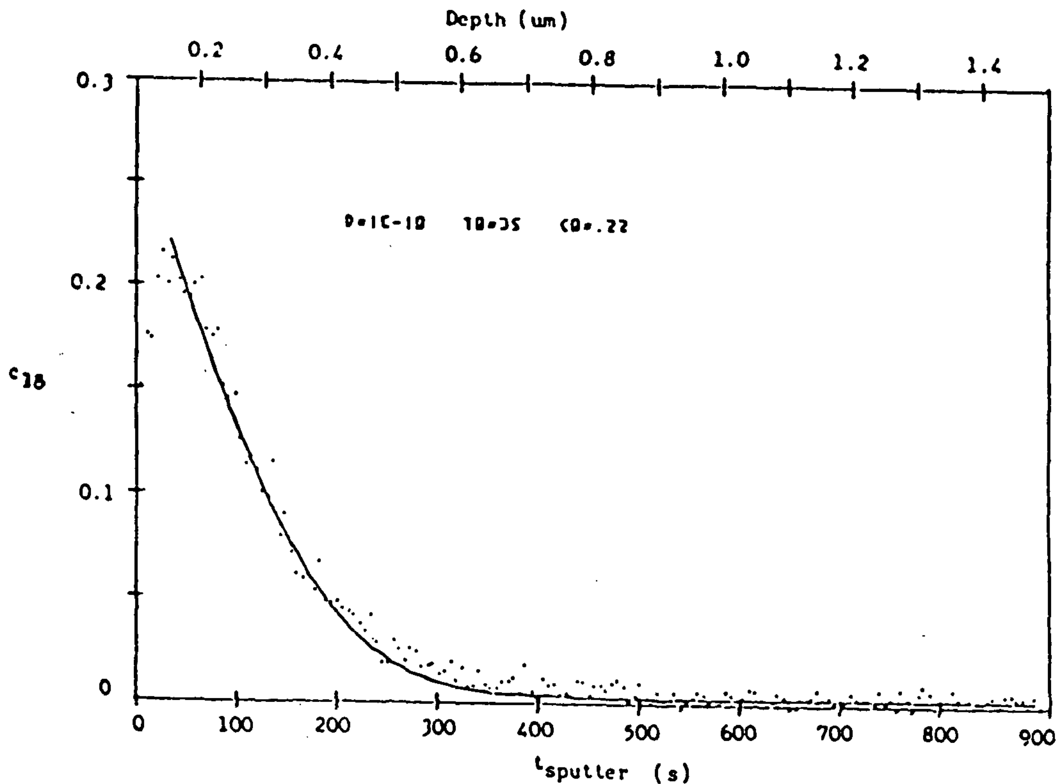

Figure 71. - PSU SIMS profile on undoped sample UD-1T exchanged at 1300° C for 1073 hr.

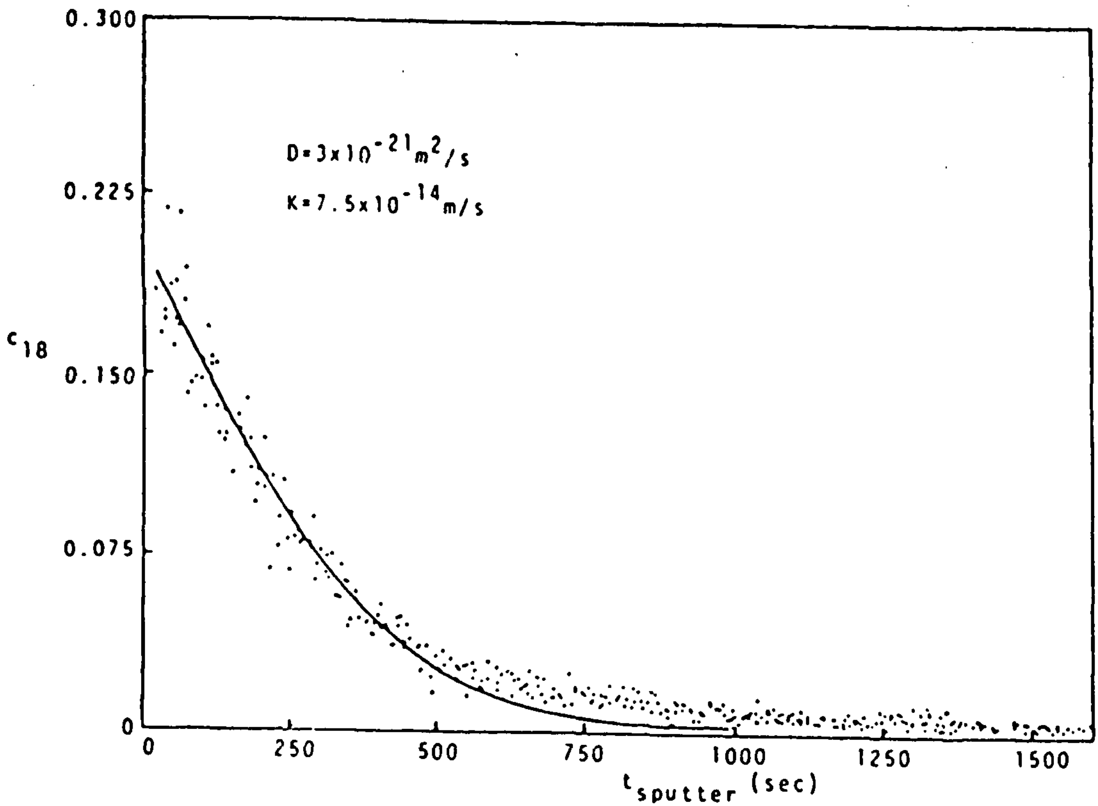

Figure 72. - PSU SIMS profile on an undoped sample UD-8 exchanged at 1415° C for 1920 hr.

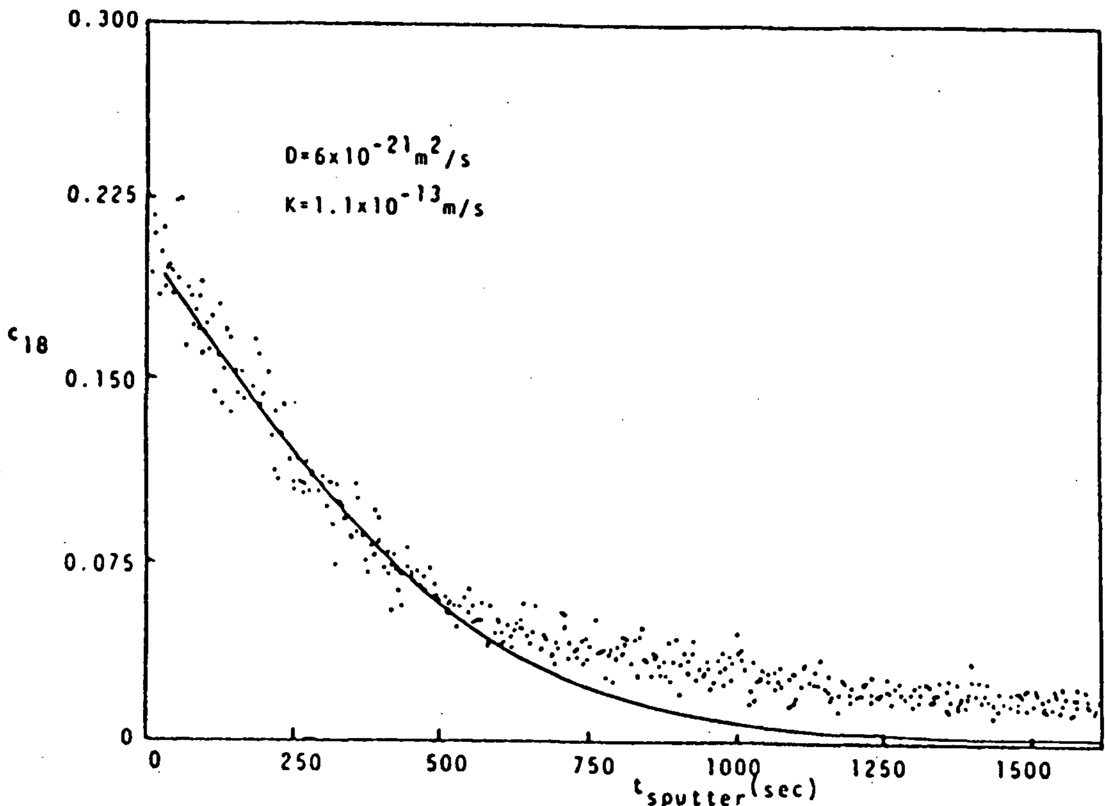

Figure 73. - PSU SIMS profile on an undoped sample UD-A exchanged at 1435° C for 1920 hr.

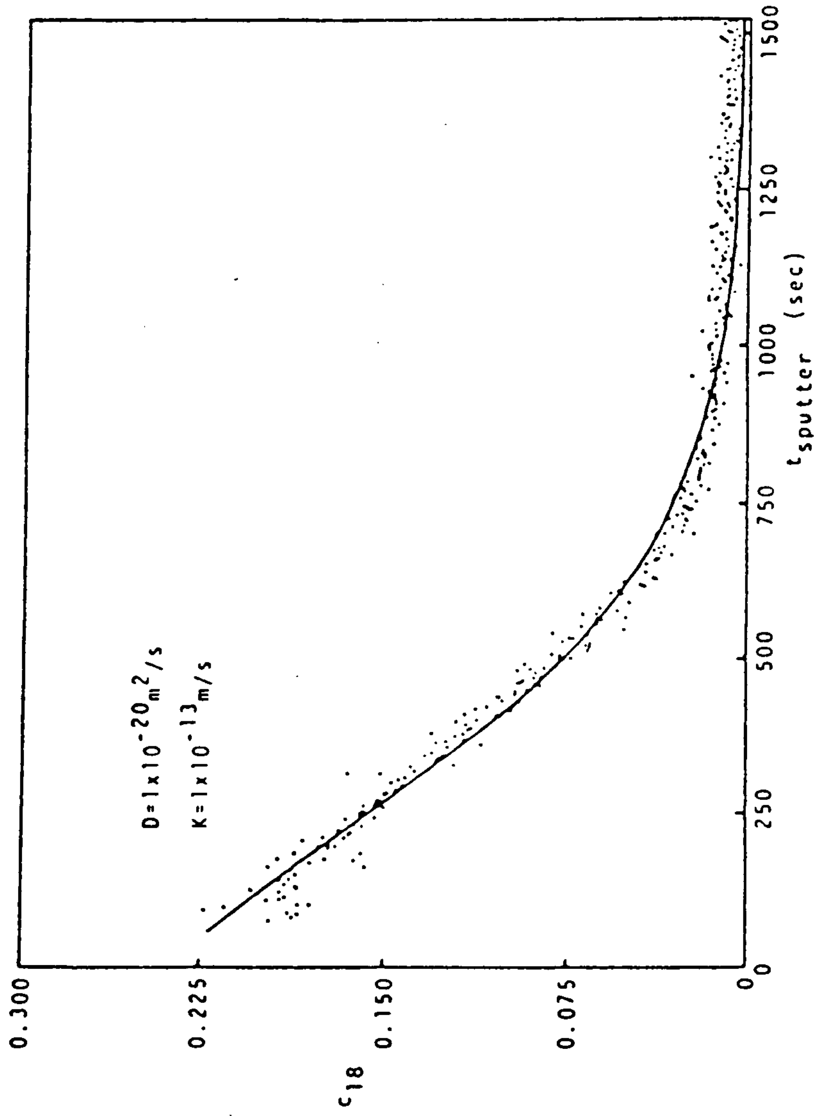

Figure 74. - PSU SIMS profile on an undoped sample UD-57 exchanged at 1458° C for 404 hr.

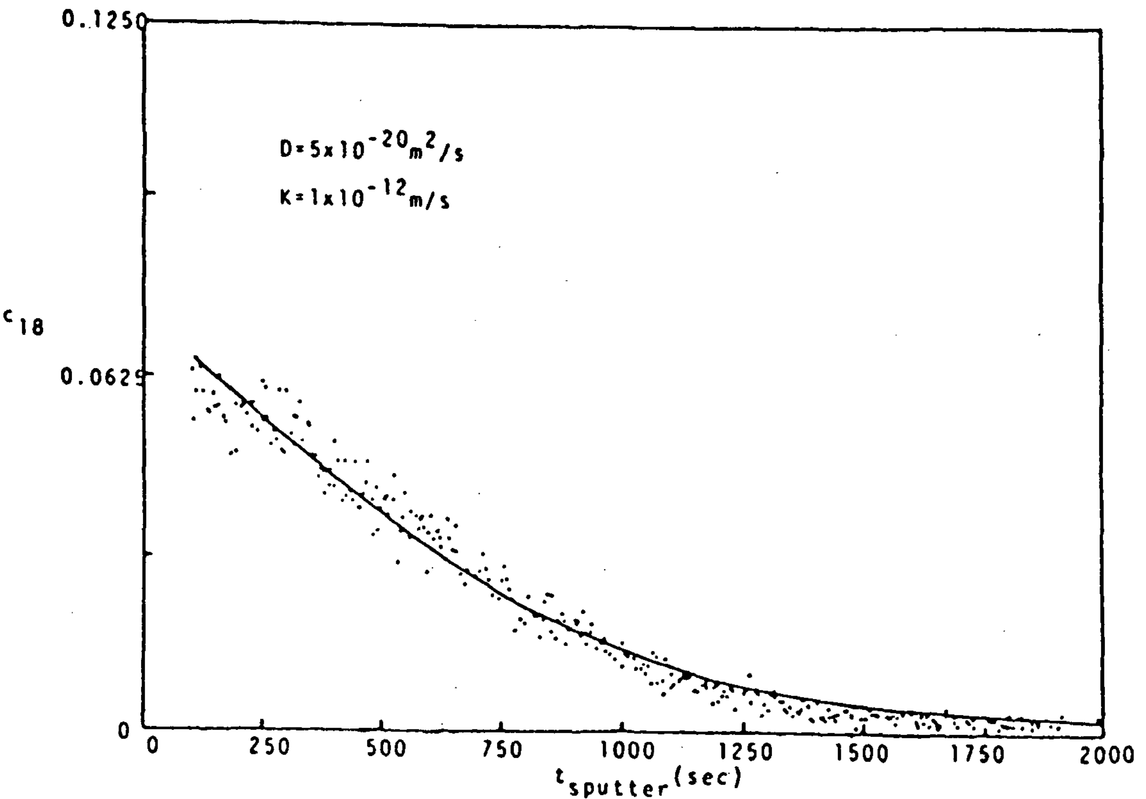

Figure 75. - PSU SIMS profile on an undoped sample UD3-30 exchanged at 1550° C for 283 hr.

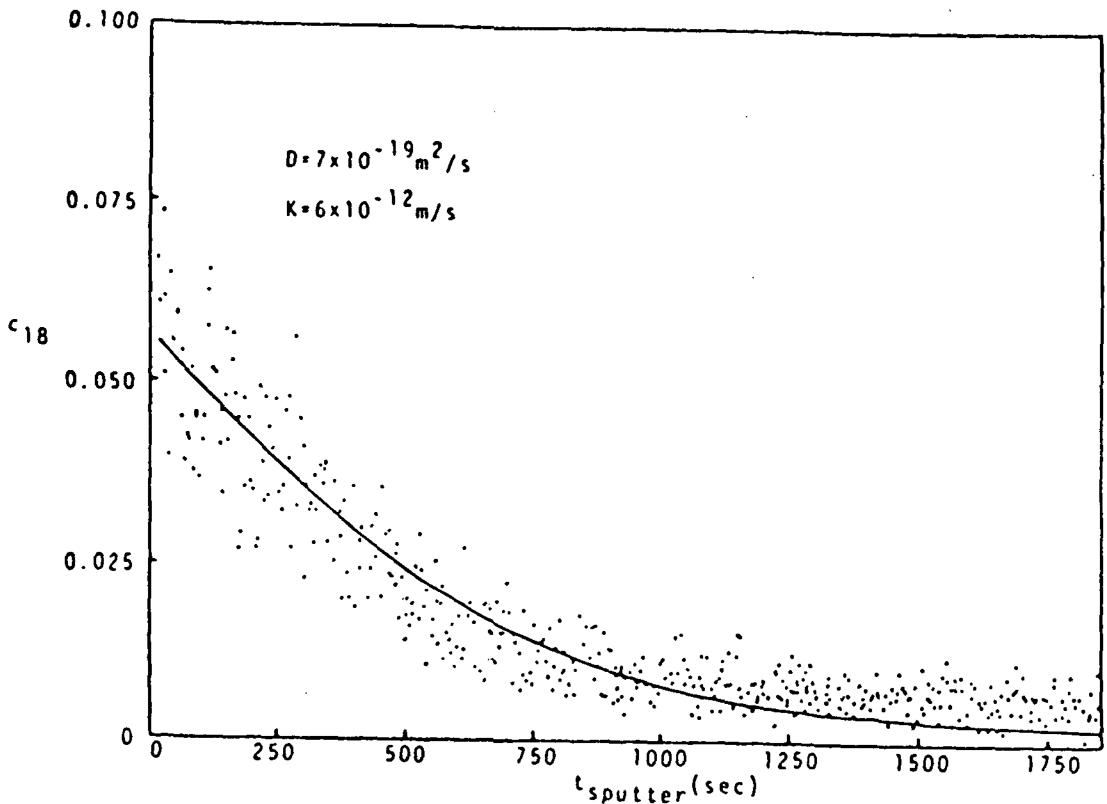

Figure 76. - PSU SIMS profile on an undoped sample UD-69 exchanged at 1677° C for 233 hr.

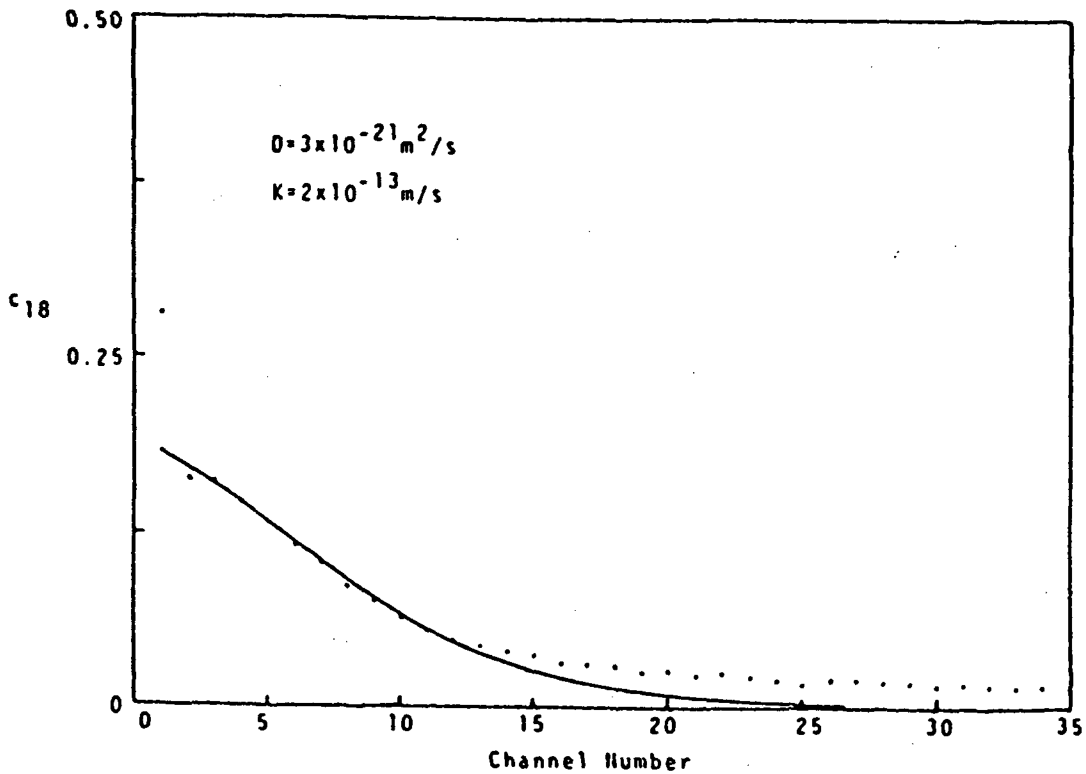

Figure 77. - UIU SIMS profile on an undoped sample UD-B exchanged at 1415° C for 1920 hr.

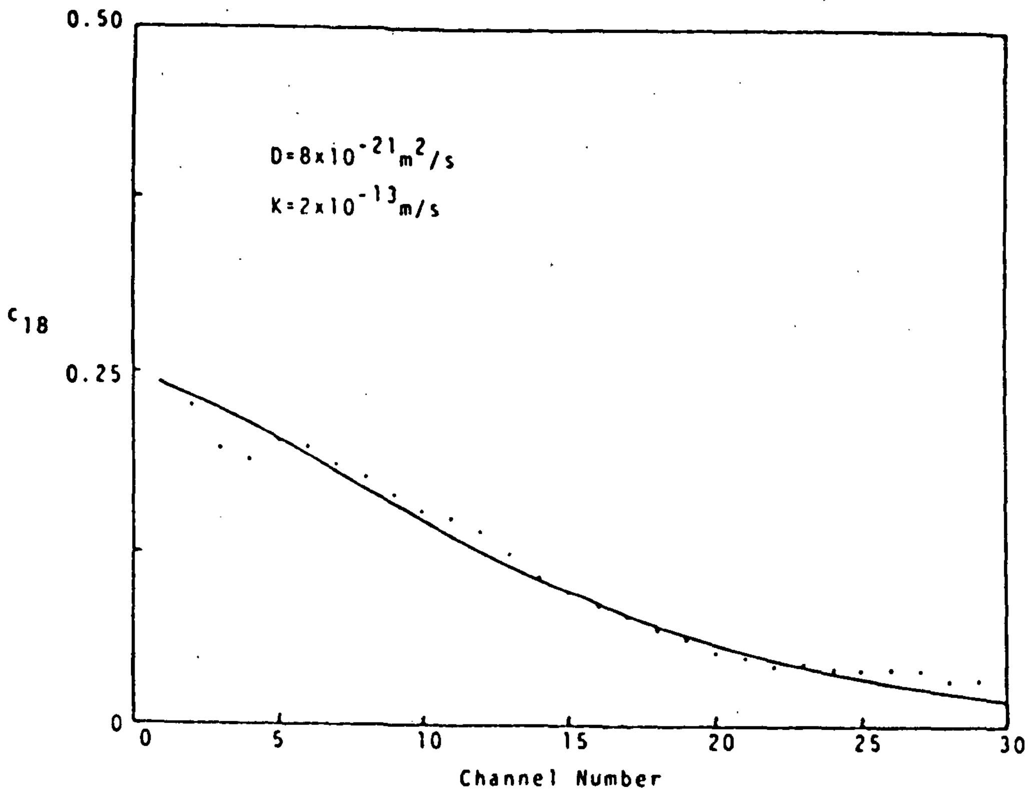

Figure 78. - UIU SIMS profile on an undoped sample UD-56 exchanged at 1415° C for 404 hr.

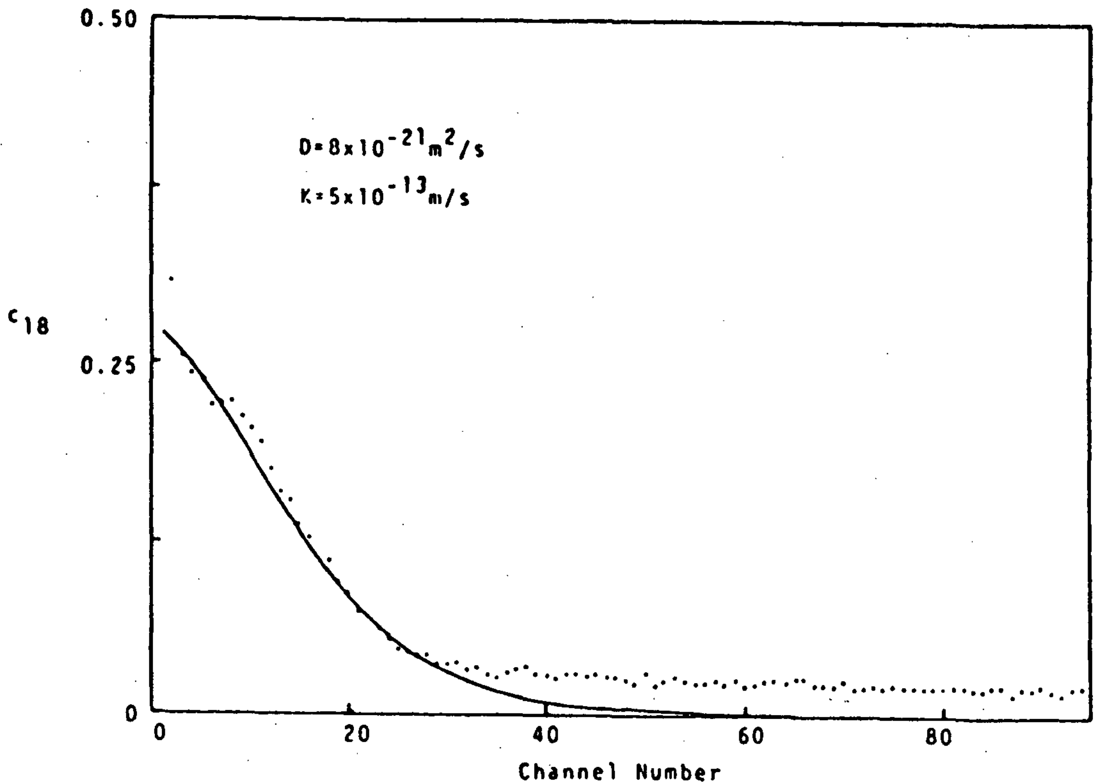

Figure 79. - UIU SIMS profile on a Ni-doped sample Ni-61 exchanged at 1458° C for 404 hr.

which appear in these profiles may well arise during the normalization procedure used to eliminate the beam contribution, and should not be taken too seriously. Evidence for this is seen in the fact that the sample UD-B shows a "tail" in the UIU profile and not in the PSU profile.

The one exception was the experiment at 1634° C which could not be fit with a single pair of D and K. The PSU profile on this specimen are shown in figure 80 (attempts to fit the proton activation data on this sample were also unsuccessful). This experiment was run with new furnace tubes and new tracer. The starting concentration of the tracer was 95 percent and it dropped to ~18 percent at the end of the run. Unfortunatenly the rate of change of the tracer concentration is unknown since fact that all but two of the gas samples, both taken near the end of the run, were broken in the mail on the way to be analyzed.

An Arrhenius plot of the diffusion coefficients determined in this work is shown in figure 81, along with a best fit line to the PSU SIMS data and a summary of the previous work. Note that the data agrees well with the previous gas exchange data, particularly with that of Reddy and Cooper and may be described by:

$$D = 1.51\times10^{-3} \exp\left(\frac{-572\ \mathrm{kJ/mol}}{RT}\right)\ m^2/s \qquad (4.2\text{-}1)$$

Note that the values obtained from proton activation are around a factor of two lower than those obtained from SIMS for the same sample. The proton activation fitting procedure involved a number of assumptions (Sec. 4.1.1) for the depth-energy relationship while with SIMS

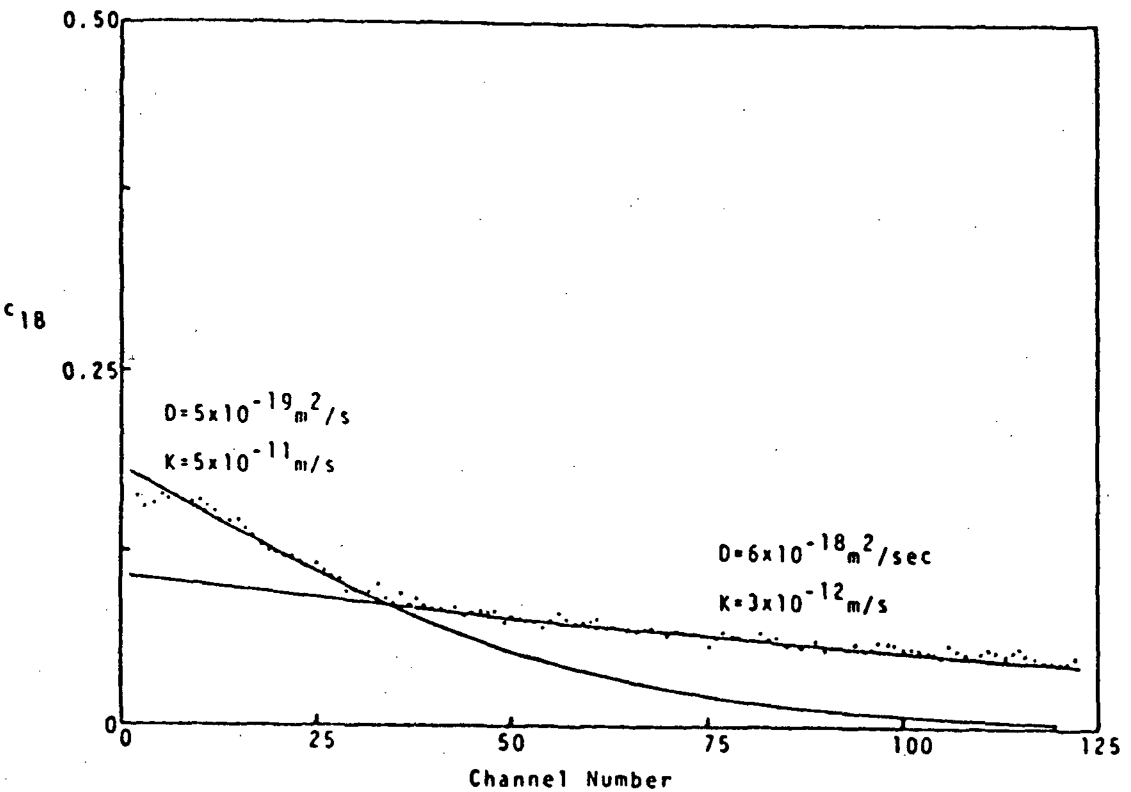

Figure 80. - UIU SIMS profile on an undoped sample exchanged at 1634° C for 98 hr with a set of new furnace tubes and a new tracer atmosphere.

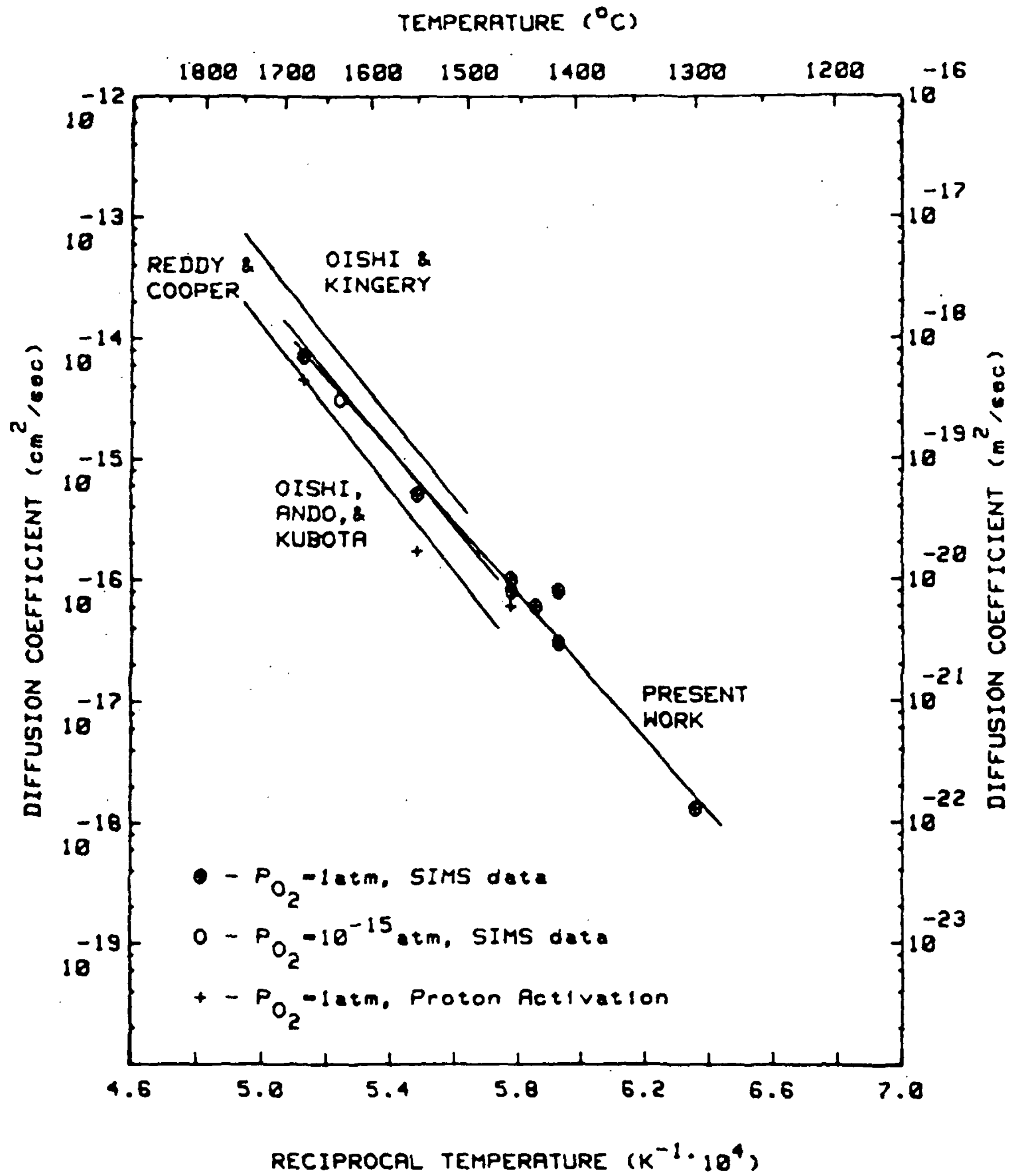

Figure 81.- An Arrhenius plot of the determined oxygen self diffusion coefficients in Al_2O_3 with an edited summary of previous work.

the only assumption was that the sputtering rate was linear. It is possible that the profilometer used to measure the crater depth was out of adjustment, however comparison of results obtained by interferometry compare well with those from the profilometer.[2] Therefore, the SIMS results are felt to be more accurate.

4.2.2 Oxygen-18 Profiles in Single Crystals at $P_{O_2} = 10^{-15}$ atm.

The tracer profiles in the samples exchanged in a CO/CO_2 atmosphere, equivalent to $P_{O_2} = 10^{-15}$ atm., looked very similar to those all four samples; two undoped, one Cr-doped, and one Ni-doped, looked the same. The profile of an undoped sample is shown in figure 82. Similar to the $P_{O_2} = 1$ atm. profiles, there is also a near surface region that appears Fickian and the presence of a low concentration, deeply penetrating "tail".

The value for D is plotted on the Arrenhius plot (fig. 81). Note that it fits very well on the line determined by the $P_{O_2} = 1$ atm. data, indicating no P_{O_2} dependence for oxygen diffusion in Al_2O_3.

A summary of all the samples analyzed by Secondary Ion Mass Spectrometry is given in table 8.

4.2.3 Oxygen-18 Profiles in Polycrystals at $P_{O_2} = 1$ atm.

The determination of oxygen profiles in the polycrystalline samples, by SIMS, proved to have complications. Recall, from Section 3.5.3, that it was necessary, with the PSU SIMS, to have an electron

[2] Personal Communication David Roach.

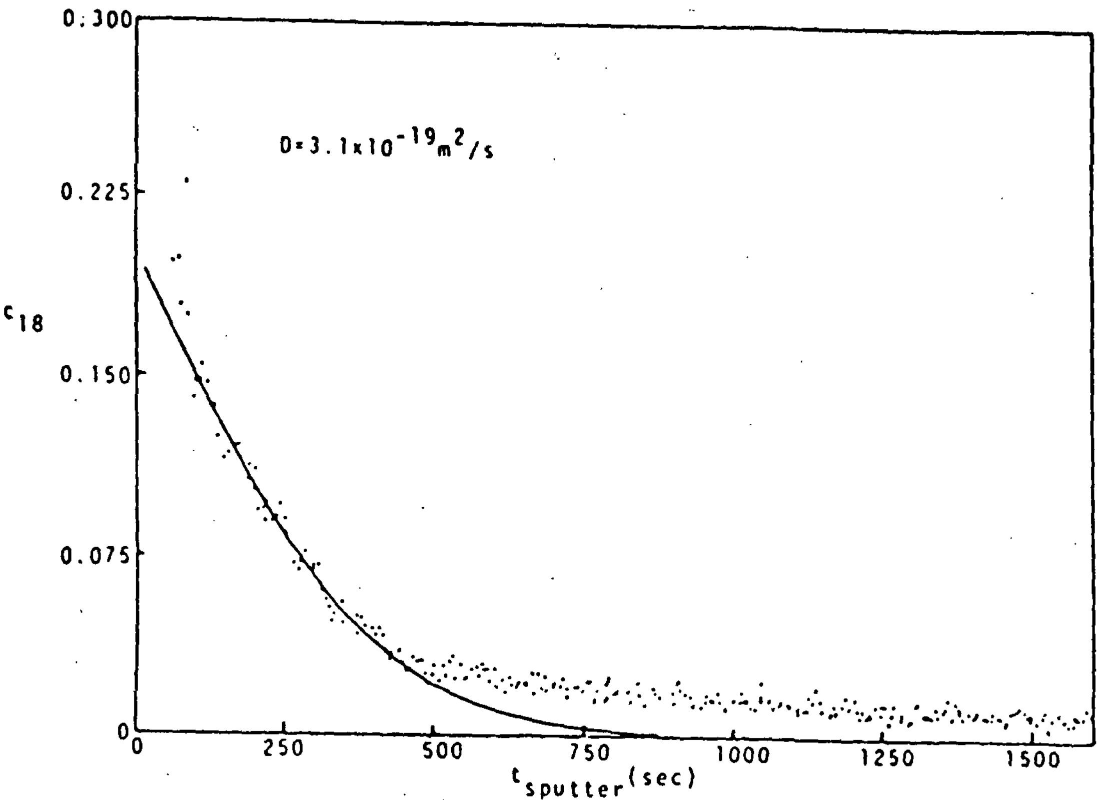

Figure 82. - PSU SIMS profile on an undoped sample exhanged at 1634° C for 8 hr at low P_{O_2}.

TABLE 8. - SUMMARY OF SAMPLES ANALYZED BY SIMS

Sample	T_{diff}(°C)	t_{diff}(s)	T_{pre}(°C)	t_{pre}(s)	D(M^2/s)	K(M^2/s)	$K \frac{t}{D}^{1/2}$
UD-B	1415	6,912,000	1630	887,400	$3x10^{-21}$	$2x10^{-13}$	10.0
UD-A	1435	6,912,000	1630	887,400	$6x10^{-21}$	$1.1x10^{-13}$	3.7
UD-57	1458	1,454,400	1400	1,814,400	$1x10^{-20}$	$1x10^{-13}$	1.2
Ni-61	1458	1,454,400	1400	1,814,400	$8x10^{-21}$	$5x10^{-13}$	6.7
UD3-30	1550	1,020,600	1515	608,400	$5x10^{-20}$	$1x10^{-12}$	4.5
UD-69	1677	83,880	1684	72,720	$7x10^{-19}$	$6x10^{-12}$	2.1
UD-LT	1300	3,864,600	1600	86,400	$1.3x10^{-22}$		

beam coincident to the Ar+ beam to avoid charging. In the case of single crystals this produced a low level (see fig. 29) constant background which could be subtracted out of the data. With the polycrystals the electron sputtered desorption (ESD) could not be dealt with in this simple way.

Shown in figure 83 is a SIMS profile on a sample of undoped, hot pressed, Al_2O_3. This sample was analyzed consecutive to a single crystal sample which had a reasonable 25 percent ESD, and the settings on the SIMS unit were unaltered between the two. The curve for sputter time less than ~1280 sec represents the count rate under normal profiling, that is when both the argon ion beam and the electron beam are striking the sample. The curve for sputter time greater than ~1280 sec represents the count rate when only the electron beam is allowed to strike the sample.

There is a sharp depression when the argon beam is stopped, however the signal rapidly returns to very near the level that was obtained during profiling. Apparently the vast majority of the ions detected were generated through grain boundary etching by the electron beam. This behavior was observed on every polycrystalline sample which was analyzed.

By reducing the argon beam current to one-third of its normal value (1.5 μA to 0.5 μA) it was possible to lower the electron beam intensity and collect data, although the ESD still produced up to a third of the counts. The resulting profiles, for undoped and singly doped (1000 ppm) with Cr, Ni, Y and Zr, are shown in figures 84 to

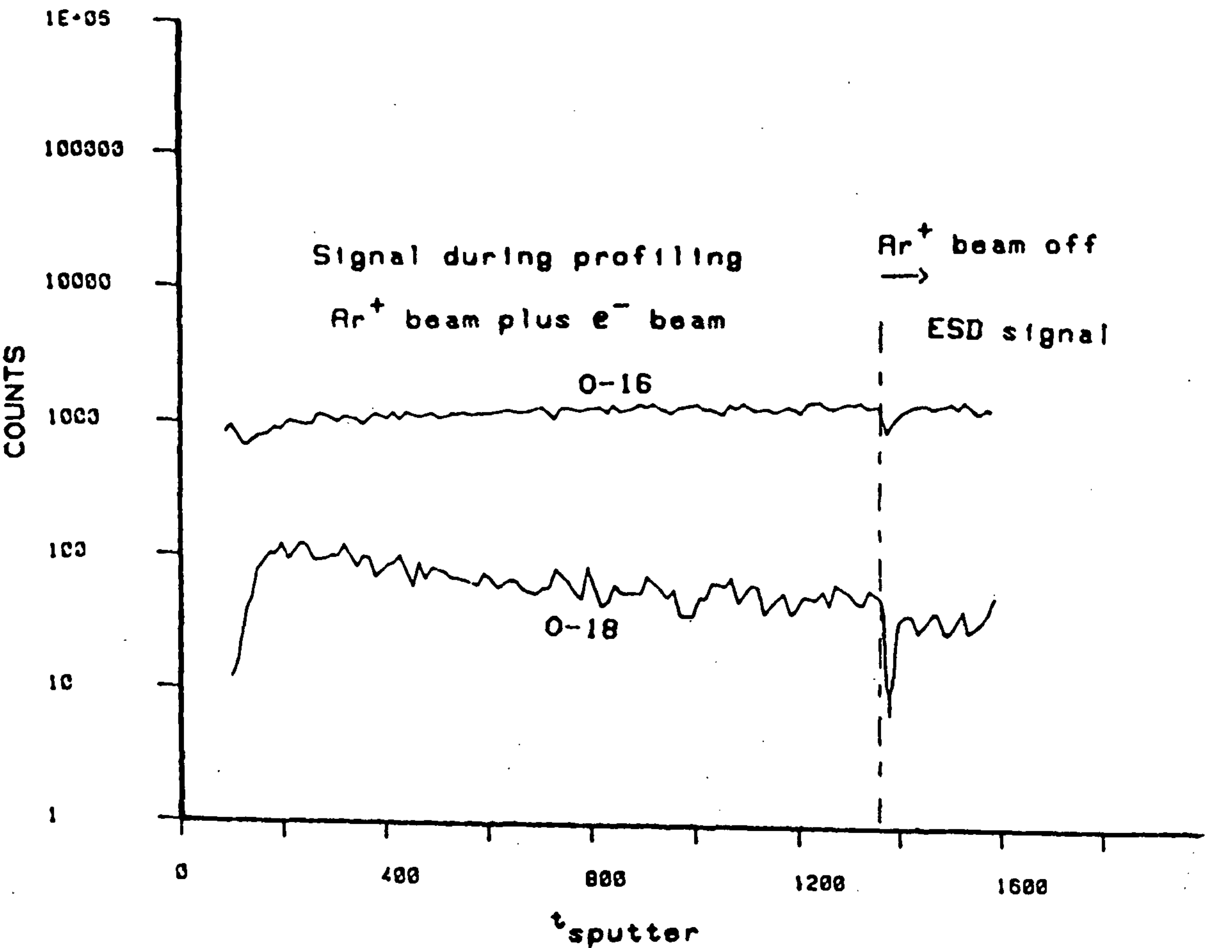

Figure 83. - PSU SIMS profile on a sample of undoped hot pressed Al_2O_3 showing the high level of electron sputtered desorption (ESD).

88. Some charging problems occurred on the Zr-doped sample and the near surface region was extrapolated.

A qualitative comparison between the profiles can be made using the heavy smooth line that appears in each figure. This line was obtained by drawing a smooth curve by eye through the undoped data. Translation along the concentration axis was allowed when the line was reproduced on the other profiles. It can be seen that this line is also a good representation of the data for the Cr-doped, Ni-doped, and Zr-doped samples. The profile from the Y-doped sample, however, appears to be different.

It is not known if this is a real result or an artifact. This Y-doped sample was found to be physically stuck to the sample shelf after the exchange. This was the only one, of the thirteen samples on the shelf, which stuck. Although no clear connection between this and the oxygen profile is seen it may be that this sample was not a good sample. Also, the ESD was not rechecked to be sure it was independent of sputter time. If the rate of etching of the grain boundaries changes (which is dependent on microstructure) or the concentration of tracer in the boundaries changes during sputtering the shape of profile may be altered.

In summary, the diffusion of oxygen in polycrystalline Al_2O_3 appears insensitive to 1000 ppm of Cr, Ni, or Zr but may be affected by 1000 ppm of Y. However, the analysis method was not optimized for this type of sample and the results are not conclusive. Due to this uncertainty quantitative fitting of the profiles was not attempted.

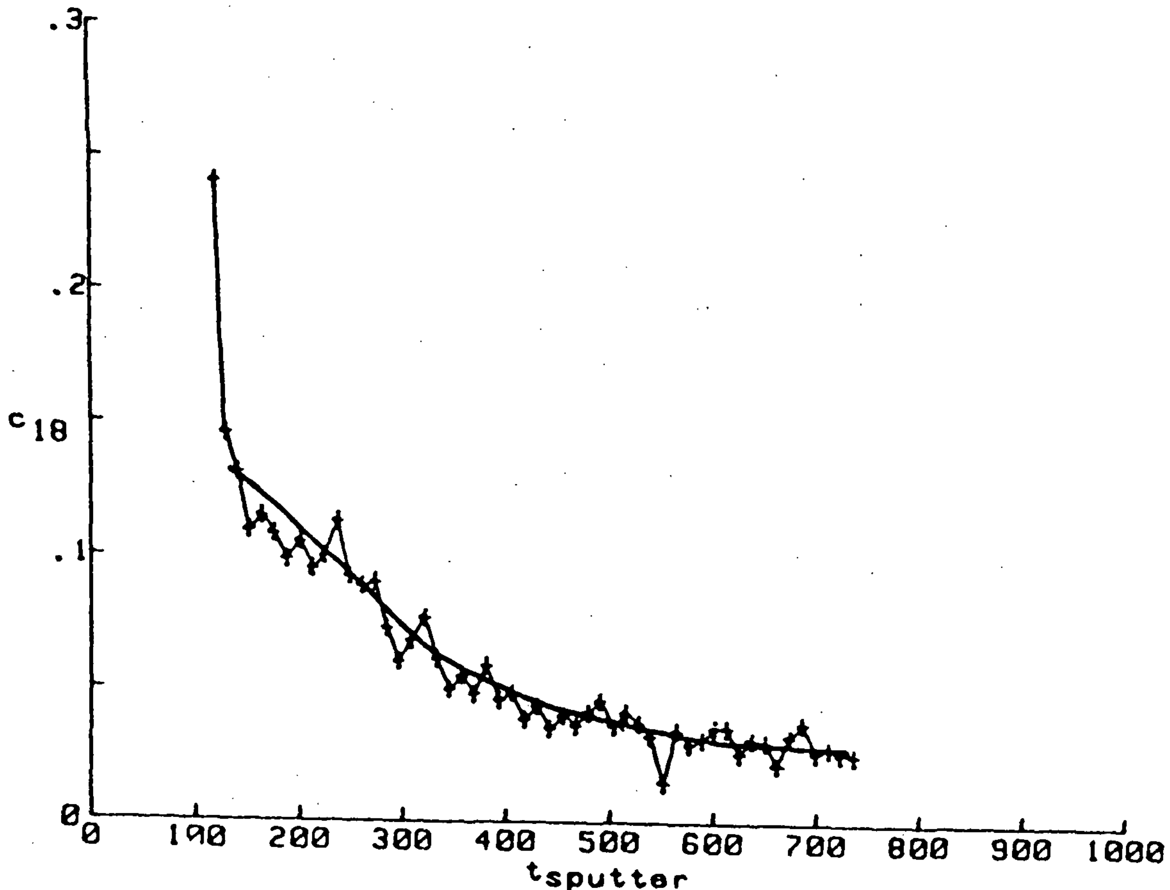

Figure 84. - PSU SIMS profile on a sample of undoped hot pressed Al_2O_3. The smooth curve is an eye fit which is used as a reference to profiles on samples of other compositions.

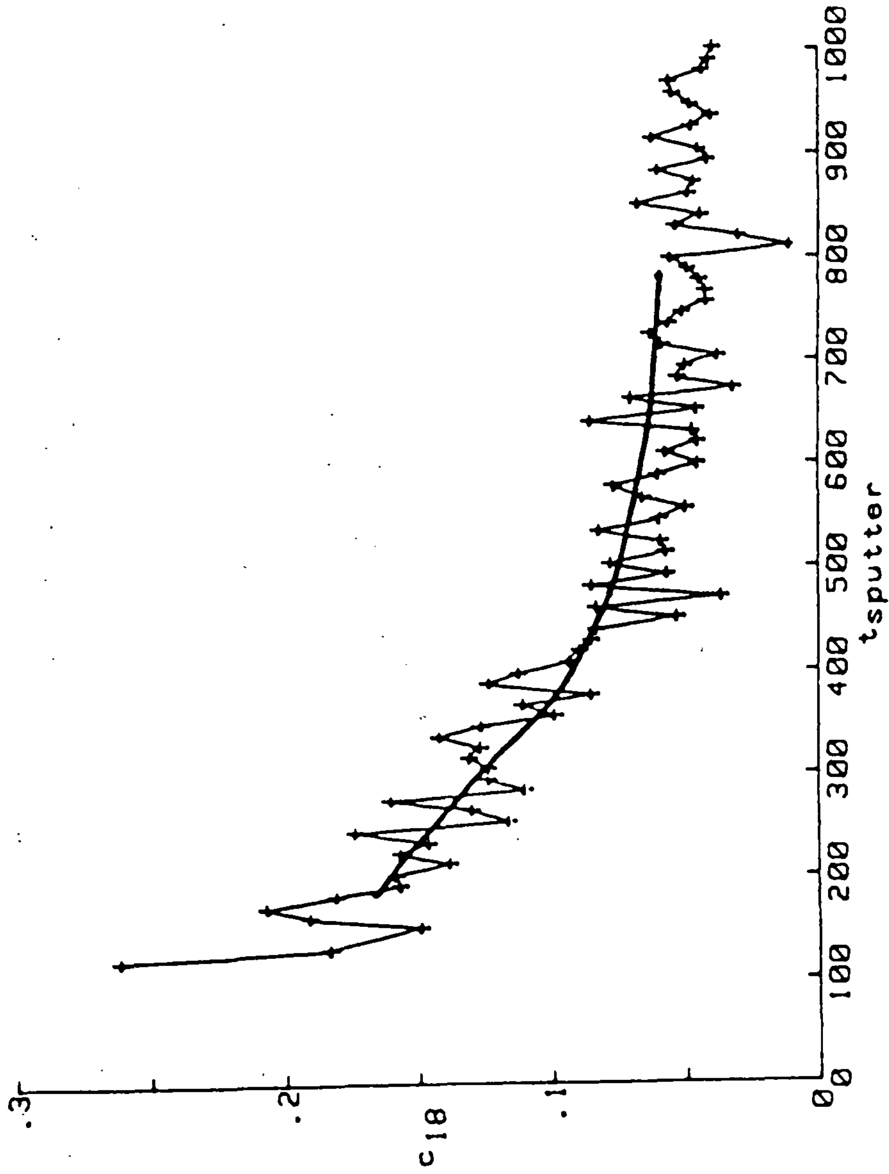

Figure 85. - PSU SIMS profile on a sample of Cr-doped hot pressed Al_2O_3. The smooth curve is the reference from the undoped profile.

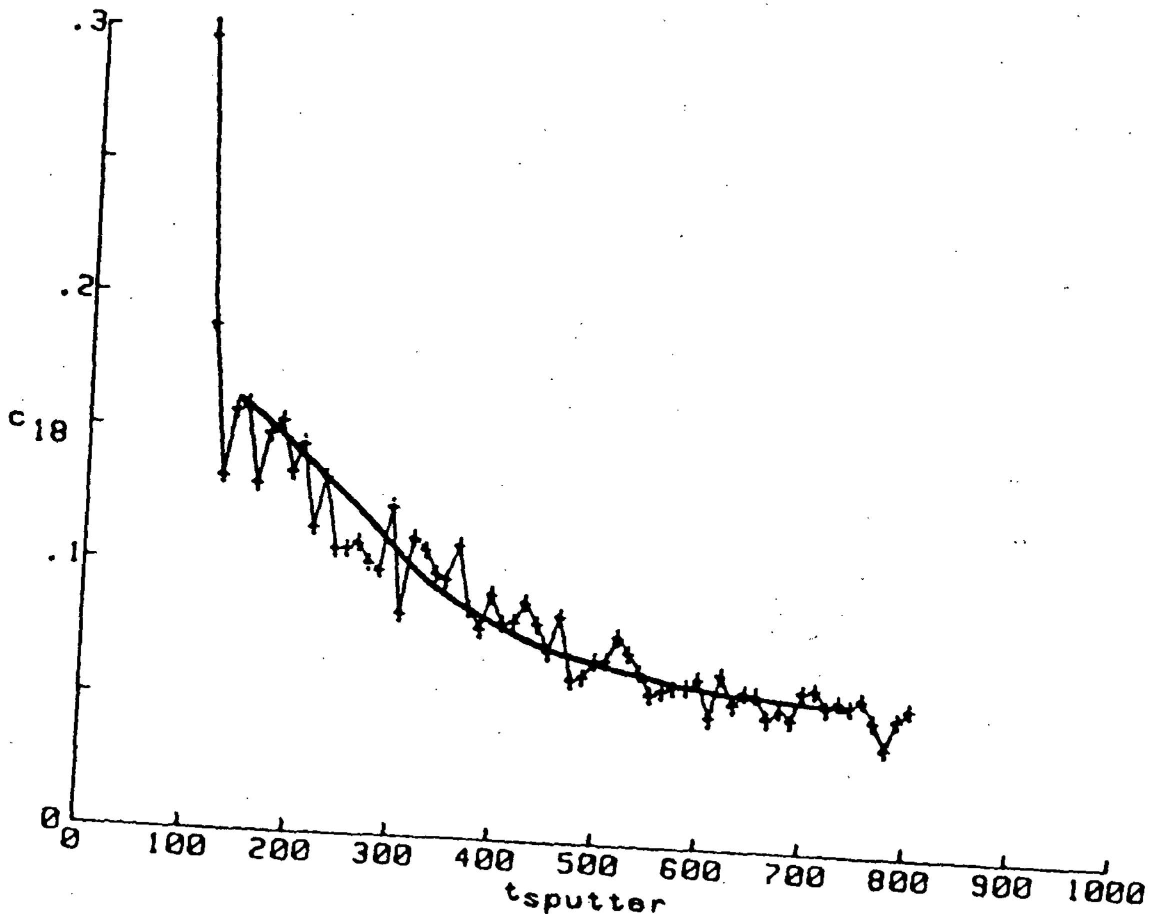

Figure 86. - PSU SIMS profile on a sample of Ni-doped hot pressed Al_2O_3. The smooth curve is the reference from the undoped profile.

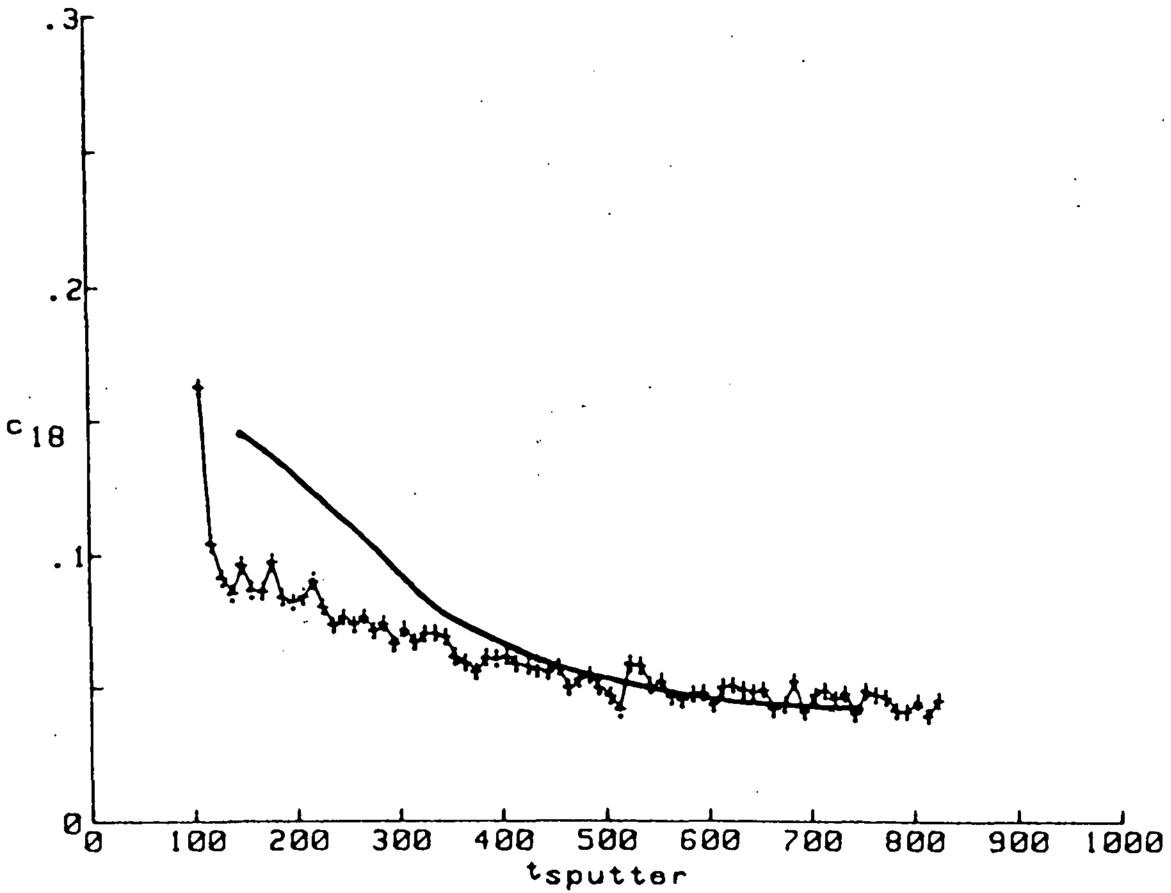

Figure 87. - PSU SIMS profile on a sample of Y-doped hot pressed Al_2O_3. The smooth curve is the reference from the undoped profile.

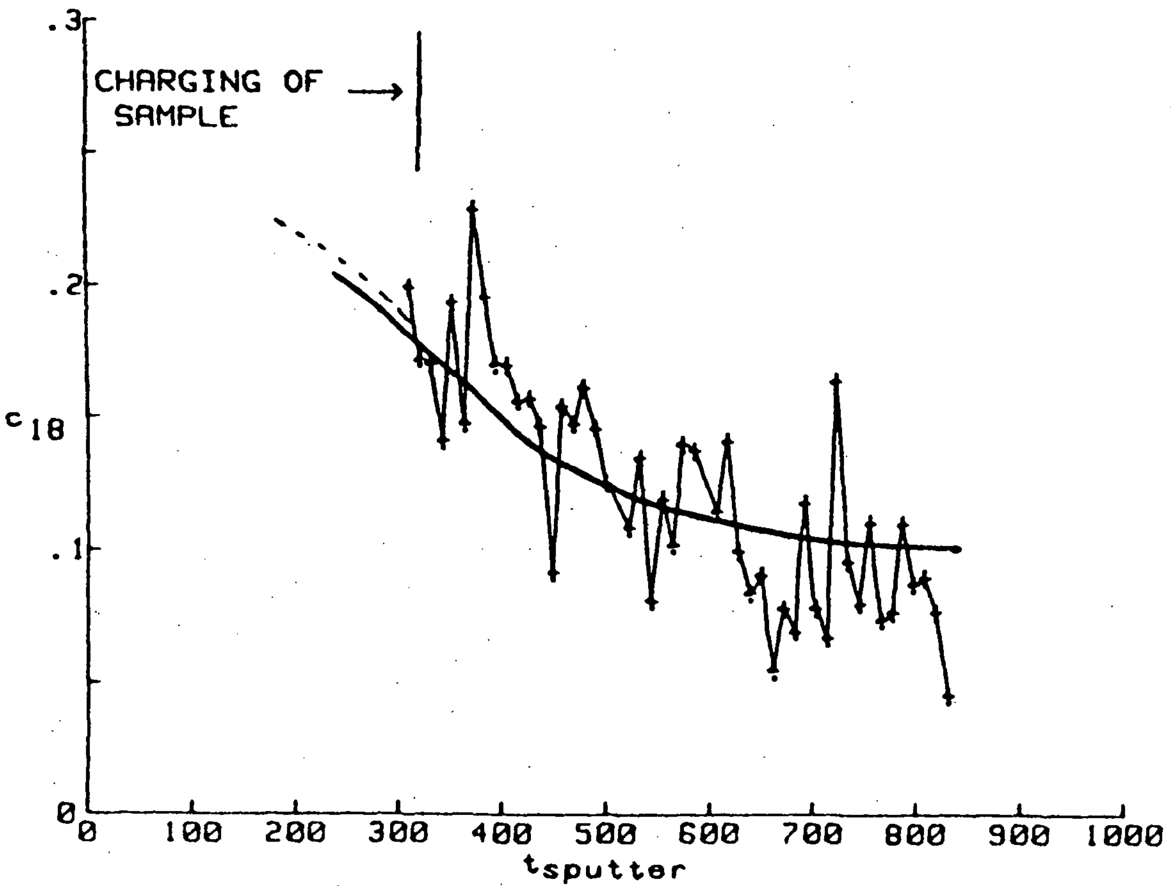

Figure 88. - PSU SIMS profile on a sample of Zr-doped hot pressed Al_2O_3. The smooth curve is the reference from the undoped profile.

4.2.4 Attempt to Profile Polycrystals at Low P_{O_2}

Samples of polycrystalline material were subjected to a low P_{O_2} preanneal (in CWRU Hot Press) and a low P_{O_2} diffusion anneal. However, due to severe surface face roughening no tracer profiles were determined.

The surface roughening is illustrated with profilometer traces of four samples shown in figure 89. It can be seen that the surface roughening in a low P_{O_2} environment is considerably greater than in 1 atm. P_{O_2}, for the same time and temperature.

The prospect of determining grain boundary diffusion coefficients in low P_{O_2}, by this method is dim. In order to get a profile which is large with respect to the surface roughness, would require tracer penetration and subsequent sputtering to depths >20 μm. Notice that with the 1 atm O_2 sample, it would be satisfactory to be at a depth of 1 μm. Also, the single crystal sample retained its finish despite the low P_{O_2}.

4.2.5 Contamination of Single Crystals

In tracer diffusion studies the assumption is made that the chemistry of the material which contains the tracer profile is characteristic of the chemistry of the bulk. In a gas exchange experiment, particularly when the diffusion coefficient is as low as in alumina, this region is only a few microns into the surface.

In order to check the validity of this assumption, the near surface region of some samples were mass analyzed by SIMS. Typical mass scans from the UIU SIMS and the PSU SIMS are shown in figures 90 and 91. Differences appear between mass scans taken with the two machines.

SURFACE ROUGHNESS OF HOT PRESSED ALUMINA

Cr 200ppm
as polished

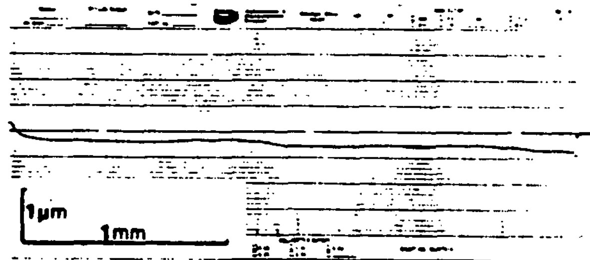

Cr 500ppm
1634°C 24hr
1atm

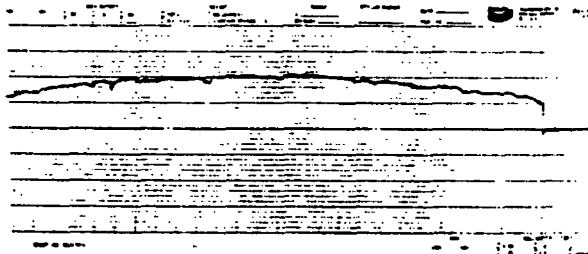

Cr 500ppm
1634°C 24hr
low Po_2

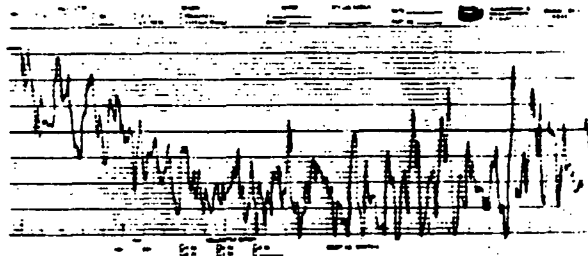

Cr Single Crystal
1634°C 24hr
low Po_2

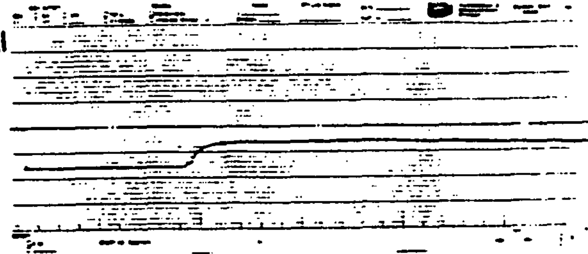

Figure 89. - Surface roughness of hot pressed alumina.

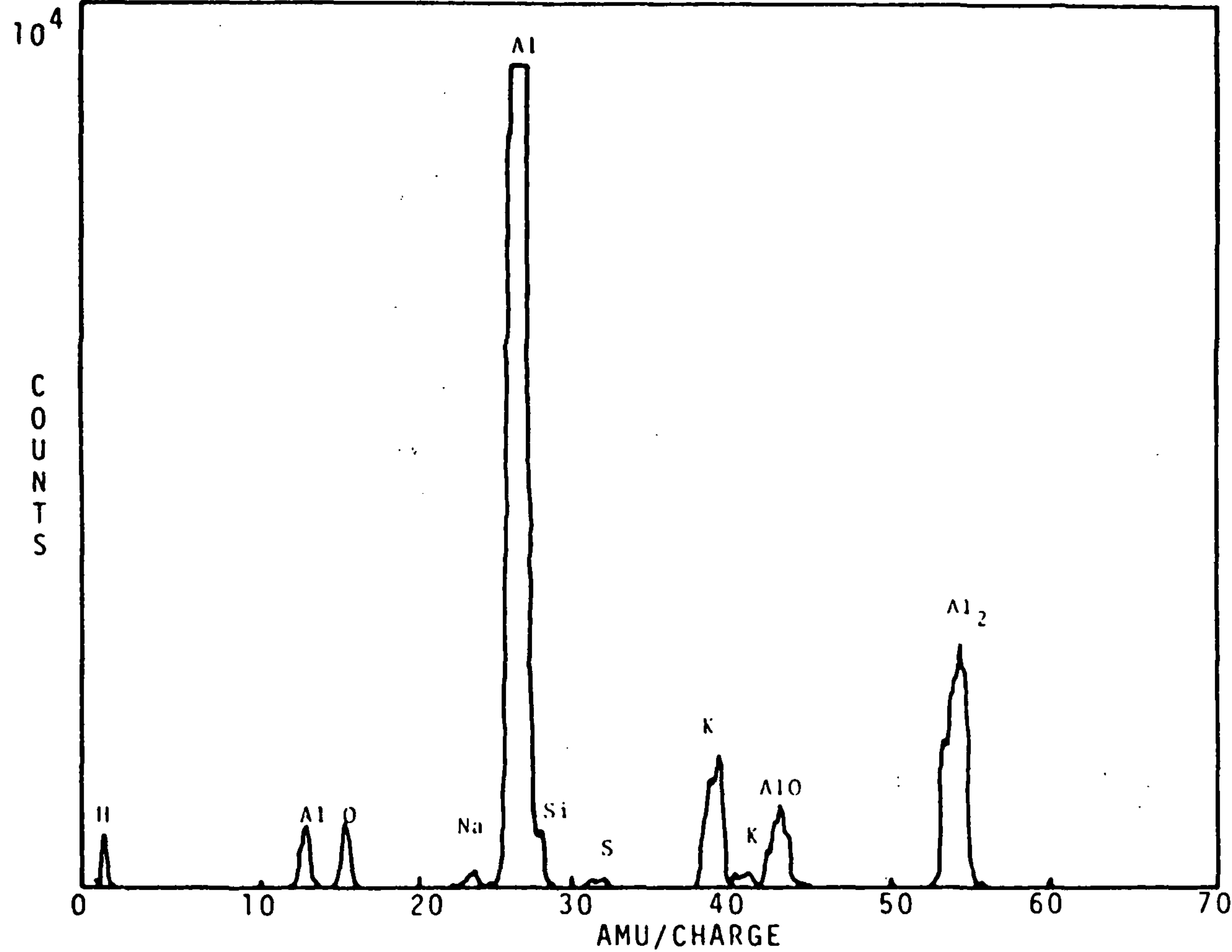

Figure 90. - PSU mass scan, typical of the PSU instrument, on an undoped as-received sample.

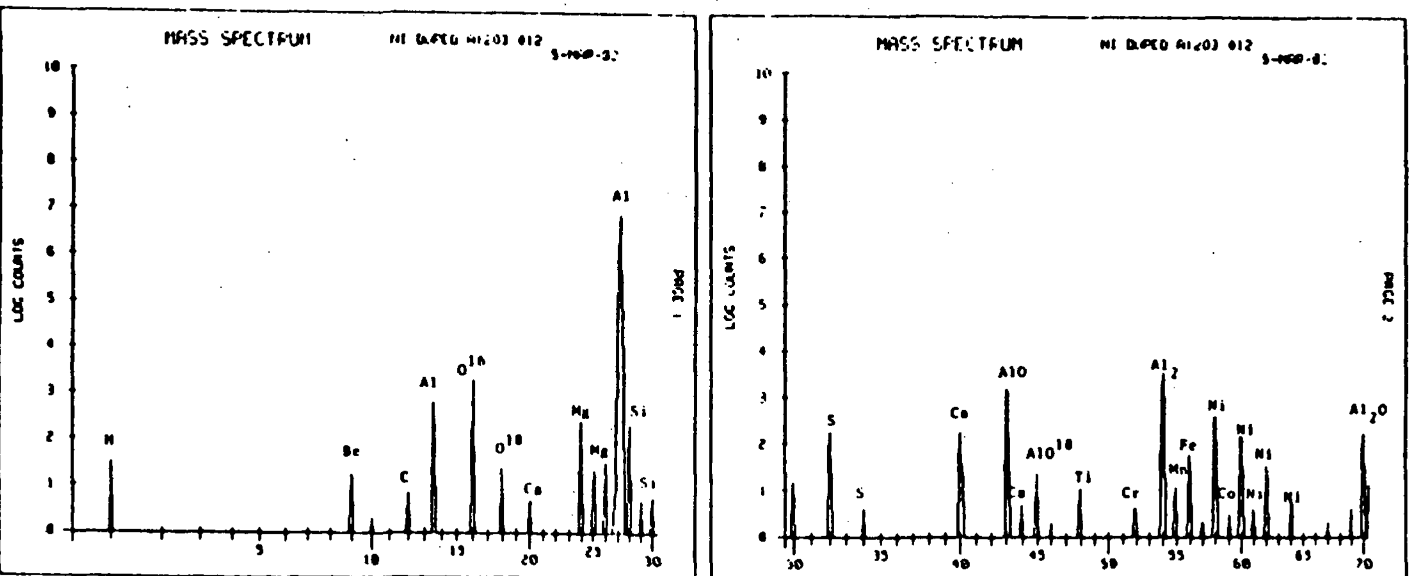

Figure 91. - UIU mass scan, typical of the UIU instrument, on a Ni-doped sample exchanged at 1330° C for 404 hr.

The scan from the UIU camera shows a greater number of peaks and has better counting statistics (note that log counts is plotted for UIU and counts for PSU). The increased counting rate probably arises from oxygen enhancement.[55]

A second, more puzzling difference is the presence, in the PSU scans, of peaks for sodium and potassium which do not appear in any of the UIU scans. Since sodium was detected in the spectrochemical analysis (table 4), it is surprising that it does not appear in the UIU scans. Potassium, on the other hand, was not detected in the spectrochemical analysis and yet it appears in the mass scans from Penn. State. The isotopes of potassium appear in the correct ratio AMU 38.96 (93 percent) and AMU (40.96 (7 percent). The argon primary beam is known to be a source of potassium however the beam contribution should be constant and gradients were found.

Fingerprint contamination is a possible source of these elements. However, if such were the case, the concentration of sodium would be expected to be tied to that of the potassium, and this is not the case. Also, the mass scans were taken after sputtering through the carbon layer and into the sample at greater than 0.1 μm which should be well past surface contamination. It may be that the difference in primary beams is the source of this discrepancy.

In order to assess the contamination of our samples, mass scans were taken on the as-received boules during and after the annealing process. All of the peak heights were normalized to the height of the Al^{++} peak. This allowed a comparison from sample to sample.

Mass scans of two undoped, as-received, samples; one from undoped no. 3 and one from material used by Reddy, are shown in figure 92. The two appear very similar. Note the presence of a little sodium, some silicon, and an indication of potassium. Also, the counting rates of the other fragments of Al_2O_3 show some fluctuation. This fluctuation, plus the knowledge that various chemical species have different sputtering yields, dependent on their environment, cautions against quantitative interpretation of these scans.

However, the qualitative comparisons show a distinct trend. Figure 93 shows scans for two samples from the undoped no. 3 boule, one as-received and one after an anneal at 1550° C. The difference is striking. After the exchange the sample picked up magnesium and calcium which were not present before. Also, peaks for silicon and potassium are distinctly larger.

Mass scans on a sample exchanged at 1410° C and a sample of as-received material, are shown in figure 94. The level of contamination is significantly less than the sample exchanged at 1550° C, despite the fact that that Dt's for oxygen were similar. There is an increase in the sodium peak and a magnesium peak appears after the exchange, while the apparent concentration of silicon has decreased. The indication that potassium is off scale stems from the fact that the peaks on the mass scan were offscale to begin with. The ratio of the peaks may not be off scale but it cannot be determined.

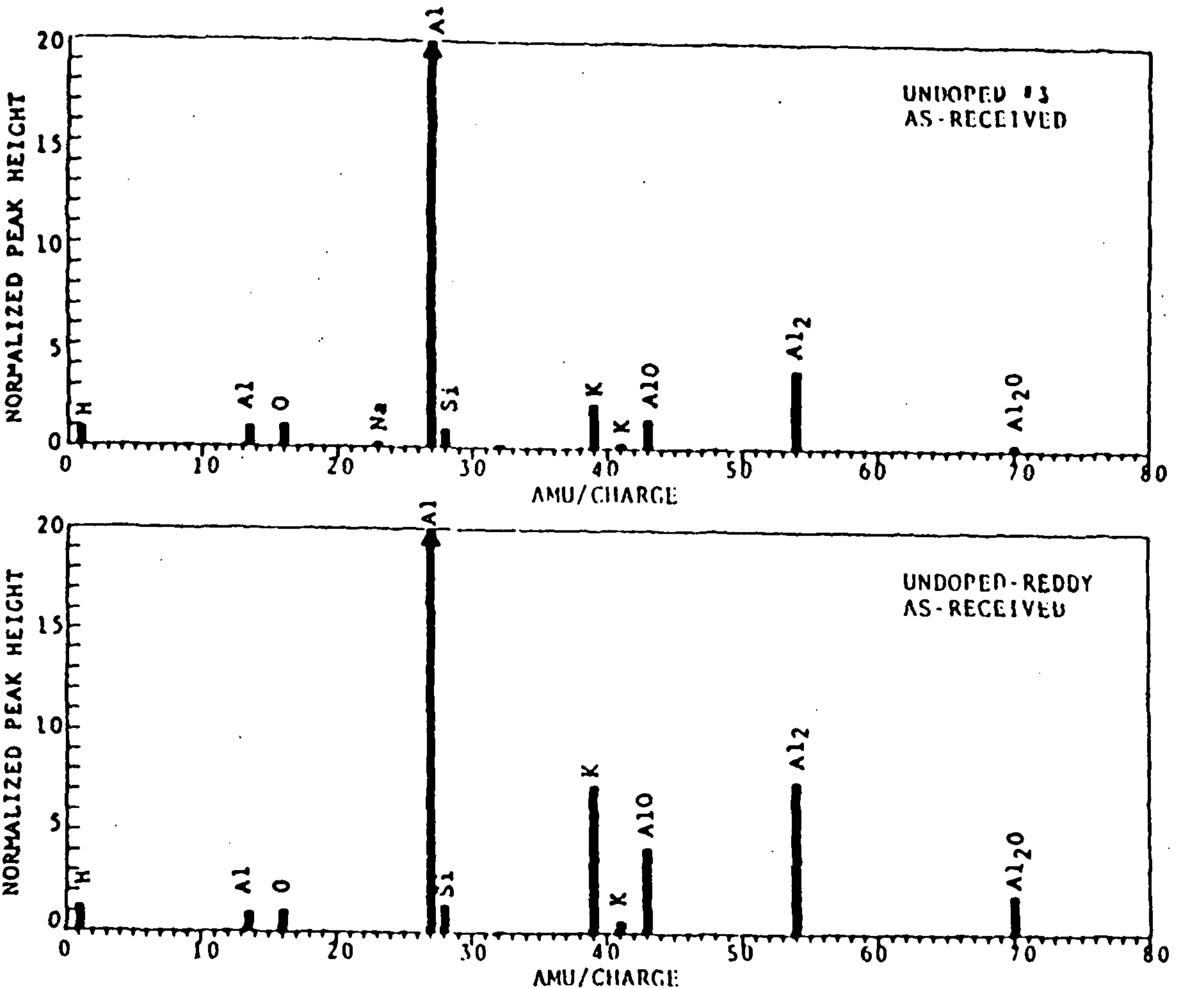

Figure 92. - PSU mass scans on undoped samples from two separate sources, one Verneuil and one Czochralski.

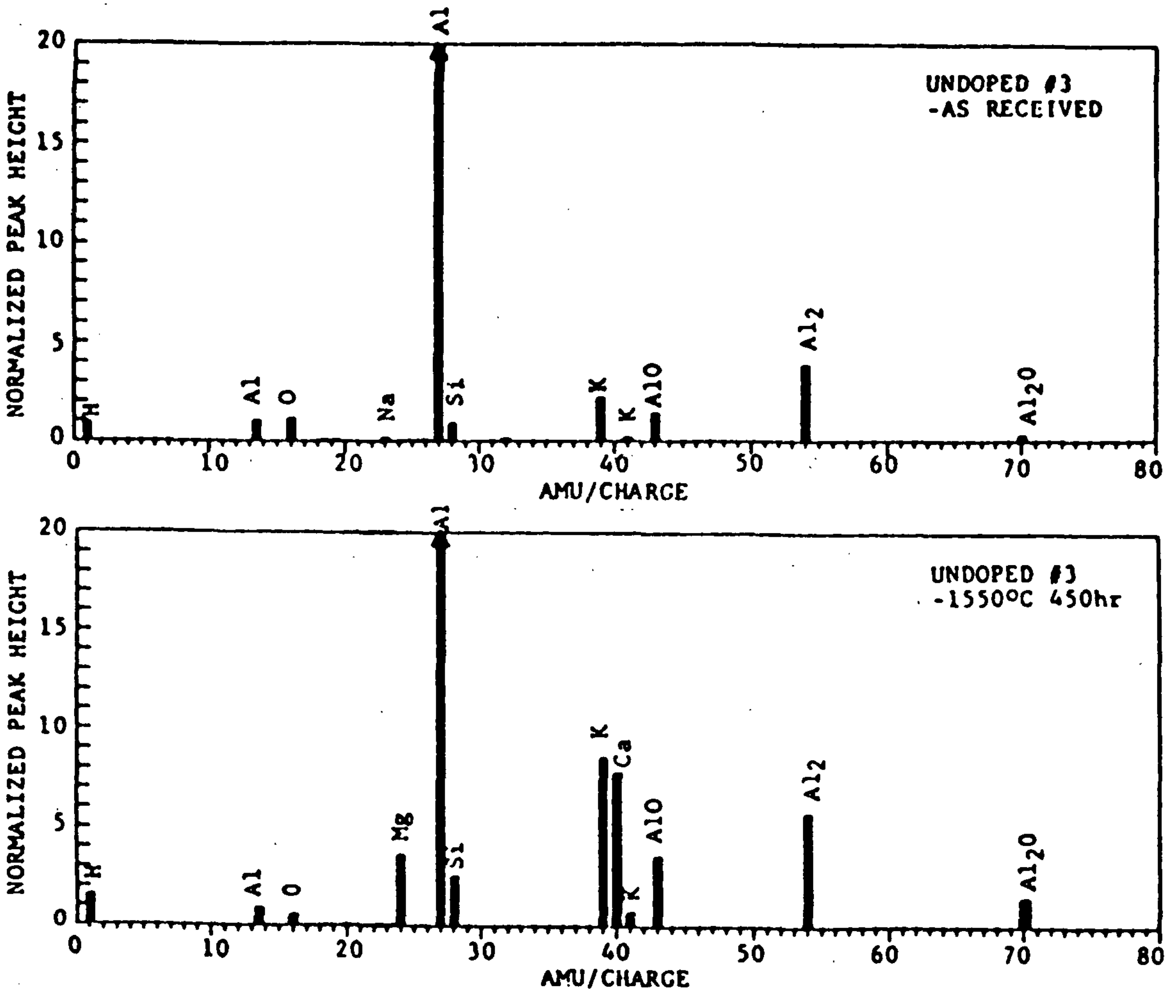

Figure 93. - PSU mass scans on two undoped samples, one as-received and one after an exhange at 1550° C for 283 hr.

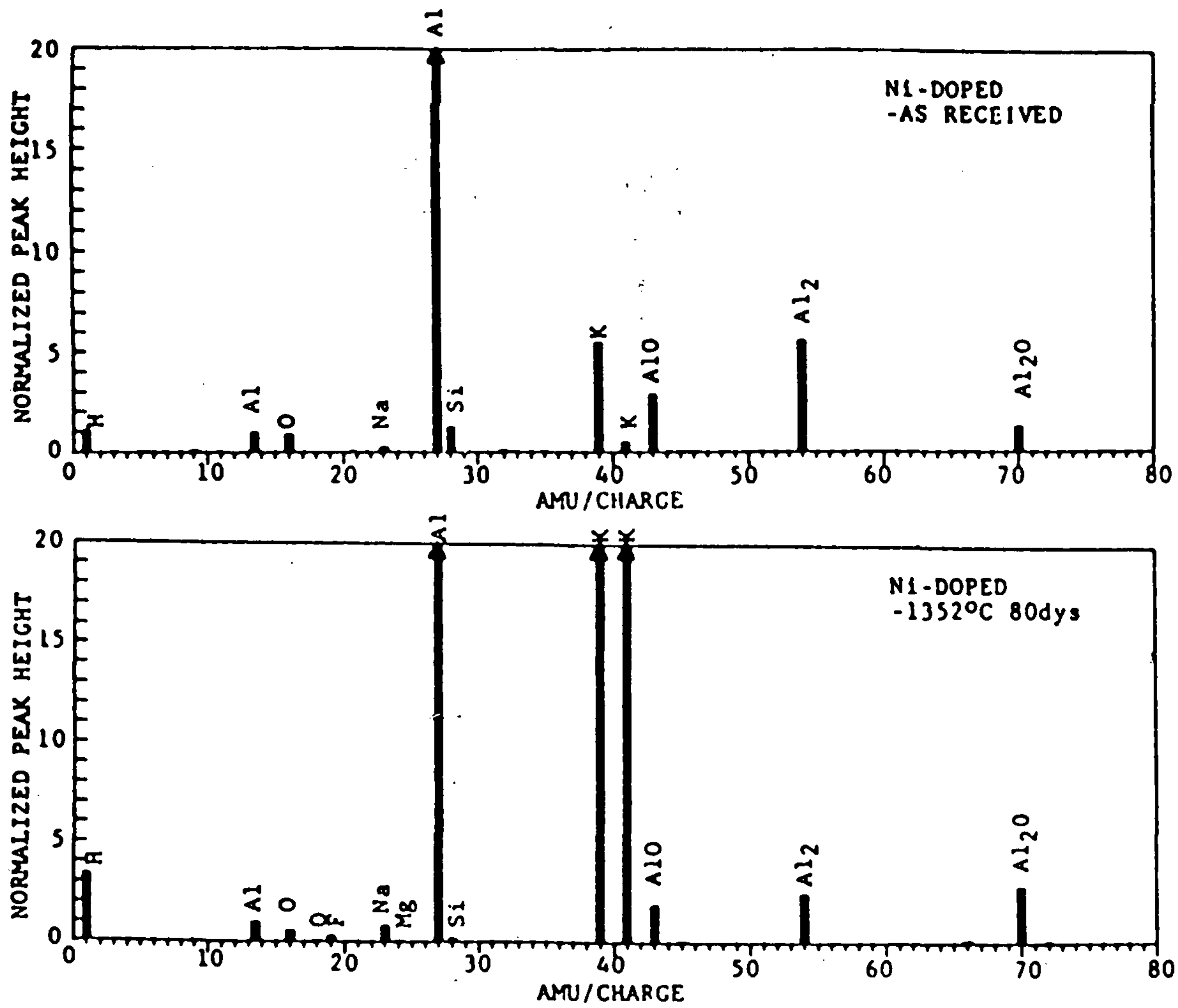

Figure 94. - PSU mass scans on two Ni-doped samples, one as-received and the other after an exchange at 1330° C for 1920 hr.

As verification of the contamination, cations were profiled along with the tracer on some samples. A plot of the counting rate of silicon normalized to that of aluminum, for the sample exchanged at 1550° C is shown in figure 95. The concentration of silicon near the surface is ~8 times that at a depth of 0.5 μm into the sample. If we assume the concentration at 0.5 μm is the background, then, based on the spectrochemical analysis, we can estimate the near surface silicon concentration to be 350 ppm.

Attempts to subtract out the background, assume a surface concentration, and fit the profile with complementary error function, proved unsuccessful, (see fig. 96). This may be due to simultaneous contamination by Ca, Mg and K.

The cations, Si, Na, Ca, and K were profiled on a sample exchanged at 1300° C. The oxygen-18 profile is shown in figure 97, and the normalized cation profiles in 98 to 101. In this sample the cation profiles are much deeper than the tracer profile. Note that the profiles all contain a spike at the surface. Also, the Si, Ca, and K profiles have negative slope indicating an inward flux, while the Na profile has a positive slope indicating an outward flux, or evaporation.

Four samples; two undoped, one Cr-doped, and one Ni-doped, were exchanged in the 1634° C low P_{O_2} experiment. The oxygen concentration profiles in all four were indistinguishable. The silicon profiles in the undoped and Cr-doped samples were also very similar. However, the silicon profile in the Ni-doped sample is distinctly

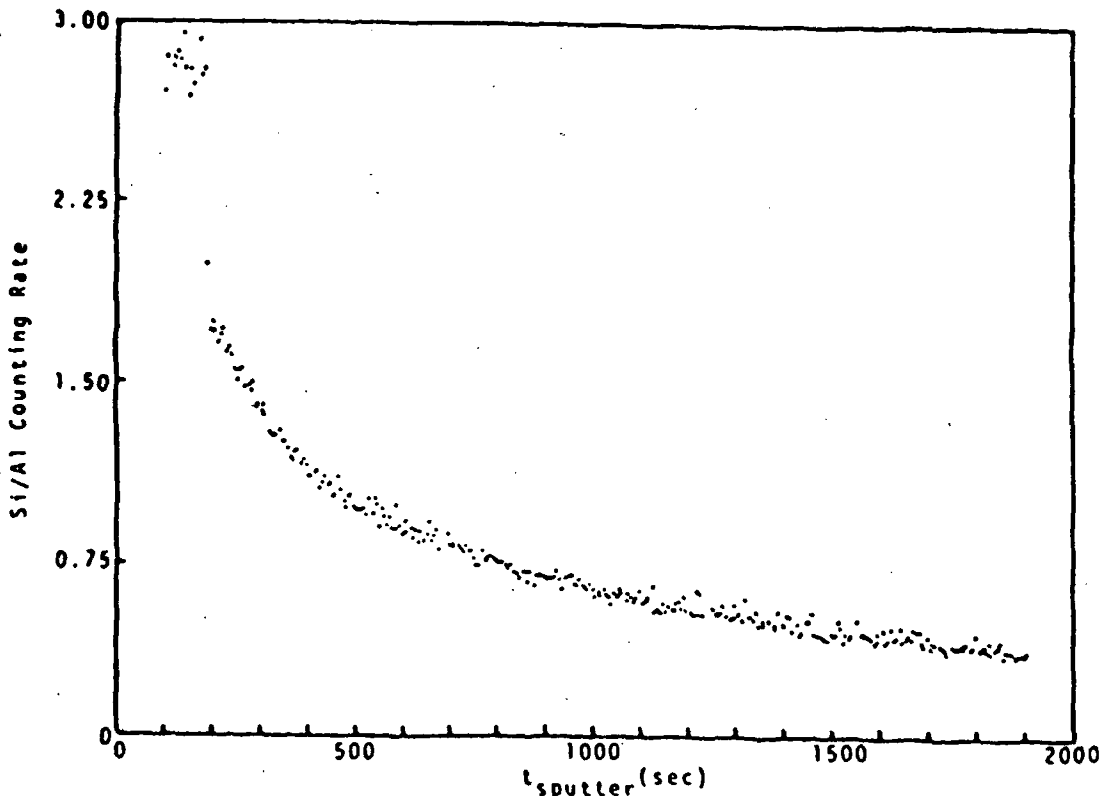

Figure 95. - PSU depth profile for silicon on an undoped sample exchanged at 1550° C for 283 hr.

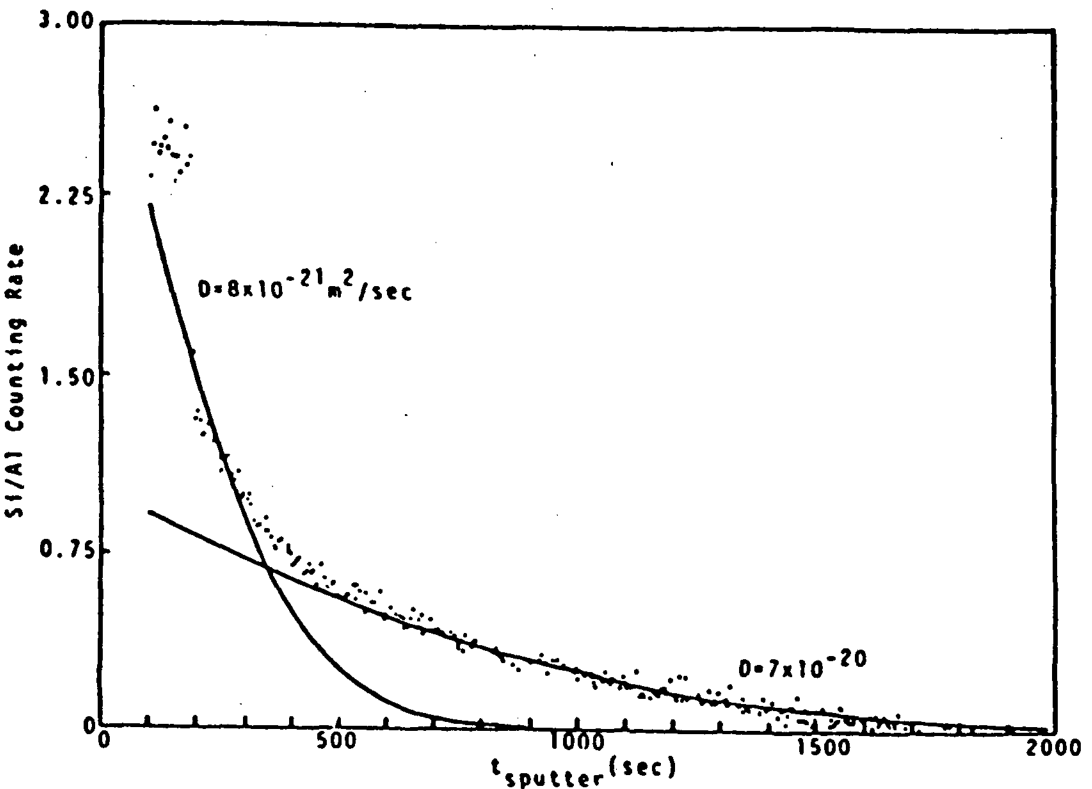

Figure 96. - Attempts to fit a complementary error function to the silicon profile.

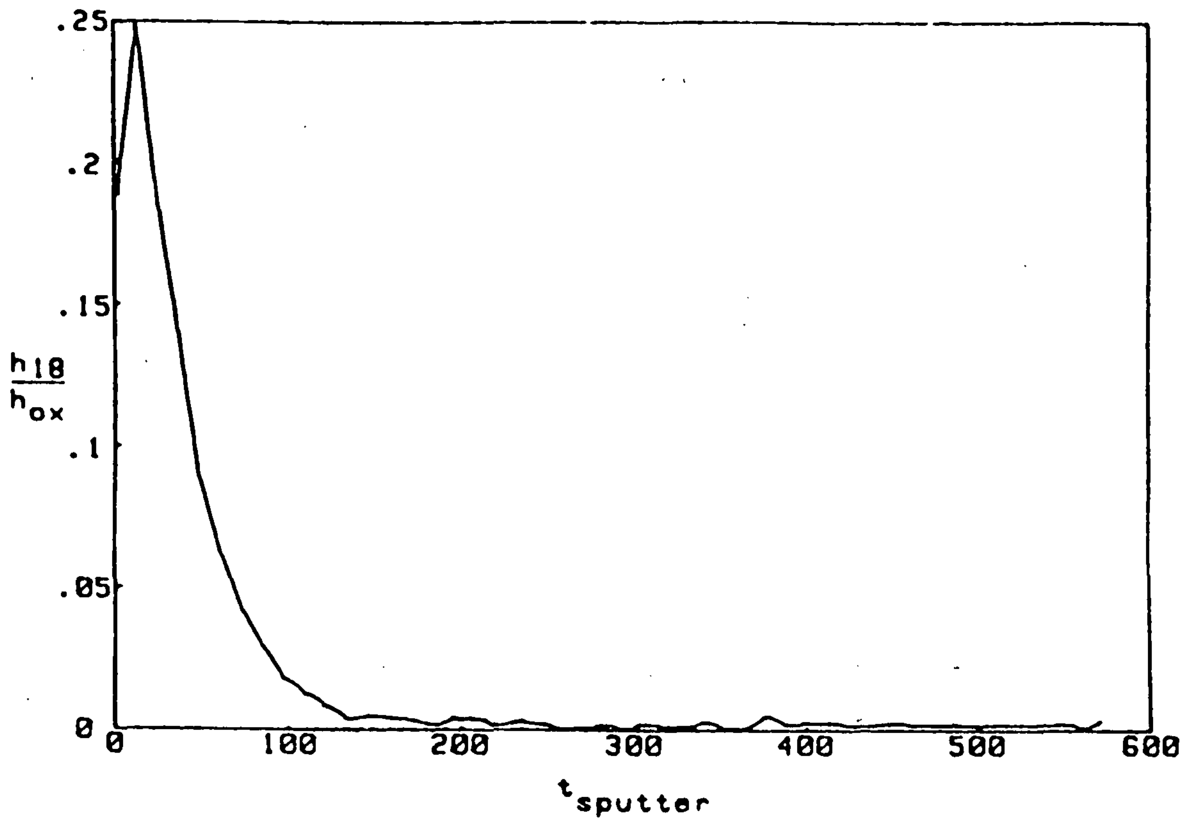

Figure 97. - PSU SIMS profile of oxygen tracer in sample UD-LT, exchanged at 1300° C for 1073 hr.

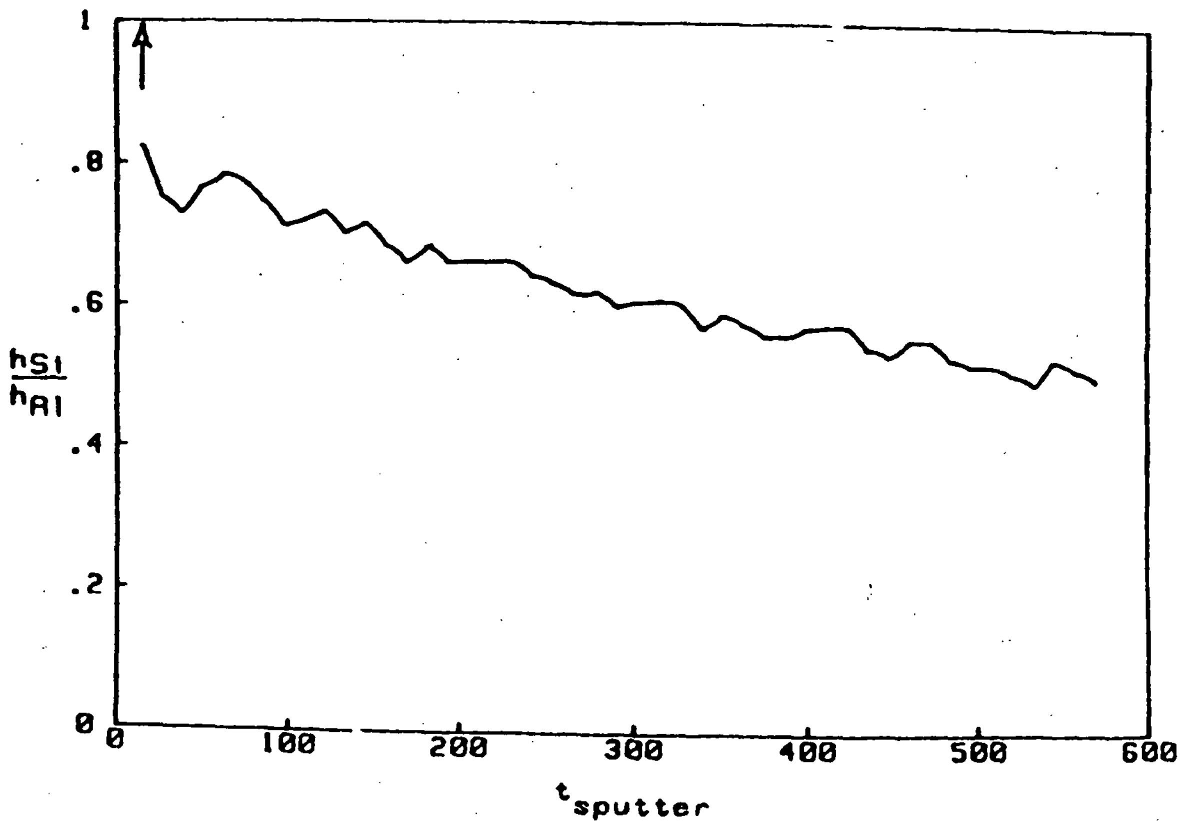

Figure 98. - PSU SIMS profile of silicon normalized to aluminum, in sample UD-LT exchanged at 1300° C for 1073 hr.

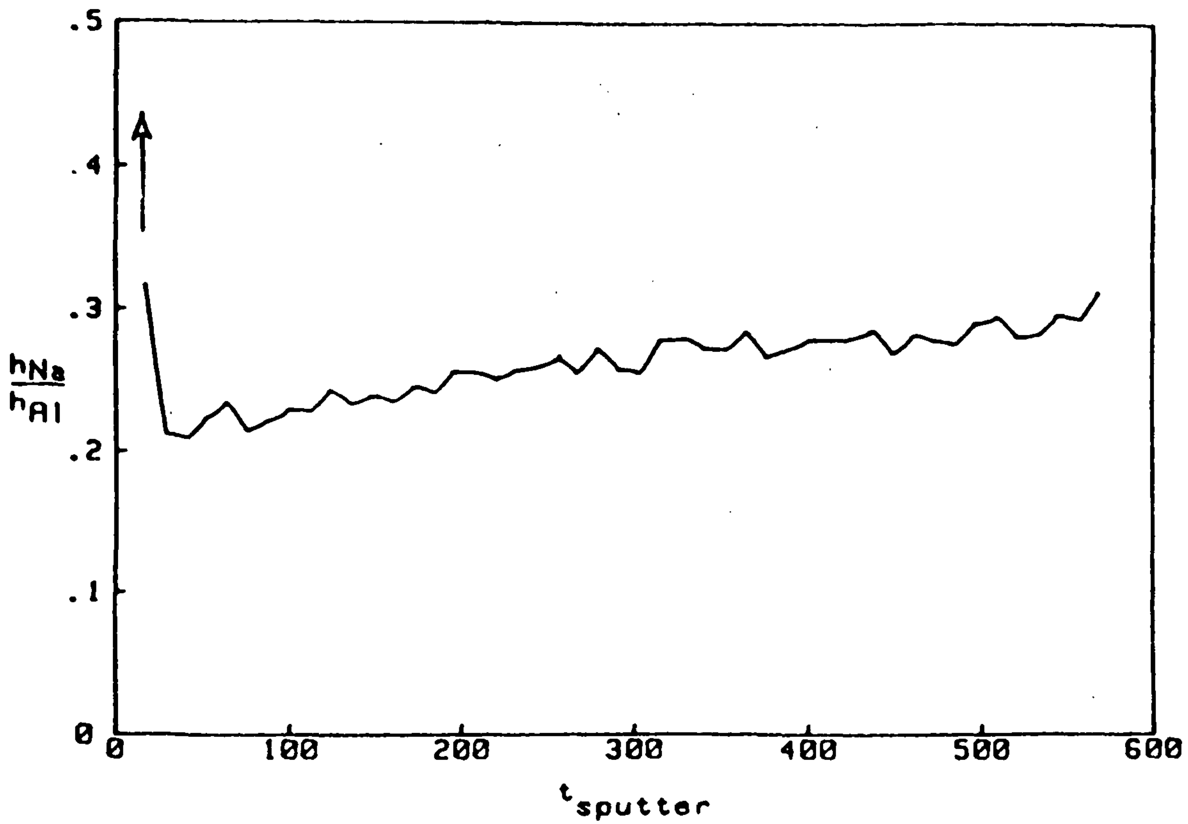

Figure 99. - PSU SIMS profile of sodium normalized to aluminum, in sample UD-LT exchanged at 1300° C for 1073 hr.

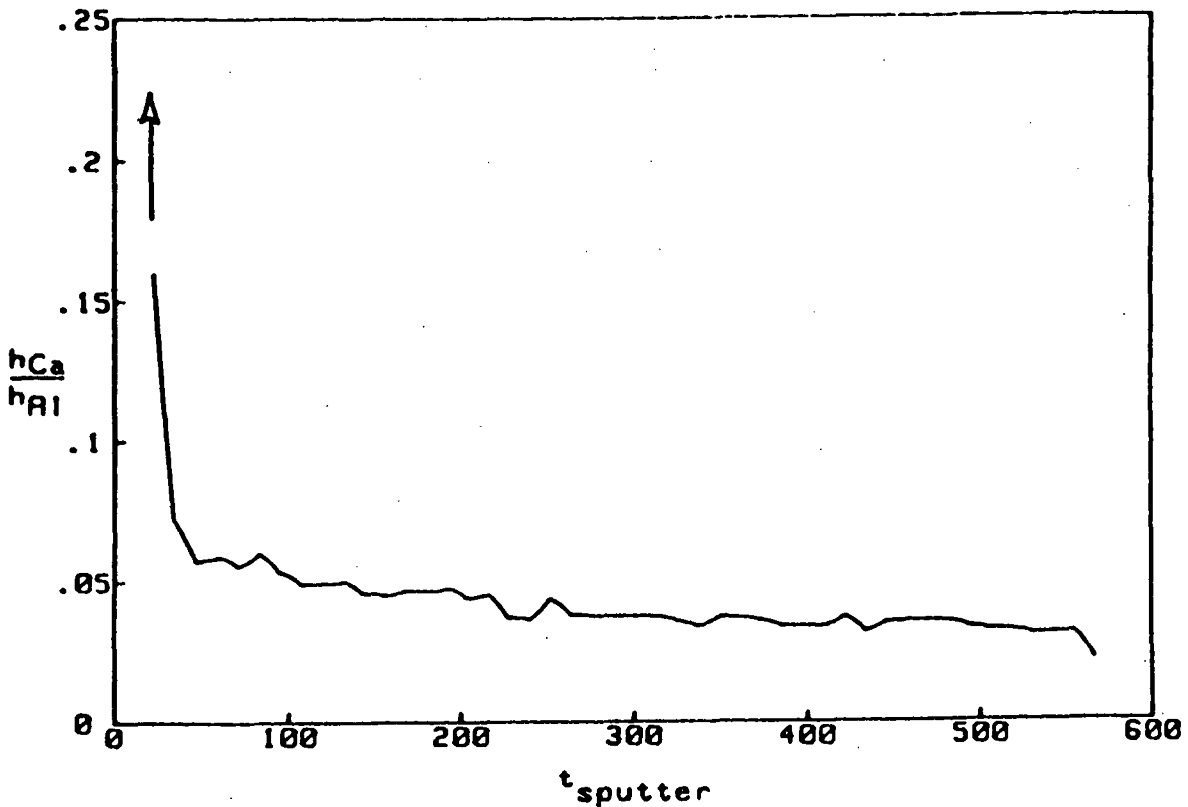

Figure 100. – PSU SIMS profile of calcium normalized to aluminum, in sample UD-LT exchanged at 1300° C for 1073 hr.

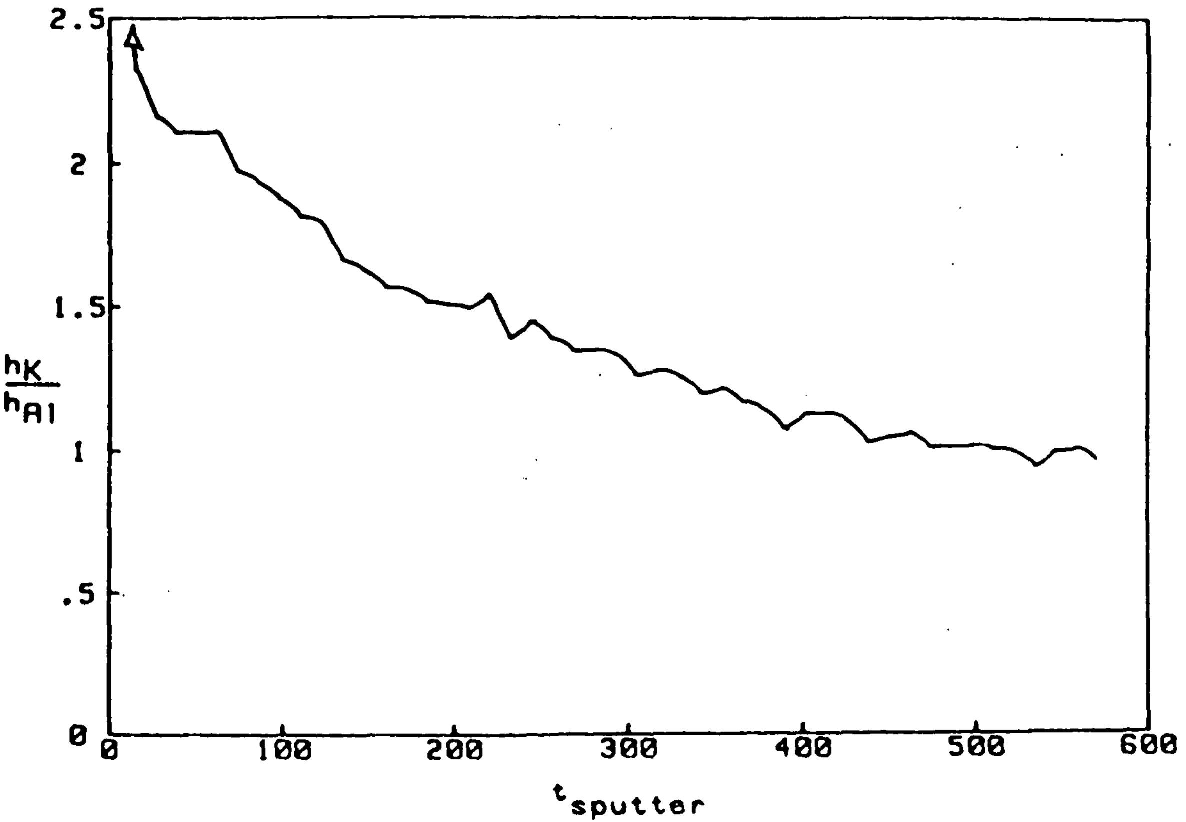

Figure 101. - PSU SIMS profile of potassium normalized to aluminum, in sample UD-LT exchanged at 1300° C for 1073 hr.

different. This is shown in figure 102. The undoped samples have just a spike of mass-28 near the surface, whereas, the penetration of silicon in the Ni-doped material is roughly equal to that of the tracer. This dependence of contamination upon dopant is interesting particuarly since a dopant effect upon oxygen diffusion is absent. It would be useful to have a reanalysis of other samples to see if this is an isolated case or if it is systematic.

The high purity Al_2O_3 furnace tube visibly changed as a function of time at annealing temperatures. The as-received tubes were smooth and a waxy yellow color. After a long time at high temperature, the color became distinctly whiter and the surface roughened.

To check on whether the material evaporating from the tubes could act as the source for the contaminants, a piece of a new and a piece of well used tube were scanned. The results are shown in figure 103. The tubes do have all the contaminants present and their concentrations do drop off after the tube is used.

Contamination of the surface of single crystal Al_2O_3 samples, after annealing in commercial "high purity" alumina tubes has been observed by both Scott[69] and Heuer[70]. The contamination was reported to consist of small droplets of a silicate glass containing Al, Ca, and K.[69]

Examination of the surfaces of our samples revealed the same type of droplets. The droplets were tenacious, they were not disturbed during the removal of a sputter deposited Pd coating from the sample by physical rubbing with a Kimwipe saturated with acetone.

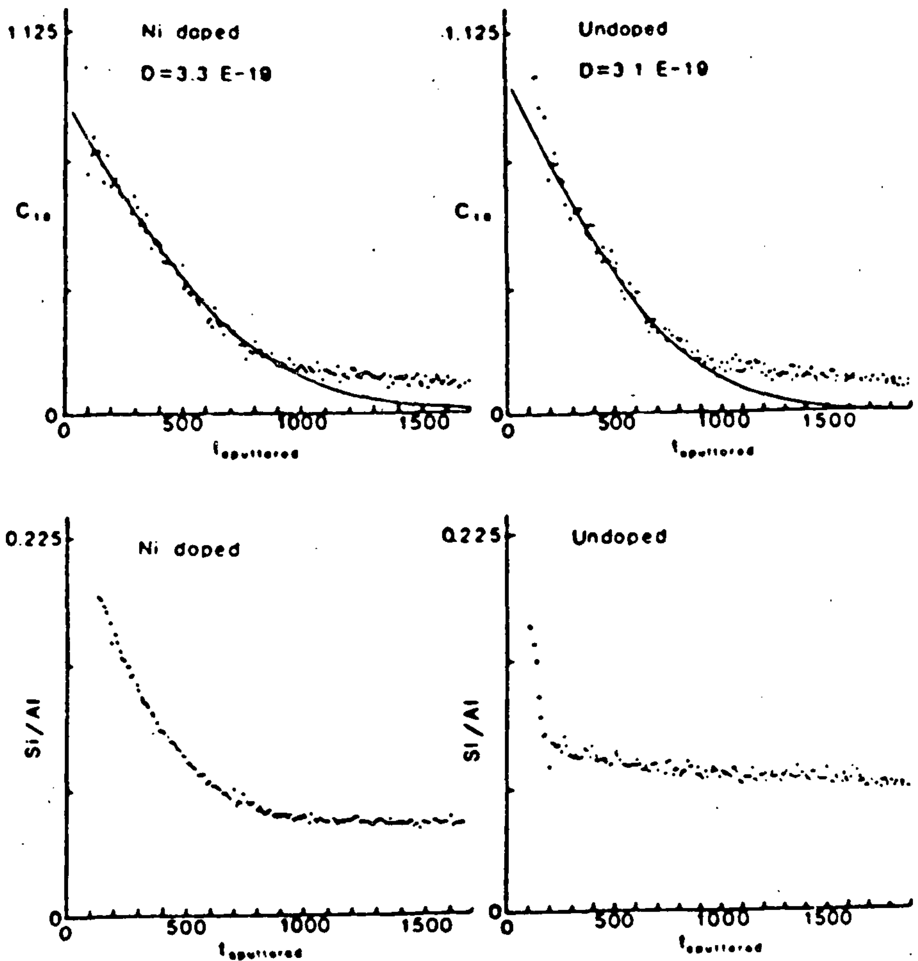

Figure 102. - Oxygen and silicon penetrations in two samples, one undoped and one Ni-doped, that were exchanged together at 1634° C for 8 hr in low P_{O_2}.

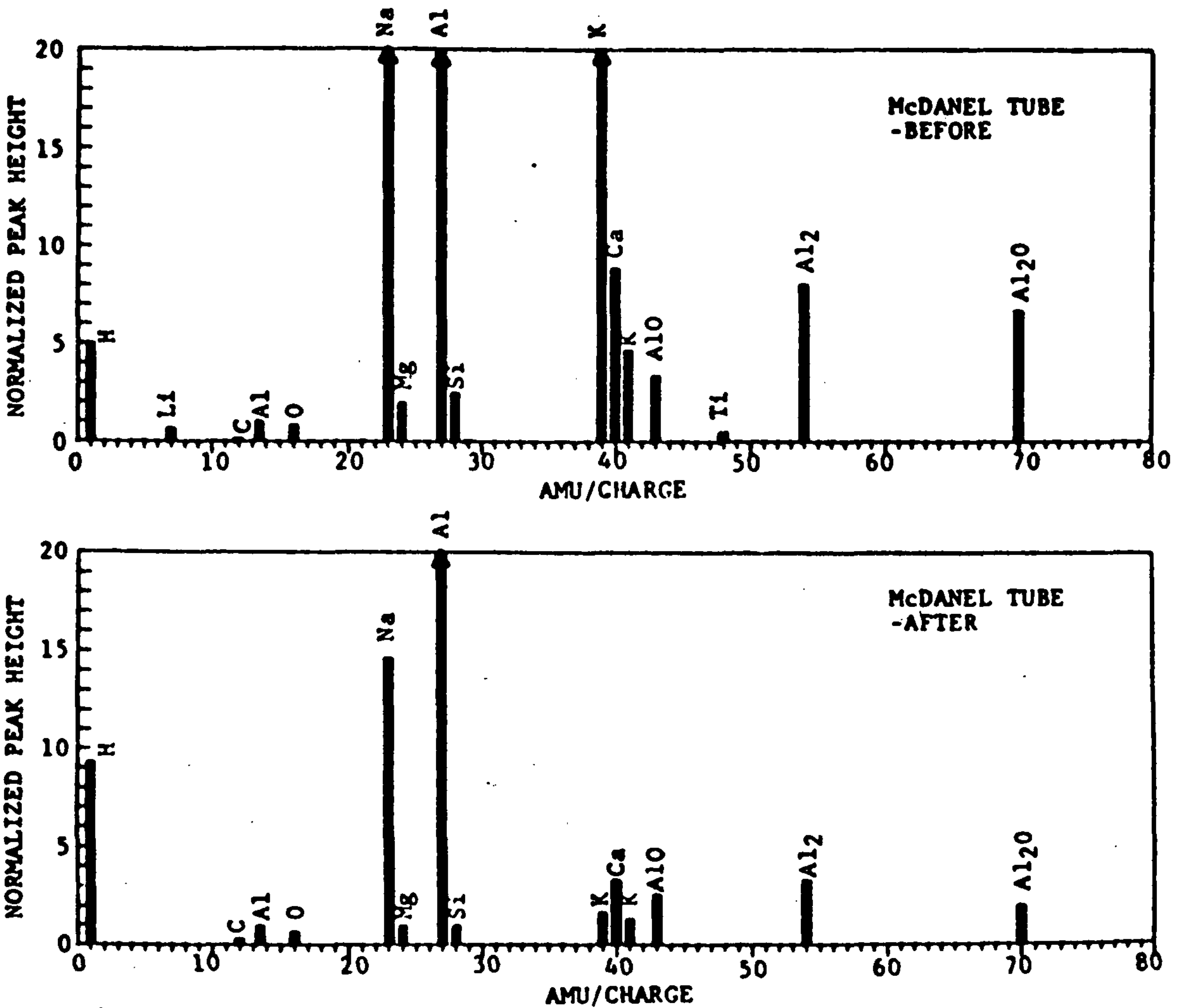

Figure 103. - PSU mass scans on samples of the furnace tube, one as-received and one after the tube had been used at high temperature for a long period of time.

They were, however, etched completely away by a 10 sec immersion in 48 percent HF.

The population and composition of the droplets varied from sample to sample, and from location to location on a single sample. Figure 104 shows typical droplet densities for two samples. The one exchanged at 1600° C has a much higher droplet density than does the sample at 1300° C, due presumably to the difference in vapor pressures of the glass formers at those two temperatures. Figure 105 shows the droplet population, both near the edge and towards the center of a single specimen. The region of the sample near the edge was rounded during polishing and surface steps developed during annealing. In this region, the droplets were less numerous and of a larger diameter than those away from the edge.

The radius of curvature may be estimated from the Newton's rings which appear in the large droplet shown in figure 106. The sample was illuminated with an Hg source and each ring corresponds to ~1/4 μm. The droplet is around 2 μm high and ~120 μm in diameter. The radius of curvature is therefore very small, $\sim 5 \times 10^{-4}$ μm. This indicates that the glass wets Al_2O_3 very well.

The chemistry of the droplets also appears to vary. Silicon was present in every case examined however the alkalis and alkaline earths differ. Increases in Mg, Ca, and K were observed by SIMS, in one sample (fig. 91) while increases in only K and Na were observed in another sample, and further one sample was analyzed with EDAX, in an SEM, found only Ca and Si present in the droplets. It is reasonable to expect the oxides evaporating from the furnace tube to change

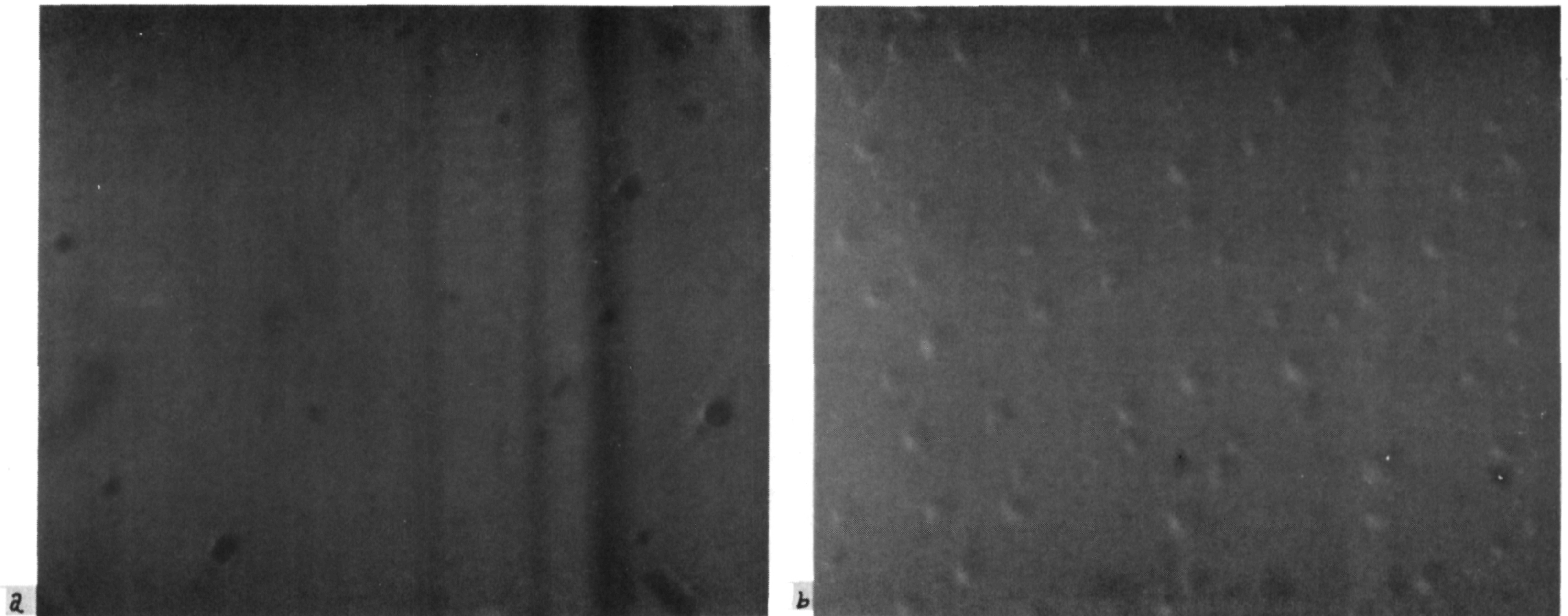

Figure 104. - Optical micrographs of the typical glass droplet populations on samples annealed at a) 1300° C and b) 1600° C. (400X)

Figure 105. - Optical micrographs of the typical glass droplet populations on a sample annealed at 1634° C a) away from the sample edge and b) near the sample edge.

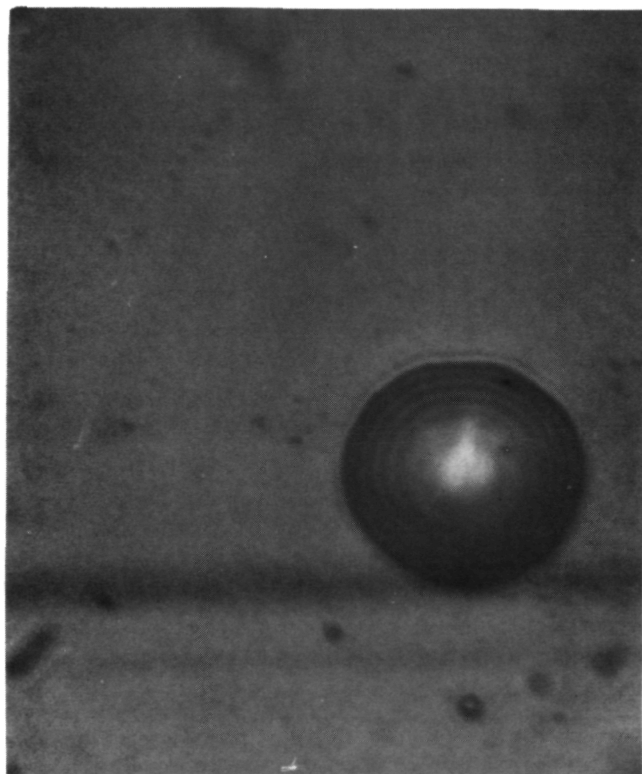

Figure 106. - Newton's rings in a glass droplet on a sample exchanged at 1300° C. (400X)

composition as a function of time. Initially, higher vapor pressure species (with high alkali content) would be dominant and at later time the glass would be depleted of alkali. The area density of the droplets varied greatly. Regions of a millimeter square were observed to have no droplets while other areas contained on the order of 10^6 droplets per square centimeter.

The existence of the droplets raised a question as to whether the cation profiles detected by SIMS are truly located within the Al_2O_3 or all generated by the sputtering of droplets during profiling.

All of the cation profiles have a very sharp, and intense counting rate during the initial stage, and then exhibit a discontinuity followed by a smooth profile (see fig. 95 and figs. 98 to 101). This is consistent with sputtering off of glass droplets and then profiling Al_2O_3. The RBS data (see fig. 47) also suggests that cations in contact with the surface during the anneal will diffuse in.

A sample which has been cut in half and the glass beads etched off of one half was analyzed. A cation profile was observed in both specimens. The magnitude in the etched sample roughly two thirds of the unetched.

4.2.6 Contamination of Polycrystals

Cation profiles similar to those in the single crystal samples were observed in the polycrystalline material. An example is shown in figure 107.

Another possible method of contamination is cross-contamination

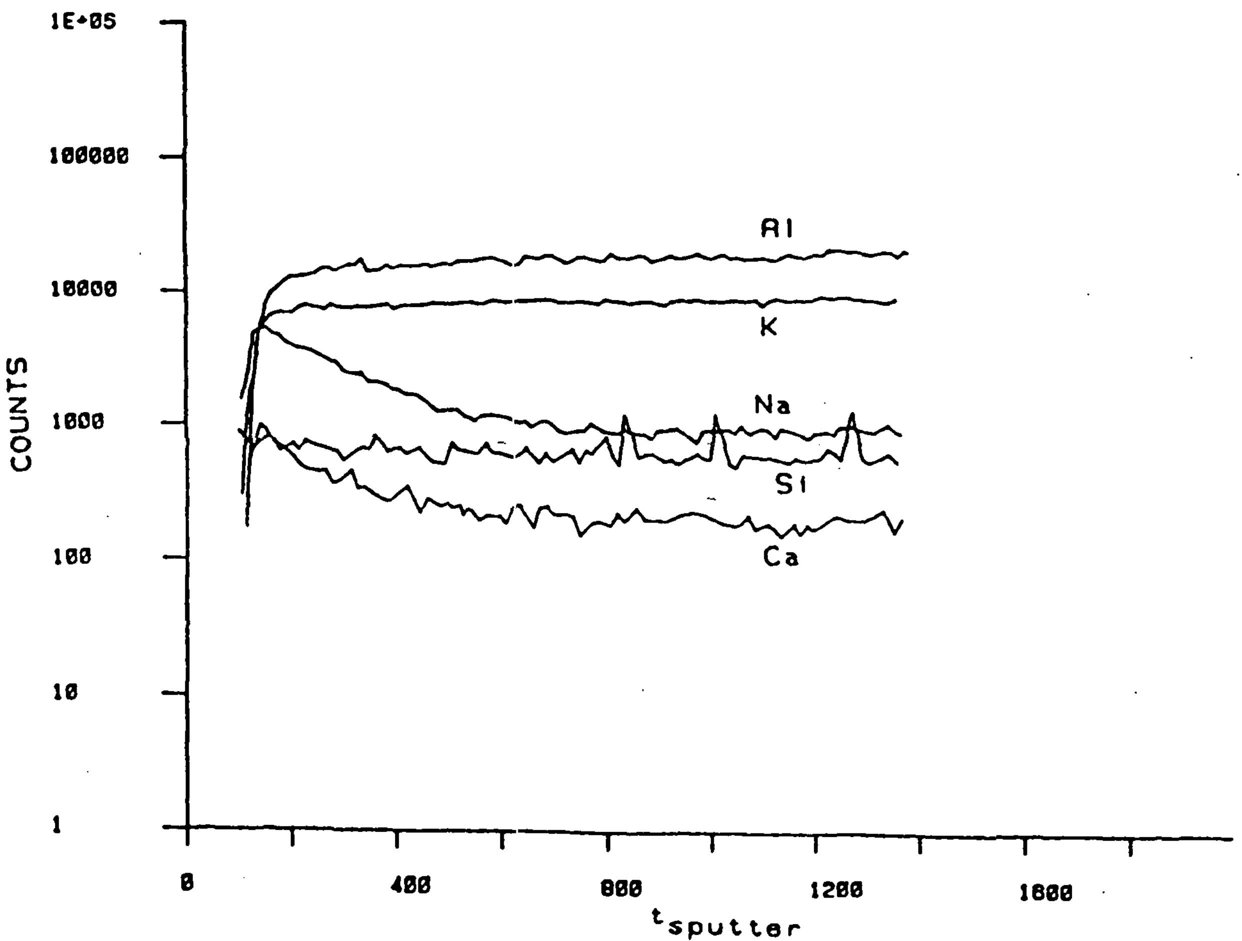

Figure 107. - Cation profiles in undoped hot pressed Al_2O_3 annealed at 1634° C. For clarity the Al profile was translated along the y-axis one decade.

between samples with different dopants. A set of hot pressed Al_2O_3 samples, singly doped with 500 ppm of Cr, Ni, Y, and Zr, were exchanged together at 1300° C for eight hours. The oxygen-18 penetration was too small to be measured. However, a profile for chromium was observed in the undoped specimen. This is shown in figure 108. The procedure of simultaneous exchange to ensure that samples will see the same diffusion anneal may be unwise, particularly for such volatile dopants as chromium.

It is also observed that the samples with dopants that produce a color, Cr and Ni, left the shelf in the annealing furnace colored after the anneal was complete. Although traces of the Y and Zr dopants were not visible, it is quite probable that they have similar behavior. Therefore, the concentration of dopant in the near surface region is lower than that of the bulk and changes with time. Therefore, the procedure for exchange of these types of samples will require considerable refinement.

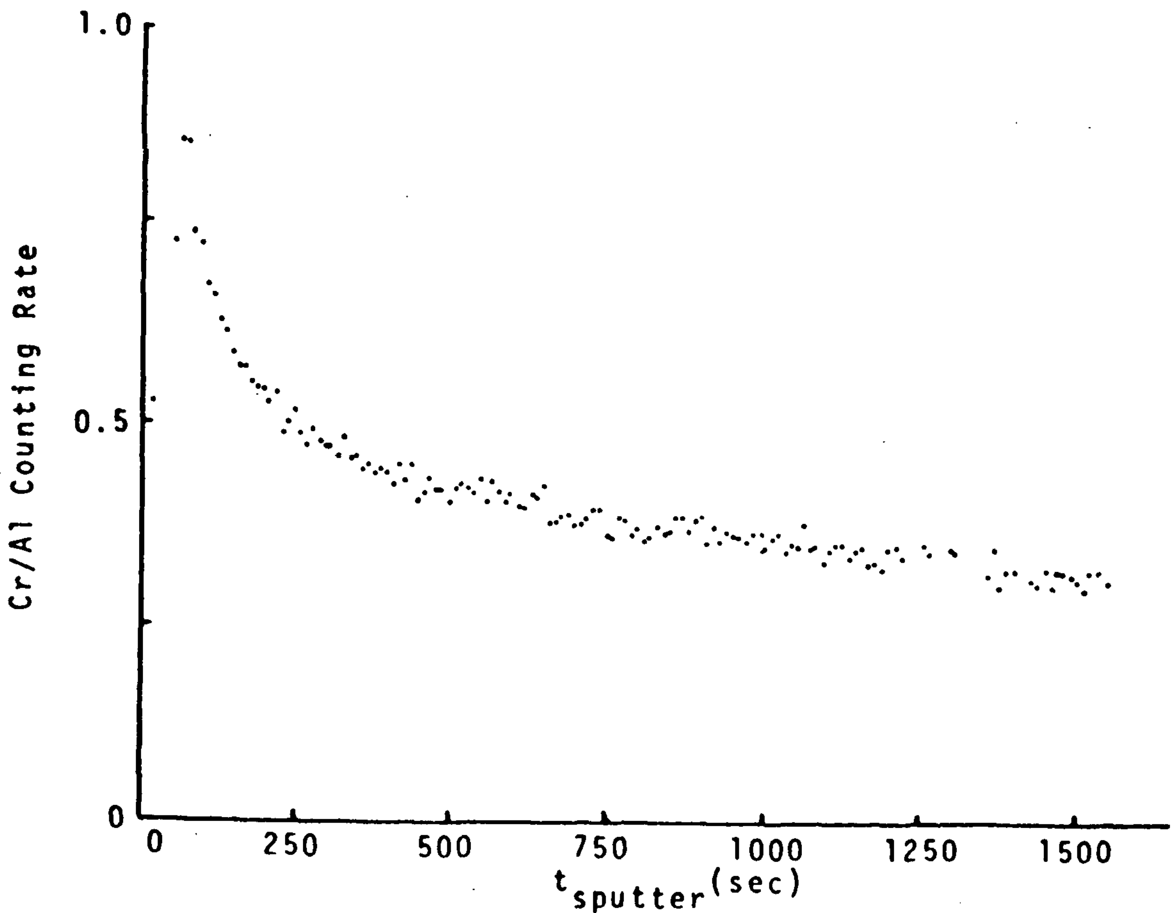

Figure 108. - PSU SIMS profile of cross contamination of Cr into the undoped sample at 1330° C.

CHAPTER V

DISCUSSION

5.1 ANALYSIS TECHNIQUES

Two quite different techniques were used in this study to determine tracer concentration profiles, SIMS and proton activation. In our proton activation work there was some evidence of misleading data due to fluorescence of our samples. Earlier workers, at C.W.R.U., would not have seen this since they used a meter long magnetic spectrometer between the sample and the detector. If it turns out, in fact, that there is a problem with photons striking the detector, it should not be a difficult problem to correct.

There remain other advantages of SIMS over proton activation.

(i) Depth Resolution - Even if the electronics and the sample were perfect, the best commercial detector gives energies $\pm$10 to 13 KeV (13 KeV corresponds to 0.03 μm in Al_2O_3), so the depth resolution would be limited. SIMS has routine depth resolution <10 Å.

(ii) Penetration - The ranges of protons and alpha particles only allow a maximum penetration of ~3 μm. This is particularly bad because of the relatively poor depth resolution. In SIMS the material can be sputtered to any depth of choice. However, concerns about machine time and taking data from the the region into which the primary beam has been implanted, also restricts practical use of SIMS to the first few microns.

(iii) Experimental and Analytical Complexity - Proton activation requires a Van de Graaf generator for protons. Also, the interaction of protons on a crystal necessitates care to avoid channeling. The primary ion beam in SIMS may also be channeled and reduce the sputtering rate. However, since the sputtering rate was determined for each sample after the experiment, a channeled beam would not lead to errors in apparent depth.

The conversion of raw data to concentration versus depth information involves many more variables with proton activation than with SIMS. Each variable carries with it an uncertainty.

(iv) Species Detected - The basis for proton activation is the very specific nature of the nuclear reaction. Only oxygen-18 is detected. The addition of RBS allowed for some chemical information however only species more massive than Al could be resolved.

SIMS allows many, up to nine, elements to be concurrently monitored. It was this feature which uncovered the contamination. Such a feature would also be of great value when studying the oxidation of metals. This would allow concentrations of cations to be monitored along with the tracer.

(v) Destructive Nature - Proton activation is essentially a nondestructive method. It is a very small fraction of the tracer which reacts. SIMS, on the other hand, is destructive. The analysis is dependent on the sputtering of material. This limits the technique to a one time analysis. However, a sample 0.5 cm square will accommodate up to twenty craters without overlapping. In practice, therefore, this is not much of a limitation.

Overall, SIMS appears a more versatile tool for diffusion work.

5.2 OXYGEN DIFFUSION

The results of this investigation may be summarized as follows:

(1) The diffusion is insensitive to impurity content. Our five boules, though not doped in the manner intended, did have different impurity levels between them. The near surface region was also demonstrated to have picked up impurities during the anneal. Despite this, our data agrees very well with that of Reddy and Cooper. Since both studies used the same system with the same supplier of 99.8 percent Al_2O_3 tubes, it might be argued that both made diffusion measurements on equally dirty samples. However, the activation energy, 615 kJ/mol, agrees very well with that of the other gas exchange studies; 648 kJ/mol for Oishi and Kingery, and 636 kJ/mol for Oishi, Ando, and Kubota. In these studies the sample was heated by induction on a Pt-Rh susceptor surrounded by a water cooled SiO_2 tube. Even if contamination occurred it would be unlikely that it would be the same as ours. The activation energy determined by Lagerlof and Heuer in their dislocation loop annihilation study was also similar, ~600 kJ/mol. The furnace in which they annealed their TEM foil was porous firebrick.

As mentioned in the literature survey, Oishi, Ando, and Kubota also found no effect on oxygen diffusion from impurities.

It is interesting to note that there is an indication that the rate of contamination of our samples by a cation impurity, Si, was dependent on dopant. In the case of the Ni-doped crystal the appar-

ent penetration by Si was deeper than in the undoped material (see fig. 102). However, it should be kept in mind that this transport takes place on the cation sublattice.

(ii) The diffusion of oxygen in α-Al_2O_3 does not depend on the partial pressure of oxygen. The diffusion coefficient determined from the sample exchange in a CO/CO_2 atmosphere, corresponding to $P_{O_2} = 10^{-15}$ atm, falls on a line determined by the $P_{O_2} = 1$ atm data.

Reddy suggested that the difference in P_{O_2} and that of Reed might be responsible for the difference between the data. In light of the CO/CO_2 experiment, this does not appear valid.

5.2.1 Thermodynamics of Point Defect Clustering

It has recently become clear that clusters of associated defects are very important in oxides. The calculations of Catlow et al., which will be discussed more thoroughly, indicate that the ratio of associated defects (clusters) to unassociated (free) defects, in α-Al_2O_3, is very large. Before attempting to interpret the results of self-diffusion experiments it is necessary to consider the thermodynamics of clusters and the possibilities for their motion.

Point defects (vacancies, interstitials, and impurities) may be treated using the thermodynamics of solutions. The host crystal is treated as a solvent and the defects as solutes. In the following discussion of defects, and defect clusters, three assumptions are made

(i) That the only interactions between defects are those between nearest neighbors, giving rise to clusters.

(ii) The kinetics of the association of defects into clusters is rapid and therefore equilibrium is maintained.

(iii) The clusters have a sufficiently long half life against breakup into free point defects that the two may be treated as separate species.

These assumptions are equivalent to having a dilute solution of atomic and molecular species.

5.2.1.1 General Background[1]

Recall that the enthalpy of a system, H, is related to the interal energy, E, the pressure, p, and the volume, V, of the system by

$$H = E + pV \qquad (5.2\text{-}1)$$

and the free energy, F, is related to the internal energy and the entropy, S, by

$$F = E - ST \qquad (5.2\text{-}2)$$

The Gibbs Function, G, then is

$$\begin{aligned} G &= F + pV \qquad (5.2\text{-}3) \\ &= E - ST + pV \\ &= H - ST \end{aligned}$$

In the case of dilute solutions the volume, energy, and enthalpy will increase linearly with small solute concentrations (at constant pressure and temperature) as

[1]This background section is paraphrased however directly from Flynn.(71)

$$V = V_o + nv \qquad (5.2\text{-}4)$$

$$E = E_o + ne$$

$$H = H_o + nh$$

where V_o, U_o, and H_o are properties of n_o mols of pure solvent in which n mols of solute are dispersed, the v, e, and h are partial molar quantities. In turn, the variables S, F, and G become

$$S = S_o + S_c + ns \qquad (5.2\text{-}5)$$

$$F = F_o - S_cT + nf$$

$$G = G_o - S_cT + ng$$

where S_c is the configurational entropy while s, f, and g are partial excess quantities. Note for the case of thermally generated free point defects, equation 2.1-11,

$$\Delta G = G_o - (G_o - S_cT + ng) = S_cT - ng \qquad (5.2\text{-}6)$$

From the above a g-function may be defined

$$g = h - sT + pv \qquad (5.2\text{-}7)$$

The chemical potential, μ, of a defect species, α, may be written as

$$\mu_\alpha = \frac{\partial G}{\partial n_\alpha} = 0 - \frac{\partial}{\partial n_\alpha}(ScT) + g_\alpha \qquad (5.2\text{-}8)$$

For crystalline solids the configuration entropy may be derived from the formula

$$S_c = k_b \ln (\pi) \qquad (5.2\text{-}10)$$

where the degeneracy, w, is the number of distinguishable configurations which the system may adopt. For the case of unassociated, or free, defects

$$S_c = - R_b\, n_\alpha \ln (c_\alpha)$$

where c_α is the concentration of defect species α. The case of a tightly bound cluster must take into account the multiplicity of configurations, m_α, which is the number of distinguishable differences in the shape and orientation of the cluster associated with each lattice site. For this case the configurational entropy may be written as

$$S_c = -R\, n_q \ln \left(\frac{c_q}{m_q}\right) \qquad (5.2\text{-}11)$$

where the subscript 'q' refers to a cluster made up of a number, q, of defects.

The chemical potential for equilibrium thermal defects (intrinsic disorder) is equal to zero, therefore for free defects

$$\mu_\alpha = \frac{\partial G}{\partial n_\alpha} = + RT \ln (c_\alpha) + g_\alpha = 0 \qquad (5.2\text{-}12)$$

or

$$c_\alpha = \exp \left(\frac{-g_\alpha}{RT}\right) \qquad (5.2\text{-}13)$$

In an analogus manner for defect cluster

$$c_q = M_q \exp \left(\frac{-g_q}{RT}\right) \qquad (5.2\text{-}14)$$

When the cluster is looked at as being formed by a reaction of free defects

$$qX \rightarrow (qX) \qquad (5.2\text{-}15)$$

The concentration of clusters may be written in terms of the free defect concentration as

$$c_q = m_q \, c_\alpha^q \exp \frac{b_q}{RT} \qquad (5.2\text{-}16)$$

with

$$b_q = q \cdot (g_1 - g_2)$$

where g_1 is the energy to form a free defect and g_2 is the energy to form and associate q defects.

5.2.1.2 Clustering in α-Al_2O_3

Four types of neutral defect clusters, directly involving the oxygen sublattice, are of interest in Al_2O_3. The first is the association of a stoichiometric set of fully ionized vacancies (a Schottky quintuplet) into a neutral cluster (a Schottky Cluster). The rationale behind considering only the Schottky Cluster and not off stoichiometric clusters, is to give a defect which is independent of both impurity level and oxygen partial pressure (as will be seen) and that association will take place to minimize electrostatic

misfit.[2] The other imaginable neutral clusters of intrinsic defects are Frenkel pairs. The existence of these are rejected because the ion in such a bound pair must minimize its energy by relaxing back to the lattice side. For this to be untrue the crystal structure would be unstable.

The second type of cluster to be considered is two substitutional acceptor ions (divalent ions on aluminum sites) with an oxygen vacancy. The third type is two substitutional donor ions (tetravalent ions on aluminum sites) with an oxygen interstitial.

The fourth type of cluster is that of a substitutional donor with a substitutional acceptor.

Consider first, Schottky quintuplets and Schottky clusters. Schottky quintuplets are formed according to the reaction

$$\text{Null} \rightarrow 2\, V_{Al}''' + 3\, V_O^{\cdot\cdot} \qquad (5.2\text{-}17)$$

with a reaction constant which may be written

$$k_s = a_1^{\,2}\, a_2^{\,3} = \exp\left(\frac{-g_s}{RT}\right) \qquad (5.2\text{-}18)$$

where a_1 is the activity of V_{Al}''' and a_2 is the activity of $V_O^{\cdot\cdot}$. Activity of a species may be written as

$$a = \gamma c$$

---

[2] Charged clusters involving impurities have been proposed to exist in for example MgO[72], and one such cluster is $Cr_{Mg}^{\cdot} - O - V_{Mg}'$, however the author is unaware of the proposition of an off-stoichiometric cluster of intrinsic defects in an ionic material.

where c is the species concentration and γ is the activity coefficient. By assuming ideal solutions, $\gamma = 1$, concentrations may be substituted into equation (5.2-18);

$$k_s = [V_{Al}''']^2 \, [V_O^{\cdot\cdot}]^3 \, \exp\left(\frac{-g_s}{RT}\right) \tag{5.2-19}$$

The association of these defects by the reaction

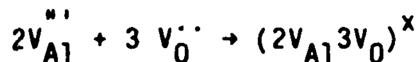

$$2V_{Al}''' + 3\,V_O^{\cdot\cdot} \rightarrow (2V_{Al}3V_O)^x$$

yields an association constant, k_a, which may be written

$$k_a = \frac{[(2V_{Al}3V_O)^x]}{[V_{Al}''']^2 \, [V_O^{\cdot\cdot}]^3} = m_s \exp\left(\frac{-g_a}{RT}\right) \tag{5.2-20}$$

where m_s is the multiplicty of configurations for Schottky Clusters. Solving for the cluster concentration yields

$$[(2V_{Al}3V_O)^x] = m_s \, [V_{Al}''']^2 \, [V_O^{\cdot\cdot}]^3 \exp\left(\frac{-g_a}{RT}\right) \tag{5.2-21}$$

This is of the form of equation (5.2-16), with $b_q = -g_a$. It can also be seen that the Schottky constant may be substituted for the free defect concentrations in equation (5.2-20). This implies

that, at constant pressure, the concentration of Schottky Clusters is uniquely determined by the temperature of the system, and is independent of concentration of impurities.

$$[(2V_{Al}3V_O)^x] = k_a k_s = m_s \exp\left(\frac{-g_a}{RT}\right) \exp\left(\frac{-g_s}{RT}\right) \qquad (5.2\text{-}22)$$

substituting for the g-functions gives

$$[(2V_{Al}3V_O)^x] = m_s \exp\left(\frac{s_a + s_s}{R}\right) \exp\left(\frac{-h_a - h_s}{RT}\right) \qquad (5.2\text{-}23)$$

Secondly, consider impurity defect clusters.

For the case of a foreign donor ion, Fd^{4+}, compensated by oxygen interstitials the incorporation reaction may be written

$$2\ FdO_2 \rightleftarrows 2\ Fd_{Al}^{\cdot} + O_i^{''} + 3O_O^x \qquad (5.2\text{-}24)$$

These defects may associate by the reaction

$$2\ Fd_{Al}^{\cdot} + O_i^{''} \rightleftarrows (2\ Fd_{Al}O_i)^x \qquad (5.2\text{-}25)$$

At this point two variables, α' and α may be defined, α' is the degree of association (the reaction proceeding to the right) and α

is the degree of dissociation (the reaction proceeding to the left). They are related by

$$\alpha' = 1 - \alpha$$

Under the simplified electroneutrality condition of

$$[Fd^{\cdot}] = 3[O_1''] \qquad (5.2\text{-}26)$$

(which is only rigorously true when there are no other charged species present, but becomes a good approximation when background charged species are of low relative concentration[3]) the concentrations of the species may be expressed as the product of the dopant level, $[FdO_2]$, and these variables;

$$[(2FdV_0)^x] = \frac{\alpha'}{3}[FdO_2] = \frac{(1-\alpha)}{3}[FdO_2] \qquad (5.2\text{-}27)$$

$$[Fd^{\cdot}_{Al}] = (1-\alpha')[FdO_2] = \alpha[FdO_2]$$

$$[O_1''] = \frac{(1-\alpha')}{3}[FdO_2] \quad = \frac{\alpha}{3}[FdO_2]$$

The association reaction constant may be expressed in terms of the degree of association as

$$k_a = \frac{\alpha'[FdO_2]}{(1-\alpha')^3\,[FdO_2]^3} = m_d \exp\left(\frac{-g_a}{RT}\right) \qquad (5.2\text{-}28)$$

---

[3]The question of when this is a valid approximation is dependent on the relative concentrations and also the power of the expression in which it is used. For example, if the donor under consideration makes up 90 percent of all those present, the 10 percent error of this assumption is magnified to 27 percent when this term is cubed.

The degree of association may be directly obtained for any values of k_a and $[FdO_2]$ from;

$$\frac{\alpha'}{(1 - \alpha')^3} = k_a \, [FdO_2]^2 \qquad (5.2\text{-}29)$$

and the concentrations of the various species determined. In the limiting cases of nearly no association and nearly total association defect concentration may be directly obtained. In the limiting case of the degree of association is small

$$(1 - \alpha')^3 \simeq 1 \qquad (5.2\text{-}30)$$

and solving for the concentration of clusters obtains

$$[(2\ FdV_O)^x] = 3\ [FdO_2]^3\ m_d \exp\left(\frac{-g_a}{RT}\right) \qquad (5.2\text{-}31)$$

It can be seen that there is a very strong dependence, third power, on the dopant concentration.

For the other limiting case it is more convenient to use the degree of dissociation. The reaction constant then becomes

$$k_a = \frac{(1 - \alpha)\ [FdO_2]}{\alpha^3\ [FdO_2]^3} = m_d \exp\left(\frac{-g_a}{RT}\right) \qquad (5.2\text{-}32)$$

In this case the degree of association is very large, therefore the degree of dissociation is small and

$$(1 - \alpha) \simeq 1$$

solving for the concentration of free oxygen interstitials obtains

$$[O_i^{\cdot\cdot}] = ([FdO_2]/m_d)^{1/3} \exp\left(\frac{+g_a}{3RT}\right) \qquad (5.2\text{-}33)$$

In the case of a large association constant the concentration of unassociated points defects depend on dopant concentration only to the 1/3 power, and the temperature dependence of the exponent has been redued by a factor of three, as compared to the unassociated case.

For a foreign acceptor, Fa, compensated by oxygen vacancies, the incorporation reaction becomes

$$2\ FaO \rightleftarrows 2\ Fa_{Al}' + V_O^{\cdot\cdot} + 2O_O^x \qquad (5.2\text{-}34)$$

The association reaction becomes

$$2\ Fa_{Al}' + V_O^{\cdot\cdot} \rightleftarrows (2Fa_{Al}\ V_O)^x \qquad (5.2\text{-}35)$$

with the electroneutrality condition

$$[Fa_{Al}'] = 3\ [V_O^{\cdot\cdot}] \qquad (5.2\text{-}36)$$

A set of equation analogous to these derived for the donor case may be obtained, for the case of very weak association the cluster concentration is given by

$$[(2\ FaV_O)^x] = 3[FaO]^3\ m_a\ \exp\left(\frac{-g_a}{RT}\right) \qquad (5.2\text{-}37)$$

and for the case of very strong association the vacancy concentration is given by

$$[V_O^{\cdot\cdot}] = ([FaO]/m_a)^{1/3}\ \exp\left(\frac{+g_a}{3RT}\right) \qquad (5.2\text{-}38)$$

Finally, consider donor acceptor clustering. In the above the assumption was made that the crystal was singly doped with either a

donor or acceptor. It is quite possible for both to be present. In this case the free oxygen vacancies and interstitials which are produced are related through the Anion Frenkel product.

$$O_O^x \rightleftarrows O_i'' + V_O^{\cdot\cdot} \qquad (5.2\text{-}39)$$

$$k_F = [O_i''] \, [V_O^{\cdot\cdot}] = \exp\left(\frac{-g_F}{RT}\right) \qquad (5.2\text{-}40)$$

The impurity-defect clusters can react to form donor-acceptor clusters according to

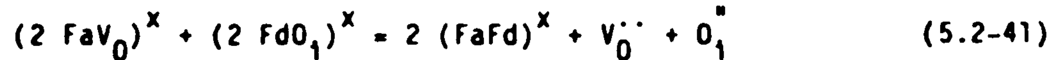

$$(2 \, FaV_O)^x + (2 \, FdO_i)^x = 2 \, (FaFd)^x + V_O^{\cdot\cdot} + O_i'' \qquad (5.2\text{-}41)$$

with a reaction constant

$$k_{da} = \frac{[(FaFd)^x]^2 \, [V_O^{\cdot\cdot}][O_i'']}{[(2 \, FaV_O)^x] \, [(2 \, FdO_i)]} = m_{da} \exp\left(\frac{-g_{da}}{RT}\right) \qquad (5.2\text{-}42)$$

The g_{da} includes the dissociation energies of the impurity-defect clusters as well as the association energy of the donor-acceptor cluster. The free defect concentrations may be replaced by the Frenkel constant reducing the energy penalty for reaction

$$k_{da} = \frac{[(FaFd)^x]^2}{[(2FaV_O)^x] \, [(2FdO_i)]} = m_{da} \exp\left(\frac{-(g_{da} - g_F)}{RT}\right) \qquad (5.2\text{-}43)$$

In order to predict the outcome of doping the g-functions of all of the above reactions, and the multiplicities of configurations for the clusters, must be known. If the g-functions are very small, so that k_a is very small, clusters can be minority species and the point defect equilibria may be dealt with using the notions of

Schottky and Frenkel disorder. This is a special case, however, and recent calculations along with some experimental evidence (which are discussed in a following section) indicate that the g-functions of at least some clusters are substantial, to the extent that clusters may be significant, perhaps dominant, contributors to diffusion.

Prior to carrying out calculations of defect equilibria it is of benefit to assess the sign and magnitude of individual terms. Consider first the geometry of clusters. The structure of α-Al_2O_3 consists of a very nearly hexagonal close packed oxygen sublattice with two thirds of the octahedral sites occupied with an aluminum ion. Each aluminum has sixfold coordination as illustrated in figure 109. The α-Al_2O_3 structure may be thought of as being made up of occupied and unoccupied octahedra. The packing sequence, which maximizes the average Al-Al distance, is shown in figure 110 and a stereographic pair of the occupied octahedra is shown in figure 111. It can be seen that each occupied octahedron shares a face with one other occupied octahedron, shares an edge with three other occupied octahedron, and shares a corner with nine other occupied octahedra. In figure 110, E shares a face with A, an edge with F, G, and H, and a corner with B, C, D, I, J, K, L, M, and N.

The true structure of Al_2O_3 differs from this idealized structure in two ways,[72] both of which arise from the fact that only two thirds of the octahedra are occupied. First, the octahedra are not regular. The edges of the faces shared between occupied octahedra are shorter than those of the unshared faces. This is due to the component of the Al-O bond along the edges being twice as great in

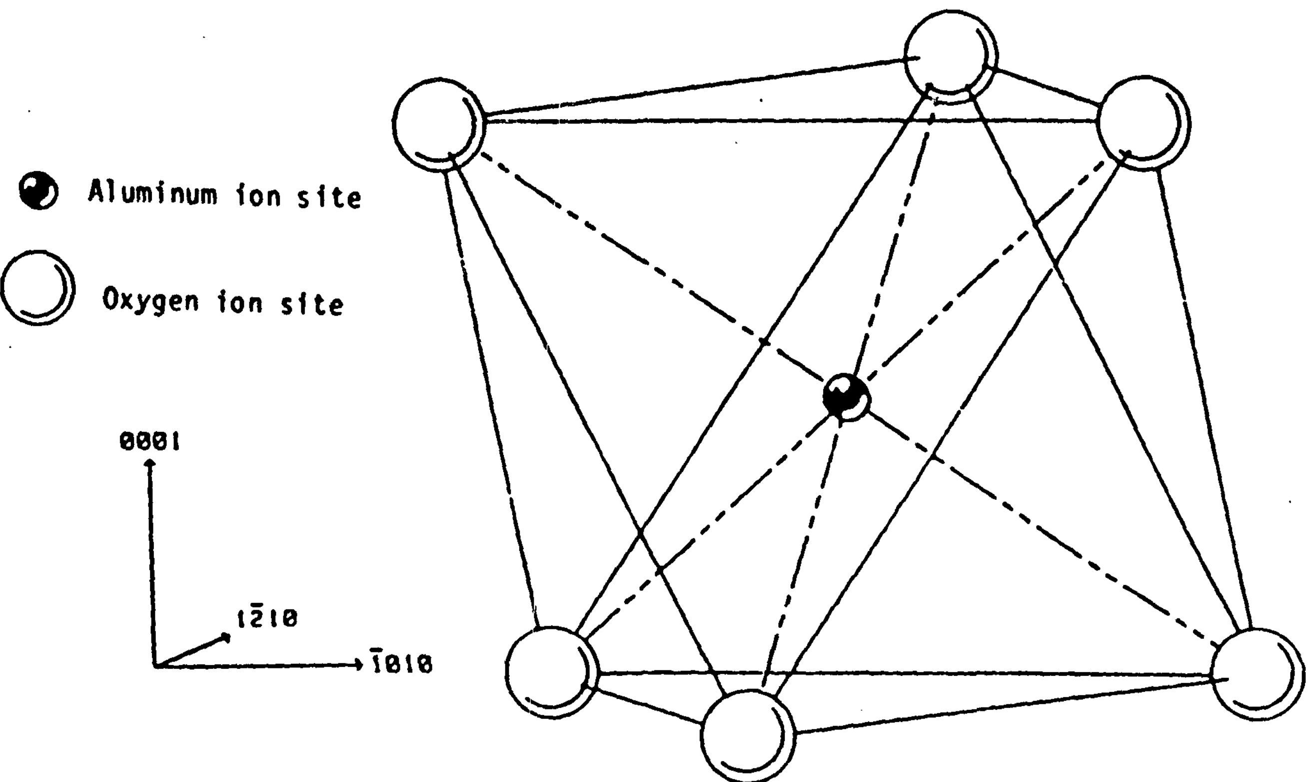

Figure 109. - Illustration of an oxygen octahedron containing a sixfold coordinated aluminum ion.

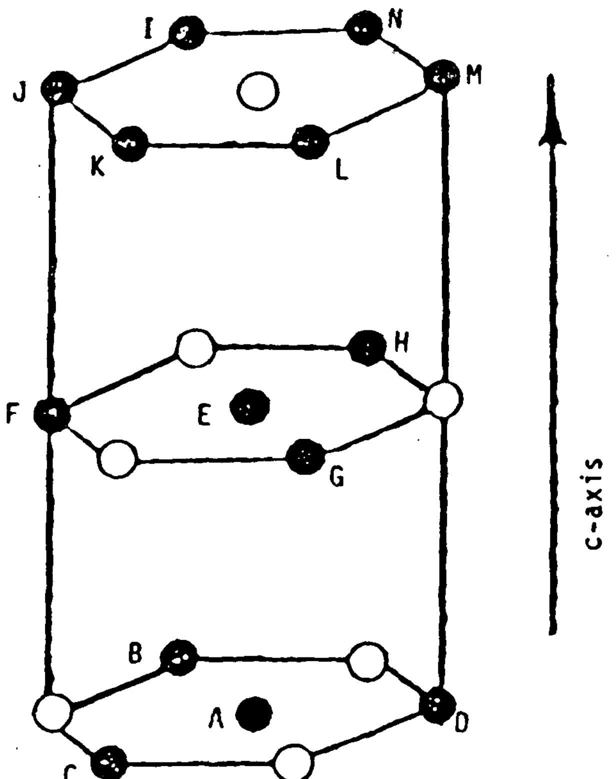

Figure 110. - Schematic of the packing sequence in Al_2O_3. The circles correspond to the octahedral sites, with the filled circles corresponding to those occupied by aluminum ions.

Right eye image

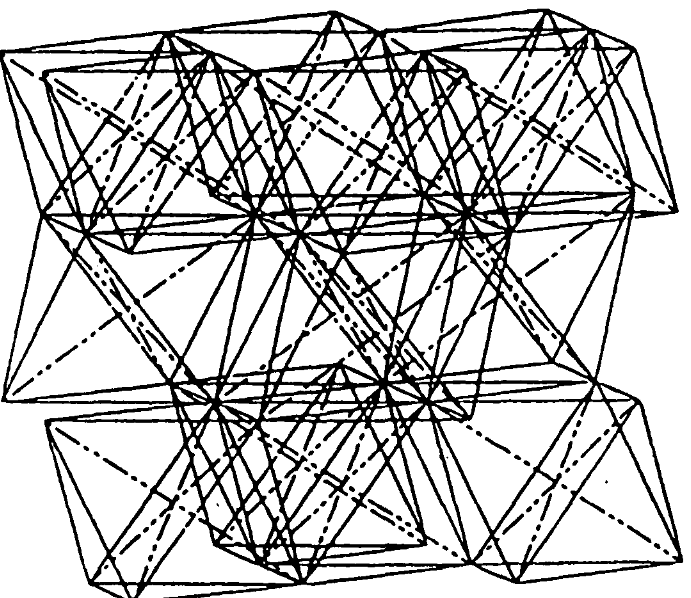

Left eye image

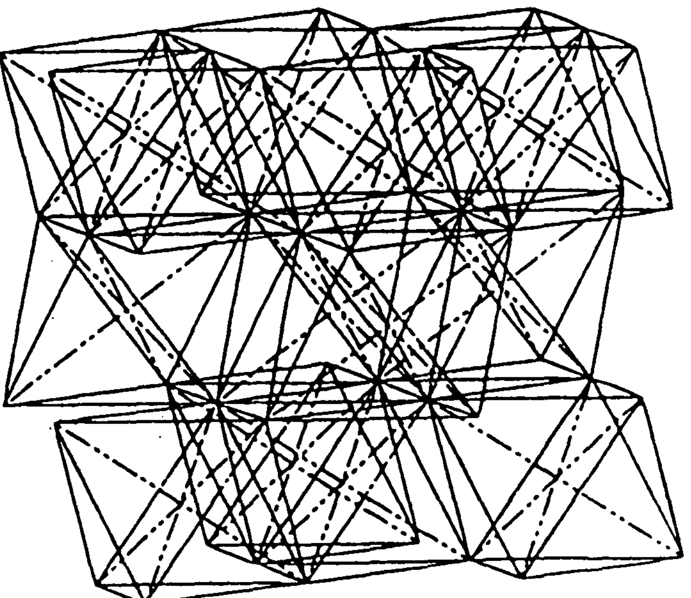

Figure 111. - Stereo pair of the packing of occupied octahedra in the idealized Al_2O_3 structure. Place binding away from viewer when viewing with crossed eyes and place binding toward viewer when using a stereographic viewer.

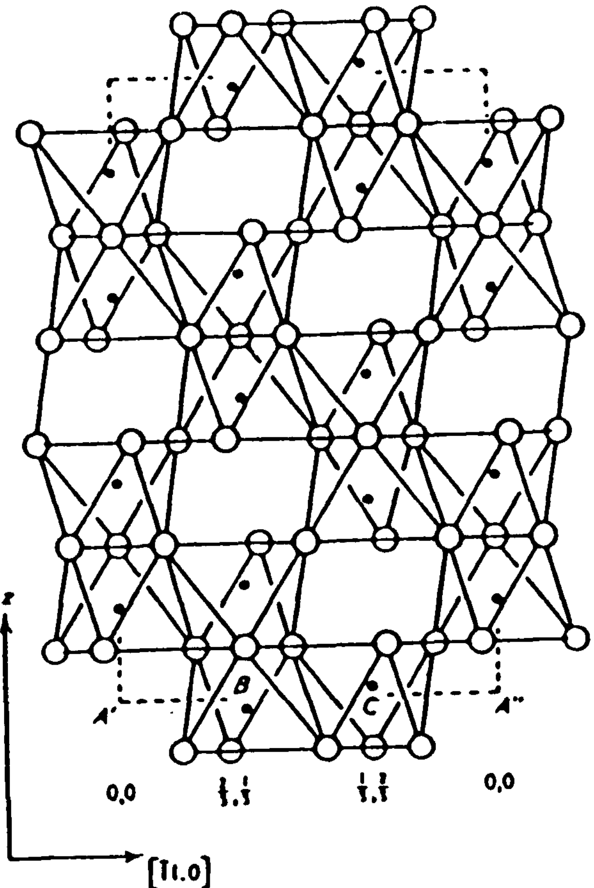

Figure 112. - Al_2O_3: projection on $(11\bar{2}0)$ of part of structure one octahedron thick (drawn with u = -0.083, w_{Al} = 0.017). Small black circles are Al in plane x + y = 1; heavy and light open circles are O lying in front of and behind this plane, as viewed from the lower right-hand corner of Fig. 11-5(b). Corners of the unit cell are indicated by broken lines, from Ref. 73.

the shared face.[72] Secondly, the cation-cation repulsion causes the aluminums to be displaced from the octahedra centers, toward the unshared face, figure 112. Note that these two relaxations of the structure have opposite effects on the Al-O bond distance. The displacement of the aluminums has the slightly greater effect and the Al-O bond is 2.5 percent shorter in the unshared face (1.89 Å) than in the shared face (1.95 Å). Bond strength is related to bond distance, however based on the fact that due to unknowns, this discussion will be forced to neglect larger dimension variations, and relaxations of defect clusters will not be taken into account; the idealized structure will be employed.

If the only constraint on cluster configurations is that it consists of an unbroken string of nearest neighbors then the Schottky Cluster could involve as many as four octahedra, see figure 113. However it seems reasonable, though arbitrary, to employ the following two rules for vacancy type clusters:

Rule 1.: The clusters involve two octahedra. It is not possible to use less than two since there is only one aluminum site per octahedra, however all clusters may be obtained using only two. Beyond avoiding the inconvenience of dealing with the large number of configurations possible when three or more octahedra are involved, this effectively minimizes the cluster equivalent diameter, and hence maximizes the local defect density, which is the driving force for the association process. Damask and Dienes[75] make a similar argument for maximizing nearest neighbors during the formation of Di- and Tri- vacancies in metal. They justify this by noting that

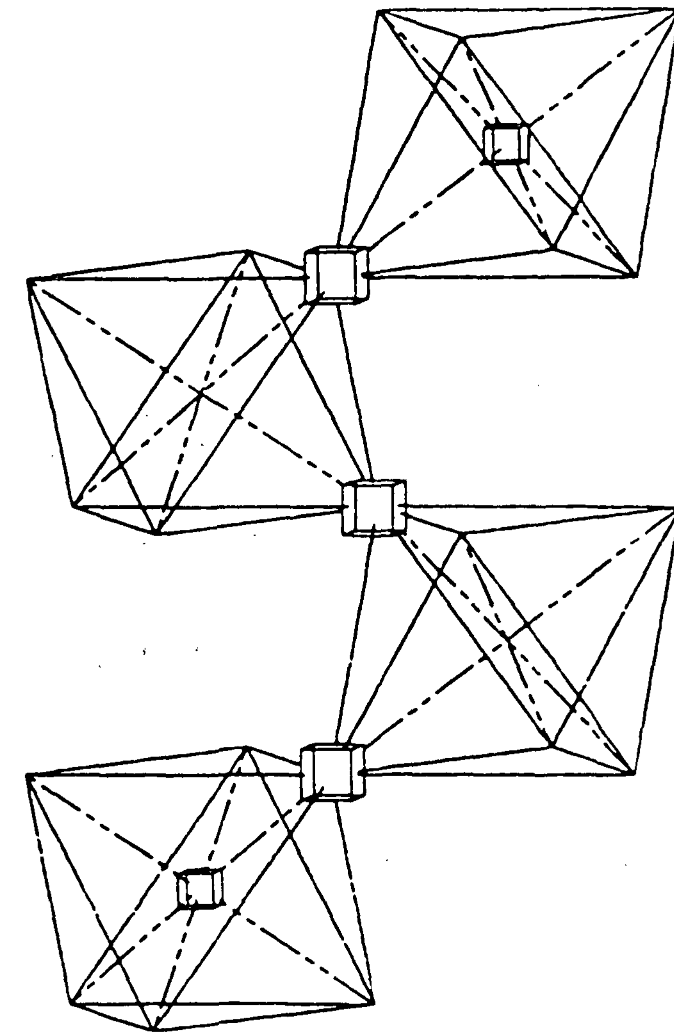

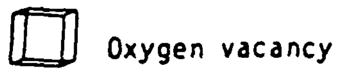

Figure 113. - Illustration of a Schottky Cluster which involves four octahedra.

the number of broken bonds is diminished when vacancies become nearest neighbors.

Rule 2.: The coordination of the defects, by oppositely charged defects be maximized, in order to achieve local neutrality. In vacancy clusters this effectively requires that the shared oxygen sites be occupied at the expense of the nonshared.

Using these rules and neglecting relaxation there are three types of Schottky clusters. The first is between face sharing octahedra, figure 114, in which the cation-cation site distance is a minimum (0.8165 times the anion-anion site distance) and the defect coordination numbers are maximized (each V_{Al} has three nn V_O and each V_O has two nn V_{Al}). The multiplicity of configurations in this case (distinct orientations over occupied sites[4]) is 1/5 since the location of all five vacancies is fixed by Rule 2. The second type of cluster is between two edge sharing octahedra, figure 115. In this the cation-cation distance is longer (equal to the anion-anion distance) and the coordination numbers are lower (average V_{Al} has 2.5 nn V_O and average V_O has 5/3 nn V_{Al}). The multiplicity of configuration is 8/5 since the nonshared oxygen vacancy may be at any of the eight nonoccupied sites without changing the average coordination numbers. The third type, between corner sharing

---

[4]The multiplicity of configurations given here is per octahedra pair, the total multiplicity is this number multiplied be the number of distinct octahedra pairs of each type which will be termed the octahdra coordination number. Refering to figure 110, it can be seen that this is equal to one for the face sharing, three for the edge sharing and nine for the corner sharing configurations.

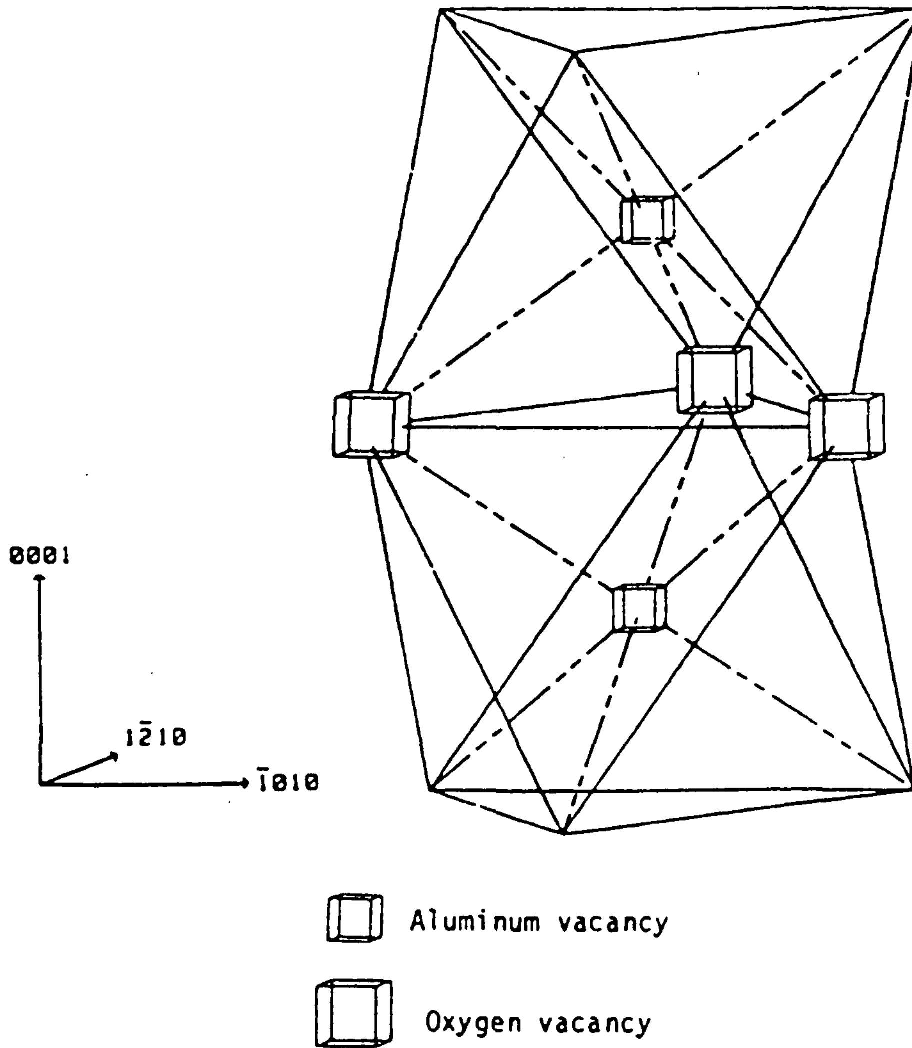

Figure 114. - Illustration of a Schottky Cluster involving two face sharing octahedra. The location of all the vacancies is fixed.

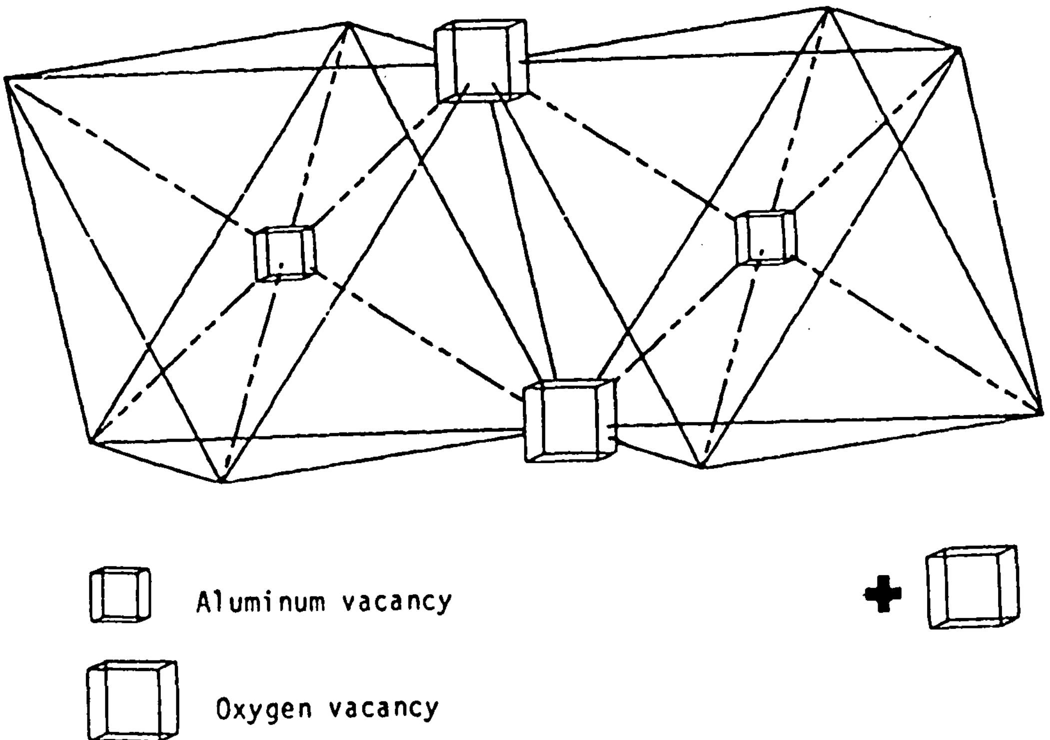

Figure 115. - Illustration of a Schottky Cluster involving two edge sharing octahedra. One oxygen vacancy has an unspecified location and may be located on any of the remaining eight unoccupied oxygen sites.

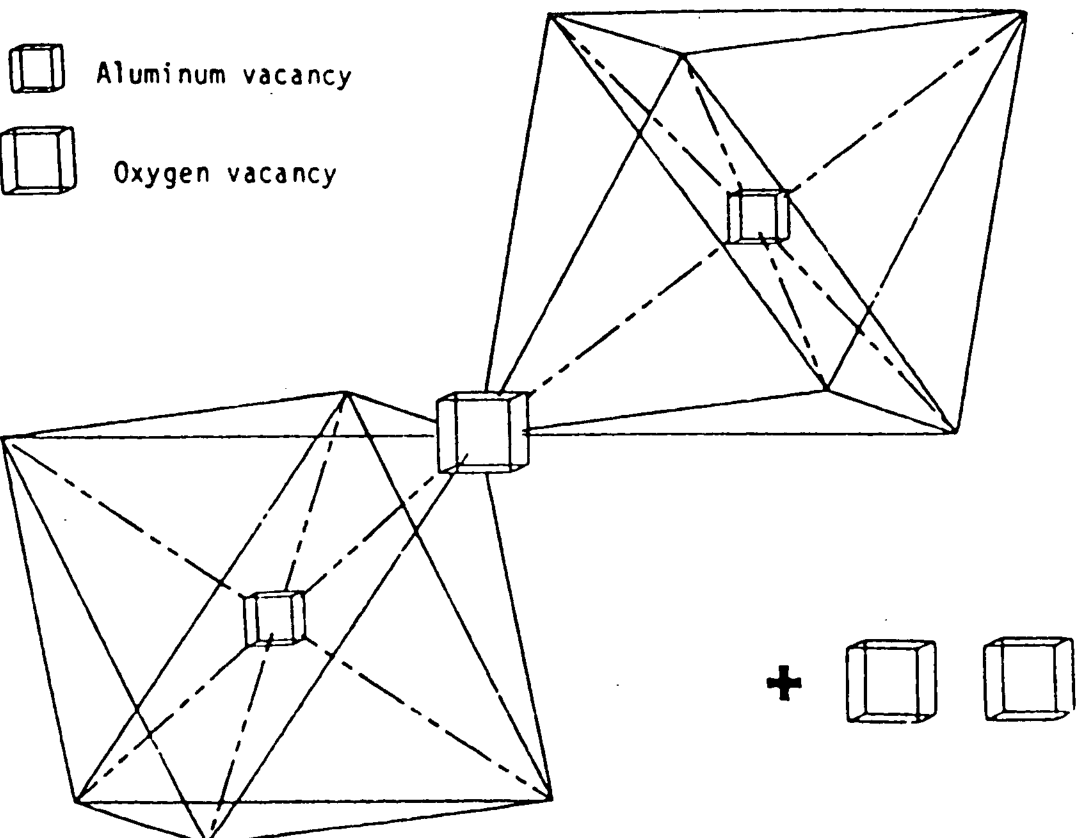

Figure 116. - Illustration of a Schottky Cluster involving two corner sharing octahedra. Two oxygen vacancies have unspecified locations and may be located on any of the ten remaining unoccupied oxygen sites.

octahedra (fig. 116), has a still larger cation-cation distance(1.3478 times the anion-anion distance) and still lower coordination numbers (average V_{Al} has 2 nn V_0 and average V_0 has 2/3 nn V_0). The multiplicity of configurations is 90/5 since the nonshared oxygen vacancies have ten equivalent sites to choose from. The differences in interdefect spacing and coordination numbers indicates that the energy of the cluster will vary with type.

The decrease in coordination of the corner sharing configuration over the face, or edge, sharing which suggests higher energy may tend be offset by the increase in the distance between the cation vacancies.

Since it is not a simple calculation to obtain the net differences, the clusters will be assumed to have the same probability of existing, in order to calculate a multiplicity of configurations. When this is true there are 835 Shottky clusters which will involve any given lattice site which gives a total multiplicity of configurations equal to 47. This enters into the preexponential of equation A1 as a positive term tending to increase the degree of association into Schottky Clusters.

For the case of a foreign acceptor cluster, Fa-V_0-Fa, there are also three types. The cation-cation distances are the same as the Schottky Clusters and in all cases the defect coordination numbers are the same (each Fd has 1/2 nn V_0 and each V_0 has 2 nn Fd). For this cluster the multiplicity of configurations is equal to the number of shared vacancy sites. For face sharing (fig. 117) m_a = 3/3,

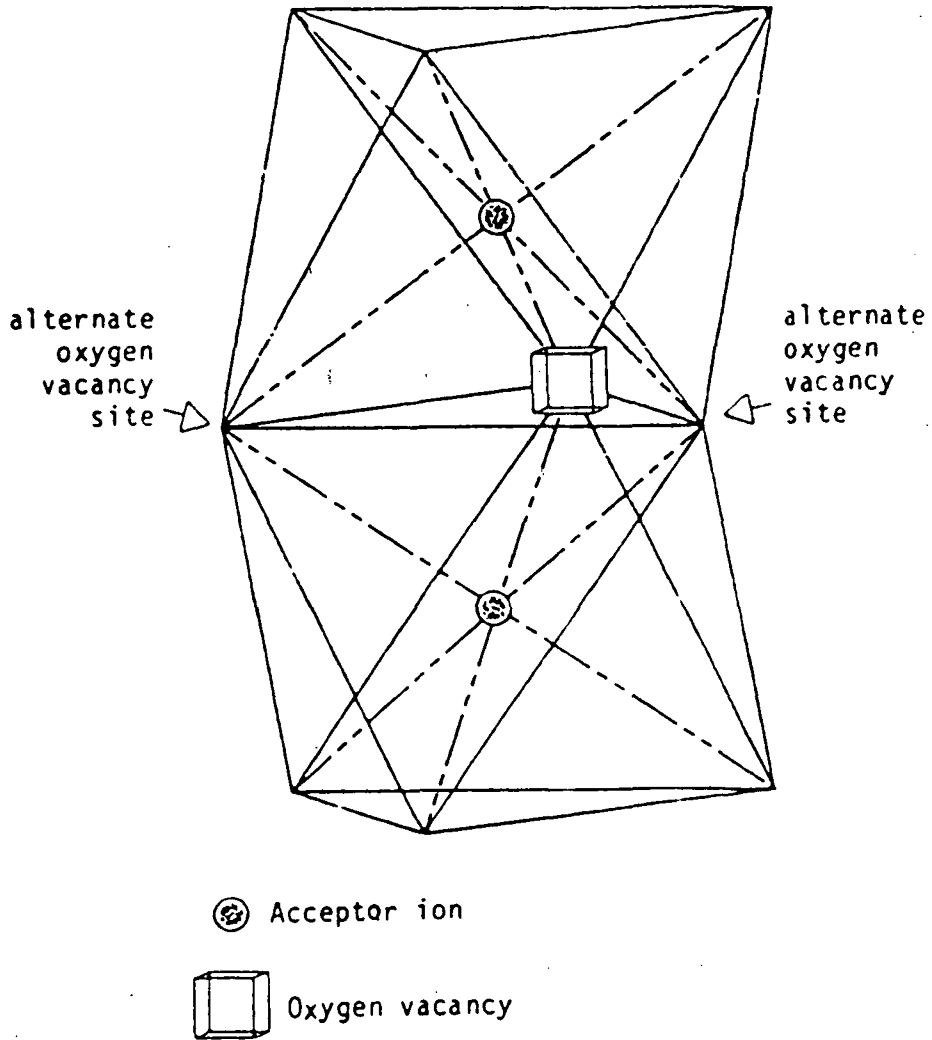

Figure 117. - Illustration of a cluster of two substitutional Acceptor impurities and an oxygen vacancy, involving two face sharing octahedra.

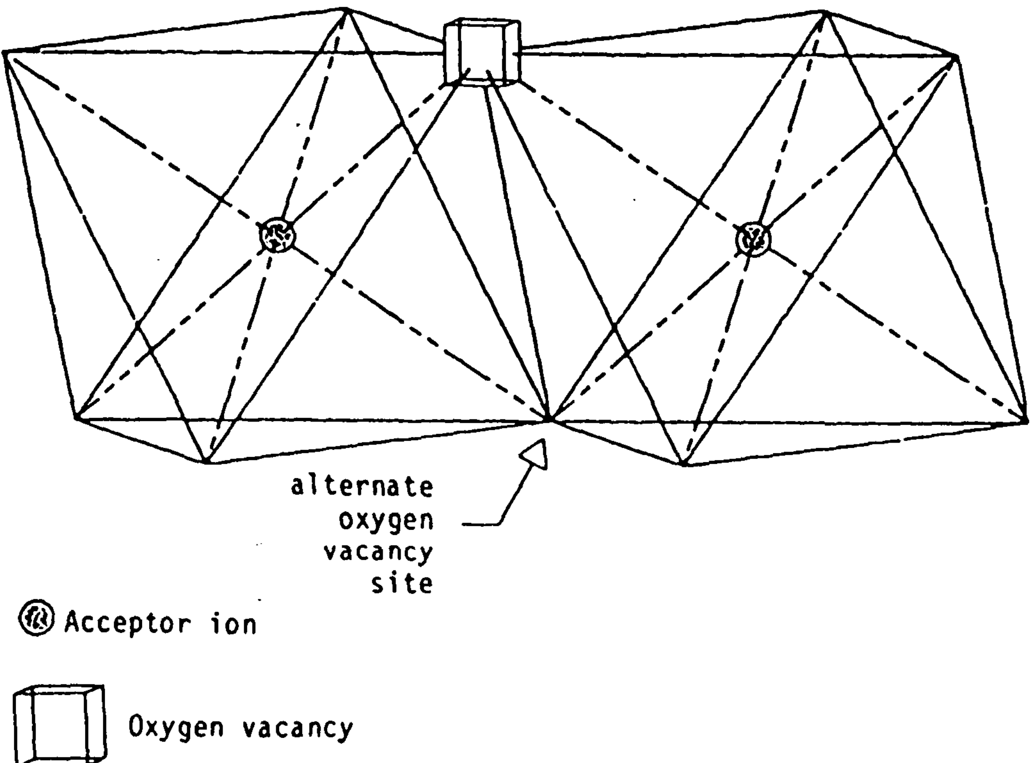

Figure 118. - Illustration of a cluster of two substitutional Acceptor impurities and an oxygen vacancy, involving two edge sharing octahedra.

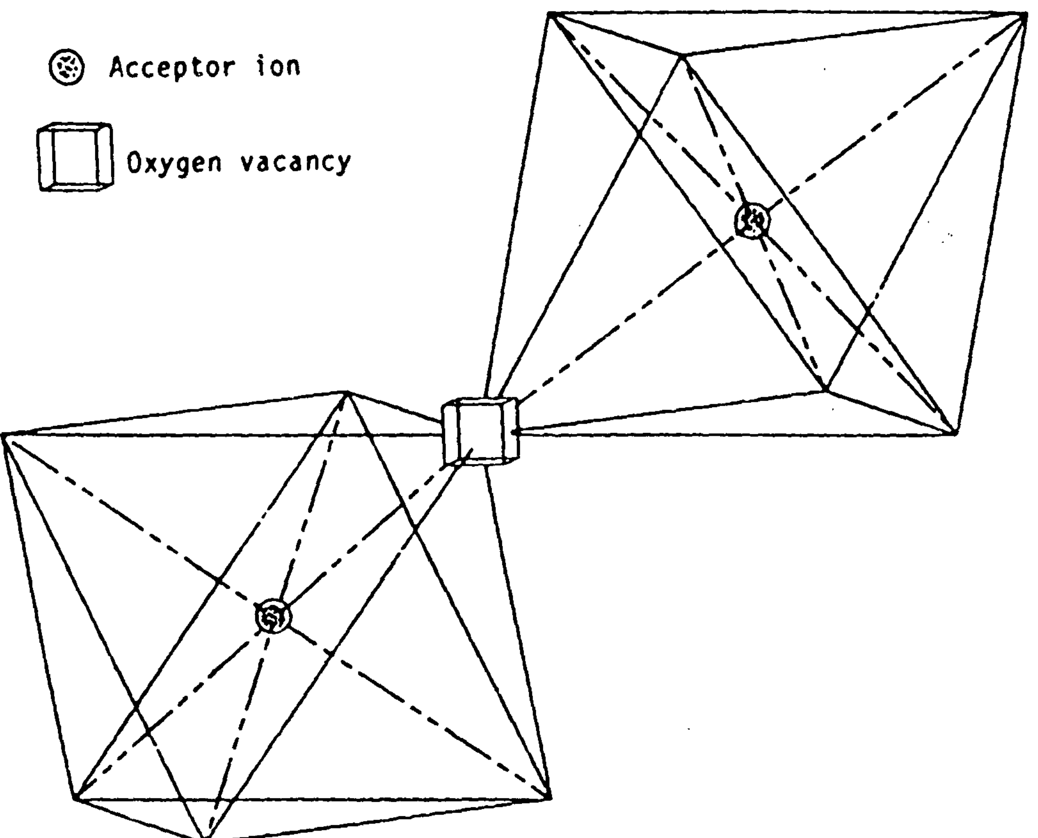

Figure 119. - Illustration of a cluster of two substitutional Acceptor impurities and an oxygen vacancy, involving two corner sharing octahedra.

for edge sharing (fig. 118) m_a = 2/3, and for corner sharing (fig. 119) m_a = 1/3. The total number of Fa-V_O-Fa clusters involving agiven lattice site is 15 which gives a total multiplicity of 5. This will enter the preexponential of equation 5.2-37 favoring association ciation of Fa-V_O-Fa clusters. The case of foreign donor clusters, Fd-O_i-Fd, is more involved, and some additional freedom will be allowed. If a di-interstitial forms and occupies an oxygen lattice site, $O_{2_O}^{''}$, the geometry is perfectly analogous to that of the acceptor cluster. If the oxygen is interstitial in the classic sense the geometry is dependent on the allowed interstitial sites. Three types of oxygen interstitial sites will be considered, a triangle, a tetrahedron, and an octahedron. In the case of two face sharing octahedra there is a triangular site, in the shared face, that is the only nearest neighbor cluster involving an oxygen interstitial, (by nearest neighbor it is meant that the Fd-O_i bond distance is less than, or equal to, the Al-O bond distance in αAl_2O_3). This is shown in figure 120. The cation-cation distance is 0.8165 and the defect coordination numbers are the same as the Fd-V_O-Fd clusters. The size misfit for interstitial is large (ideal radius ratio for triangular site is $\geq$ 0.155, and is in this case = 1), while the donor-interstitial distance is minimized, 0.4032. It has been pointed out by Gourdin and Kingery[71] that radius ratios in ionic materials may be misleading.

There are six tetragonal sites around each octahedral site. If these are availed to the interstitial a number of possibilities occur. In the case of face sharing octahedra the oxygen interstitial may

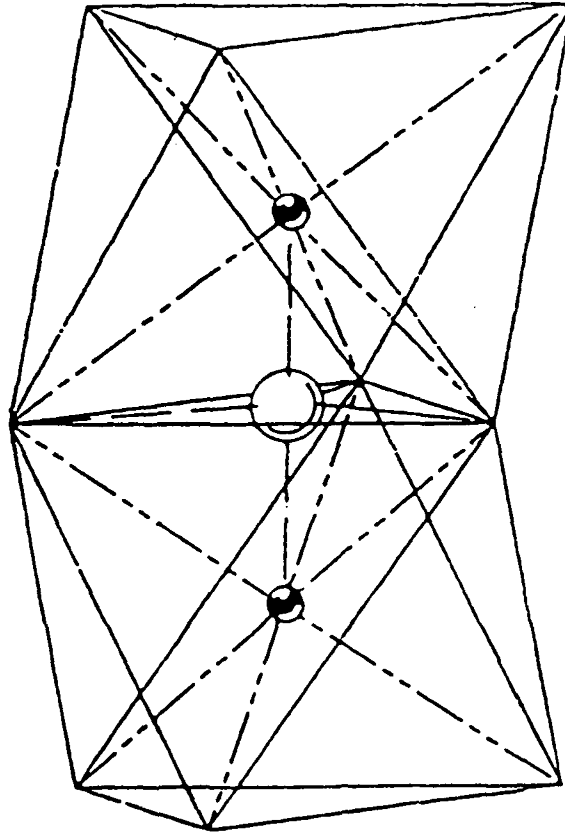

Donor ion

Interstitial oxygen ion

Figure 120. - Illustration of a cluster of two donor impurities and an oxygen interstitial, involving two face sharing octahedra with the triangular site occupied.

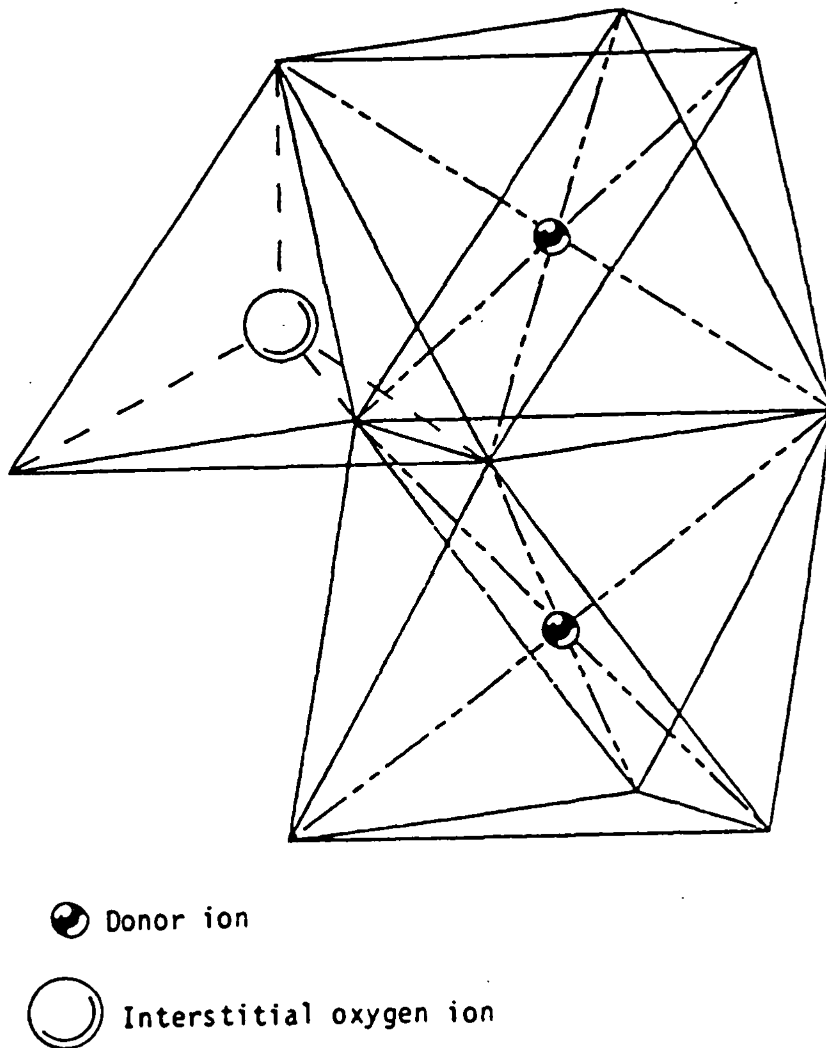

Figure 121. - Illustration of a cluster of two donor impurities and an oxygen interstitial, involving two face sharing octahedra and a tetrahedron. There are twelve equivalent tetrahedra in this configuration.

equivalently occupy any one of the twelve total tetrahedra, figure 121. In this face sharing configuration, however, the distance between the positive and negative defect increases (from 0.4082 to 0.5774) and the interstitial is a nearest neighbor to only one of thedonors, the coordination numbers are cut in half. This suggests a higher energy cluster though to what degree is unknown.

In the octahedra edge sharing configuration, with tetrahedral occupancy, figure 122, the coordination numbers are restored (each Fd_{Al} has 1 nn O_i and each O_i has 2 nn Fd_{Al}). The cation-cation distance is increased and the radial misfit is smaller (ideal radius ratio for tetrahedron is $\geq$ 0.225), compared to the face sharing, triangular occupancy, configuration. However, the Fd-O_i distance, 0.5774 is longer. The interstitial may occupy either of two equivalent tetrahedra.

In the octahedral corner sharing configuration, with tetrahedral occupancy (fig. 123), the oxygen interstitial, like face sharing, can only be a nearest neighbor to one of the donors. To retain a next nearest neighbor relation with the other donor there are four equivalent tetrahedra.

Since only two thirds of the octahedral sites are occupied with aluminum ions, one third remains available to the oxygen interstitials. This cluster has the least radial misfit (ideal radius ratio $\geq$ 0.414 for octahedral site) but involves three octahedra and the distance between oppositely charged defects is maximized. If only linear clusters are allowed (in order to maximize the Fd-Fd distance) then, referring back to figure 110, each lattice site involves one

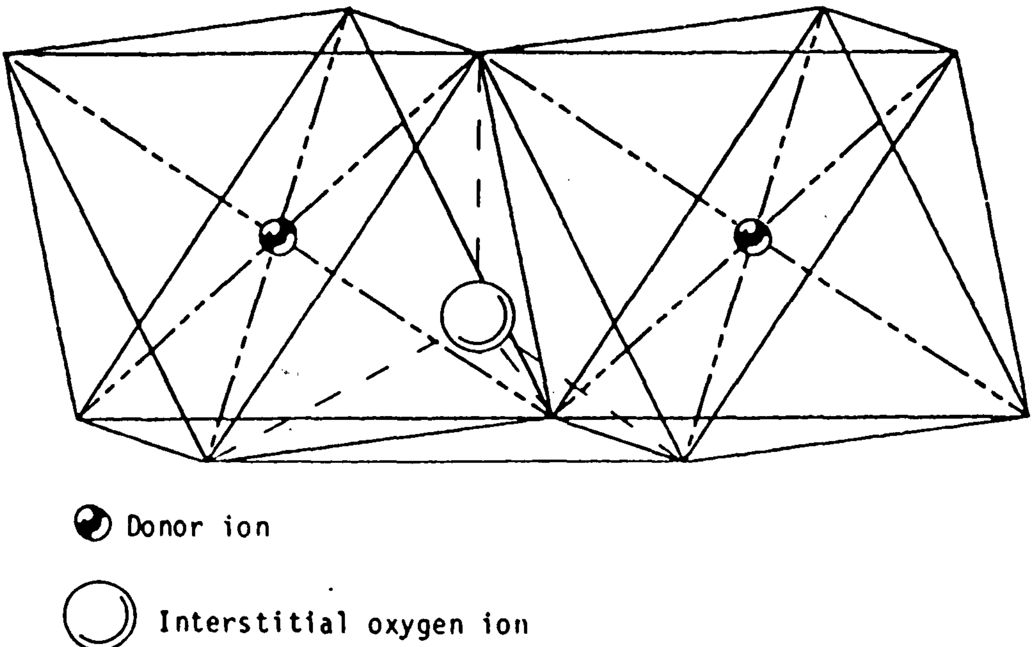

Figure 122. - Illustration of a cluster of two donor impurities and an oxygen interstitial, involving two edge sharing octahedra and a tetrahedron. There are two equivalent tetrahedra in this configuration.

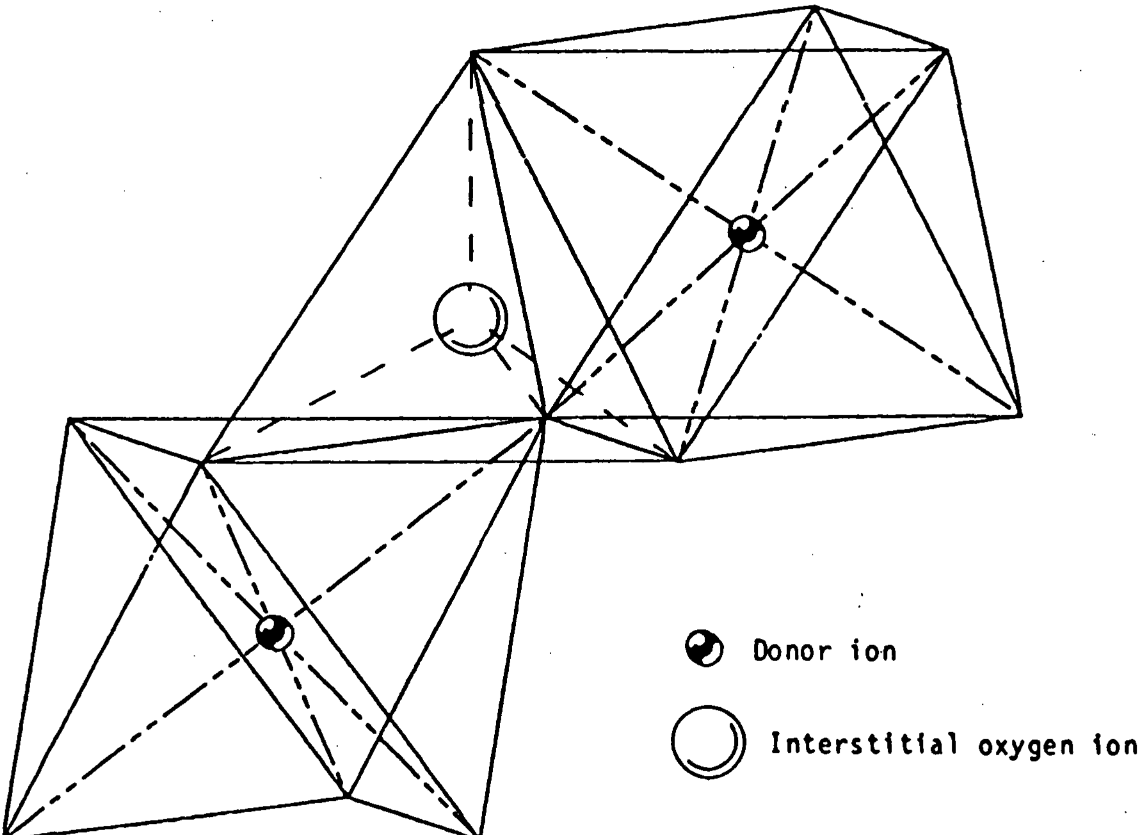

Figure 124. - Illustration of a cluster of two donor impurities and an oxygen interstitial, involving three face sharing octahedra.

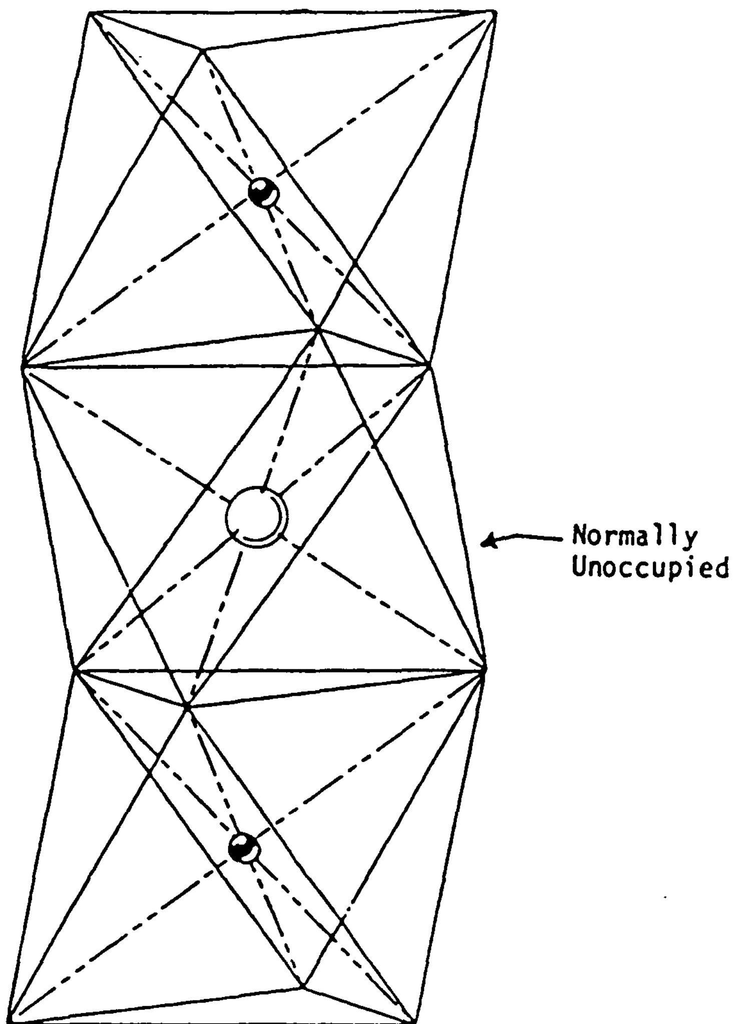

Donor ion

Interstitial oxygen ion

Figure 124. - Illustration of a cluster of two donor impurities and an oxygen interstitial, involving three face sharing octahedra.

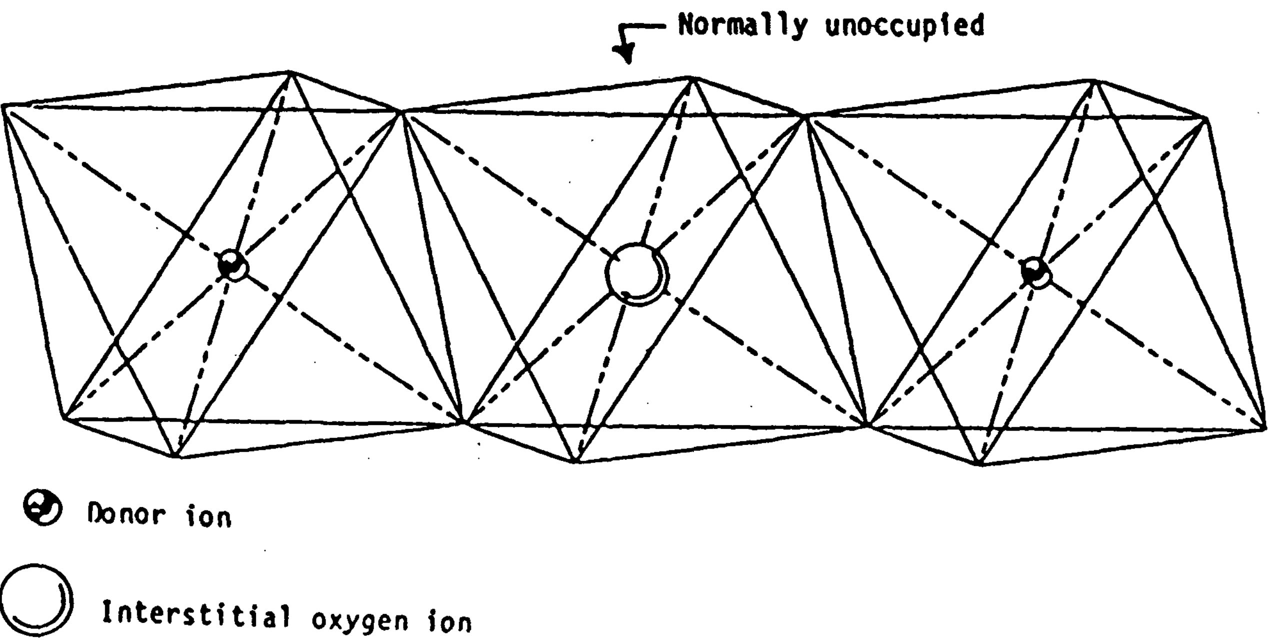

Figure 125. - Illustration of a cluster of two donor impurities and an oxygen interstitial, involving three edge sharing octahedra.

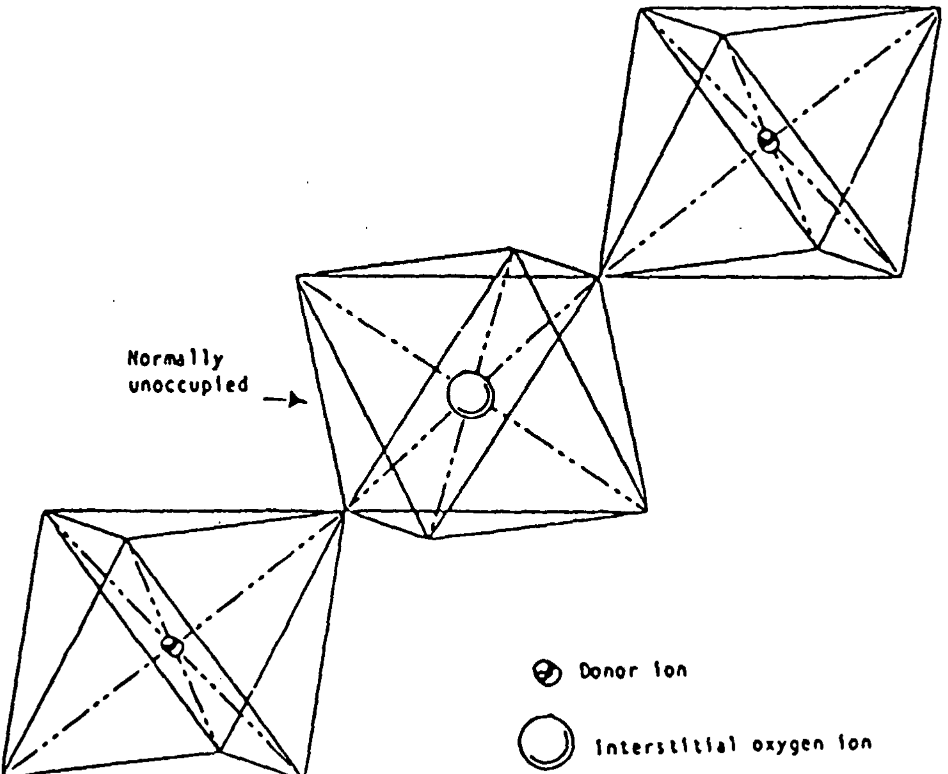

Figure 126. - Illustration of a cluster of two donor impurities and an oxygen interstitial, involving three corner sharing octahedra with the normally unoccupied octahedral site filled.

face sharing configuration along the c-axis (fig. 124), six edge sharing configurations in the basal plane (fig. 125), and three corner sharing configurations along < 1011 > (fig. 126).

Thus, with three types of interstitial sites allowed, there are 68 clusters which will occupy any given Al site giving a multiplicity of configurations of 34. If the highly asymmetric clusters, with tetraganal interstitials, are unstable the multiplicity drops to 10. As with the other two clusters this will enter the pre-exponential to favor clustering.

Donor-acceptor clusters have thirteen total configurations, the number of octahedra in contact, and therefore a multiplicity of configurations equal to 1/2 for each octahedra pair

These results are summarized in table 9.

Consider now, the change in entropy on clustering. The partial excess entropy term differs for the two types of clusters. In the Schottky cluster case it contains a formation entropy and an association entropy term while the $Ti-O_i-Ti$ cluster contains only an association entropy term. In both cases, however, any change in entropy arising from the association process will result in a change in cluster concentration.

The partial excess energy term arises from local electronic, vibrational, and elastic changes arising the defects. It is assumed that all the electrons are in the ground state and the electronic contributions will be ignored. Flynn points out that significant electronic changes occur in materials such as transition metals.

The vibrational contribution may be written as

TABLE 9. – UNRELAXED CLUSTER PARAMETERS

Cluster	Type (shared feature)	Octahedra* coordination number	Multiplicity** of configuration per octahedra	Cation-cation distance	Ave V_{Al} coord	Ave V_O coord	Distance between nn + ve defect and -ve defect
Schottky	Face	1	1/5	0.8165	3	2	0.7071
	Edge	3	8/5	1.000	2.5	5/5	0.7071
	Corner	9	90/5	1.3478	2	2/3	0.7071
					Ave Fa_{Al} Coord	Ave O_i Coord	
FaV_OFa	Face	1	1/3	0.8165		2	0.7071
	Edge	3	2/3	1.000	1	2	0.7071
	Corner	9	1/3	1.3478	1	2	0.7071
					Ave Fd_{Al} Coord	Ave V_O Coord	
FdO_iFd	Face (Tri)	1	1/2	0.8165	1	2	0.4082
	2-Oct face (Tet)	1	12/1	0.8165	1/2***	1***	0.5774
	Edge (Tet)	3	2/2	1.0000	1	2	0.5774
	Corner (Tet)	9	4/2	1.3478	1/2	1	0.5774
	3-Oct Face (Oct)	1	1/2††	1.6330	1***	2***	0.8165
	Edge (Oct)	3	1/2	2.0000	1	2	1.0000
	Corner (Oct)	9	1/2	2.6556	1	2	1.4141
					Ave Fd_{Al} Coord	Ave Fa_{Al} Coord	
FdFa	Face	1	1/2	0.8165	1	1	0.8165
	Edge	3	1/2	1.0000	1	1	1.0000
	Corner	9	1/2	1.3478	1	1	1.3478

*Octahedra coordination number is equal to the number of distinct octahedra pairs associated with any given lattice point.

**Multiplicity of configurations is equal to the number of distinguishable configurations, within the octahedra, divided by the number of occupied sites. The total multiplicity of configurations per cluster type is equal to the multiplicity of configurations per octahedra multiplied by the octahedra coordination number.

***Note that there are oxygen sites between the cations and interstitials in these clusters.

†Normalized to the length of an edge on an octahedron, which is equal to the oxygen-oxygen distance in the idealized structure.

††Allowing only linear configurations.

$$S_v = - \frac{\partial q}{\partial T_p} = - k_b \sum \ln \left(\frac{w'_\alpha}{w_\alpha}\right) \qquad (5.2\text{-}44)$$

where ω_α refers to the phonon frequencies for the perfect crystal and ω'_α refers to the phonon frequencies after the introduction of defects. Stripp and Howard (quoted in ref. 71) find for an FCC lattice a value of $S_v = 1.74k_b$ for a vacancy however they also found an association $S_v = -0.24k_b$ when a divacancy forms. Mahanty, Maradudin, and Weiss (quoted in ref. 71) found that divacancy formation in a simple cubic lattice also has a negative S_v.

The elastic contributions consist of a strain term, S_s,

$$S_s = - 8\pi r^3 \eta^2 \frac{\partial \mu}{\partial T} \qquad (5.2\text{-}45)$$

where

η is the strain

μ is the shear modulus

r is the distance at which ηr is established

and a dilation term, S_d

$$S_d = \frac{16\pi}{3} r^3 \eta \alpha \mu \qquad (5.2\text{-}46)$$

α is thermal expansion coefficient.

These terms are both positive for vacancy formation in alkali halides[71] because the neighboring atoms relax outwards. The effect on these terms of associating the free defects into clusters is not known. However, the results of Pederson[74], on an FCC Lennard-Jones system shows that the formation entropy (which is the sum of all

three terms) of two free vacancies, $3.44k_b$, is greater than that of a divacancy, $3.18k_b$ and the formation entropy of three vacancies, 5.16, is greater than any of the trivacancy configurations examined, 4.65 to 4.73.

In summary it appears that the preexponentials, in the defect concentration equations, contain terms of opposite sign. Defect association to clusters increases the multiplicity while decreasing the entropy. The net change for Schottky clusters may be positive or negative when the values for Al_2O_3 are employed, indications are that it will be positive, but in either case it appears to be small. The product for the impurity defect clusters will, also, vary from 1 by only a small amount.

Due to the uncertainty of their value, and its temperature independence, the preexponentials, for all reactions, will be assigned unity. This is felt to give a lower limit on cluster concentration.

The partial excess enthalpy, at constant pressure, is equal to the change in internal energy of the system provided the system plus a pV term. In condensed systems the pV term is small and may be neglected.

With the above approximations, and estimations, the reaction constants for defect reactions may be calculated only taking into account the change in internal energy. For example, the formation of Schottky defects has a reaction constant

$$k_s = [V_{Al}^{'''}]^2 \, [V_O^{''}]^3 = \exp\left(\frac{-g_s}{RT}\right) \simeq \exp\left(\frac{-E_s}{RT}\right) \qquad (5.2\text{-}47)$$

5.2.1.3 Cluster Mobilities

The mobility of defects, which determines the extent of self-diffusion, is dependent on their jump frequencies. An impurity boundto a defect may have a different jump frequency, with respect to the defect, than do the host lattice ions. In addition, the jump fre- quencies of host ions themselves, may be altered by the presence of the cluster. Clusters are often thought of as inherently less mobile than isolated point defects. Damask and Dienes[75] point out that this is not necessarily so. For example, divacancy clusters are more mobile than isolated vacancies, in metals. They also postulate that an impurity bound to a vacancy may cause the defect to interact more often with the host ions as well as the impurity. Also, in a review of fast diffusion of impurities in metal (when impurity diffusion is much faster than self-diffusion), by Warburton and Turnbull[76], the same mechanism, enhanced jumping of vacancy due to a bound impurity, is cited and a number of cases attributed to this are referenced.

It is not clear therefore how jumping frequencies will be altered in the defect clusters in Al_2O_3. They may be higher or lower than in pure Al_2O_3.

The correlation coefficient, f, may also be expected to be different for clusters and isolated defects. Complexity reduces the correlation coefficient since a larger number of coordinated jumps must be made to move a unit distance and hence there are more opportunities for backward jumps (jump opposing the direction of the cluster motion) to be made. For example, the value of f for self-

diffusion by a vacancy mechanism in FCC metals is 0.78146[77] while for a divacancy f is 0.475[78], or slightly more than half. In ionic solids the situation is more complex owing to the differences in jump frequencies of the constituents of the cluster,[77] which as just discussed are unknown.

The vacancy clusters may move within the following constraints:

1. No dissociation of clusters. Each jump is to a stable configuration.

2. No cooperative jumps. All defects are allowed to move independently.

Within these rules the clusters may accomplish mixed direction motion, that is, motion which has a component both parallel and perpendicular to the c-axis.

Illustration of possible paths for the Schottky Cluster, and the Fa-V_0-Fa cluster, are shown in figures 127 and 128. Only forward jumps, those which aid in cluster translation are shown. It can be seen that in order to get from one set of face sharing octahedra to another requires 11 atomic steps in the case of the Schottky Cluster and only 7 steps are necessary for the F_a-V_0-F_a. (Note, if a more favorable starting location has been chosen, the Fa-V_0-Fa cluster could have made it in 6). In addition to being long sequences, each jump requires the selection of one direction from a number of possibilities. For example, in the case of the Schottky Cluster, once the jump from 1 to 2 has been made, in any of three equivalent directions, the next jump depends on the probability of which vacancy jumps next and where it jumps to. For the step 2 to 3 to take place

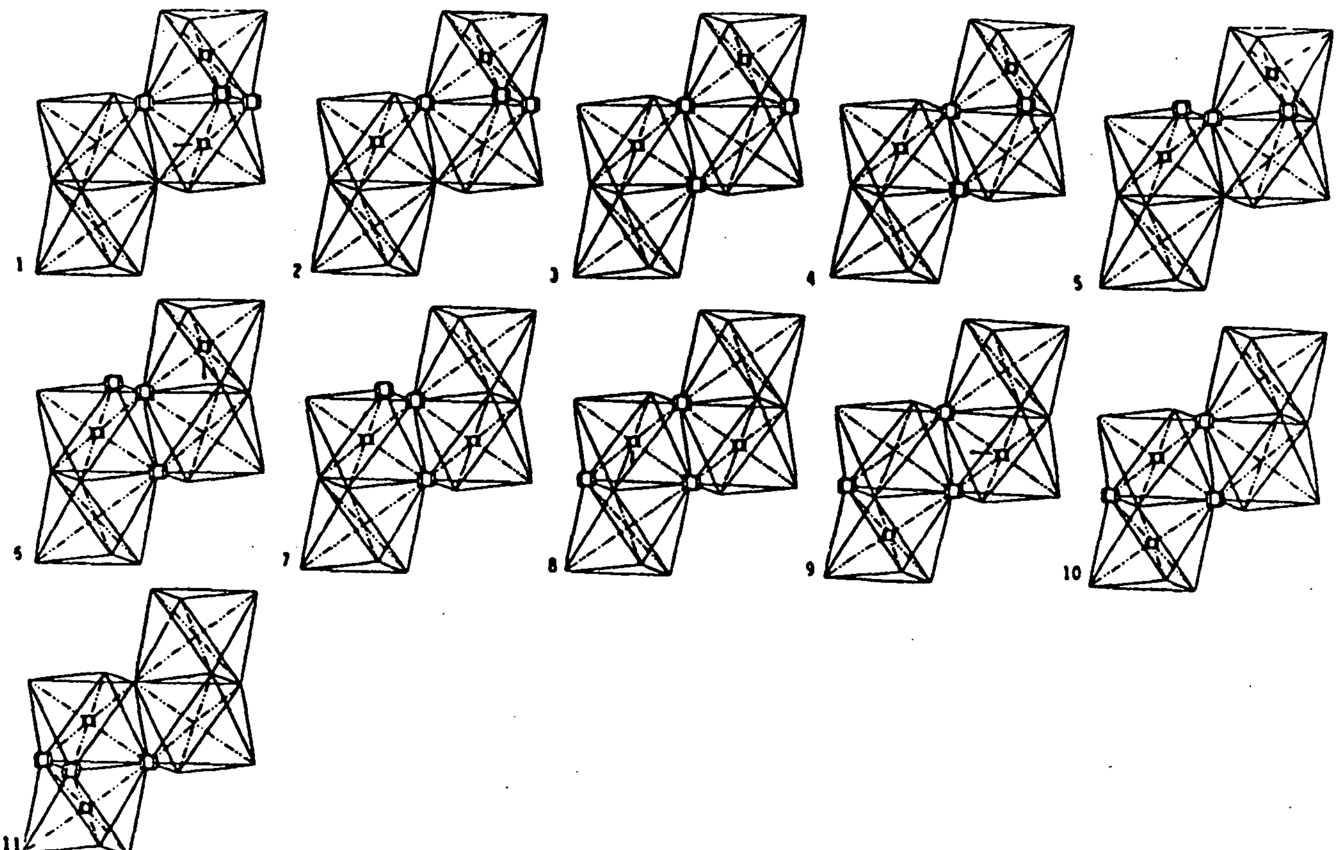

Figure 127. - Illustration of a possible mechanism for the motion of a Schottky Cluster, maintaining nearest neighbor relationships.

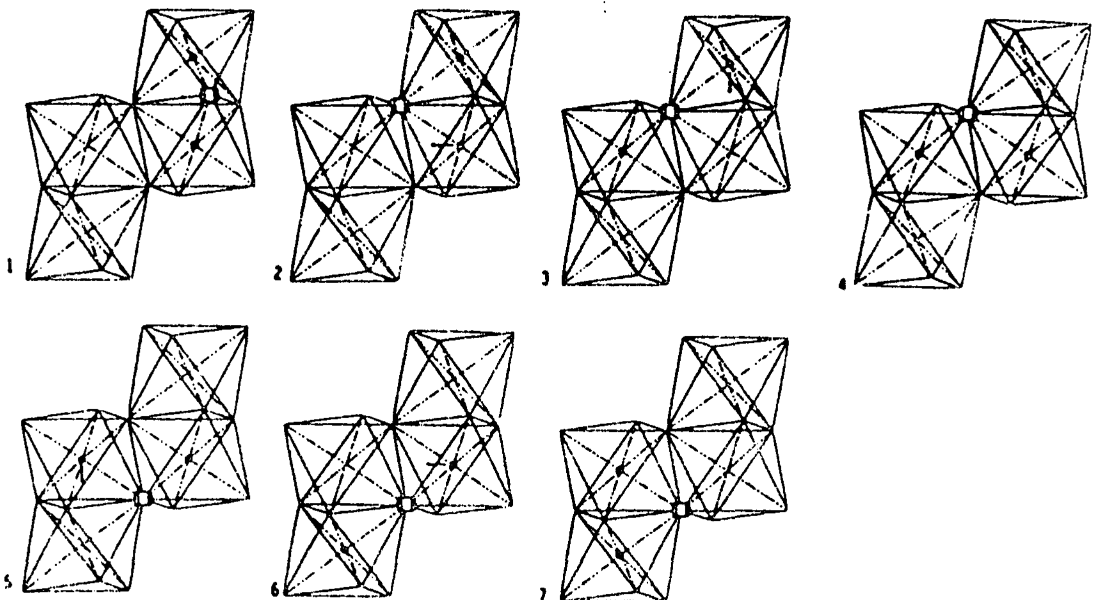

Figure 128. - Illustration of a possible mechanism for the motion of a cluster of two acceptor impurities and an oxygen vacancy, maintaining nearest neighbor relationships.

requires the vacancy to jump (which depends on relative jump frequencies for V_{Al} and V_O) and that it jump in one out of the three directions possible under rule 1. It is obvious that an eleven step process will involve vastly more than eleven jumps.

In the case of donor interstitial clusters the ability for motion, through point jumping, depends on the available sites for the interstitial. If the asymmetric clusters are not allowed there would be no stable corner sharing cluster and the motion described above would not be possible. If these asymmetric clusters are allowed then a possible jumping sequence (7 steps) is shown in figure 129, for the donor clusters involving only two octahedra. The three octahedra clusters can only move if a partial dissociation is allowed, since the various stable form cannot be obtained through single jumps. An illustration of a possible motion of this type of cluster is shown in figure 130.

Based on the number of steps in the point jumping schemes, the impurity clusters may be expected to be more mobile than the Schottky Clusters. However, the energy of each jump has to be taken into account. They are, unfortunately, unknown. The initial jump for the two octahedra donor clusters, figure 128, seems to be, intuitively, a high energy jump. Likewise, the partial dissociation of the three octahedra donor clusters (fig. 124) would be expected to have a significiant energy penalty. While the potential of being misled by intuition is recognized, it is possible that barriers of sufficient energy exist that these clusters are effectively trapped in their original configurations.

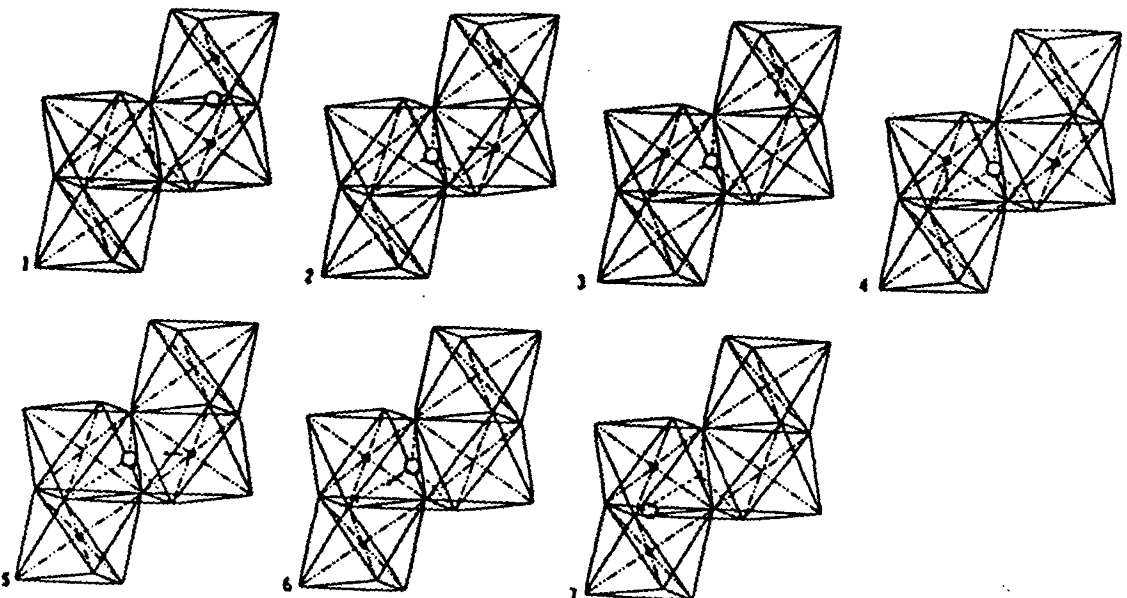

Figure 129. - Illustration of a possible mechanism for the motion of a cluster of two donor impurities and an oxygen interstitial, which requires the interstitial to go to a tetrahedral site.

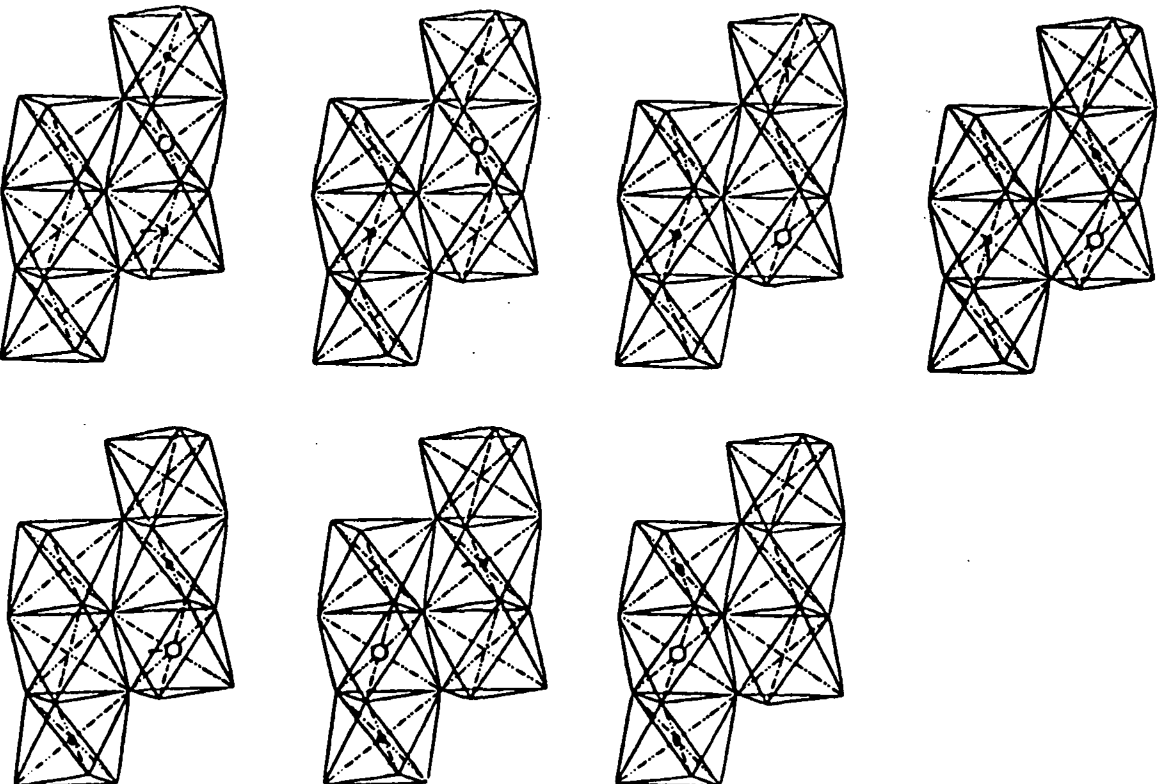

Figure 130. - Illustration of a possible mechanism for the motion of a cluster of two donor impurities and an oxygen interstitial, involving three face sharing octahedra.

Obviously, the existance of low energy cooperative jumps would greatly reduce the correlation problem. It is also necessary to have cooperative jumps for any cluster to move directly from one set of a given type of octahedra to another set of the same type, e.g., edge sharing to edge sharing.

Another aspect which cannot be intuitively predicted is the role of lattice relaxation around the cluster. The difficulty in predicting relaxations is illustrated in the work of Vineyard and Gibson[79] on a tetravacancy in copper (FCC). Figure 131 shows their findings, a tetravacancy in a tetrahedral configuration (with nn maximized) was unstable, i.e., had a negative binding energy. However, if the vacancies were shared between six sites, and two of the face centered atoms grossly relaxed inward, the configuration was stable, stability was increased when the sharing was among eight sites.

It is clear that a great deal of the information necessary to predict the atomic detail of clustering, and cluster motion is currently unavailable.

5.2.2 Impurity Insensitivity of Oxygen Self-Diffusion

For diffusion to be independent of the presence of aliovalent impurities, either the mechanism must involve a defect whose concentration is itself not sensitive to the impurities, or the effect of the impurities must be buffered out.

The degree of the latter effect can be illustrated using the calculations of Catlow et al. It may be recalled that in the case of Ti-doping (Donor) the choice of potential had such an influence

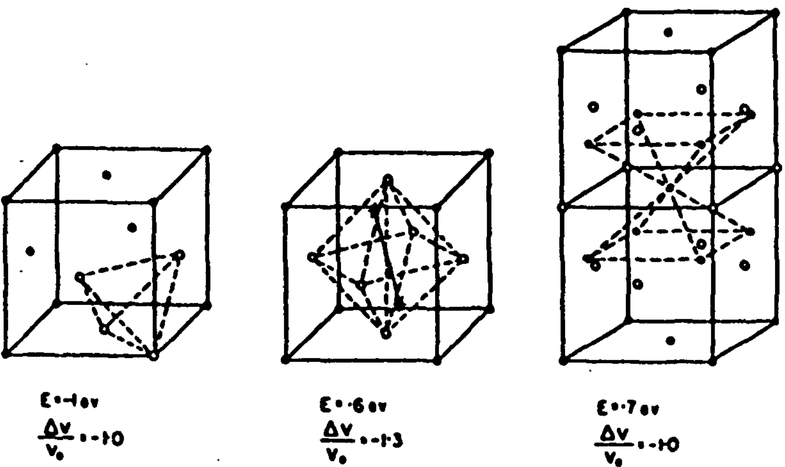

Figure 131. - Schematic configurations of three tetravacancies calculated to be stable (or metastable) in copper. Vacated lattice sites are shown by open circles. Grossly relaxed atoms are shown by large dots. Relaxation of other atoms not depicted. Binding energies and volume changes also listed (ref. 79, Gibson and Vineyard).

that the selection of a dominant mode of compensation was not possible. For the sake of clarity only one example will be examined; the case of oxygen interstitials produced by donor doping will be selected.[5]

Using the energies of Catlow, et al., the cluster dissociation constants were calculated using the expression

$$k_d = \exp\left(\frac{E_b}{RT}\right) \tag{5.2-48}$$

and the results are shown in table 10. It can be seen that up to temperatures near the melting point, the dissociation constants are small and the defect equilibria in doped Al_2O_3 cannot be accurately predicted without taking clustering into account.

The binding energy of the donor cluster is expected to depend on the particular donor involved. For example, Gourdin and Kingery calculated defect energies in MgO and found that E_b for the complex $(2Fd_{Mg}O_i)^x$ was -127 kJ if the donor was Al^{3t} and -166 kJ (30 percent more) if the donor was Fe^{3t}. For the purpose of the following discussion of donor doping in Al_2O_3 consider the following three species, all compensated by oxygen interstitials:

---

[5] The calculated binding energies for clusters (503 kJ for $(3Ti_{Al}V_{Al})$) and 293 kJ for $(2Ti_{Al}O_i)$) tends to favor domination by aluminum vacancy compensation. However, only one, arbitrarily chosen, configuration was investigated in each case. For vacancy mode this was three titaniums (on sites F, G, and H in fig. 110) surrounding one Al vacancy (site E). For interstitials this was analogous to that in figure 124. It is certainly possible that the favoritism could be reversed when an exhaustive study is made, thus a freedom of choice is allowed. It should be noted that it is not the binding energy of any particular cluster which lies beneath this argument but the consistently high magnitude of all that were calculated.

TABLE 10. - THE DISSOCIATION CONSTANT, K_d, FOR DIFFERENT CLUSTERS AS A FUNCTION OF TEMPERATURE

T°C	$(2Ti_{Al}O_i)$	$(3Ti_{Al}V_{Al})$	$(2Mg_{Al}V_O)$	$(2Mg_{Al}Mg_i)$
500	1.46854E-20	9.79684E-35	2.25522E-17	1.57956E-16
600	2.74612E-18	7.70413E-31	1.81987E-15	1.01989E-14
700	1.75218E-16	9.58546E-28	5.95578E-14	2.79591E-13
800	5.15258E-15	3.15963E-25	1.01735E-12	4.13491E-12
900	8.51326E-14	3.87551E-23	1.07115E-11	3.86304E-11
1000	9.05309E-13	2.23290E-21	7.79124E-11	2.54053E-10
1100	6.82248E-12	7.12782E-20	4.24457E-10	1.26988E-09
1200	3.90833E-11	1.42175E-18	1.83695E-09	5.10173E-09
1300	1.79332E-10	1.93829E-17	6.59877E-09	1.71744E-08
1400	6.85842E-10	1.93365E-16	2.03440E-08	5.00063E-08
1500	2.25463E-09	1.48816E-15	5.52400E-08	1.29066E-07
1600	6.52635E-09	9.21058E-15	1,34818E-07	3.01042E-07
1700	1.69668E-08	4.73889E-14	3.00580E-07	6.44403E-07
1800	4.02197E-08	2.08177E-13	6.20267E-07	1.28174E-06
1900	8.80599E-08	7/98048E-13	1.19740E-06	2.39306E-06
2000	1.79958E-07	2.71817E-12	2.18155E-06	4.22913E-06

(1) Ti^{4+} with E_b rounded to -300 kJ

(2) A hypothetical donor, $H2^{4+}$, with E_b = -200 kJ (30 percent less than Ti)

(3) A hypothetical donor, $H4^{4+}$, with E_b = -400 kJ [6] (30 percent more than Ti)

Also as an example, a temperature of 1600° C typical of a self-diffusion experiment is chosen for the system. With the above, the following comparisons may be made.

[6]Note: -400 kJ is a reasonable value for a cluster binding energy it is 100 kJ less than that calculated by Catlow, et al. for the cluster (3 Ti_{Al} V_{Al}).

- Intrinsic vs. Doping

It is of interest to compare the number of free interstitials produced by doping with the number of thermally generated free interstitials at our example temperature, 1600° C.

The concentration of thermally generated defects may also be estimated using the calculations of Catlow, et al. Recall that Frenkel disorder was predicted to be dominant when the empirical potential was employed while Shottky disorder was predicted with the non-empirical potential.

In the case of Frenkel domination the electroneutrality condition is

$$[V_O^{\cdot\cdot}] = [O_i''] \qquad (5.2\text{-}49)$$

and an estimation of the interstitial population may be obtained by simply substituting this into the reaction constant, which is

$$k_{AF} = [V_O^{\cdot\cdot}]\,[O_i''] \simeq \exp\left(\frac{-E_{AF}}{RT}\right) \qquad (5.2\text{-}50)$$

giving

$$[O_i''] = \exp\left(\frac{-E_{AF}}{2\ RT}\right)^{7} \qquad (2.5\text{-}51)$$

In the case of Schottky disorder dominating the electroneutrality condition is

---

[7]Note the defect energies given table 1 are per defect, for example, E_{AF} = 2 defects/Frenkel pair = 366 kJ/mole of defects = -732 kJ/ mole of Frenkel pair.

$$2\,[V_O^{\cdot\cdot}] = 3\,[V_{Al}^{'''}] \qquad (5.2\text{-}52)$$

with this the concentration of oxygen vacancies may be obtained from the Schottky reaction constant

$$[V_O^{\cdot\cdot}]^3\,[V_{Al}^{'''}]^2 = \exp\left(\frac{-E_s}{RT}\right) \qquad (5.2\text{-}53)$$

giving

$$[V_O^{\cdot\cdot}] = \left(\frac{3}{2}\right)^{2/5} \exp\left(\frac{-E_s}{5RT}\right) \qquad (5.2\text{-}54)$$

substituting this into equation (5.2-55) and solving for the concentration of interstitials obtains

$$[O_i] = \left(\frac{2}{3}\right)^{2/5} \exp\left(\frac{-E_{AF} - \frac{1}{5}E_s}{RT}\right) \qquad (5.2\text{-}55)$$

Using equation (5.2-56) with Catlow, et al.'s empirical results and equation (5.2-58) with Catlow, et al.'s non-empirical results, intrinsic oxygen interstitial populations were calculated and the results are given in table 11. At 1600° C:

with Frenkel domination

$[O_i] = 6.21\times10^{-11}$ mol fraction

$= 6.21\times10^{-5}$ ppm

with Schottky domination

$[O_i] = 1.79\times10^{-31}$ mol fraction

$= 1.79\times10^{-25}$ ppm

These calculated energies thus predict extremely low levels of thermal interstitials. The number of extrinsic defects for the three donors, Ti, H2, and H4, were determined as a function of dopant

TABLE 11. - ESTIMATES OF INTRINSIC OXYGEN INTERSTITIAL CONCENTRATIONS BASED ON THE CALCULATIONS OF CATLOW ET AL.

Temperature (°C)	Assuming Frenkel domination (empirical potential	Assuming Schottky domination (non-empirical potential)
1100	1.19 E-14	1.20 E-42
1200	1.05 E-13	8.35 E-40
1300	7.02 E-13	2.52 E-37
1400	3.74 E-12	3.85 E-35
1500	1.65 E-11	3.33 E-33
1600	6.21 E-11	1.79 E-31
1700	2.04 E-10	6.42 E-30
1800	5.99 E-10	1.63 E-28
1900	1.59 E-09	3.07 E-27
2000	3.88 E-09	4.48 E-26

level, 10 to 1000 ppm, using an iterative procedure and equation (21). The results are given in table 12 and shown in figure 132.

The dependencies vary considerably depending on the binding energy. However at very low dopant level the degree of dissociation becomes determined by the concentration and the interstitial concentration for all three donors is within a factor of three. In all cases the concentration of free interstitials produced by doping is vastly greater (factor of 10^5 for 10 ppm of the most weakly bound donor) than that of the thermally generated free defects. The effect of dopants is not buffered away in the perfect singly doped case.

- Heavy doping vs. Background Donors

A second valuable comparison is the difference in free interstitials present in otherwise pure cyrstals containing a background donor level of 10 or 50 ppm and in a heavily doped, 800 ppm, crystal.

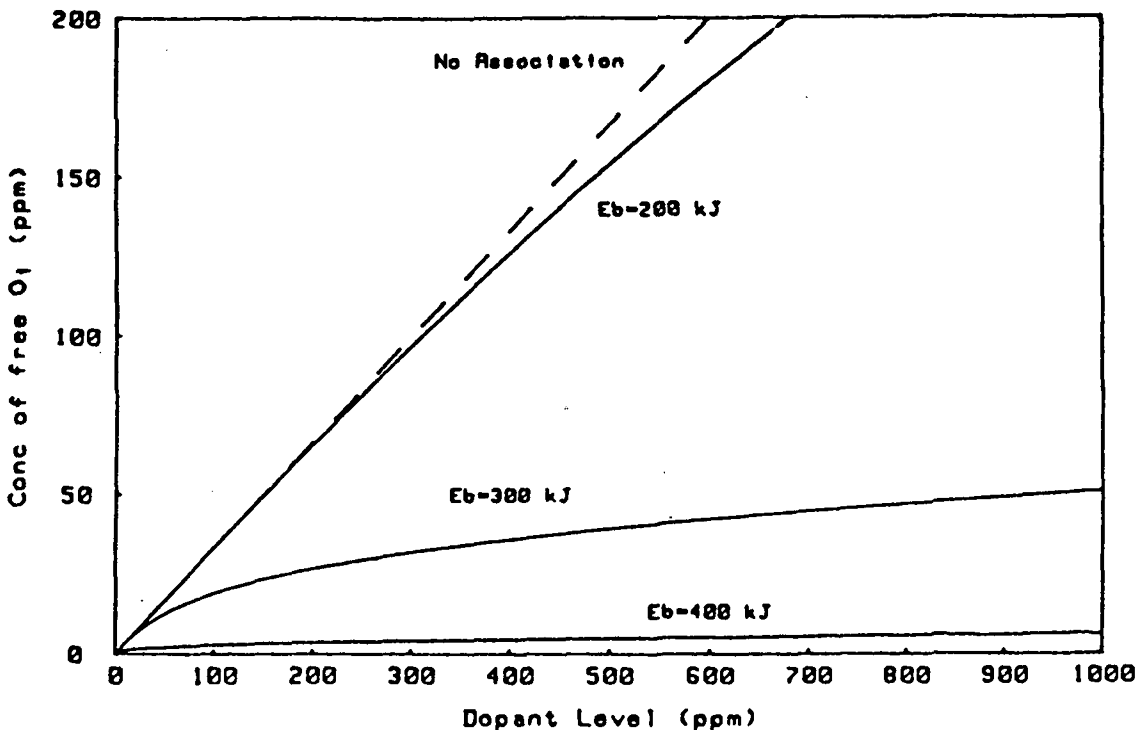

Figure 132. - Plot of the concentration of free oxygen interstitials produced by doping with hypothetical donors with different cluster binding energies versus dopant level, at 1600° C.

TABLE 12. - ESTIMATES OF THE CONCENTRATIONS OF FREE OXYGEN INTERSTITIALS

PRODUCED BY DONOR DOPING AT 1600° C

	H4 Eb = ⁻400 kJ/mol		T1 Eb = ⁻300 kJ/mol		H2 Eb = ⁻200 kJ/mol	
Dopant level	Degree of dissociation	$[O_1]$	Degree of dissociation	$[O_1]$	Degree of dissociation	$[O_1]$
10 ppm	0.356	1.8 ppm	0.978	4.9 ppm	0.999+	5.0 ppm
50	.134	3.4	.752	18.8	.999	24.9
100	.086	4.3	.570	28.5	.996	49.8
200	.055	5.5	.401	40.1	.986	98.5
300	.042	6.3	.319	47.9	.969	145.3
400	.035	7.0	.270	53.9	.948	189.7
500	.030	7.5	.236	59.0	.925	231.3
600	.027	8.1	.211	63.4	.901	270.2
700	.024	8.4	.192	67.2	.876	306.5
800	.022	8.8	.177	70.7	.851	340.4
900	.020	9.0	.164	73.9	.827	372.1
1000	.019	9.5	.154	76.9	.804	401.8

It is clear from table 12 and figure 133 that the result is dependent on the binding energy of dopant donor and, for the 50 ppm case, the binding energy of the background donor. Consider doping 800 ppm of the three example donors.

(i) A crystal doped 800 ppm of H2. In this case, the heavy doping will produce a population of free interstitials large (340 ppm) compared to a background produced by any of the donors (at $[FdO_2]$ = 10 ppm the $[O_1]$ = 2 to 5 ppm; and at $[FdO_2]$ = 50 ppm the $[O_1]$ is 3 to 25 ppm).

Also, note that when doping with H2, across the whole range 10 to 800 ppm, the $[O_1] \simeq 1/2\ [FdO_2]$ as is expected when there is total dissociation. H2, then, is an example of a donor whose effects can be accurately predicted when clustering is neglected.

(ii) A crystal doped with 800 ppm of Ti. In this case the heavy doping will produce a population of interstitials which, while substantial 70 ppm, is much lower than H2. This level of interstitials may be considered large compared to a 10 ppm background. However when the background is 50 ppm this depends on the nature of the background.

The $[O_1]$ = 70 ppm produced by the dopant may be considered large with respect to the $[O_1]$ = 3 ppm produced by a 50 ppm background of H4. However, in the case of a 50 ppm background of either Ti or H2, a significant fraction of the free interstitials present (21 percent and 20 percent, respectively) will be produced by the background donor.

In addition, when doping with Ti near 10 ppm $[O_1] \simeq 1/2\ [Fd\ O_2]$ however at $[FdO_2]$ = 800 ppm this is reduced to $[O_1] < 1/10\ [FdO_2]$. Based on this, significant errors are to be expected in predictions of the effects of Ti-doping which ignore clusters.

(iii) A crystal doped with 800 ppm of H4. In this case the dopant produced a level of free interstitials, 9 ppm, which is only slightly greater than that produced by a 10 ppm background and which is more than a factor of 2 smaller than that produced by a 50 ppm of either Ti or H2.

At high dopant levels, ~800 ppm, the $[O_1] = 1/100\ [FdO_2]$ which is dramatically different than the unassociated case. Predictions of the effect of H4 doping are critically dependent on the binding energy of H4, and the binding energy of any background donor.

- Donor doping with backgound acceptors and donors

Additional complications occur when both acceptors and donors are present in the background, in the absence of association. When total donors exceed total acceptors, all of the acceptors can be compensated by equation (5.2-41) and a net donor population will exist.

The percentage of each donor which exist in acceptor-donor clusters, donor-interstitial clusters, and as free ions is not necessarily uniform. For example, large acceptor ions may prefer to associate with small donor ions in order to have the average radius approach that of aluminum. The existance of this type of preference can lead to the segregation of various donors and acceptors into different types of clusters. A strongly ionizing donor added as a

dopant could conceivably be used up in the neutralization of acceptors and liberate a very weakly ionizing donor.

Therefore, in addition to knowing the concentrations of all the impurities, it is necessary to know the g-functions of all of the possible cluster forms in order to make meaningful prediction of the defect chemistry.

In summary,

(i) Doping, despite clustering, produces free defect concentrations which are large compared to the population of thermally generated defects.

(ii) Clustering diminishes concentration dependencies and therefore the ability of dopants to swamp out the free defects produced by background impurities. Also, the sensitivity of free defect concentrations to cluster binding energies indicates that impurity levels below detectability limits can have significant contributions.

(iii) Predicting defect equilibria in crystals with 100 ppm background impurities requires a great deal of information which is currently unavailable. That which is available suggests much of the impact of doping will be buffered out. Also, changes in the free defect population produced through control of the oxygen partial pressure with be similarly buffered, bound clusters will dissociate to provide defects sufficient to annihilate those produced by the P_{O_2} change.

The second circumstance by which oxygen diffusion would be independent of impurity concentration, is if the defect was both

neutral and involved a stochiometric number of sites. Aliovalent impurities alter the concentrations of charged point defects in order to satisfy the constraints of charge neutrality and site balance. There is no need for the population of neutral species to change with aliovalent dopants.

Both neutral interstitials and stoichiometric neutral clusters have been proposed as dominating anion diffusion in a number of materials. In a study of diffusion under a field in NaCl, Chemla[80] found that a certain impurity, Cs, obeyed the Nernst-Einstien relation while anion impurities P and S were affected to a much smaller, 1/10, degree than predicted by the relation. Similar work on self-diffusion under an electric field by Nelson[81] indicated also that cation diffusion obeyed the relation while anion diffusion deviated from this expectation. Based on this, the suggestion was made that anion diffusion obtains a significant contribution from Schottky divacancies, $(V_{Na}V_{Cl})^{x}$.

Studies[82-85] of anion self-diffusion in III to V and II to VI compounds MX also lead to the proposition of neutral species, neutral interstitials, S_i^x in CdS and Te_i^x in GaTe, as well as Schottky clusters $(V_{Pb}V_S)^x$ in PbS.

Results in the oxides of MgO and Al_2O_3, as well, have led to the proposal of neutral species. The insensitivity of oxygen diffusion in MgO has been attributed to the transport being governed by Schottky divacancies.

Kroger and co-workers[50 and 51] observed that there is no grain boundary contribution to ionic conductivity despite a significant enhancement of oxygen diffusion by grain boundaries. Based on this, grain boundary diffusion was proposed to take place by a netural atomic interstial O_i^x, or a neutral molecular interstitial, $O_{2_i}^x$.

Schottky clusters are another possible neutral species (recall from equation (5.2-20) that the concentration of these clusters is uniquely fixed by the temperature). Although the population of un-associated Schottky defects is small, the population of Schottky clusters need not be. It is dependent on the binding energy of the clusters since

$$[(3V_O 2V_{Al})] \approx \exp \frac{-(E_s + E_b)}{RT} \tag{5.2-56}$$

For the case of Al_2O_3, this binding energy has not been calculated. It would be of great interest to have such information. Gourdin and Kingery calculated the binding energy for the Schottky divacancy and found it to be substantial, -257 kJ. If, in Al_2O_3, the pattern of clusters from aliovalent solutes is followed, in which $k_a < 10^{-6}$, it would not be difficult to imagine the diffusion of oxygen being governed by the cluster mechanism even if there is a competing mechanism by a more mobile species, for example, V_O. This follows since, in the case where the defects interact, it is the product of the mobility and concentration of the species determine its contributon

$$D_{eff} = c_1 D_1 + c_2 D_2 \tag{5.2-57}$$

5.2.3 P_{O_2} Dependence

Let us consider the P_{O_2} dependence of the three netural species, O^x_1, $O^x_{2_1}$, and $(3V_O 2V_{Al})^x$.

(i) In the case of $O^x_{2_1}$, using the reaction:

$$O_2(g) \rightarrow O^x_{2_1} \qquad (5.2\text{-}58)$$

which will give:

$$k = \frac{[O^x_{2_1}]}{P_{O_2}} \qquad (5.2\text{-}59)$$

Therefore:

$$[O^x_{2_1}] \propto P_{O_2} \qquad (5.2\text{-}60)$$

(ii) In the case of O^x_1, the reaction will be:

$$\frac{1}{2} O_2(g) \rightarrow O^x_1 \qquad (5.2\text{-}61)$$

which will give:

$$k = \frac{[O^x_1]}{P^{1/2}_{O_2}} \qquad (5.2\text{-}62)$$

Therefore:

$$[O^x_1] \propto P^{1/2}_{O_2} \qquad (5.2\text{-}63)$$

(iii) In the case of $(3V_O 2V_{Al})$ no P_{O_2} dependence will occur since neither k_s or k_a depends on P_{O_2}.
The experimental evidence, though restricted to one data point indicates no dependence on P_{O_2} and is therefore consistent with the Schottky Cluster model.

In summary point defect clustering allows two separate explanations for the insensitivity of oxygen diffusion to the presence of aliovalent impurities and changes in oxygen partial pressure. In the first the clusters are considered to have mobilities which are negligible compared to that of the free defects. The clusters serve as point defect traps and a buffering action is responsible for the insensitivities. In the second explanation clusters are considered mobile and the exsistence of intrinsic defect clusters is postulated. These clusters augment the thermally generated defect population and oxygen diffusion is the result of intrinic behavior. Further work is needed to decide between the two.

5.2.4 Non-Fickian Tracer Profiles

While the near surface region (<0.75 to 1.00 μm) could be adequately described by a solution to Ficks second law, the profiles contained, to varying degrees, low level deeply penetrating tails, extending past the furthest depth probed, ~2μm in proton activation. Typically the concentration in the tail was 2 to 7 times the natural abundance. The tails appeared in both the proton activation spectra and SIMS profiles indicating that they are not artifacts of the analysis method.

Similar tails were observed by Reddy[16]. His results may be summarized as follows:

1. All as-received samples showed this deviation from Fick's law.

2. The magnitude of the tail did not correlate to the average native dislocation content. His crystal with the lowest dislocation density had the tail of the highest magnitude.

3. Preannealing the crystal affected the magnitude of the tail but not in a consistent manner. Three samples were preannealed in a vacuum (10^{-2} to 10^{-3} torr), two of these samples had tails, one did not. Samples which had been preannealed in an oxidizing atmosphere were reported to have no tails, or tails of lower magnitude. (Note that in the present work all samples, exchanged at P_{O_2} = latm were preannealed in air, despite this tails occurred).

Reddy concluded that the tails did not occur by short circuit diffusion alone since the tail did not correlate with variations in dislocation density among his samples. An unreasonable pipe radius, on the order of a micron, had to be assumed to account the level of enrichment observed. He proposed two explanations. The first was based on the presence of excess vacancies quenched in during crystal growth. In this case the diffusion of tracer into the sample is enhanced along a dislocation and then is enhanced radially away from the dislocation due to the wind of excess vacancies annihilating at the dislocation. The lack of dependence on dislocation density was ascribed to differing concentrations of excess vacancies dominating.

Were this effect to be the source of the tails then samples which were preannealed and diffusion annealed together would be expected to show similar, though nonfickian, profiles. However, tail magnitudes in the current work are seen to vary between such samples. Figures 133 and 134 show the proton activation spectra from two sets of samples, two from the Ni-doped boule and two from the undoped no. 1 boule. All four samples were preannealed together. During the exchange anneal the samples were split into two pairs, of one sample from each boule, located on two different shelves in the exchange apparatus. In both cases, the samples from the same boule had tails of differing degree. The difference in temperature between the two shelves, ~40° C, is not the source of the variation since the high temperature sample had the more pronounced tail in one case while the low temperature sample did in the other. In summary, tail magnitude varied within groups of equivalently equilibrated samples. Note also that atmosphere effects cannot be responsible (for example, amount of CO_2 or N_2 which leak into the apparatus) since all these were exchanged in the same atmosphere.

The second proposition offered by Reddy is the coexistence of two noninteracting oxygen species, molecular oxygen interstitials and oxygen lattice defects. Such a situation has been proposed to explain the oxygen transport across vitrious silica films (see Appendix A). However, there are two reasons for its rejection in Al_2O_3. The first is the expected P_{O_2} dependence. The concentration

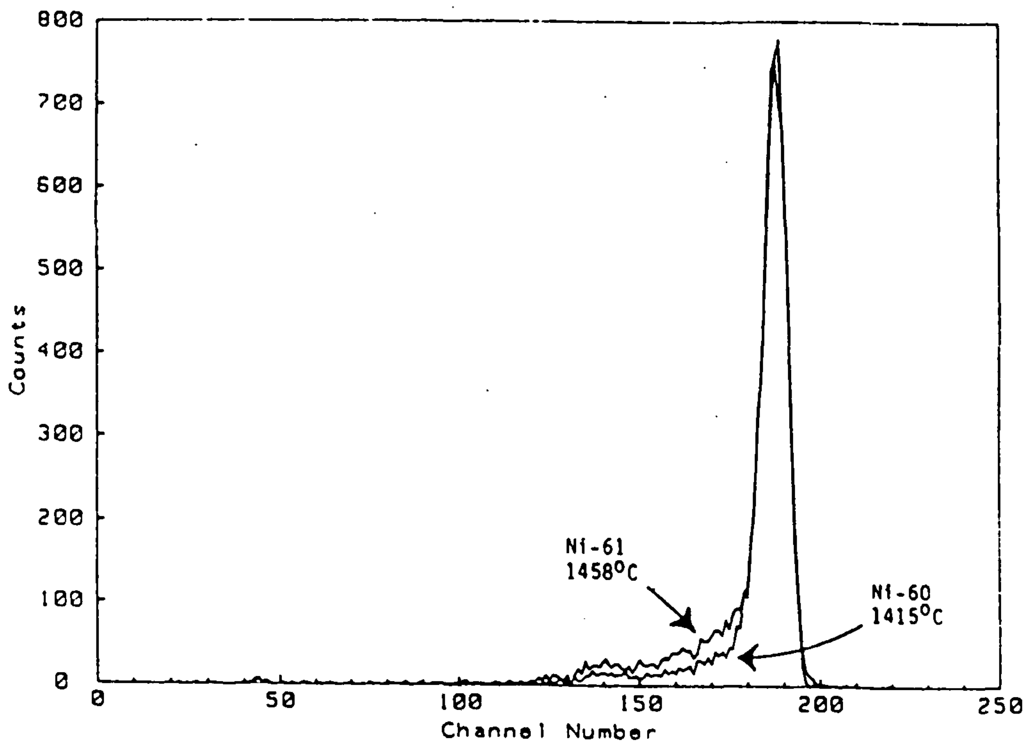

Figure 133. - Comparison of the magnitudes of the tails observed in two samples from the Ni-doped boule which were pre-annealed together and exchanged on two different shelves during the same run. The hotter sample has the bigger tail.

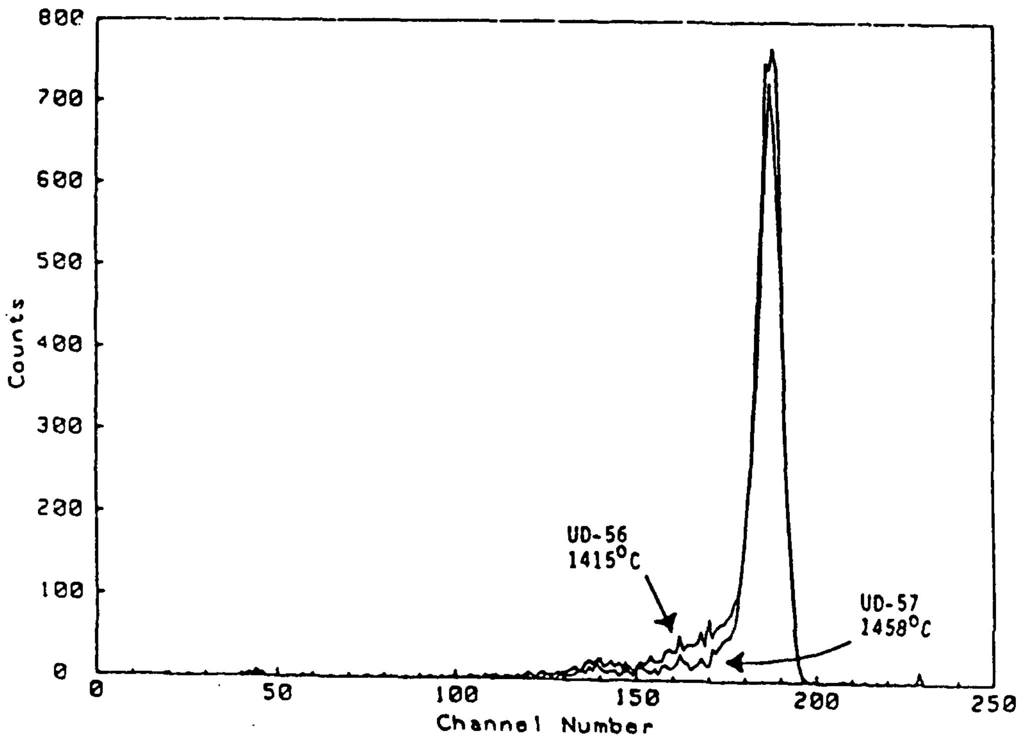

Figure 134. - Comparison of the magnitudes of the tails observed in two samples from the undoped boule which were pre-annealed together and exchanged on two different shelves during the same run. The hotter sample had the smaller tail.

of dissolved molecular oxygen interstitials is linearly dependent on the oxygen partial pressure. However, the tail in the specimen exchanged at a $P_{O_2} = 10^{-15}$ atm. had a tail comparable to the samples exchanged at $P_{O_2} = 1$ atm. Secondly, experiments on the permeation of sintered alumina tubes (99.8 percent Al_2O_3) by Hayes, Budworthy, and Roberts found the material permeable to oxygen yet not to argon or nitrogen. If the oxygen was permeating as a noninteracting molecular species, argon with its smaller molecular radius (Ar - 2.88 Å, O_2 - 2.98 Å) would also be expected to be transported.

The coexistance of contamination and impurity-defect clustering offers another possible source for tails. When the cation impurities are diffusing in they may drag with them an oxygen defect. Donors may conceivably drag noninteracting interstitials.

In this case the flux of tracer would simply be the sum of the flux due to self-diffusion and one-half of the flux of the contaminant, since

$$[O_1] = 1/2\ [(2FdO_1)^x]$$

with the assumption that the diffusion coefficients are not functions of position, the solution for a semi-infinite slab is

$$c_{18}(x,t) = c_1 \text{ erfc } \left(\frac{x}{2\sqrt{D_O t}}\right) + 1/2\ c_1 c_{Fd} \text{ erfc } \left(\frac{x}{2\sqrt{D(2Fd_{Al}O_1)^t}}\right)$$

where c_1 is the concentration of tracer in the lattice at the surface (equals gas for $K \to \infty$) and c_{Fd} is the concentration of the donor impurities in the lattice at the surface.

In this case the magnitude of the tail is directly related to the concentration of impurity and an observable tail would require a large level of contamination.

For example, a tail three times the natural abundance, or 0.6 percent, when using an atmosphere of 50 percent enriched O-18, would require more than 2 percent of the cation sites to be occupied by impurities. This seems unreasonable given the solubility limits of ~200 ppm given for donor impurities.[25] It would be possible for tracer to accumulate if the donor-interstitial cluster were a very much faster diffusing species and interacted infrequently with the lattice. However, a sample which was demonstrated to have cation profiles, VD-LT (exchanged at 1300° C), did not have a tail in its profile.

It remains to find a satisfactory explanation for the tails.

CHAPTER VI

CONCLUSIONS

On the basis of this work the following conclusions can be made:

1.) SIMS has several advantages over proton activation for tracer studies. That of greatest importance is the superior depth resolution and the ability to detect a greater number of species.

2.) The contamination of the samples was the result of the use of commercial high purity Al_2O_3 tubes.

3.) The oxygen diffusivity determined was in agreement with that determined in previous gas exchange studies in absolute magnitude, although the determined activation energy was lower.

4.) Two models for oxygen diffusion in alumina are consistent with the diffusion coefficient being independent of impurities and P_{O_2}. The first involves a buffer action arising from impurity point defect clustering and the second involves the existance of Schottky Clusters, $(3V_O 2V_{Al})^x$. Both models can be justified by extrapolation from the defect energy calculations of Catlow, et al.

CHAPTER VII

Suggestions for Future Work

1.) Contamination by furnace tubes was a serious problem in this work. The design and construction of an apparatus which will minimize the level of contamination is essential.

2.) A study of diffusion under a constant applied electric field would be of value. Diffusion which occurs by neutral Schottky Clusters should be unaffected by this field while ionized point defects would be. A gas exchange experiment using porous platinum electrodes is one possible scheme.

3.) It would be of interest to carry out another set of experiments using a solid state source of tracer. It is important to establish that diffusion coefficients are not a function of particular experiment techniques.

4.) SIMS with its excellent depth resolution should allow direct measurement of diffusion coefficients at low temperature where only inferred values currently exist.

5.) It would be of great interest to have the calculations of Catlow, et al., extended to include various cluster orientations, clusters of intrinsic defects and the energies of motion for both point defects and clusters.

REFERENCES

1. F. A. Golightly, F. H. Stott, G. C. Wood: "The Influence of Yttrium Additions on the Oxide-Scale Adhesion to an Iron-Chromium-Aluminum Alloy," Oxid. Met. 10, 163 (1976).

2. J. K. Tien and F. S. Petit: "Mechanism of Oxide Adherence on Fe-25 Cr-4Al (Y or Sc) Alloys," Met. Trans. 3, 1587 (1972).

3. I. M. Allam, D. P. Whittle, and J. Stringer: "The Oxidation Behavior of CoCrAl Systems Containing Active Element Additions," Oxid. Met. 12, 35 (1978).

4. F. A. Golightly, F. H. Scott, and G. C. Wood: "The Relationship Between Oxide Grain Morphology and Growth Mechanisms for Fe-Cr-Al and Fe-Cr-Al-Y Alloys," J. Electrochem. Soc. 126, 1035 (1979).

5. M. M. El-Aiat and F. A. Kroger: "Yttrium an Isoelectric Donor in α-Al_2O_3," J. Am. Ceram, Soc. 65, 280 (1982).

6. N. L. Peterson: "Isotope Effects in Diffusion" in Diffusion in Solids; Recent Developments A.S. Nowick and J.J. Burton, Eds, Academic Press, New York (1975).

7. J. Crank: The Mathematics of Diffusion, Clarendon Press, Oxford, (1956).

8. H. Yinnon: "A Proton Activation Study of Oxygen Diffusion in Multicomponent Glass-forming Systems," Ph.D. Thesis, Case Western Reserve University (1979).

9. R. C. Robin: "An Improved Proton Activation Analysis for Oxygen Diffusion," Ph.D. Thesis, Case Western Reserve University (1971).

10. P. G. Shewmon: Diffusion in Solids, McGraw-Hill, N.Y. (1963).

11. Y. Oishi and W. D. Kingery: "Self-Diffusion of Oxygen in Single Crystal and Polycrystalline Aluminum Oxide," J. Chem. Phys. 33, 480 (1960).

12. D. J. Reed and B. J. Wuensch: "Ion-Probe Measurement of Oxygen Self-Diffusion in Single-Crystal Al_2O_3," J. Amer. Cer. Soc. 63, 88 (1980).

13. D. J. Reed: "Ion Probe Measurement of Oxygen Self-Diffusion in Aluminum-Oxide," Sc.D. Thesis, Massachusetts Institute of Technology (1977).

14. R. D. Monahan and J. W. Halloran: "Single-Crystal Boundary Migration in Hot-Pressed Aluminum Oxide," J. Amer. Cer. Soc. 62, 564 (1979).

15. K. P. R. Reddy and A. R. Cooper: "Oxygen Diffusion in Sapphire" J. Am. Ceram. Soc. 65, 634 (1982).

16. K. P. R. Reddy: "Oxygen Diffusion in Close Packed Oxides," Ph.D. Thesis, Case Western Reserve University (1979).

17. Y. Oishi, K. Ando, and K. Matsuhiro: "Self-Diffusion Coefficient of Oxygen in Vapor-Grown Single-Crystal Alumina," Yogyo-Kyokai-Shi 85, 54 (1977). Quoted in ref. 15.

18. Y. Oishi, K. Ando, and Y. Kubota: "Self-Diffusion of Oxygen in Single Crystal Alumina," J. Chem. Phys. 73, 1410 (1980).

19. A. E. Paladino and W. D. Kingery: "Aluminum Ion Diffusion in Aluminum Oxide," J. Chem. Phys. 37, 957 (1962).

20. G. J. Dienes et al.: "Shell-Model Calculation of Some Point-Defect Properties in α-Al_2O_3," Phys. Rev. B, 11, 3060 (1975).

21. C. R. A. Catlow, R. James, W. C. Mackrodt, and R. F. Stewart: "Defect Energetics in α-Al_2O_3 and Rutile TiO_2," Phys. Rev. B, 25, 1006 (1982).

22. T. P. Jones, R. L. Coble, and C. J. Mogab: "Defect Diffusion in Single Crystal Aluminum Oxide," J. Am. Ceram. Soc. 52, 331 (1969).

23. E. M. Akul'Onok et al.: "Diffusion of Point Defects Participating in Solid-Phase Chemical Reactions (Trap Diffusion): Demonstration for the $Ti^{3+} \rightarrow Ti^{4+}$ Transition in Corundum," J. Solid State Chem. 26, 17 (1978).

24. R. T. Cox: "Chemical Reactions and Mass Transport Processes in Donor and Acceptor doped Aluminum Oxide Crystals," J. Phys. (Paris) Colloq. 9, 333 (1973).

25. J. J. Rasmussen and W. D. Kingery: "Effects of Dopants on the Defect Structure of Single-Crystal Aluminum Oxide," J. Am. Ceram. Soc. 53, 436 (1970).

26. K. H. Lee and J. H. Crawford, Jr.: "Additive Coloration in Sapphire," Appl. Phys. Lett. 33, 273 (1978).

27. C. F. Bauer and D. H. Whitmore: "Characterization of Paramagnetic Hole Centers in Al_2O_3 and Al_2O_3: Fe by Optical and EPR Absorption," J. Solid State Chem 11, 38 (1974).

28. K. Eigenmann and H. H. Gunthard: "Valence States, Redox Reactions and Biparticle Formation of Fe and Ti Doped Sapphire," Chem. Phys. Lett. 13, 58 (1972).

29. D. S. McClure: "Optical Spectra of Transition-Metal Ions in Corundum," J. Chem. Phys. 36, 2757 (1962).

30. S. A. Marshall, T. T. Kikuchi, and A. R. Reinberg: "Paramagnetic Resonance Absorption of Divalent Nickel in $-Al_2O_3$ Single Crystal," Phys. Rev. 125, 453 (1962).

31. R. Muller and H. H. Gunthard: "Spectroscopic Study of the Reduction of Nickel and Cobalt Ions in Sapphire," J. Chem. Phys, 44, 365 (1966).

32. D. W. Peters, L. Feinstein, and C. Peltzer: "On the High-Temperature Electrical Conductivity of Alumina," J. Chem. Phys. 42, 2345 (1965).

33. K. Kitazawa and R. L. Coble: "Electrical Conduction in Single-Crystal and Polycrystalline Al_2O_3 at High Temperatures," J. Am. Ceram. Soc. 57, 245 (1974).

34. B. V. Dutt, J. P. Hurrell, and F. A. Kroger: "High Temperature Defect Structure of Cobalt-Doped α-Alumina," J. Am. Ceram. Soc. 58, 420 (1975).

35. B. V. Dutt and F. A. Kroger: "High Temperature Defect Structure of Iron Doped α-Alumina," J. Am. Ceram. Soc. 58, 474 (1975).

36. S. K. Mohapatra and F. A. Kroger: "Defect Structure of α-Al_2O_3 Doped with Magnesium," J. Am. Ceram. Soc. 60, 141 (1977).

37. S. K. Mohapatra and F. A. Kroger: "Defect Structure of α-Al_2O_3 Doped with Titanium," J. Am. Ceram. Soc. 60, 381 (1977).

38. S. K. Mohapatra and F. A. Kroger: "The Dominant Type of Atomic Disorder in α-Al_2O_3," J. Am. Ceram, Soc. 61, 106 (1978).

39. S. K. Mohapatra, S. K. Tiku, and F. A. Kroger: "The Defect Structure of Unintentionally Doped α-Al_2O_3 Crystals," J. Am. Ceram. Soc. 62, 50 (1979).

40. S. K. Tiku and F. A. Kroger: "Energy Levels of Donor and Acceptor Dopants and Electron and Hole Mobilities in α-Al_2O_3," J. Am. Ceram. Soc. 63, 31 (1980).

41. M. M. El-Aiat and F. A. Kroger: "Hydrogen Donors in α-Al O ,"$_2$J$_3$ Appl. Phys. 53, 3658 (1982).

42. M. M. El-Aiat and F. A. Kroger: "Yttrium, An Isoelectric Donor in
α-Al_2O_3," J. Am. Ceram. Soc. 65, 280 (1982).

43. W. R. Rao and I. B. Cutler: "Effect of Iron Oxide on the Sintering Kinetics of Al_2O_3," J. Am. Ceram. Soc. 56, 588 (1973).

44. R. D. Bagley, I. B. Cutler, and D. L. Johnson: "Effect of TiO_2 on the Initial Sintering of Al_2O_3," J. Am. Ceram. Soc. 53, 136 (1970).

45. R. J. Brook: "Effect of TiO_2 on the Initial Sintering of Al_2O_3," J. Am. Ceram. Soc. 55, 114 (1972).

46. R. E. Mistler and R. L. Coble: "Rate Determining Species in Diffusion Controlled Processes in Al_2O_3," J. Am. Ceram. Soc. 54, 60 (1971).

47. D. Delaunay, A. M. Huntz, and P. Lacombe: "The Influence of Yttrium on the Sintering of Al_2O_3," J. Less Common Met. 70, 115 (1980).

48. G. W. Hollenberg and R. S. Gordon: "Effect of Oxygen Partial Pressure on the Creep of Polycrystalline Al_2O_3 Doped wit Cr, Fe, or Ti," J. Am. Ceram. Soc. 56, 140 (1973).

49. P. A. Lessing and R. S. Gordon: "Creep of Polycrystalline Alumina, Pure and Doped with Transistion Metal Impurities," J. Mat. Sci, 12, 2291 (1977).

50. L. D. Hou, S. K. Tiku, H. A. Wang, and F. A. Kroger: "Conductivity and Creep in Acceptor-Dominated Polycrystalline Al_2O_3," J. Mat. Sci, 14, 1877 (1979).

51. M. M. El-Aiat, L. D. Hou, S. K. Tiku, H. A. Wang, and F. A. Kroger: "High-Temperature Conductivity and Creep of Polycrystalline Al_2O_3 Doped with Fe and/or Ti," J. Am. Ceram. Soc. 64, 174 (1981).

52. B. J. Pletka, T. E. Mitchell, and A. H. Heuer: "Solid Solution Hardening of Sapphire (α-Al_2O_3)," Phys. Stat. Sol. (a), 39, 301 (1977).

53. D. S. Phillips, T. E. Mitchell, and A. H. Heuer: "Precipitation in Star Sapphire III. Chemical Effects Accompanying Precipitation," Phil, Mag. A. V. 42 417 (1980).

54. B. Cockayne and B. Lent: "A Complexity in the Solidification Behavior of Molten Yttrium Aluminum Garnet ($Y_3Al_5O_{12}$)," J. Cryst. Growth 46, 371 (1979).

55. J. A. McHugh: "Factors that Influence an Elemental Depth Concentration Profile," National Bureau of Standards Spec. Publ. 427, 179 (1975).

56. H. H. Andersen and J. F. Ziegler: Hydrogen, Stopping Powers and Ranges in All Elements, Pergamon Press, N.Y. (1977).

57. J. F. Ziegler: Helium, Stopping Powers and Ranges in All Elemental, Matter, Pergamon Press, N.Y. (1977).

58. C. F. Williamson, J. P. Boujot, and J. Picard: "Tables of Range and Stopping Power of Chemical Elements for Charged Particles of Energy 0.5 to 500 MeV," CEA-R, 3042 (1966).

59. D. Halliday: Introductory Nuclear Physics, 2nd Ed, John Wiley and Sons New York (1955).

60. L. D. Major, Jr.: "Proton Activation Studies of the Thermal Oxidation of Silicon," MS Thesis, Case Western Reserve University (1975).

61. J. Ziegler, Ed: New Uses of Ion Accelerators, Plenum Press, New York (1975).

62. H. Yinnon: "A Proton Activation Study of Oxygen Diffusion in Multicomponent Glass Forming Systems" Ph.D Thesis, Case Western Reserve University (1979).

63. B. Hockey: "Plastic Deformation of Aluminum Oxide by Indentation and Abrasion," J. Amer. Ceram. Soc. 54 [5], 223 (1971).

64. W. K. Chu: "Material Analysis by Nuclear Backscattering Formalism" in New Uses of Ion Accelerators; edited by J. Ziegler, Plenum, New York (1975) p. 135.

65. Bob McCune (Ford Motor Co.) Personal Communication.

66. G. Amsel: Personal Communication, 1980.

67. J. A. Champion: "The Electrical Conductivity of Sapphire and Ruby Crystals," Proc. Brit. Ceram. Soc. 10, 51 (1968).

68. W. D. Scott: "Impurity Deposits on Alumina Crystals," J. Am. Ceram. Soc. 52, 454 (1969).

69. A. H. Heuer: "Investigation of the Temperature Dependence of the Strength of Corundum Crystals." Ph.D Thesis, University of Leeds (1966).

70. C. P. Flynn: Point Detects and Diffusion, Clarendon Press, Oxford, (1972).

71. W. H. Gourdin and W. D. Kingery: "The Defect Structure of MgO Containing Trivalent Cation Solutes: Shell Model Calculations: J. Mat. Sci. 14, 2053 (1979).

72. H. Megaw: Crystal Structure: A Working Approach, Saunders, Philadelphia (1973).

73. L. B. Pedersen: "Energies, Volumes and Entropies of Formation of Point Defects in fcc Lennard-Jones Systems," Cryst. Lattice Defects, 3, 145 (1972).

74. A. C. Damask and G. J. Dienes: Point Defects in Metals: Gordon and Breach London, (1963).

75. W. K. Warburton and D. Turnbull: "Fast Diffusion in Metals"; in Diffusion in Solids: Recent Developments; A.S. Nowick and J.J. Burton, Eds., Academic Press, Inc., New York (1975).

76. J. R. Manning: Diffusion Kinetics for Atoms in Crystals; Van Nostrand-Reinhold, Princeton, N.J. (1968).

77. R. E. Howard: "Random Walk Method for Calculating Correlation Factors: Tracer Diffusion by Divacancy and Impurity-Vacancy Pairs in Cubic Crystals," Phys. Rev. 144, [2] 650 (1966).

78. G. H. Vineyard and J. B. Gibson, "Clusters of Vacancies in Copper," Bull. Amer. Physic. Soc. 6 158 (1961).

79. M. Chemla: "Migration of S in Sodium Chloride in an Electric Field," "Comptes Redus," 234, 2064, (1952); "Diffusion and Migration of Cs^+ in Single Crystals of NaCL," Comptes Rendus 236, 484 (1953); "Diffusion of Radioactive Ions in Crystals. Applications," Ann. Phys. (Paris) 1 [13] 959 (1956).

80. V. C. Nelson and R. J. Friauf: "Diffusion of Vacancies and Vacancy Pairs in Sodium Chloride," J. Phys. Chem. Solids 31, 825 (1970).

81. M. S. Seltzer and J. B. Wagner, Jr.: "Diffusion of Sulfur-35 in Single Crystals of Lead Sulfide as a Function of Stoichiometry and Doping Additions," J. Phys. Chem. Solids 26, 233 (1965).

82. P. M. Borsenberger and D. A. Stevenson: "Self-Diffusion of Cadmium and Tellurium in Cadmium Telluride," J. Phys. Chem. Solids 29, 1277 (1968).

83. V. Kumar and F. A. Kroger: "Self-Diffusion and the Defect Structure of Cadmium Sulfide," J. Solid State Chem. 3, 387 (1971).

84. H. H. Woodbury and R. B. Hall: "Diffusion of the Chalcogens in the II-VI Compounds," Phys. Rev. 157, 641 (1967).

85. Y. Oishi Personal Communication 1982.

APPENDIX A

The Thermal Oxidation of Silicon

I. Introduction

Beyond its general scientific interest, the study of the passive oxidation of silicon is of commercial value. The thermal oxidation of silicon plays a key role in MOS technology and, since oxygen transport through SiO_2 is involved in the oxidation process, knowledge of the mechanistics is helpful in the understanding of glasses.

A number of different mechanisms have been proposed for the thermal oxidation of silicon. Also, there are indications that the mechanism of oxygen transport in vitreous silica (v-SiO_2) is complex. This work was undertaken to identify different contributions to oxygen mobility and to assess the contribution of each in thermal oxidation.

It is found that oxygen is mobile both within the network and as a permeating species. Network diffusion, however, does not contribute to scale growth.

II. Literature Review

(1) Silicon Oxidation Kinetics

The thermal oxidation of silicon has been shown to produce a scale of v-SiO_2 and the kinetics of this oxidation has been shown to

be of a linear-parabolic type[1,2]. With this type of kinetics, the thickness of the scale after time, t, is given by:

$$x^2 + Ax = Bt$$

where x is the oxide thickness, B/A is the linear rate constant K_1, and B is the parabolic rate constant K_p.

Linear oxidation kinetics are expected when the rate of oxidation is controlled by the reaction of the oxidant[1] with the metal. Parabolic kinetics, on the other hand, are expected to occur when the oxidation reaction is controlled by the diffusion of the re- agents across an existing scale. Oxidation which is initially controlled by reaction rate may undergo a transition to parabolic kinetics as the scale thickness increases. Irene[2] has shown that the values of both the linear and the parabolic rate constants are functions of water content and silicon substrate orientation. The nature of the dependence of the parabolic rate constant on substrate orientation is unclear. It is not obvious that diffusion through the v-SiO_2 should be affected by the parent silicon orientation.

Investigations of the kinetics of the growth of thin scales where linear kinetics dominate, lead Ghez and Van der Meulen[3] to conclude the two simultaneous reactions are responsible for oxidation. They propose the following set:

---

[1]An oxidant is a chemical reagent that oxidizes. Oxygen is one example but there are many others, e.g., water.

(i) Silicon reaction with molecular oxygen

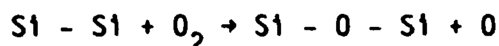

$Si - Si + O_2 \rightarrow Si - O - Si + O$

(ii) Molecular oxygen dissociation and silicon reaction with atomic oxygen

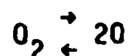

$O_2 \rightleftarrows 2O$

$Si - Si + O \rightarrow Si - O - Si$

Irene[4] analyzed the curvature in an Arrenhius plot of the linear rate constants and also came to the conclusion that two simultaneous reactions occur. However, the reactions were not specified.

As reported by Major[5] the values for the parabolic rate constant and its temperature dependence showed wide variation. The sensitivity to the ambient water content shown by Irene[2] may contribute to the scatter. Deal and Grove[1] also suggest that the apparent discrepancies may be due to force fitting data with a parabolic law when it is inappropriate.

(2) Silicon Oxidation Mechanisms

Marker experiments by Atalla[6] and Jorgenson[7] both indicate that the growth of the oxide takes place at the oxide-metal interface. The linear dependence of the growth rate, in the parabolic regime, on oxygen partial pressure was observed by both Ligenza and Spitzer[8] and Deal and Grove[1] which suggests that the oxidant is molecular oxygen.

Ligenza and Spitzer also observed that samples successively oxidized in oxygen-16 and oxygen-18 contained more oxygen-18 than could

be accounted for by scale growth. This indicates that the oxygen within the network undergoes exchange with oxygen in the ambient gas.

Jorgenson(7) found that when a battery circuit was used to apply a field across a scale during growth, it was possible to enhance or retard the growth rate. This was asserted to indicate that the transported species was ionic. Based on this, Irene(2) proposed that the oxygen molecules were doubly charged and Deal and Grove proposed that they were singly charged. Raleigh(9) however, has reinterpreted Jorgenson's work and pointed out that oxidation involves the transport of electroneutral species and therefore an electric field cannot provide a steady state driving force. Rather, Raleigh suggests that the battery circuit provides an external path for charge which allows ionic species which were previously limited by electrical charge flux to participate in the oxidation.

In 1978, Major(5) carried out a set of experiments above the temperature range of 900° to 1200° C in which silicon coupons were oxidized in oxygen-18 for a time to produce 1/2 μm thick SiO_2. The atmosphere was then switched to oxygen-16 and the oxidation was allowed to proceed until a full micron of oxide was grown. The location of the tracer was determined using proton activiation. The results are shown in figures 1 to 4.[2]. At low temperatures, 900° C, the location of the bulk of the second isotope(16) is located near the oxide-metal interface while at the high temperature, the

---

[2]Note that the isotope order in these spectra is the reverse (O-18), then O-16) of that employed in all the other studies mentioned.

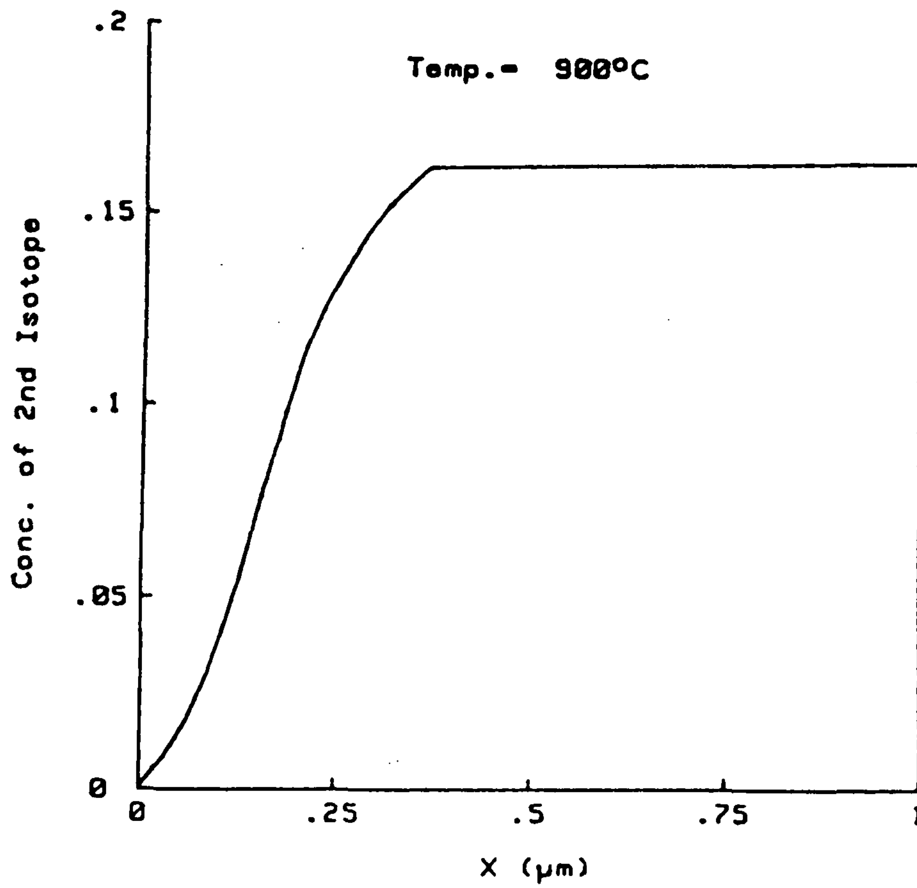

Figure 1. - Best fit concentration profile of Major's sample oxidized at 900° C.

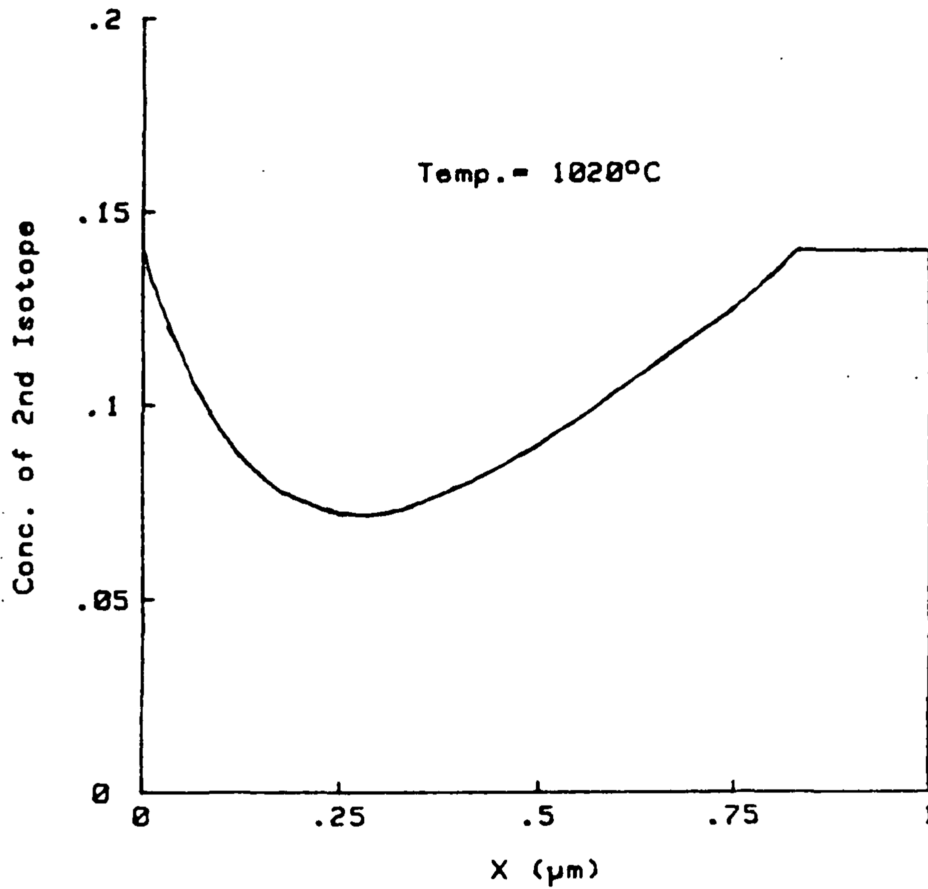

Figure 2. - Best fit concentration profile of Major's sample oxidized at 1020° C.

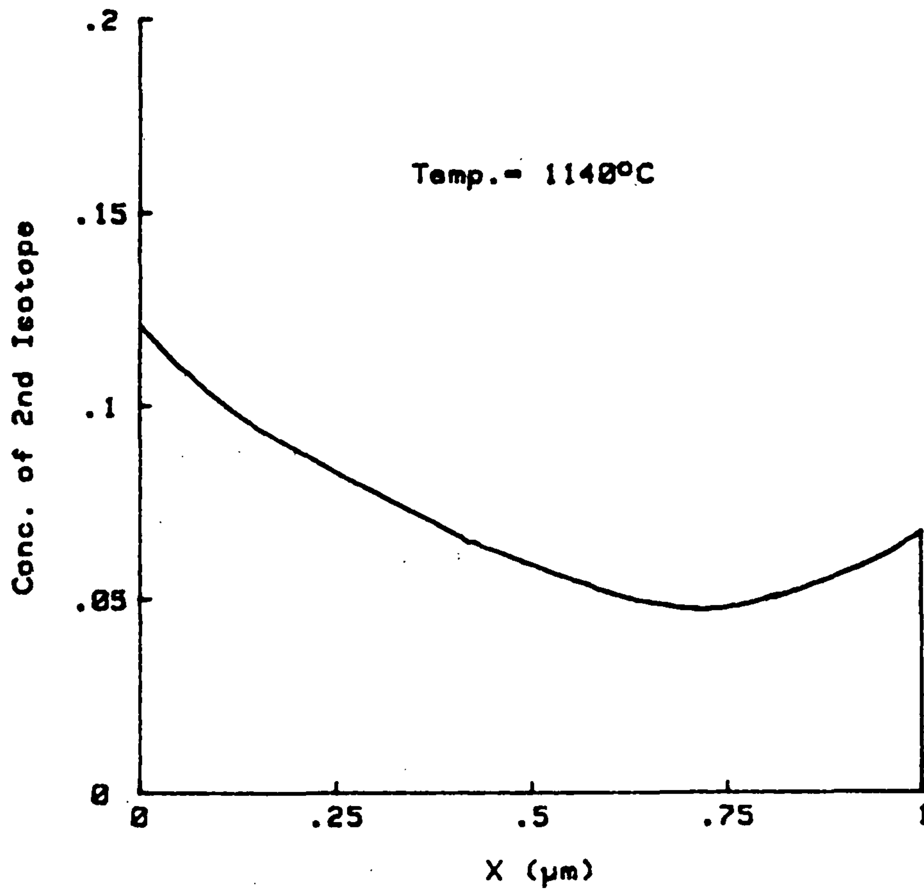

Figure 3. - Best fit concentration profile of Major's sample oxidized at 1140° C.

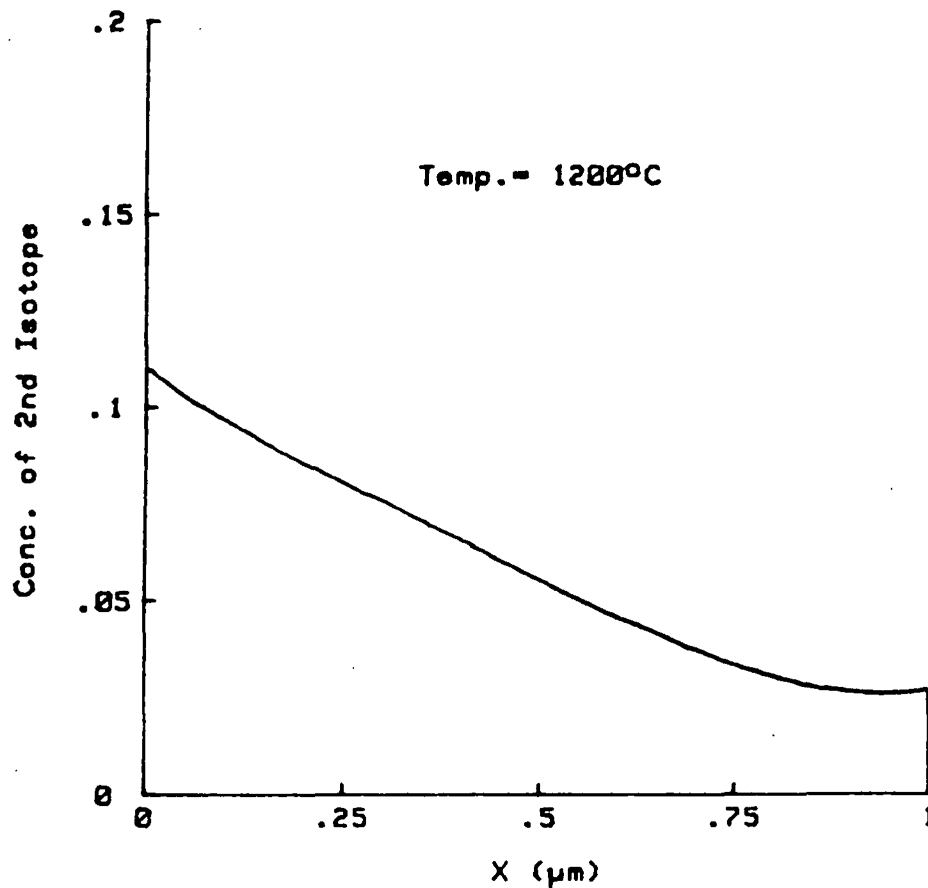

Figure 4. - Best fit concentration profile of Major's sample oxidized at 1200° C.

second isotope(16) is located near the gas-oxide interface. At intermediate temperatures the second isotope(16) is distributed between the two interfaces. In order to account for this shift a model was proposed in which oxygen molecular inter- stitials permeate the scale to react with the metal. During the permeation these interstitials were thought to exchange with the network oxygen. If the rate of lattice exchange was small at 900° C the tracer would be deposited at the oxide-metal interface. If, as the temperature increased, the rate of exchange with the lattice also increased, then the tracer would be found increasingly toward the gas-oxide interface. Clark[10] has developed a numerical solution to this model.

Also in 1978, Rosencher, et al.,[11] carried out a double oxidation experiment at 930° C. They also used an activation technique, however it was a resonance technique with better depth resolution. With this technique, the tracer profiling (see fig. 5) was found to consist of a large block of tracer near the oxide-metal interface and a narrow spike of tracer at the gas-oxide interface. This indicate that, at least at 930° C, the majority of the tracer was incorporated into the scale at the oxide-metal interface, suggesting growth by a permeating species.

In 1981, Christy and Condon[12] carried out a double oxidation experiment at 700° C, analyzing their samples with SIMS. The resulting profiles have features which suggest that artifacts exist. The profiles are shown in figure 6. The oxide-metal interface is reported to be around 3 min. of sputter time. The total oxygen signal

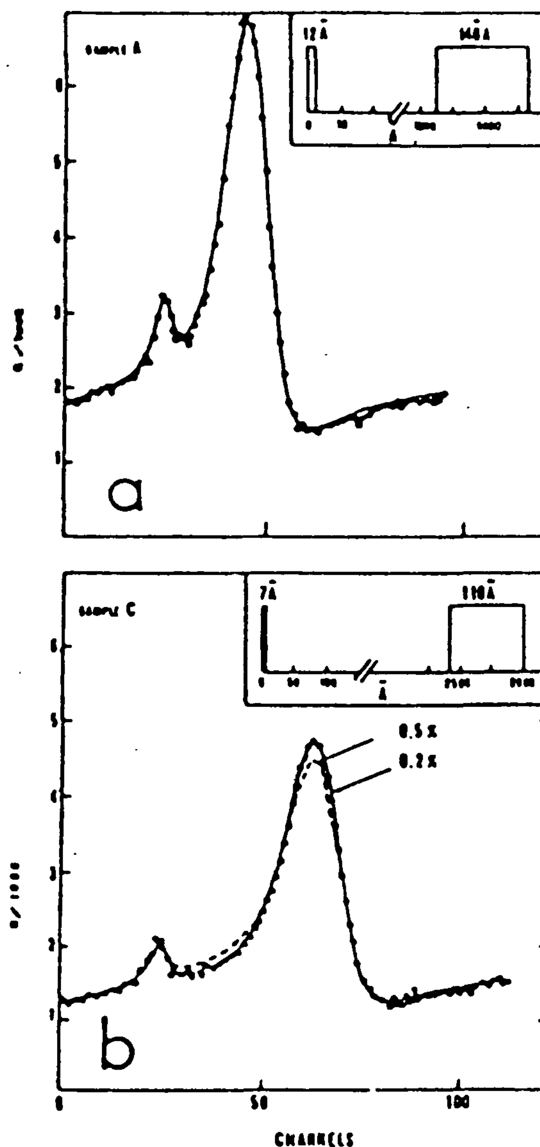

Figure 5. - Typical ^{18}O concentration profile measurements using the 2-keV-side $^{18}O(p,\alpha)$ ^{15}N reaction near the 629-keV resonance. Channel 0 corresponds to 619.6 keV; the energy step is 384 ev/channel. The solid lines show the best fit calculated assuming ^{18}O concentration depth profiles represented in the insets, the depth scale origin being the external surface of SiO_2. The concentrations in the extreme regions were taken constant and equal to that of the gas, 99.7 percent, whereas in the bulk it was taken equal to natural, 0.2 percent. Respective equivalent thicknesses of these regions are indicated (see Table II), from ref. 11.

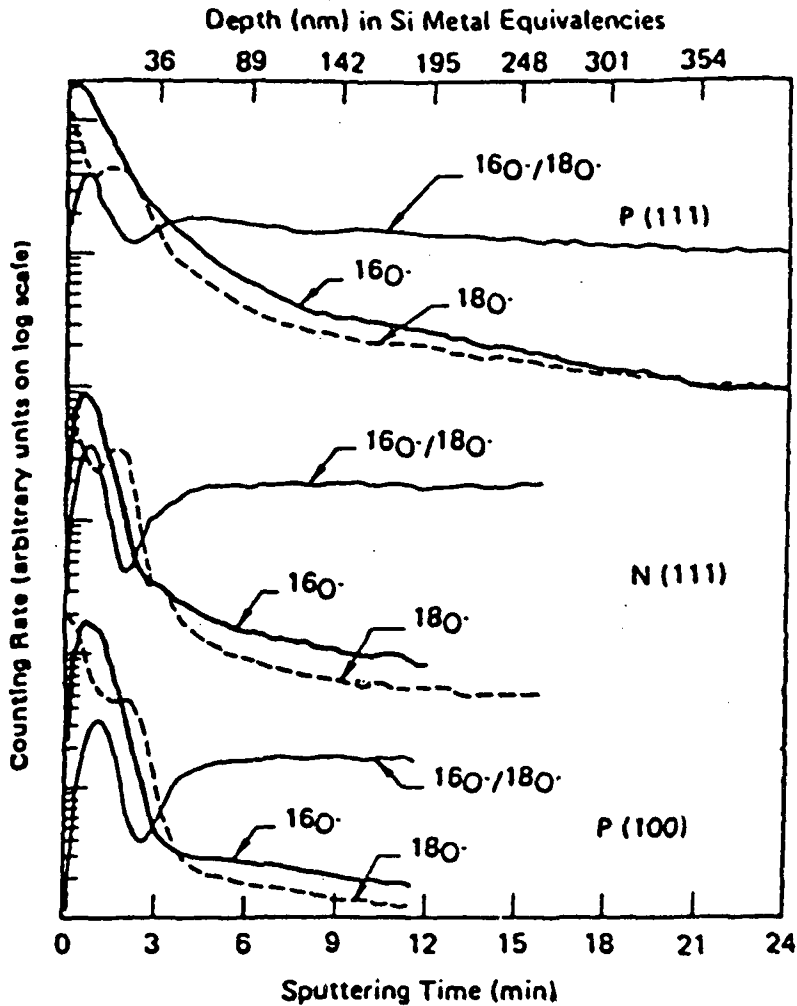

Figure 6. - Typical IMMA depth profiles of oriented silicon wafer which had been oxidized at 700° C with $^{16}O_2$ for 10 days followed by $^{18}O_2$ for 10 days. (Actual oxide depth is about twice the silicon metal equivalence depth. The location of x_s, the defined transformation boundary, is at about 3 min sputtering time.), from ref. 12.

appears to vary across the SiO_2. This is a reminder that SIMS is not a quantitative instrument without standards. After the oxide-metal interface the profile shows that the concentration of oxygen does not decrease rapidly. This might arise if the interface were rough or if there is an appreciable solubility of oxygen in silicon, however, as pointed out by Helms[13] in his discussion neither is the case. The shape of the profiles are consistent with the edge effects or a poorly focussed primary beam. Though excellent depth resolution is claimed no standards were presented and on the basis of the poor profiles, the model presented in their paper is considered to be unproven.

In 1982, Revesz and Schaeffer[14] proposed that the v-SiO_2 scale contains "channels" of increased structural order similar to tridymite. Their model considers scale growth to arise from two processes, network diffusion and permeation by molecular interstitials. The channels are proposed to exist in sufficient number that transport phenomena are dominated by them but also at a low enough concentration that they are not detectable by electron or X-ray diffraction. It is also stated that permeation is greater in channels while network diffusion is decreased. Further, it is stated that slow oxidation or heat treatment of the scale will increase the level of ordering and a corresponding increase in permeation and a drop in network diffusion will occur. Note that it is necessary for these effects to balance each other for parabolic kinetics to be observed. The credibility of this model would be greatly enhanced if there were diffraction (or perhaps charged particle channeling)

evidence to confirm the structural changes.

(3) Diffusion of Oxygen in v-SiO_2

There have been five studies of the diffusion of oxygen in v-SiO_2.

In 1961, Norton[15] studied and permeation of gaseous oxygen through a membrane of v-SiO_2 and found the diffusion coefficient could be described by:

$$D = 2.88\times10^{-8} \exp\left(\frac{-113 \text{ kJ/mol}}{RT}\right) \text{ m}^2/\text{s}$$

In 1962, Haul and Dumbgen[16] studied the rate of uptake of tracer by SiO_2 and found that the diffusion coefficient could be described by:

$$D = 4.3\times10^{-6} \exp\left(\frac{-234 \text{ kJ/mol}}{RT}\right) \text{ m}^2/\text{s}$$

In 1963, Sucov[17] monitored the tracer uptake from a finite source by tiny silica cylinders and found that the diffusion coefficient could be described by:

$$D = 1.5\times10^{-2} \exp\left(\frac{-297 \text{ kJ/mol}}{RT}\right) \text{ m}^2/\text{s}$$

In 1965, Williams[18] also monitored the tracer uptake by either silica fibers or bulbs and found the diffusion coefficient to be described by:

$$D = 2.0\times10^{-13} \exp\left(\frac{-113 \text{ kJ/mol}}{RT}\right) \text{ m}^2/\text{s}$$

In 1982, Yinnon[19] studied diffusion of oxygen in v-SiO_2 by exposing samples to a tracer enriched gas and then determining the tracer profile by proton activation. This procedure has the advan-

tage that the determined value for the diffusion coefficient must satisfy both the quantity of tracer in the sample and the shape of the profile. It was found that this was true for samples exchanged at temperatures below 800° C. At higher temperatures, however, the profile could not be fitted with a single diffusion coefficient; but could, be described by two diffusion coefficients (see fig. 7). This was suggestive of two independent diffusion mechanisms. The near surface regions of their profile yielded diffusion coefficients which could be described by;

$$D = 2.1 \times 10^{-14} \exp\left(\frac{-110\ kJ/mol}{RT}\right)\ m^2/s$$

In summary, the range of reported values for the diffusion of oxygen in v-SiO_2 varies over a wide range. The work of Yinnon and Cooper indicates that the presence of more than one operative diffusion mechanism, which may be sensitive to P_{H_2O}, surface condition, and temperature, may contribute to the scatter.

III. Experimental Procedure

(1) Samples

The single crystal silicon samples used in this study were oriented in the (001) direction and were p-type with a resistivity of 12.4 ohm-cm.

Prior to experimentation the silicon was immersed in an HF solution to etch off existing oxide, washed with acetone, then methanol, and finally rinsed with distilled water.

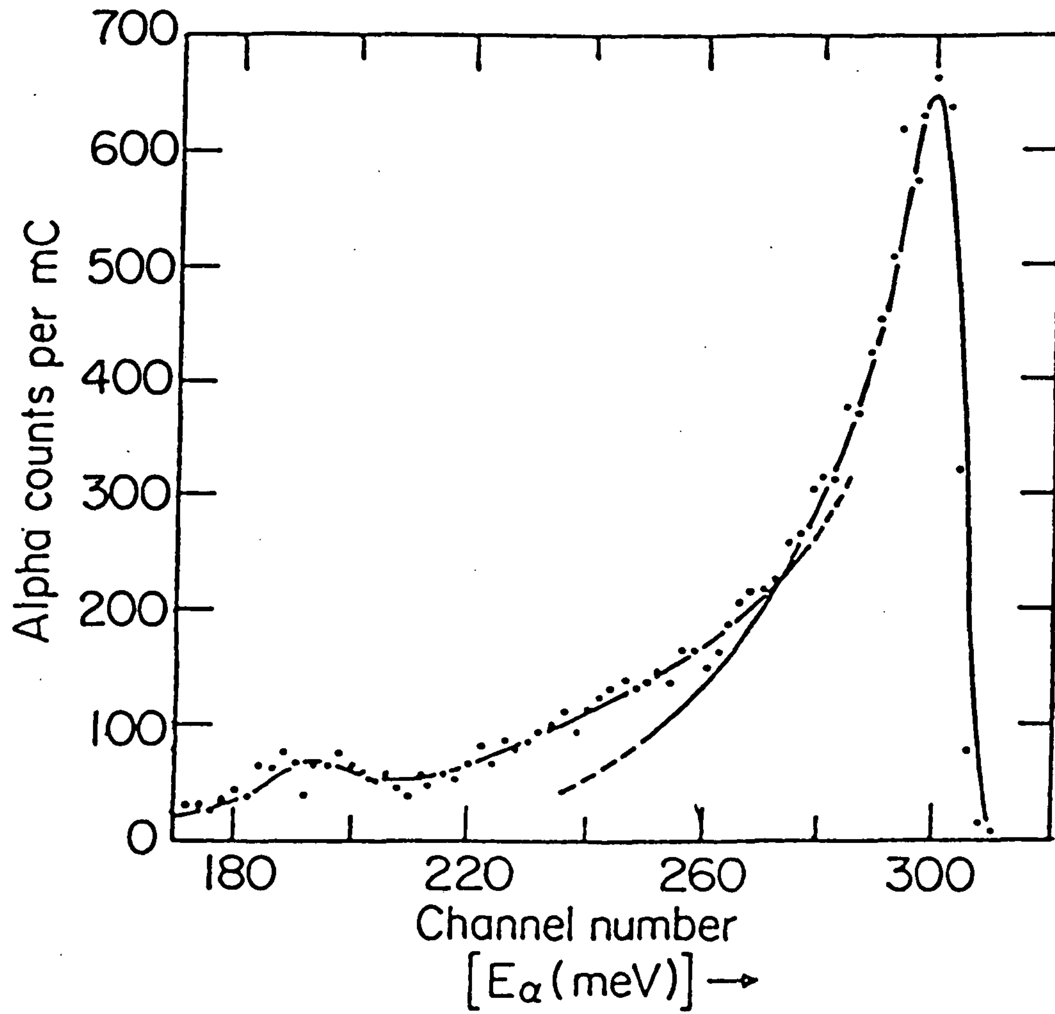

Figure 7. - Tracer profile of Yinnon's sample showing a discontinuity.

(2) Thermal Oxidations

The apparatus described in the main text section for oxygen diffusion in Al_2O_3 was also used to carry out the thermal oxidations. The first oxidation was carried out either in tank oxygen which had been passed over drierite for 24 hours at room temperature or in air with the relative humidity measured with the wet bulk/dry bulb technique. The second oxidation was carried out using the tracer stored in the zeolite flask, which was also passed over drierite for 24 hours. Typically the sample was cooled to room temperature between the two oxidations. This was not desired but rather due to unavoidable equipment limitations.

IV. <u>Results</u>

(1) Qualitative Interpretation

Two samples were oxidized simultaneously on separate shelves at different temperatures, 967° and 1055° C. The oxidation in natural oxygen took place for 3 hr. at 25 min. and the tracer oxidation for 15 hours.

These samples were analyzed using proton activation and the resulting spectra are shown in figures 8 and 9. It was found that these spectra could only be fit with a concentration profile similar to those assumed by Rosencher, et al., which consisted of the bulk of the tracer near the oxide-metal interface and a very narrow profile near the oxide-gas interface, (see figs. 10 and 11). The fit was somewhat insensitive to assumed concentration profiles, that is,

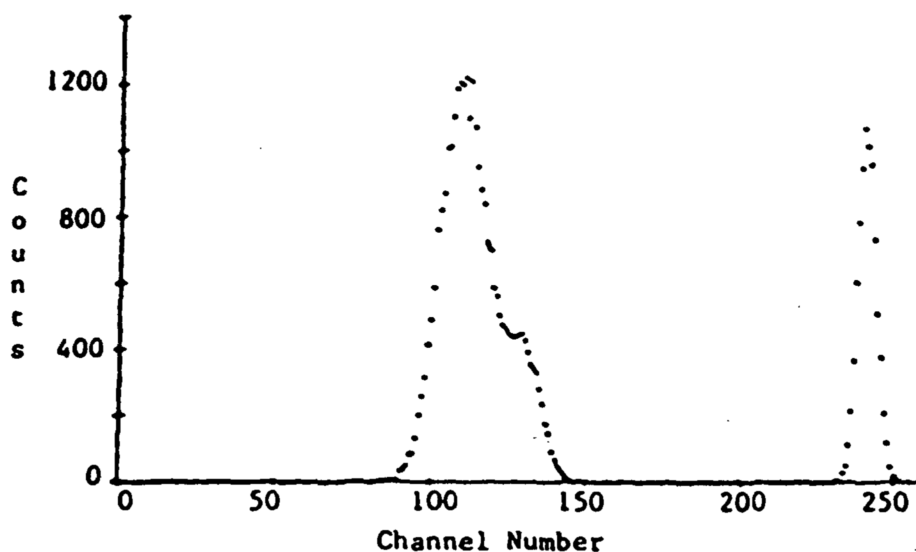

Figure 8. - Proton Activation spectrum of silicon doubly oxidized at 967° C.

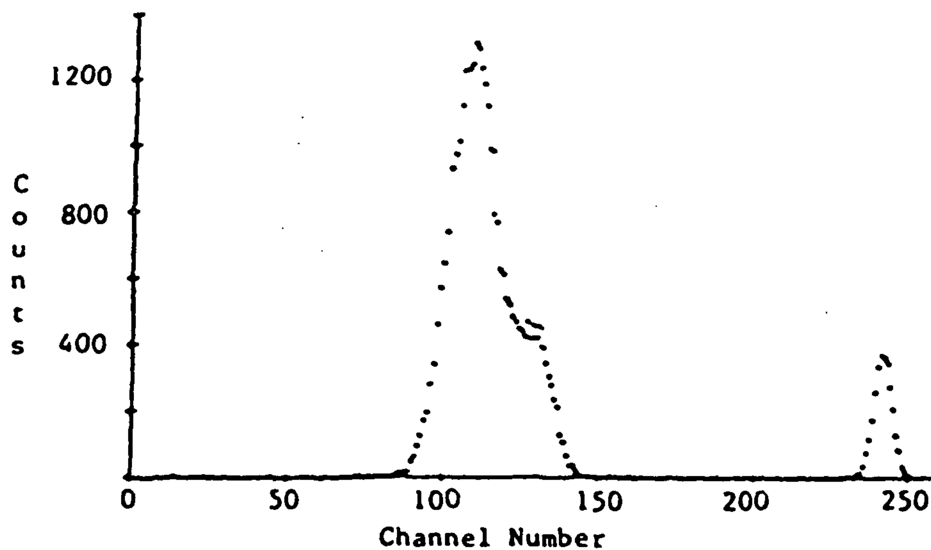

Figure 9. - Proton Activation spectrum of silicon doubly oxidized at 1055° C.

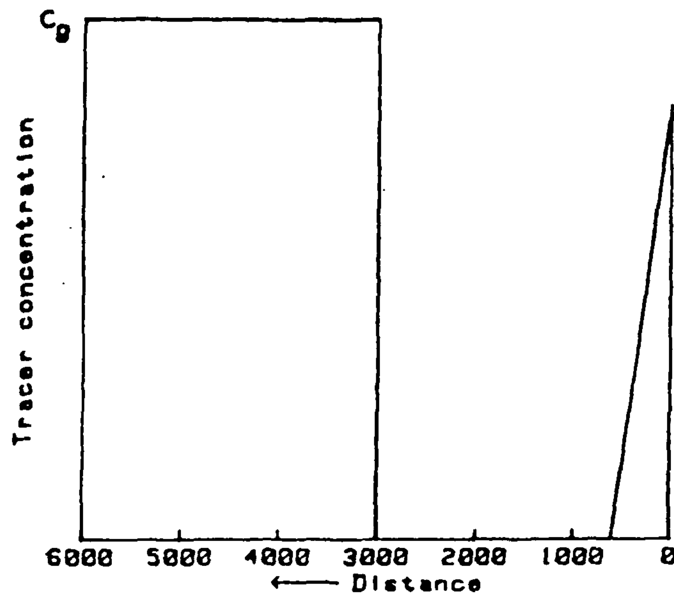

Figure 10. - Assumed concentration profile.

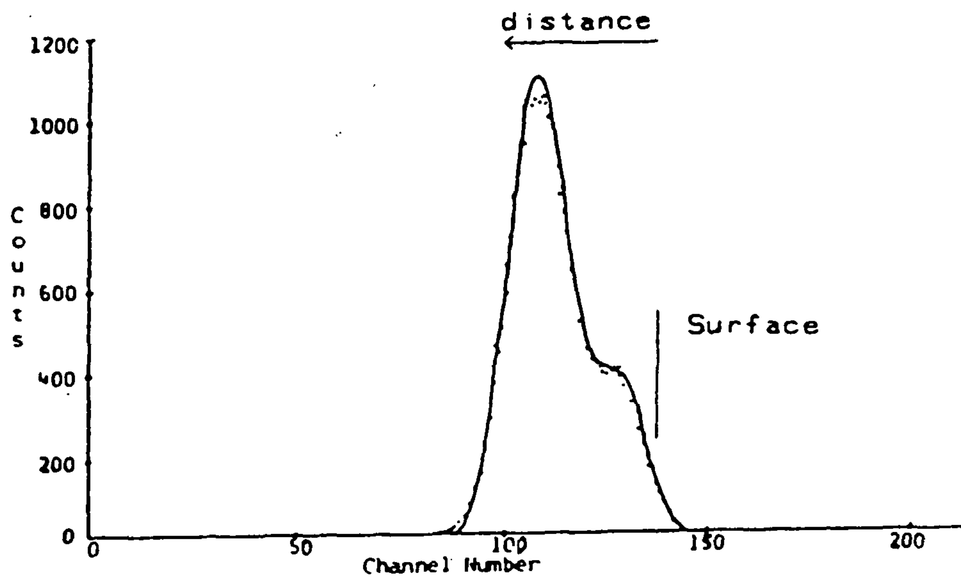

Figure 11. - Fite of assumed concentration profile to proton activation spectrum.

the depth resolution was poor enough so that small scale changes in the profile were not reflected in the spectrum.

One of these samples was re-examined with SIMS. The profile of oxygen-18 and oxygen-16 is shown in figure 12. Due is the much better depth resolution of this technique the two regions of tracer concentration are distinct. The concentration of tracer in both is very near that of the gas, ~40 percent. A region corresponding to the natural abundance of tracer can be seen toward the middle of the scale.

The numerical solution by Clark based on the model of Major and Cooper, does predict near surface enrichments for particular ratios of diffusion to exchange however it does not predict the midscale region of natural abundance to occur at these ratios. With this region of natural abundance the model would predict no tracer near the oxide-gas interface. Note also that in the SIMS spectra the O-18 and O-16 signals are complementary and the Si/SiO_2 interface is sharp.

Three samples were simultaneously oxidized in air at 1000° C for 2 hours. Subsequent to this they were individually oxidized in a tracer enriched atmosphere for times of 3.5 min.[1], 11.5 min., and 37 min. The resulting SIMS profiles are shown in figures 13 to 15. By inspecting these profiles it is clear that tracer is accumulating at both the gas-oxide and the oxide-metal interfaces.

---

[1]These values are approximate because at these short times, the time required to bleed in and remove the tracer is not negligible.

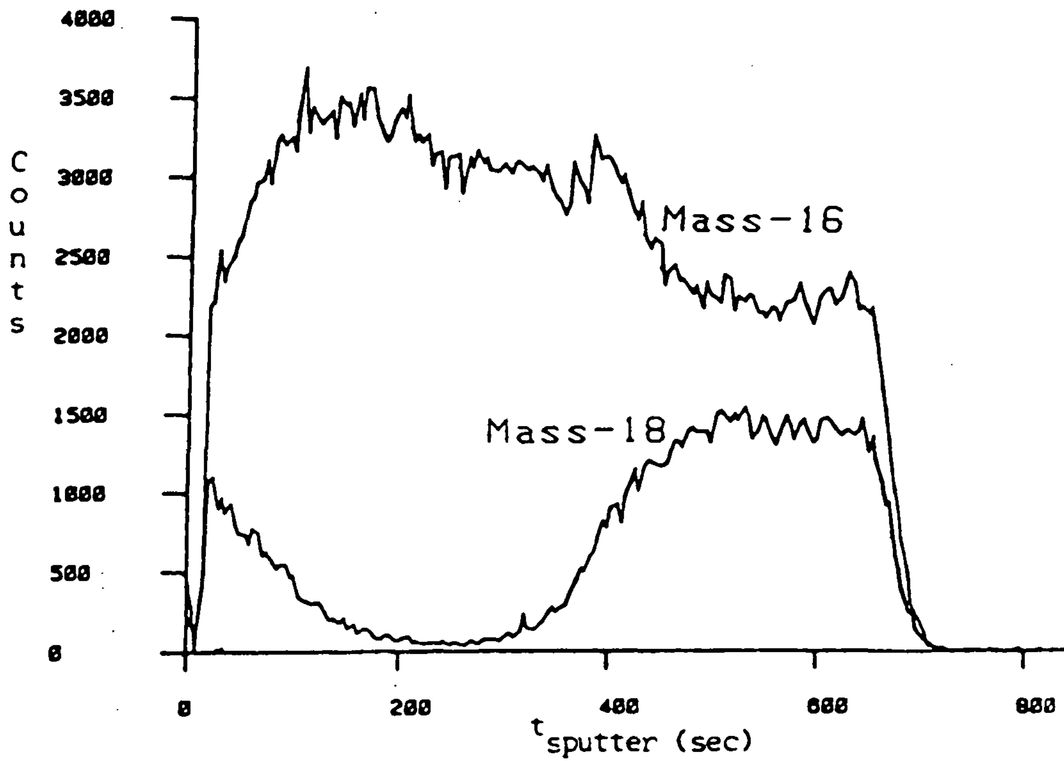

Figure 12. - SIMS profile on a sample oxidized for 3.4 hr in O^{16} and for 15 hr in O^{18} at 967° C.

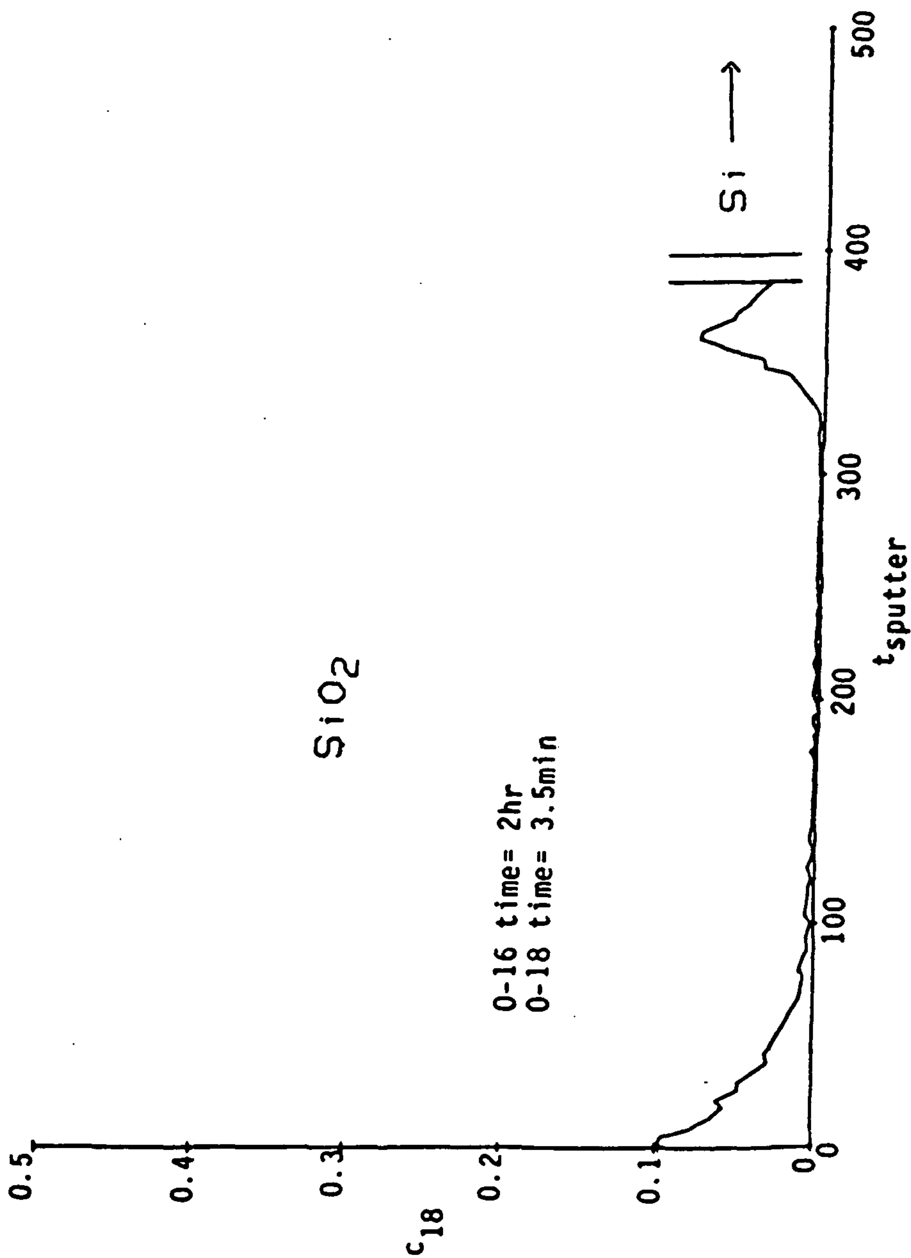

Figure 13. - SIMS profile of sample 2/3.5.

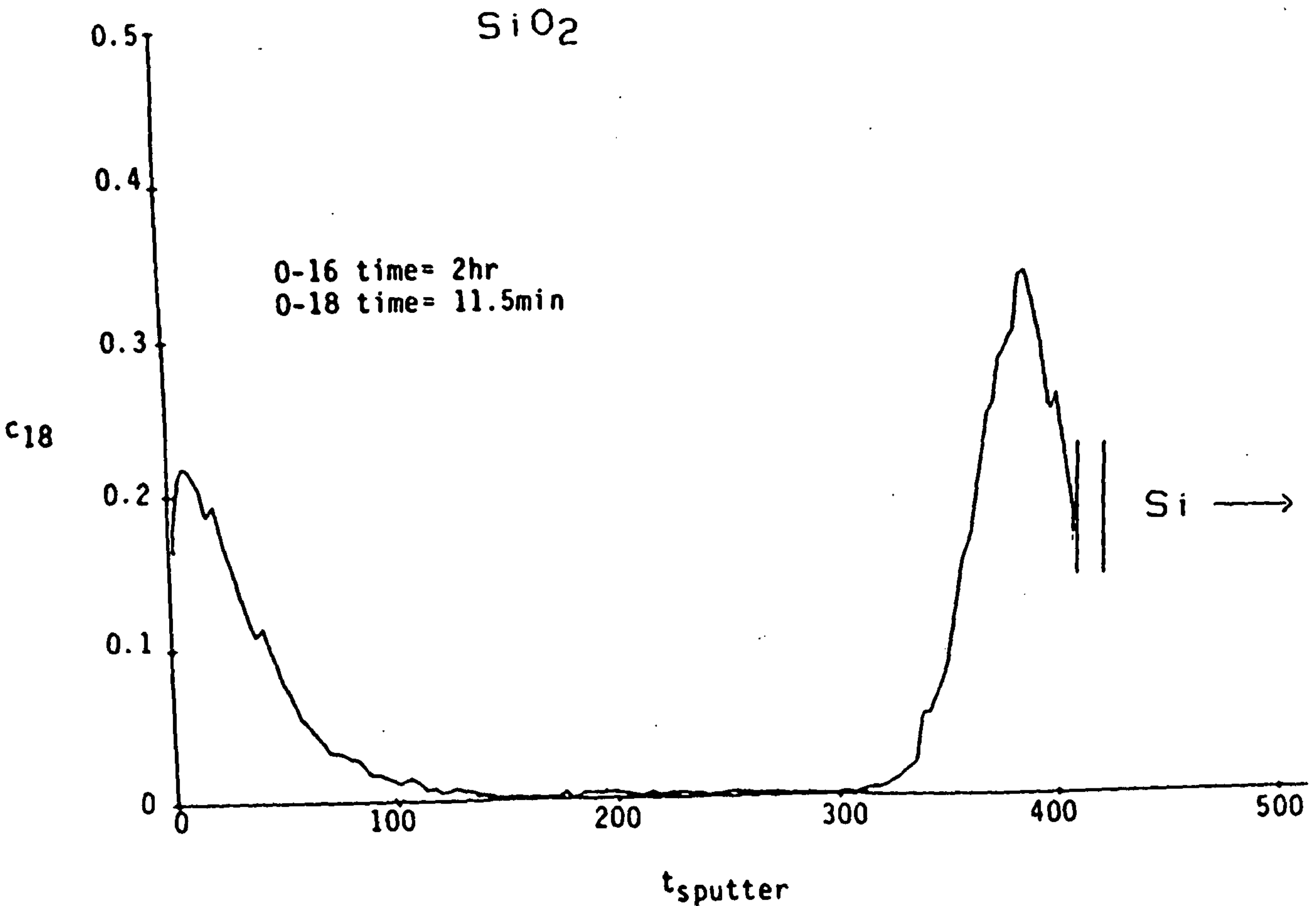

Figure 14. - SIMS profile of sample 2/11.

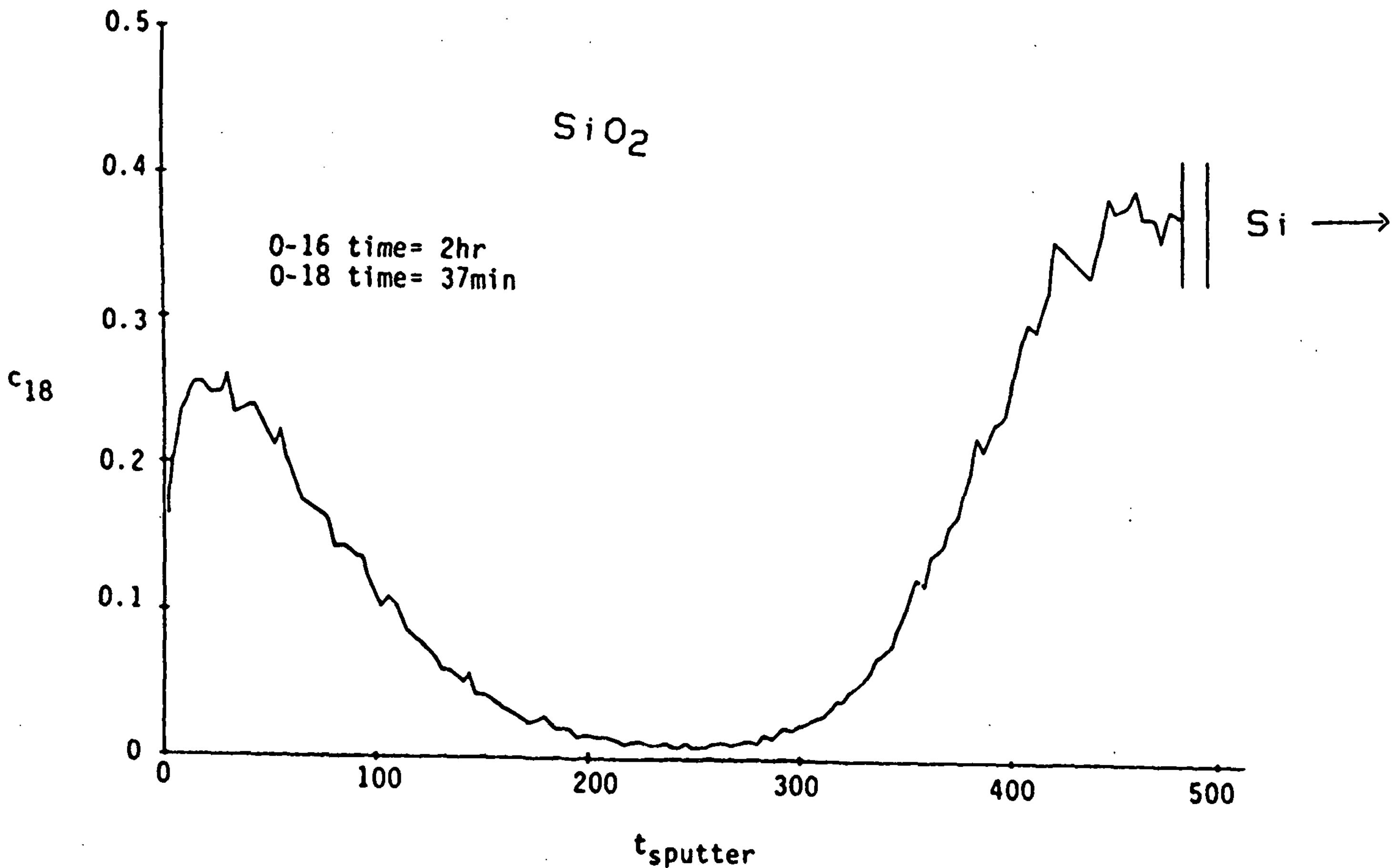

Figure 15. - SIMS profile of sample 2/37.

These regions are separated by a large region devoid of tracer. This implies that they occur by distinct mechanisms. Ordinary gas exchange and self diffusion can give rise to a tracer profile of the type which is observed near the gas-oxide interface while the profile which occurs oxide-metal interface may arise from permeating interstitials which do not frequently interact with the network. Thus from this qualitative inspection there appears to be two independent mechanisms for oxygen transport, network diffusion and permeation.

Secondly, the peak height of the deep profile in the 11.5 min. and the 30 min. experiments (figs. 2 and 3) is greater than that of the near surface profiles. When permeation is the dominating contributor to scale growth and the concentration of tracer at the oxide-metal interface would be expected to accurately reflect the concentration of tracer in the source of gas, since all new oxide is formed with this composition. Any network contribution to growth at this stage would dilute the concentration of tracer at the oxide-metal interface since the network oxygen adjacent to this interface is of lower tracer concentration. The fact that the profile at the gas-oxide interface does not attain the value of tracer in the gas indicates that the kinetics of the reaction between the gas and solid play, at least, a limited role. Unfortunately the concentration of tracer in the gas was not known precisely enough to allow a quantitative determination of the surface reaction coefficient. Note when the tracer exchances take place for longer times, for example 8 hours as in figure 16, the gas-oxide and the oxide-metal

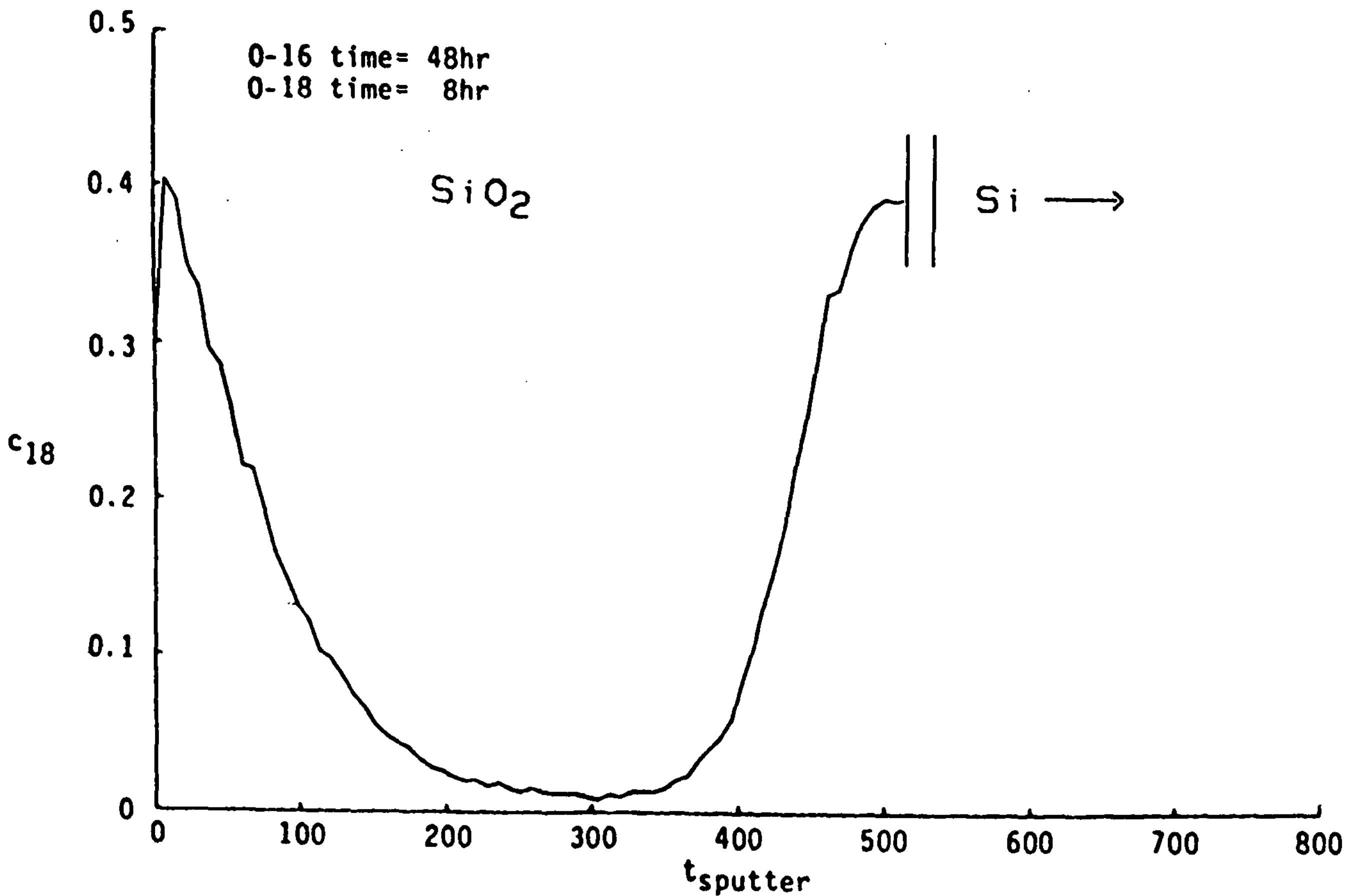

Figure 16. - SIMS profile of sample 48/8.

interface profiles have very near the same tracer concentrations indicating that the surface reaction coefficient is most important at short times.

(2) Mathematics of Double Oxidation Experiments

The thermal oxidation of silicon has been shown to follow linear-parabolic kinetics[2], that is, at short oxidation times the thickness of the oxide scale is directly proportional to the oxidation time while at long oxidation times the thickness of the scale is proportional to the square root of the oxidation time. A basic analysis of linear-parabolic kinetics when the oxidation reaction occurs at the metal oxide interface has been given by Deal and Grove[1]. What follows is essentially a restatement of their work. It should be noted that this treatment assumes there is only one transport mechanism across the growing scale.

Consider a semi-infinite slab of silicon covered with an initial film of SiO_2 sufficiently thick that steady state has been reached (see schematic shown in fig. 17). In this case the oxidant must go through the following stages:

(i) It is transported from the bulk gas to the gas-oxide interface where it reacts or is absorbed.

(ii) It is transported from the gas-oxide interface towards the oxide-metal interface.

(iii) It reacts at the oxide-metal interface to form SiO_2. The assumption of steady state means these three fluxes are equal.

The steady state fluxes are mathematically modeled as follows. The flux, J_1, of the oxidant from the gas to the surface of the

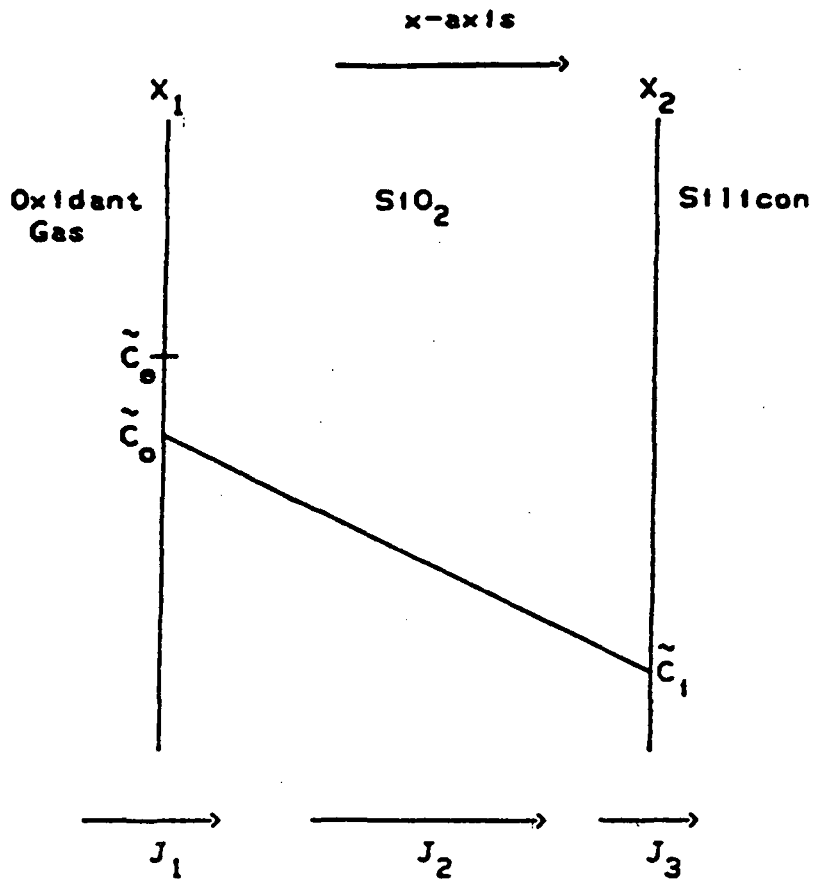

Figure 17. - Schematic of fluxes during oxidation.

oxide is:

$$J_1 = K(\tilde{c}_e - \tilde{c}_o) \quad \text{(A-1)}$$

where K is a surface reaction coefficient, $\tilde{c}_e$ is the equilibrium concentration of oxidant in the scale and $\tilde{c}_o$ is the concentration of oxidant in the scale at $X = 0$. Note: $\tilde{c}_o$ should not be considered to be normal $O^{=}$ in network.

The flux of oxidant across the oxide layer, J_2, given by Fick's First Law:

$$J_2 = -D_{eff} \frac{\partial \tilde{c}}{\partial x} \quad \text{(A-2)}$$

where $\partial \tilde{c}/\partial x$ is the concentration gradient of oxidant across the scale and D_{eff} is the effective diffusion coefficient which is not necessarily equal to the self diffusion coefficient, as will be discussed. It follows from the assumption of steady state that the flux, J_2, is not a function of position within the scale. When D_{eff} is also independent of position the consequence is that $\partial \tilde{c}/\partial x$ is also a constant and equation (A-2) may be rewritten as:

$$J_2 = D_{eff} \frac{(\tilde{c}_o - \tilde{c}_1)}{(X_2 - X_1)} \quad \text{(A-3)}$$

The flux corresponding to the oxidation reaction is given by a first reaction:

$$J_3 = k_s \tilde{c}_1 \quad \text{(A-4)}$$

Also from steady state it may be stated that:

$$J = J_1 = J_2 = J_3 \quad \text{(A-5)}$$

From these equalities it is possible to solve for C_1 and C_0:

$$\tilde{c}_1 = \frac{\tilde{c}_e}{1 + k_s/K + k_s(X_2 - X_1)/D_{eff}} \tag{A-6}$$

$$\tilde{c}_o = \frac{\tilde{c}_e(1 + [k_s(X_2 - X_1)/D_{eff}])}{1 + k_s/K + k_s(X_2 - X_1)/D_{eff}} \tag{A-7}$$

It is easy to see by back substitution of A-6 into A-4 that:

$$J = J_3 = \frac{k_s\tilde{c}_e}{1 + k_s/K + k_s(X_2 - X_1)/D_{eff}} \tag{A-8}$$

Now, the rate at which the oxide grows is given by:

$$N_1 \frac{d}{dt}(X_2 - X_1) = J = \frac{k_s\tilde{c}_e}{1 + k_s/K + k_s(X_2 - X_1)/D_{eff}} \tag{A-9}$$

where N_1 is the molar density of oxygen in the scale. With the initial condition that:

$$(X_2(t) - X_1(t))_{t=0} = X_i$$

where X_i is an arbitrary initial thickness of oxide and integration, the following expression is obtained:

$$(X_2 - X_1)^2 + A(X_2 - X_1) = B(t + \tau) \tag{A-10}$$

where

$$A = 2\, D_{eff}\left(\frac{1}{k_s} + \frac{1}{K}\right)$$

$$B = \frac{2 D_{eff} \tilde{c}_e}{N_1}$$

and

$$\tau = \frac{x_1^2 + Ax_1}{B}$$

Note τ corresponds to a shift in the time coordinate to account for the initial oxide thickness, x_1, solving for $(X_2 - X_1)$ gives

$$(X_2 - X_1) = \frac{A}{2} \{ 1 + (\frac{t + \tau}{A^2/4B}) \}^{1/2} - \frac{A}{2} \quad \text{(A-11)}$$

For short times such that $(t + \tau) << A^2/4B$ this reduces to linear kinetics where:

$$(X_2 - X_1) = \frac{A}{B} (t + \tau) \quad \text{(A-11b)}$$

And for long times such that $(t + \tau) >> A^2/4B$ this reduces to parabolic kinetics where:

$$(X_2 - X_1) = B^{1/2} (t + \tau)^{1/2} \quad \text{(A-11c)}$$

The above analysis of Deal and Grove may be applied to the analysis of a "double oxidation" experiment. In this type of experiment a semi-infinite slab of silicon is thermally oxidized for a given time τ to give an initial oxide thickness X_1. At time τ the isotopic makeup of the atmosphere is altered, in this study by increasing the isotopic fraction of oxygen-18, and the oxidation is allowed to continue. After the oxidation is terminated, the location

of the tracer is determined by such techniques as proton activation or SIMS in order to give insight into the underlying mechanisms.

It has been shown that tracer enrichments develop independently at both the gas-oxide interface and the oxide-metal interface. The implication of this is that oxygen may be transported across the scale by two independent mechanisms. In the following discussion oxygen will be considered to be mobile through the network by a defect mechanism and also mobile through noninteracting interstitials.

The expression for the incorporation of tracer when convection plays a role is:

$$J_{18} = -D \frac{\partial c}{\partial x} + vc \tag{A-12}$$

where c is now the fractional concentration of tracer and v is the convective velocity.

There are two separate types of contributions to the velocity term. One occurs due to a moving boundary or flow of the system, while the other one results from the oxygen potential gradient across the scale. The latter is analogous to vacancy "wind" under a field considered by Manning. Equation (A-12) may be rewritten as:

$$J_{18} = -D_{sd} \frac{\partial c}{\partial x} + c - \frac{D_{eff} \tilde{c}}{RT} \frac{\partial \mu}{\partial x} + v_{mb}c \tag{A-13}$$

where D_{sd} is the self diffusion of oxygen, D_{eff} is the ambipolar diffusion coefficient responsible for oxidation, c is the concentration of oxygen-18, $\tilde{c}$ is the concentration of the defect responsible for network diffusion, $\partial\mu/\partial x$ is the chemical potential gradient in oxygen, and v_{mb} is the velocity of the moving boundary.

It is convenient to consider the two profiles within each sample independently and use two sets of coordinates. For the profile near the gas-oxide interface the observer A in figure 18, which is fixed to the gas-oxide interface is appropriate and the coordinate system x_a is used. In this coordinate system X_1 is defined as zero and x is positive towards the oxide-metal interface.

The convective velocity due to a moving boundary seen by observer A is zero since all growth takes place at the oxide-metal interface and A-13 reduces to:

$$J_{18} = -D_{sD} \frac{\partial c}{\partial x} + c \cdot \frac{D_{eff}\, \tilde{c}}{RT} \frac{\partial \mu}{\partial x} \qquad \text{(A-14)}$$

Now let us examine the near surface profiles developed in two samples, one of which was oxidized in air for 16 hours and the other for 48 hours. Both samples were then oxidized in a tracer enriched atmosphere for 8 hours.

Figure 19 shows a superposition of the SIMS profiles from these samples. The near surface profiles are seen to be coincident. The tracer concentration profiles are identical for both. Since the self diffusion term is uninfluenced by oxide thickness, the convective terms from the chemical potential gradient must also be equivalent for the two samples to have the same tracer fluxes.

$$c \cdot \frac{D_{eff}\, \tilde{c}}{RT} \frac{\partial \mu_1}{\partial x_1} = c \cdot \frac{D_{eff}\, \tilde{c}}{RT} \frac{\partial \mu_2}{\partial x_2}$$

With the assumptions of ideal solution, steady state and parabolic kinetics this equality may be rewritten:

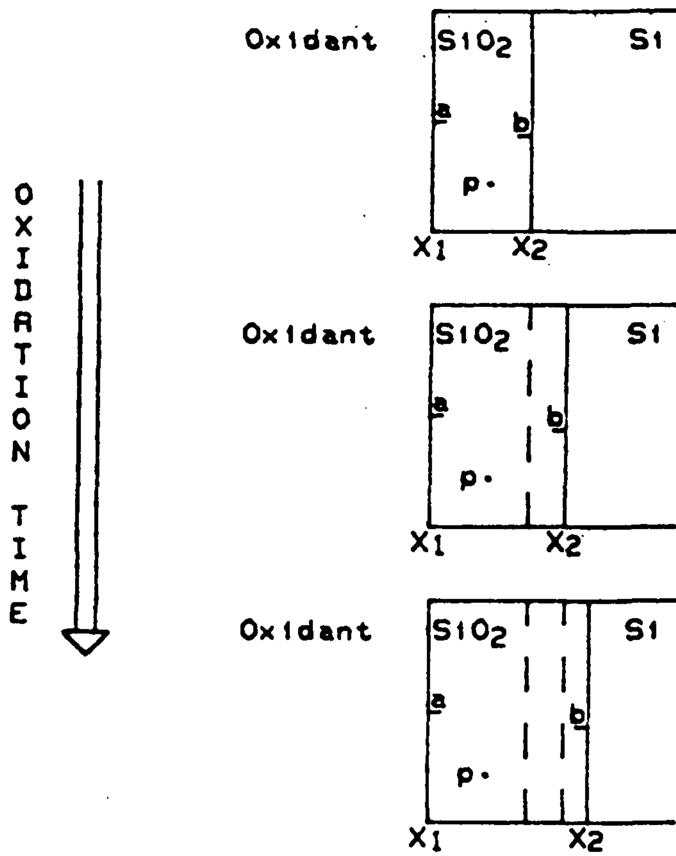

Two coordinate systems
in x_a $X_1=0$ and X_2 is considered moving and positive
in x_b $X_2=0$ and X_1 is considered moving and positive

Figure 18. - Schematic of coordinate systems for double oxidation.

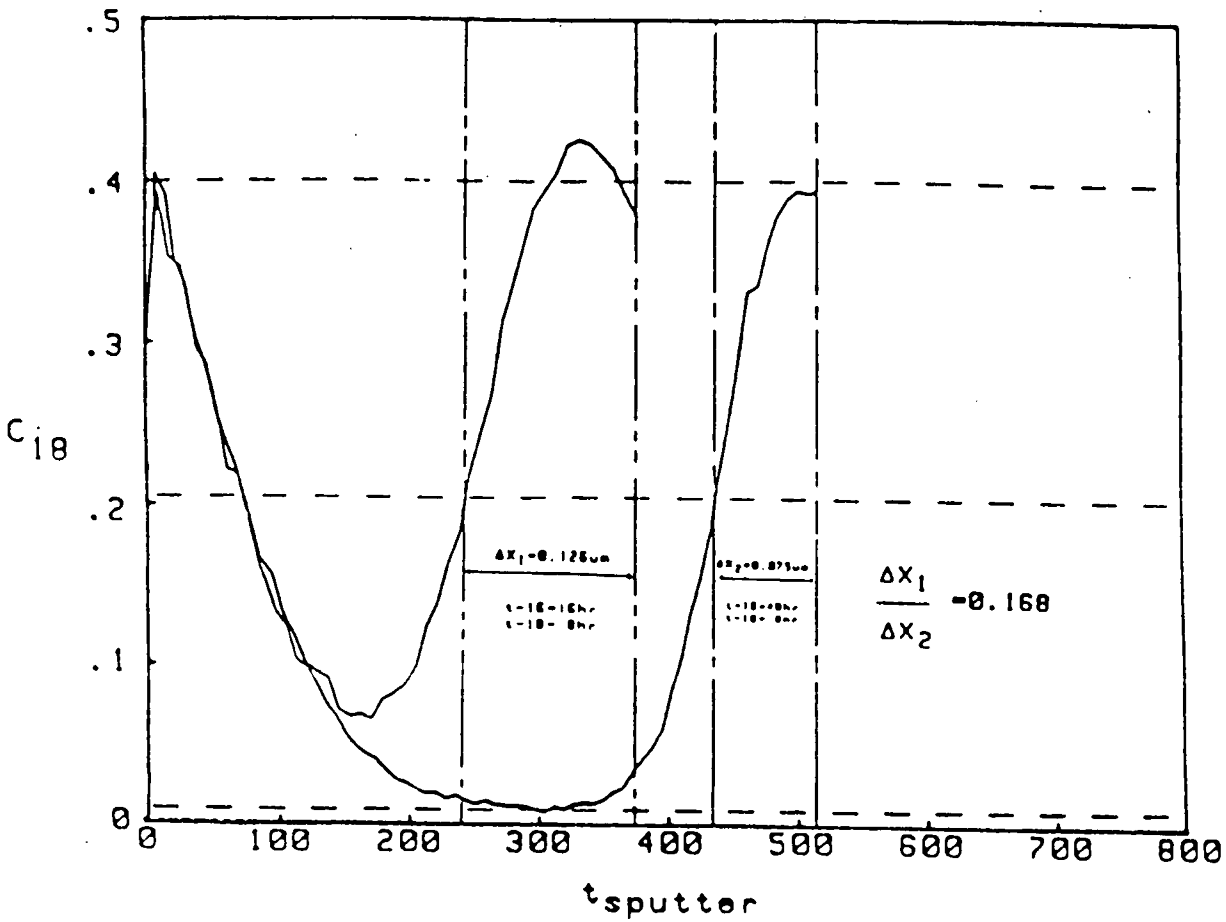

Figure 19. - Superposition of SIMS profiles from 2 samples, one oxidized for 48 hr in air the other for 16 hr. Both then were oxidized for 8 hr in $^{18}O_2$, at 1000° C.

- ideal solution

$$\mu = RT \ln \tilde{c}$$

$$\frac{\partial \mu}{\partial x} = \frac{RT}{\tilde{c}} \frac{\partial \tilde{c}}{\partial x}$$

- steady state

$$\frac{\partial \tilde{c}}{\partial x} = \frac{(\tilde{c}_0 - \tilde{c}_1)}{X_2 - X_1}$$

- parabolic kinetics

$$X_2 - X_1 = B^{1/2} (t_2 + \tau_1)^{1/2}$$

$$c \cdot D_{eff} \frac{(\tilde{c}_0 - \tilde{c}_1)}{B^{1/2} (t_1 + \tau_1)^{1/2}} = c \cdot D_{eff} \frac{(\tilde{c}_0 - \tilde{c}_1)}{B^{1/2} (t_2 + \tau_2)^{1/2}}$$

The only experimental variable in this term is the time, $(t + \tau)^{1/2}$. When $t_1 + \tau_1 \neq t_2 + \tau_2$ the only way these may be equal is if a constant has a value of zero or infinity. Infinite value of any of these may be rejected on physical grounds. Because the value of $\tilde{c}_0$ and $\tilde{c}_1$ are fixed at the edges of the scale and the parabolic rate constant is non zero it follows that the effective diffusion network coefficient is zero. This is a bit surprising since oxygen is mobile in the network. It would be expected to travel down the oxygen activity gradient. However, as previously mentioned, it is pointed out by Raleigh that the motion of ionic species across the network must involve the transport of electrical charge. Raleigh

cites experimental work of Schmalzried which indicated that at 1000° C SiO_2 is a pure ionic conductor. Further the work of Jorgenson, interpreted by Raleigh, indicates that when an external path for electrons is provided, an increase in the oxidation rate is observed. In sum this indicates that at temperature 1000° C the electrical conductivity of SiO_2 is sufficiently low that no network diffusion of an ionic species is permitted to relieve the activity gradient.

The superposition of the profiles in figure 7 also provide an opportunity to test a prediction of the model of Revesz and Schaeffer[14]. Recall that this model predicts that the network diffusivity will decrease as annealing time increases, and that the permeation rate will increase. The coincidence of the self diffusion profile indicates that the network diffusion coefficient is unaffected by the 32 hour difference in annealing time prior to exposure to tracer.

The quantity of tracer which was incorporated into the scale may be accurately estimated by taking the distance from the oxide-metal interface to the point at which the tracer concentration drops to 1/2 of its plateau value. This is illustrated in figure 19. The experimental value of 1.68 compares very well with a value of 1.62 calculated on the basis of parabolic kinetics indicating that the rate of permeation is also unchanged. The prediction of Revesz and Schaeffer is not borne out.

Now consider the flux of tracer into the oxide near the oxide-metal interface. The fact that the tracer is being carried by a

species which does not interact with the network until reacting at the oxide-metal interface allows the specification of a boundary condition at X_2. The background produced due to the presence of a permeating species is in the ppm range and may be neglected. In this case it is convenient to use a coordinate system fixed to the oxide-metal interface with X_2 and X, seen as positive and moving.

From the point of view of observer B, x = 0 at X_2, there is a convective flux of oxygen that is equal to the growth rate of the scale given by:

$$\frac{\partial}{\partial t}(X_2 - X_1) = \frac{\partial}{\partial t}\left(\frac{A}{2}\left\{1 + \left(\frac{t+\tau}{A^2/4B}\right)\right\}^{1/2} - \frac{A}{2}\right) = \frac{1}{A/B}\left\{1 + \left(\frac{t+\tau}{A^2/4B}\right)\right\}^{-1/2} \quad \text{(A-16)}$$

For long times when the oxidation may be approximated by parabolic kinetics:

$$\frac{\partial}{\partial t}(X_2 - X_1) = \frac{\partial}{\partial t} B^{1/2}(t+\tau)^{1/2} = \frac{B^{1/2}}{2(t+\tau)^{1/2}} \quad \text{(A-17)}$$

Therefore the flux of tracer into the oxide near observer B is:

$$J_{18} = -D_{sD}\frac{\partial c}{\partial x} + c \cdot \frac{B^{1/2}}{2(t+\tau)^{1/2}} \quad \text{(A-18)}$$

In partial differentiation form the diffusion equation (A-12) takes the form:

$$\frac{\partial c}{\partial t} = -\frac{\partial J}{\partial x} = D\frac{\partial^2 c}{\partial x^2} - v\frac{\partial c}{\partial x} \quad \text{(A-19)}$$

This equation has been solved (see Appendix C) for both the case of constant v and the case where v has a time dependancy of $t^{-1/2}$, under the simple boundary conditions

$$c(x,t) = 1 \quad X = 0 \text{ and } t > 0$$

$$c(x,t) = 0 \quad X \rightarrow \infty \text{ and } t \geq 0$$

and the initial condition

$$c(x,t) = 0 \quad 0 \leq X \leq \infty \text{ and } t = 0$$

However, the double oxidation experiment requires a moving boundary with a time dependancy of $(t + \text{const})^{-1/2}$. The solution to the partial differential equation with this type of coefficient remains ellusive. When τ is small compared to t it may be neglected and v has the character of $t^{-1/2}$. When τ is large compared to t the value of v may be taken as a constant.

Three samples were fit using solutions to the diffusion equation. One sample was oxidized at 960° C under 0-16 for 3.5 hours and the 0-18 for 15 hours. Two samples were oxidized at 1000° C. One was oxidized under 0-16 for 16 hours and the other one was oxidized for 48 hours. Then both were oxidized together under tracer for 8 hours.

Other samples such as those shown in the qualitative discussion were not in the regime of the parabolic kinetics and quantitative fits were not attempted.

The predicted profiles were obtained by superimposing a near surface and a deep profile. In all cases the near surface or gas-oxide interface profile was generated using assumed values for the diffusion coefficient in the familiar solution for a semi-infinite slab

$$c(x,t) = c_0 \text{ erfc } \left(\frac{X}{2\sqrt{Dt}}\right)$$

For the deep or oxide-metal interface profiles, two different solutions were used. It was found that for the samples exchanged at 1000° C the use of average velocity, by treating $t + \tau$ as a constant, produced small, 10 percent, errors (see figs. 20 and 21) and the solution for constant v was employed:

$$C(\theta,\phi) = \frac{1}{2} \{\text{erfc}(\theta - \phi) + \exp(4\theta\phi)\text{erfc}(\theta + \phi)\}$$

where

$$\theta = \frac{X}{2 \sqrt{Dt}}$$

$$\phi = \sqrt{\frac{v^2 t}{4D}} = \frac{v}{2} \sqrt{\frac{t}{D}}$$

v = velocity of the moving boundary

In the case of the sample exchanged at 960° C it was found that the boundary velocity might be better approximated using a $t^{1/2}$ times a constant, see figure 22, and the solution for $v = v(t^{-1/2})$ was used.

$$C(x,t) = \frac{\text{erfc } \left(\frac{X}{2\sqrt{Dt}} - \frac{\beta}{\sqrt{D}}\right)}{\text{erfc } \left(\frac{-\beta}{\sqrt{D}}\right)}$$

where

$$\beta = v \, t^{1/2}$$

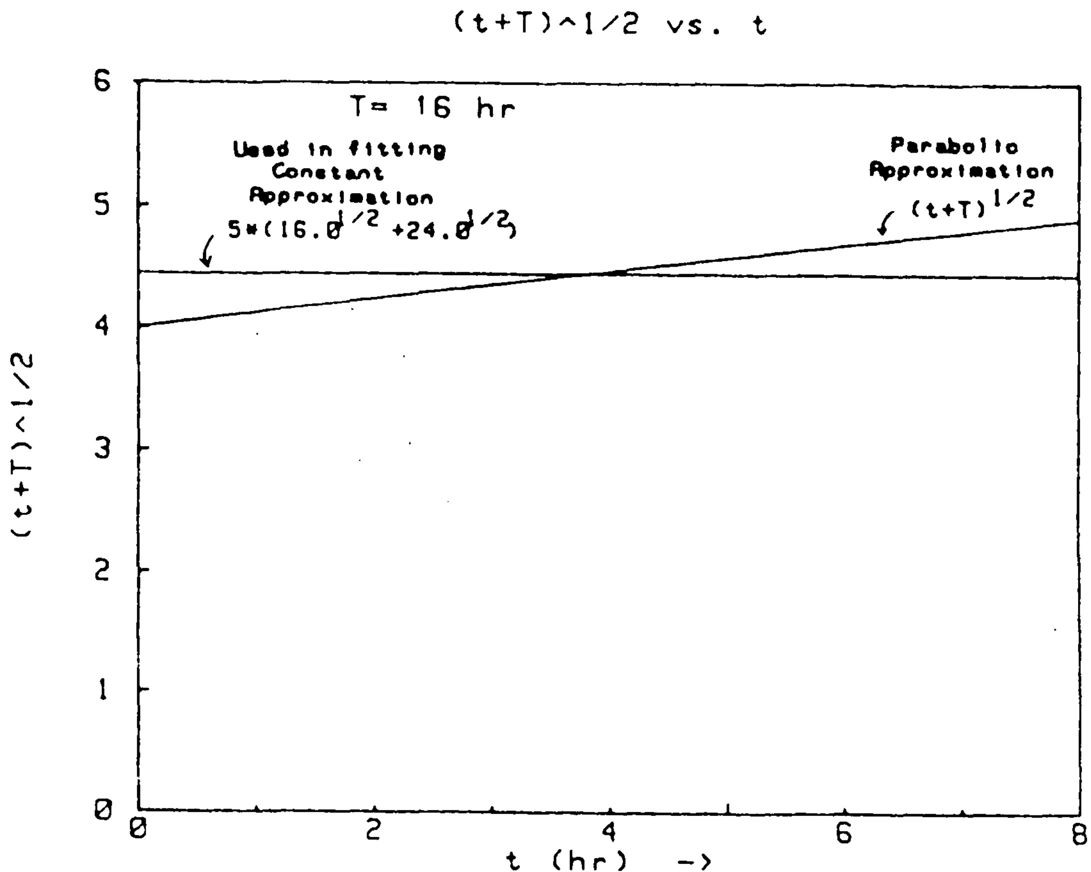

Figure 20. - Illustration of the velocity approximations for sample 16/8.

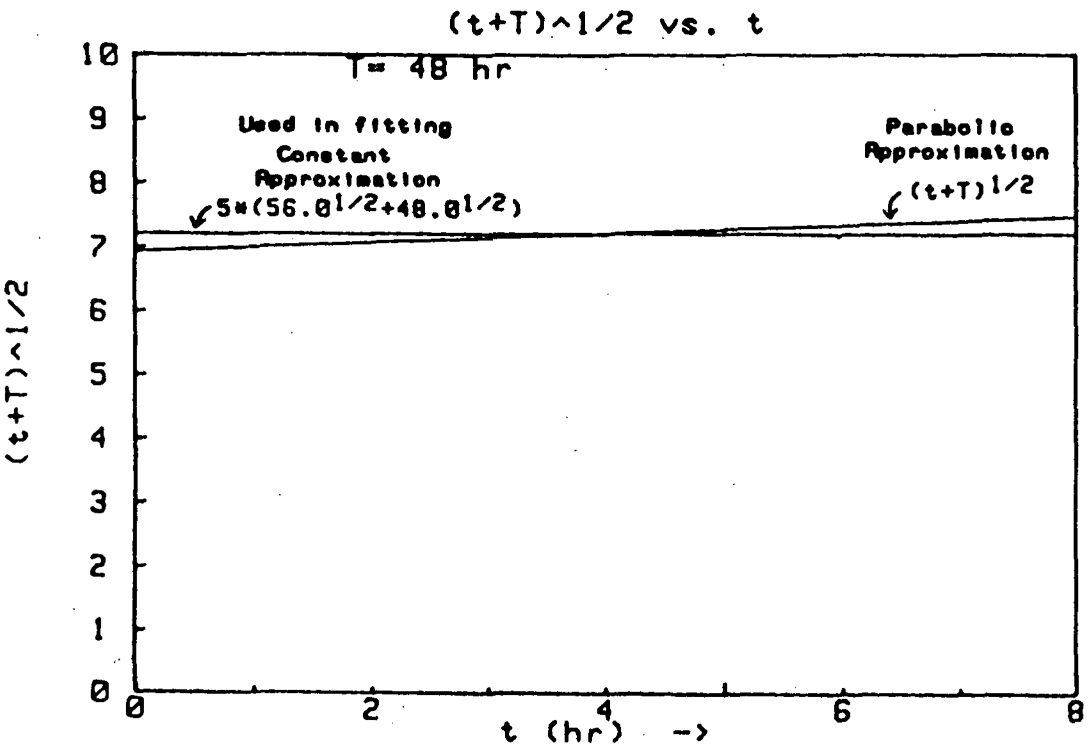

Figure 21. - Illustration of the velocity approximations for sample 48/8.

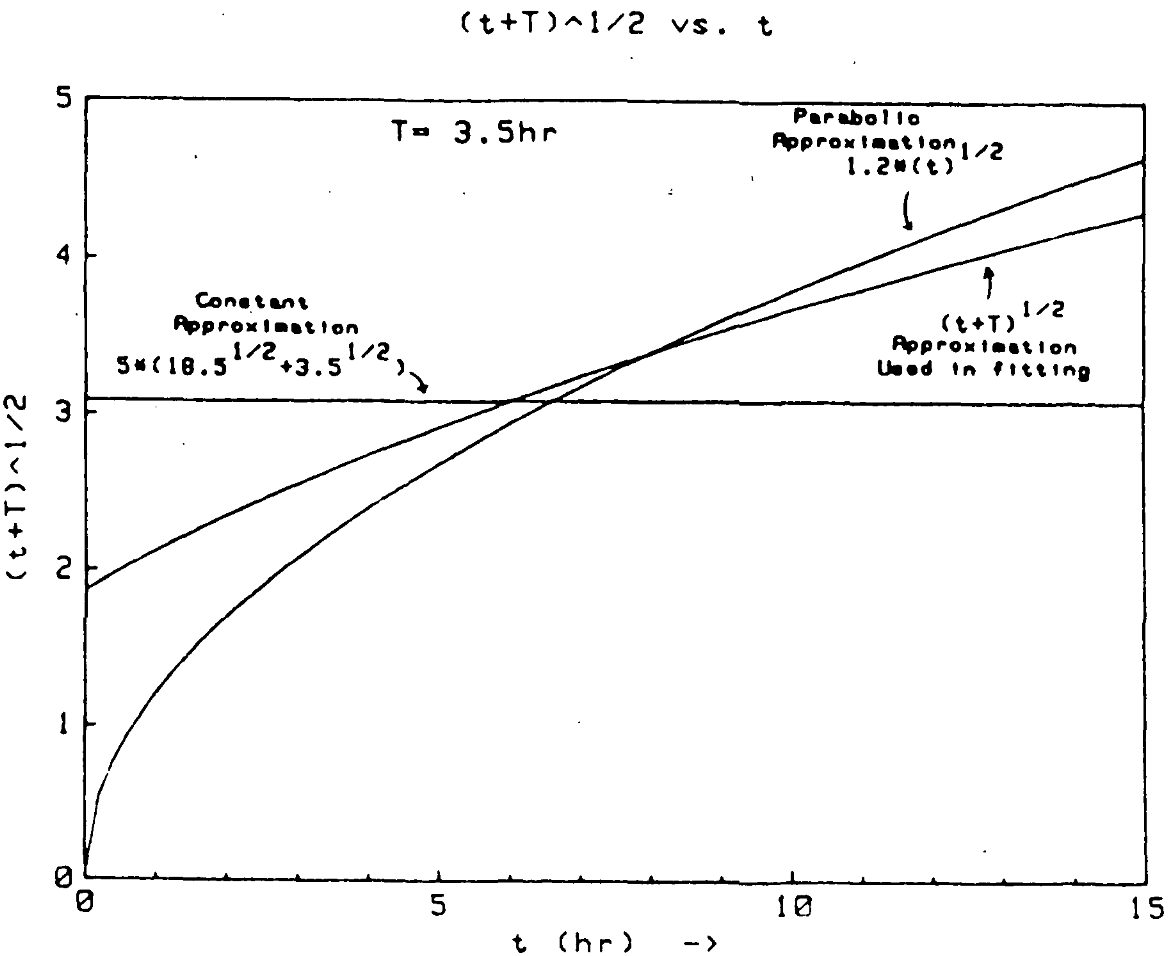

Figure 22. - Illustration of velocity approximations of the SiO_2/Si interface for the sample 3.5/15.

The SIMS profiles for the samples as well as the predicted fits are shown in figures 23 to 25. Good fits could be obtained provided different values of the diffusion coefficients were allowed for near surface and deep profiles. The fact that differing values were required may be due to differences in composition as a function of position. The difference may also be contributed to by the known approximations in the model, which include:

(i) The neglection of reactions rate constants are both the gas-oxide interface (where there is qualitative evidence that it is required) and oxide-metal interface,

(ii) The assumption that the boundaries move at a rate which is known to be different than reality, and

(iii) The assumption that the growth kinetics are pure parabolic.

This knowledge, coupled with the fact that the apparent diffusivities differ only by a factor less than five leads to the conclusion that these are fairly reliable estimates. The values are only the low side of the reported values for oxygen diffusivity in v-SiO_2. This may be due to the fact that tracer uptake studies cannot separate out the components of the two mechanisms.

Values for the parabolic rate constant may be extracted from the boundary velocity term. The value obtained at 960° C, K_p = 9700 $Å^2$/min compares well with a linear interpolation of the data of Irene for a 25 ppm H_2O K_p = 8000 $Å^2$/min. The values obtained at 1000° C k_p = 30,900 $Å^2$/min and K_p = 28,000 $Å^2$/min for the 18 and 48 hour samples respectively, also compare well with Irene's values

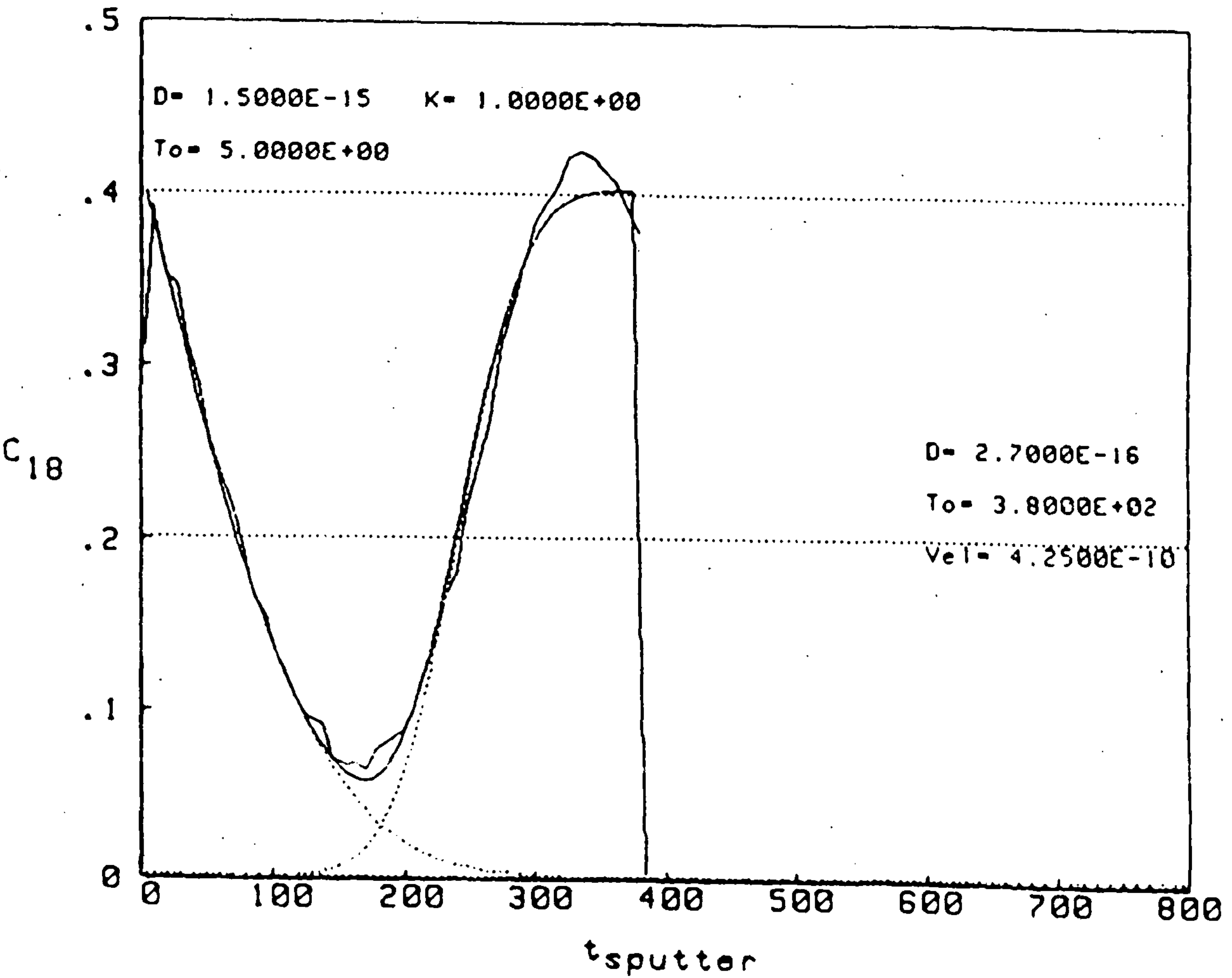

Figure 23. - SIMS profile and fit to a sample oxidized in air for 16 hr and for 8 hr in $^{18}O_2$.

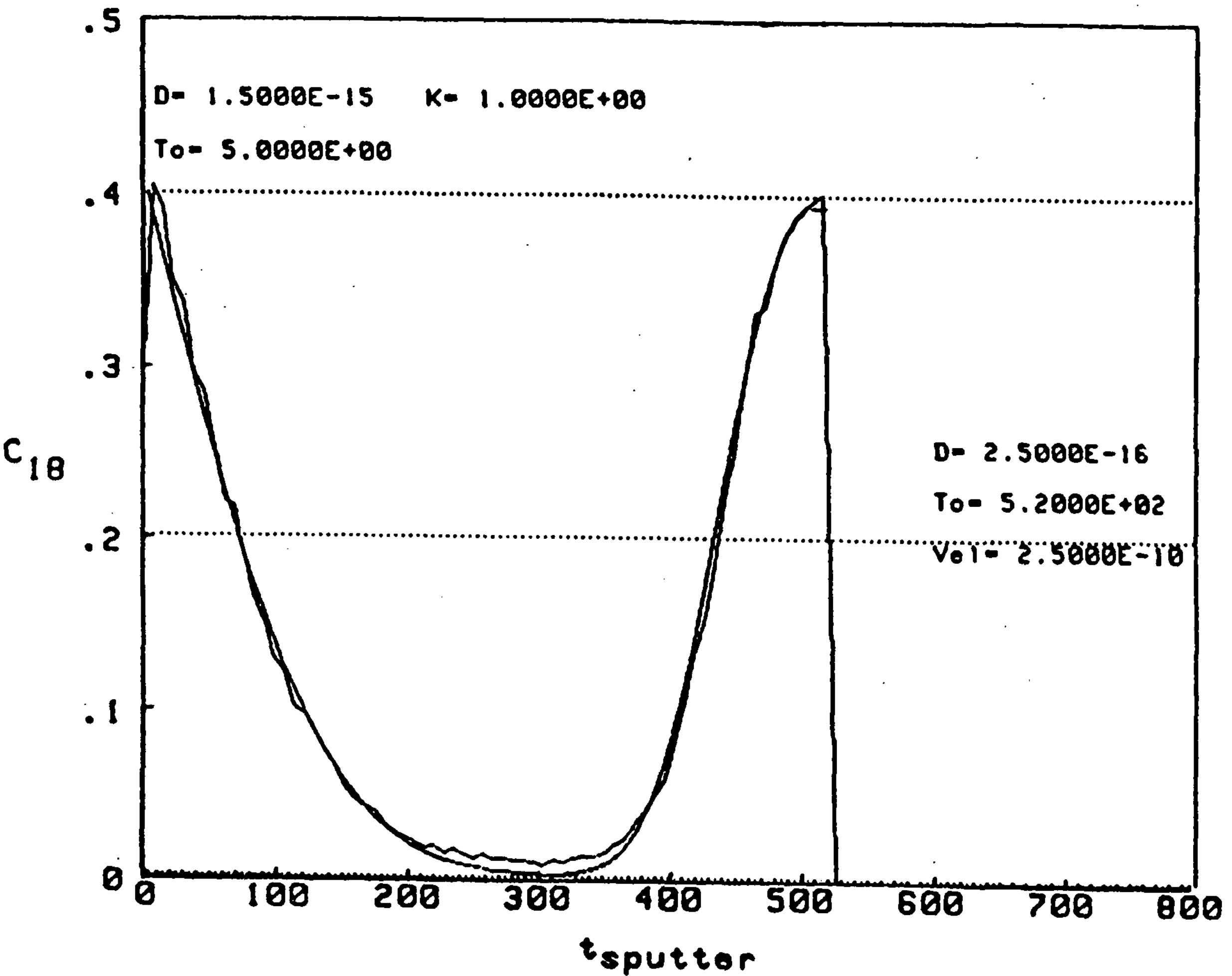

Figure 24. - SIMS profile and fit on a sample oxidized for 48 hr in air and 8 hr in $^{18}O_2$.

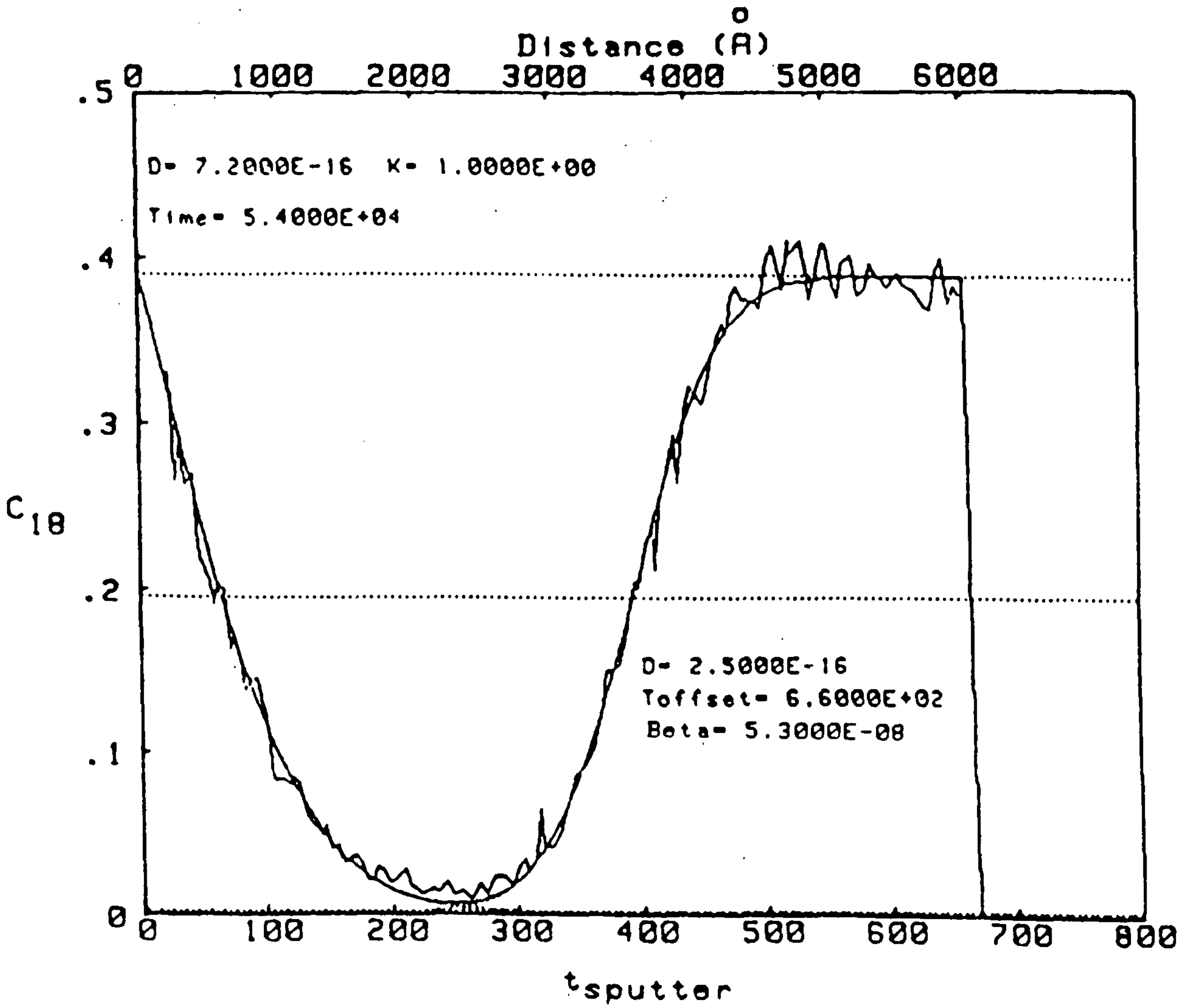

Figure 25. - SIMS profile and fit to a sample oxidized for 3.5 hr in $^{16}O_2$ and 15 hr in $^{18}O_2$.

K_p = 12,000 $Å^2$/min. The differences could easily arise from low levels of water contamination.

The results are summarized in table A-I.

V. Summary

It has been shown that SIMS is an excellent tool for the study of silicon oxidation through the double oxidation technique. This is primarily due to the very good depth resolution.

It has also been shown that in a double oxidation experiment there are two independent fluxes of tracer into the scale, a self diffusive flux within the network and a permeative flux through the scale to the metal. Further, the flux of oxygen through the network is pure self diffusion and does not contribute to scale growth. The motion of the network ionic species is prevented due to the very low electrical conductivity. It is plausible that scales grown on heavily doped silicon may contain impurities sufficient to increase the conductivity and allow network diffusion to contribute to growth.

TABLE A-I. SUMMARY OF DOUBLE OXIDATION RESULTS

Temperature, °C	Time-16	Time-18	D_{near} surface	D_{deep}	K_p
960	3.5 hr	15 hr	7.2×10^{-16} cm^2/s	2.5×10^{-16} cm^2/s	9700 $Å^2$/min
1000	16	8	1.5×10^{-15}	2.7×10^{-16}	30,900
1000	48	8	1.5×10^{-15}	2.5×10^{-16}	28,000

It has been observed that heavily doped silicon displays increased rates of oxidation[21].

Finally, a model is given which, though refinements are needed, predicts very well the tracer profiles in the double oxidation experiments.

VI. Suggestions for Future Work

1. The apparatus employed in this work was not well suited for either low P_{H_2O} experiments or for switching the isotopic atmosphere at temperature. All further work should be carried out in a thoughtfully designed setup.

2. The temperature range investigated was very limited. It would be an advantage to extend it. It is also important to carry out experiments at several time ratios at each temperature.

3. The development of the near surface profile under a battery circuit such as Jorgenson's holds the possibility of determining the effective charge on the ionic species diffusing in the network.

4. It would be of interest to experiment with heavily doped silicon. If there is a network component to oxidation it should produce a detectable convection effect on the near-surface profile.

1. B. E. Deal and A. S. Grove: "General Relationship for the Thermal Oxidation of Silicon," J. of Applied Physics, 36, 3770 (1965).

2. E. A. Irene: The Effects of Trace Amounts of Water on the Thermal Oxidation of Silicon in Oxygen," J. Electro. Chem. Soc., 121, 12, 1613 (1974).

3. R. Ghez and Y. J. van der Meulen: "Kinetics of Thermal Growth of Ultra- Thin Layers of SiO_2 on Silicon, Pt. 2-Theory," J. Electrochem. Soc., 119, 8, 1100 (1972).

4. E. A. Irene: "Evidence for a Parallel Path Oxidation Mechanism at the Si-SiO_2 Interface," Appl. Phys. Lett. 40, 1, 74 (1982).

5. L. D. Major, Jr.: "Proton Activation Studies of the Thermal Oxidation of Silicon," M.S. Thesis, Case Western Reserve Univ. (1975).

6. M. M. Atalla; Semiconductor Surfaces and Films, Met. Soc. Conf., Vol. V (1959).

7. P. J. Jorgenson: "Effect of an Electric Field on Silicon Oxidation," J. Chem Phys., 37, 1874 (1962).

8. J. R. Ligenza and W. G. Spitzer: "The Mechanisms for Silicon Oxidation in Steam and Energy," J. Phys. Chem. Solids, 14, 131 (1960).

9. D. O. Raleigh: "Transport Processes in the Thermal Oxidation of Silicon," J. Electrochem. Soc., 113, 782 (1966).

10. R. A. Clark: "Oxidation by Interstitial Oxygen Transport with Exchange," to be published.

11. E. Rosencher, A. Straboni, S. Riga, and G. Amsel: "An O study of the Thermal Oxidation of Silicon in Oxygen," Appl. Phys. Lett., 34, 254 (1979).

12. S. S. Cristy, and J. B. Condon: "A Model for Oxidation of Silicon by Oxygen," J. Electrochem. Soc., 128, 10, 2170 (1981).

13. C. R. Helms: "Discussion Section, 'A Model for Oxidation of Silicon by Oxygen,'" J. Electrochem. Soc., 129, 6, 1375 (1982).

14. A. G. Revesz and H. A. Schaeffer: "The Mechanism of Oxygen Diffusion in Vitreous SiO_2," J. Electrochem Soc., 129, 2, 357 (1982).

15. F. J. Norton: "Permeation of Gaseous Oxygen Through Vitreous Silican," Nature, 191, 701 (1961).

16. R. Haul and G. Duembgen: "Oxygen Mobility in TiO_2, SiO_2, and Fused Quartz by Heterogeneous Isotopic Exchange," Z. Elektrochem., 66, 636 (1962).

17. E. W. Sucov: "Diffusion of Oxygen in Vitreous Silican," J. Amer. Cer. Soc., 46, 14 (1963).

18. E. L. Williams: "Diffusion of Oxygen in Fuel Silican," J. Amer. Cer. Soc., 48, 190 (1965).

19. H. Yinnon: "A Proton Activation Study of Oxygen Diffusion in Multicomponent Glass Forming Systems," Ph.D. Thesis, Case Western Reserve Univ. (1979).

20. J. R. Manning: Diffusion Kinetics for Atoms in Crystals, Van Nostrand-Reinhold, Princeton, N.J. (1968).

21. C. P. Ho and J. D. Plummer: "Si/SiO_2 Interface Oxidation Kinetics: A Physical Model for the Influence of High Substrate Doping Levels, I. Theory," J. Electrochem. Soc., 126, 9, 1516 (1979).

APPENDIX B

The Thermal Oxidation of Silicon Carbide

I. Introduction

Silicon carbide, SiC, in increasing use as a high temperature structural material. Under oxidizing conditions, its usefulness in this capacity is often limited by degradation due to oxidation. During passive oxidation silicon carbide, as well as other silicon based materials (e.g., Si_3N_4 and $MoSi_2$) are protected through the formation of a v-SiO_2 film analogus to that formed on silicon metal.

Another potential application of SiC is as a semiconductor material[1]. In this case thermal oxidation may be used to form a protective film for the SiC surface during device fabrication.

A number of studies of the passive oxidation of SiC have been carried out*, however there remain points which are not well under stood. During passive oxidation the rate of oxidation is controlled by mass transport across the v-SiO_2, the thicker the scale becomes the slower the oxidation rate.

---

*Thomas K. Glasgow (NASA Lewis Research Center) had undertaken a thorough, unpublished literature review on this topic, which was drawn upon for this discussion.

In 1964, Moltzfeldt[2] proposed that the passive oxidation, in dry air, of both silicon and silicon carbide was controlled by the inward transport of oxygen from the gas across the scale to the metal or carbide. This was based on the similarity of the activation energies for the oxidation of both materials and that for the permeation of oxygen through a v-SiO_2 membrane. As discussed in Appendix A, this appears to be correct for the case of silicon, however for SiC the situation appears more complex. In addition to the production of SiO and SiO_2, the oxidation of SiC can produce other products, either CO, CO_2 or ternary Si-C-O compounds. The rate of the oxidation reaction is dependent both on the rate at which the oxidants arrive at the interface and the rate at the products are removed. Since at least 1959[3], it has been recognized that it is possible for outward diffusion of secondary oxides to be responsible for the observation of parabolic kinetics. It has been proposed by several workers[4-6] that the controlling step is the outward diffusion of CO. However, Pampush, et al.[7] examined oxidized powders using infared spectroscopy and found no absorption bands which could be attributed to the double bonds found in CO and CO_2. Instead they found bands corresponding to single C-O bonds and proposed that the reaction product to be a ternary Si-O-C phase. Further complexity is found in the work of Fitzer and Ebi, this work reports three different activation energies for the passive oxidation of SiC. They propose that above 1400° C the outward diffusion of CO is controlling; between 1200° to 1400° C short circuit transport along cristobalite interfaces con-

trols; and below 1200° C the inward transport of oxygen through bulk v-SiO_2 controls.

In addition, as a result of the polar form of the crystal, the oxidation kinetics are very sensitive to crystallographic orientation. Harris[8] reports that the (0001) carbon face exhibits oxidation rates seven times greater than that of the (0001) silicon face. This has been confirmed by Munch and Pfaffender[9] as well as Costello[9].

The current work involved the double oxidation technique (described in Appendix A) using single crystal silicon carbide, over the temperature range 1300° to 1400° C, in an effort to gain some understanding of the mechanistics of SiC oxidation. The results indicate that the mechanism for oxidation of SiC is different from the non-interacting interstitial mechanism for the oxidation of silicon.

II. Experimental Procedure

Samples The experiments done in this work were collaborative with either Diane Mieskowski* (CWRU) or John Costello** (PSU), details of the samples may be found in references 10 and 11. Essentially the samples were high purity, light green, single crystals. All experiments were carried out exposing the (0001) carbon face, with the more rapid kinetics, to the oxidizing atmosphere.

---

*Currently at NASA Lewis Research Center, Cleveland, OH.
**Currently at Army Materials Research Lab., Ft. Monmouth, NJ.

Experimental Procedure The apparatus described in the main text and also used for the silicon oxidation, was used to carry out these thermal oxidations by the prccedure described in Appendix A.

Analysis of tracer profiles was by both proton activation and SIMS.

III. Results and Discussion

The double oxidation experiments were carried out at two temperatures, 1300° and 1400° C. Several time ratios of isotopic exposure were used, which are outlined in table B1, note sample 1 received three separate oxidations. In all cases a uniform concentration of tracer throughout the scale was found. This result may be contrasted with the results of double oxidation results on silicon metal.

TABLE B1

Sample number	Temperature	Isotopic exposure		
		1st	2nd	3rd
1*	1400° C	20 hr O-16	20 hr O-18	60 hr O-16
2*	1400° C	20 hr O-18	60 hr O-16	----------
3**	1300° C	2 hr O-16	3 min O-18	----------
4**	1300° C	2 hr O-16	11 min O-18	----------
5**	1300° C	2 hr O-16	35 min O-18	----------

*with D. Meiskowski.
**with J. Costello.

As discussed in Appendix A the profiles from silicon have four main features;

(1) A major accumulation of tracer near the oxide metal interface indicating the oxidation reaction took place at this interface.

(2) A region of very low tracer concentration in the center of the scale indicating the transport of oxidant is by a non-interacting mechanism.

(3) A region of tracer enrichment at the gas-oxide interface developed through pure self diffusion.

(4) A sharp interface, ~10 Å, between the oxide and the metal.

A profile from a silicon sample oxidized for 3.5 hrs in O-16 and then 15 hrs in O-18, at 960° C, is shown in figure 1. A profile from a silicon carbide sample oxidized for 2 hrs in O-16 and then 35 min in O-18 is shown in figure 2. The counting rate for O-16 and O-18 are parallel throughout the profile. Also the interface between the oxide and the carbide is wide, ~500 Å. The counting rate for carbon gradually increases across the interface. The counting rate for silicon apparently decreases however this is an artifact due to oxygen enhancement, which is well known in SIMS. This type of interface was observed by Suzuki, et al.[1].

The uniform concentration of tracer throughout the scale is inconsistent with control by the transport of a non-interacting defect. In the case of control by inward diffusion of non-interacting oxygen a profile similar to those observed on silicon would be expected. If, on the other hand, control is by outward diffusion of non-interacting carbon monoxide the tracer profile should reflect gas

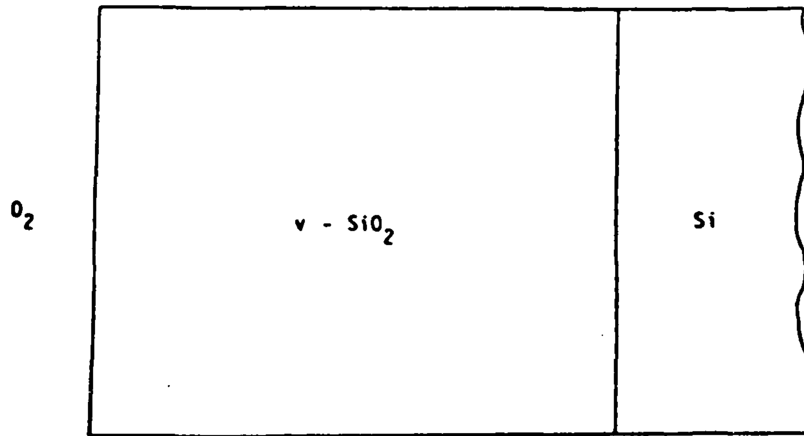

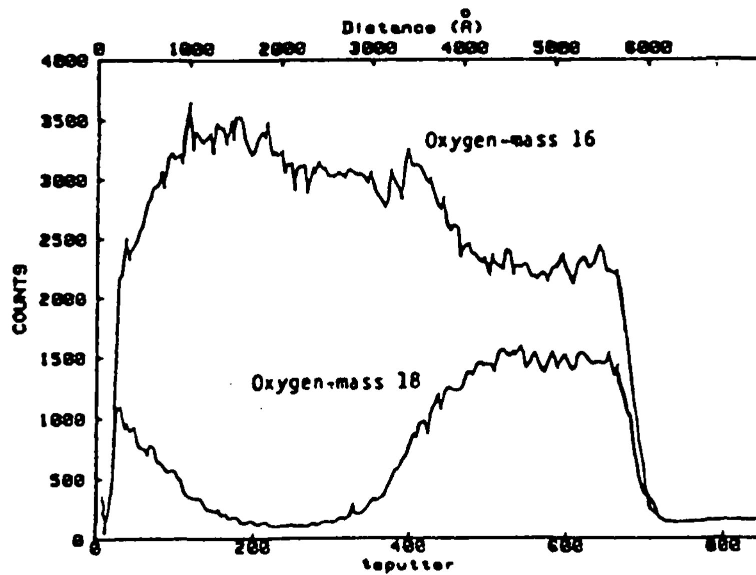

Figure 1. - SIMS profile of the v-SiO_2 scale formed on silicon metal thermally oxidized at 960° C for 3.5 hr under O-16 and then for 15 hr under O-18.

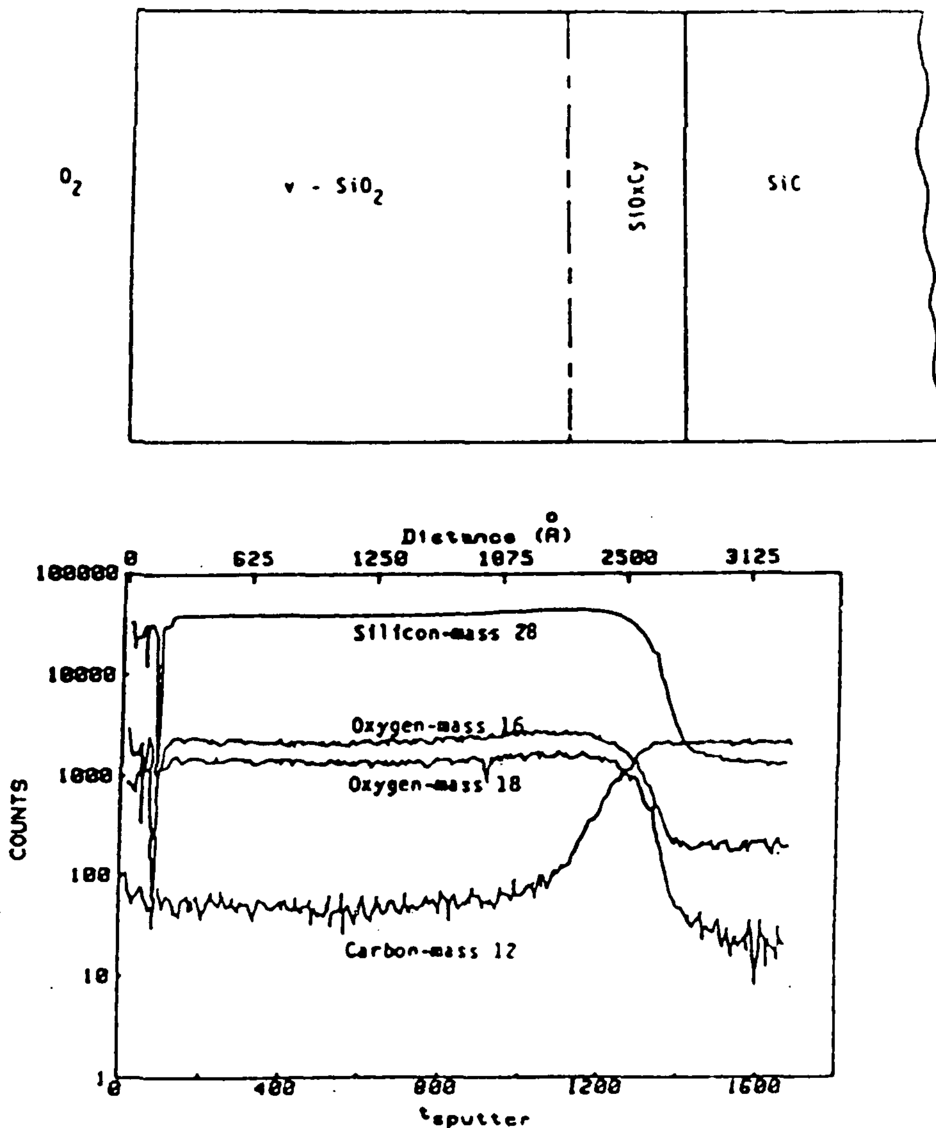

Figure 2. - SIMS profile of the v-SiO_2 scale formed on silicon carbide thermally oxidized at 1300° C for 2 hr under O-16 and then for 35 min under O-18.

with, and self diffusion into the silica film. If $\sqrt{Dt}$ is many times the thickness of the scale, self diffusion could produce a uniform tracer concentration. However $\sqrt{Dt}$ in all experiment was less than the scale thickness. In some cases as small as a tenth of the scale thickness. In these cases surface exchange and self diffusion would be expected to produce a profile with a maximum at the gas-oxide interface which decreases to zero toward the metal-oxide interface.

The profile would tend toward uniformity if the inwardly diffusing oxidant interacted frequently with the network, though the work of Clark[12] indicates at least a small gradient would always exist. Also the silicon oxidations, though at 1000° C, indicate that inward diffusing oxygen is non-interacting. A second circumstance by which a uniform profile could be produced is if exchange and diffusion through the dissolved, outwardly diffusing, reaction product phase was much faster than the exchange and diffusion into the bulk silica. The result of this would be a uniform source of tracer across the scale from which the tracer could diffuse.

IV. Conclusions

1. Double oxidation experiments indicate that there are mechanistic differences between the thermal oxidation of SiC at 1300° to 1400° C and the thermal oxidation of Si at 960° to 1000° C.

2. The uniform tracer profiles which occur during double oxidation experiments indicate that transport of either the oxidant of the

reaction product proceeds by a mechanism which is interactive with the network.

3. The interface between the scale and the carbide is much wider than in the case of silicon and is enriched in carbon.

V. Suggestions for Future Work

1. In order to examine the interface in more detail it would be an advantage to employ an oxygen primary beam in order to avoid discontinuous oxygen enhancement.

2. It would be useful to extend the temperature ranges of investigation for both SiC and Si to allow more direct comparison.

3. A systematic investigation of the carbon distribution, over a range of temperature, is needed.

1. A. Suzuki, H. Matsunami, and T. Tanaka; "Auger Electron Spectroscopy Analysis of Thermal Oxide Layers of Silicon Carbide," J. Electrochem. Soc., 125, 1896 (1978).

2. K. Motzfeldt; "On the Rates of Oxidation of Silicon and of Silicon Carbide in Oxygen, and Correlation with the Permeability of Silica Glass," Acta Chemica Scan., 18 1596 (1964).

3. R. F. Adamsky; "Oxidation of Silicon Carbide in the Temperature Range 1200° to 1500°," J. Phys. Chem., 63, 305 (1959).

4. S. C. Singhal; "Oxidation Kinetics of Hot Pressed SiC," J. Mat. Sci. 11, 1246 (1976).

5. W. W. Pultz and W. Hertl; "SiO_2 and SiC Reaction at Elevated Temperatures," Trans. Faraday Soc. 62, 2499 (1966).

6. D. Mieskowski, T. R. Mitchell, and A. H. Hever; "Bubble Formation in Oxide Scales on Silicon Carbide," to be published.

7. R. Pampush, W. Ptak, S. Jones, and J. Stoch; "Formation of Ternary Si-O-C Phase(s) During Oxidation of SiC," Mat. Sci. Monog. 1980, 6, Issue: Energy Ceramics, 435 (1980)

8. R. C. A. Harris, "Oxidation of 6-H SiC Platelets," J. Amer. Cer. Soc. 58, 7 (1975).

9. W. VonMunch and I. Pfaffender; "Thermal Oxidation and Electrolytic Etching of Silicon Carbide," J. Electrochem. Soc., 112, 642 (1975).

10. J. A. Costello; "Kinematics of and Microstructural Changes During Oxidation of Silicon Carbide Materials," Ph.D. Thesis, The Pennsylvania State University (1983).

11. D. M. Mieskowski; "The Oxidation of Silicon Carbide," M. S. Thesis, Case Western Reserve Univ. (1982).

12. R. A. Clark; "Oxidation by Intestitial Oxygen Transport with Exchange," to be published.

APPENDIX C

Solutions to the Diffusion Equation Including Convection

Introduction

Many diffusion problem of interest contain moving boundaries or occur under an external driving force. Both of these situations introduce a convection term into the diffusion equations. Fick's First law may be written

$$J = -D \frac{\partial c}{\partial x} + vc \tag{C-1}$$

where

J is the flux of the species of interest

D is the diffusion coefficient of the species

$\frac{\partial c}{\partial x}$ is the concentration gradient of the species

v is the convective velocity

c is the concentration of the species

When v is not a function of position. Fick's Second law

$$\frac{\partial c}{\partial t} = - \frac{\partial J}{\partial x} = D \frac{\partial^2 c}{\partial x^2} - v \frac{\partial c}{\partial x} \tag{C-2}$$

The time dependence of v, however, varies depending on the problem of interest. For a double oxidation experiment (See Appendix A) the velocity may be written in the form

$$v = \frac{\beta_1}{(t + \tau)^{1/2}} \tag{C-3}$$

where β_1 and τ are both constants. In the case of dissolution, or growth, of crystals limited by the rate of diffusion through the metl (see Chapter[1]) the velocity is of the form

$$v = \frac{\beta_2}{t^{1/2}} \tag{C-4}$$

where β_2 is a constant. When diffusion of a charged species takes place under a constant applied field a velocity is introduced which is constant

$$v = \beta_3 \tag{C-5}$$

Note that (C-4) and (C-5) are the limiting forms of (C-3)

$$v = \frac{\beta_1}{(t + \tau)^{1/2}} \simeq \frac{\beta_1}{t^{1/2}} \qquad \text{For} \quad t >> \tau$$

and

$$v = \frac{\beta_1}{(t + \tau)^{1/2}} \simeq \frac{\beta_1}{\tau} \rightarrow \text{const.} \qquad \text{For} \quad t << \tau$$

It is also the case that in many diffusion profiles are sufficiently small with respect to the experimental sample that the problem may be considered one dimensional and semi-infinite. Boundary conditions for this type of problem are

$$c(x,t) = 1 \qquad \text{For} \quad x = 0 \quad t > 0 \tag{C-6}$$

$$c(x,t) = 0 \qquad \text{For} \quad x \rightarrow \infty \quad t \geq 0$$

and the initial condition is

$$c(x,t) = 0 \qquad \text{For} \quad 0 \leq x \leq \infty \quad t = 0$$

In the following the solution to the partial differential equation (C-2) under the boundary conditions (C-6) will be obtained for two cases. The first will consider the velocity to depend on $t^{-1/2}$ and the second will consider a constant velocity.

CASE I

PDE $$\frac{\partial c}{\partial t} = D\frac{\partial^2 c}{\partial x^2} - \frac{\beta_2}{t^{1/2}}\frac{\partial c}{\partial x} \qquad \text{(C-7)}$$

BC_s $c(o,t) = 1$

$c(o,t) = 0$

IC $c(x,o) = 0$

It proves convenient to first transform the independent variable x.

Define $$z = x - 2\frac{\beta_2}{t^{1/2}}\cdot t = x - 2\beta_2 t^{1/2} \qquad \text{(C-8)}$$

and $\tau = t$

transforming the terms of the PDE gives

i) $$\frac{\partial c}{\partial x} = \frac{\partial c}{\partial z}\cdot\frac{\partial z}{\partial x} + \frac{\partial c}{\partial \tau}\frac{\partial \tau}{\partial x} = \frac{\partial c}{\partial z}$$

ii) $$\frac{\partial^2 c}{\partial x^2} = \frac{\partial}{\partial z}\left(\frac{\partial c}{\partial z}\right)\frac{\partial z}{\partial x} = \frac{\partial^2 c}{\partial z^2}$$

iii) $$\left(\frac{\partial c}{\partial t}\right)_x = \left(\frac{\partial c}{\partial t}\right)_z\frac{\partial z}{\partial x} + \frac{\partial c}{\partial z}\frac{\partial z}{\partial t}$$

$$= \frac{\partial c}{\partial t} - \frac{\beta_2}{t^{1/2}}\frac{\partial c}{\partial z}$$

combining this term finds

$$\frac{\partial c}{\partial t} - \frac{\beta_2}{t^{1/2}}\frac{\partial c}{\partial z} = D\frac{\partial^2 c}{\partial z^2} - \frac{\beta_2}{t^{1/2}}\frac{\partial c}{\partial z}$$

canceling terms gives

$$\frac{\partial c}{\partial t} = D\frac{\partial^2 c}{\partial z^2} \tag{C-9}$$

A known solution to this[2] is

$$c(z,t) = A \text{ erfc } \left(\frac{z}{2\sqrt{Dt}}\right) \tag{C-10}$$

where A is a yet to be determined constant. Transforming the solution back to x-space gives

$$c(x,t) = A \text{ erfc } \left(\frac{x}{2\sqrt{Dt}} - \frac{\beta_2}{\sqrt{D}}\right) \tag{C-11}$$

By application of the boundary condition

$$C(o,t) = 1$$

It can be seen that the constant A is given by

$$A = \left[\text{erfc } \left(-\frac{\beta_2}{\sqrt{D}}\right)\right]^{-1} \tag{C-12}$$

and the final solution is

$$c(x,t) = \frac{\text{erfc } \left(\frac{x}{2\sqrt{Dt}} - \frac{\beta_2}{\sqrt{D}}\right)}{\text{erfc } \left(-\frac{\beta_2}{\sqrt{D}}\right)} \tag{C-13}$$

This may be written in terms of the dimensionless parameters

$$\theta = \frac{x}{2\ \ Dt} \quad \text{and} \quad \varphi = \frac{\beta_2}{\sqrt{D}}$$

as

$$c(\theta,\varphi) = \frac{\text{erfc } (\theta - \varphi)}{\text{erfc } (-\varphi)} \tag{C-14}$$

Plots of this function versus Theta for various values Phi are shown in figures 1 and 2. A transition from a pure erfc, at $\varphi=0$, to a

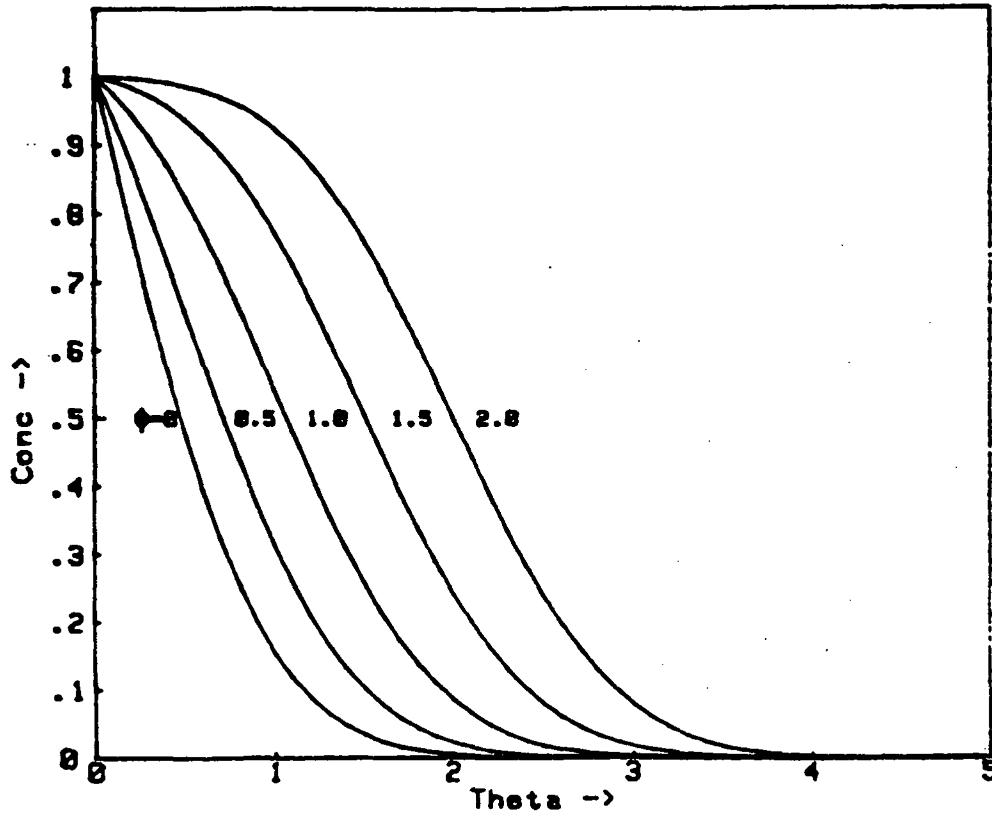

Figure 1. - Plots of the solution to the diffusion equation for $v=B/t^{1/2}$ for various ϕ.

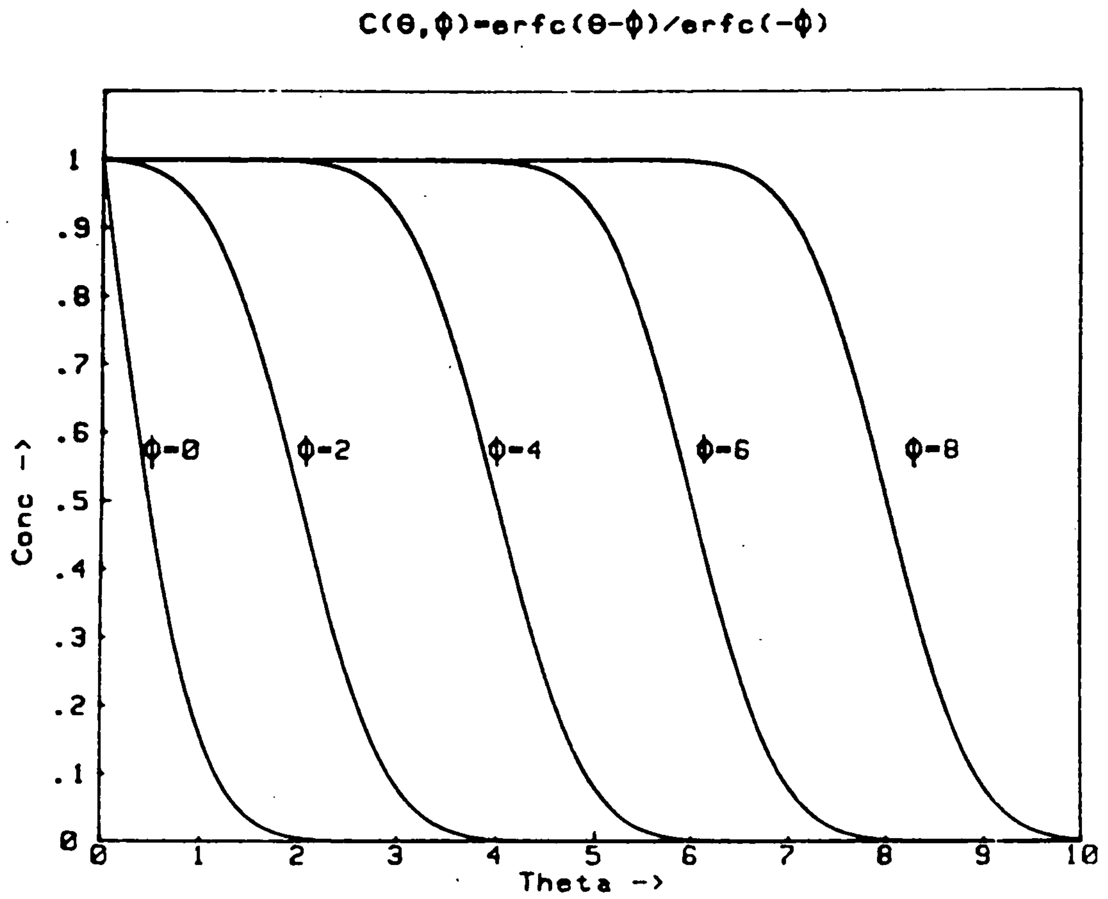

Figure 2. - Plots of the solution to the diffusion equation for $v=B/t^{1/2}$ for various ϕ.

normalized and displaced erfc, $\varphi>3$ can be seen. This behavior arises because the value of the denominator in C-14 becomes essentially constant for $\varphi>3$, see figure 3.

CASE II

PDE $\frac{\partial c}{\partial t} = D\frac{\partial^2 c}{\partial x^2} - \beta_3\frac{\partial c}{\partial x}$

BCS $c(o,t) = 1$
$c(\infty,t) =$

IC $c(x,o) = 0$

In this case it is convienient to transform the dependent variable c.[3]

Define $c(x,t) = u(x,t)\cdot w(x,t)$

where $u(x,t) = \exp\ (\beta_3(x-\beta_3 t/2)\ /2D)$

In order to simiplify the transformation of the equation the chain rule is applied to give

$$\frac{\partial c}{\partial t} = \frac{\partial c}{\partial u}\frac{\partial u}{\partial t} + \frac{\partial c}{\partial w}\frac{\partial w}{\partial t} \quad \text{and} \quad \frac{\partial c}{\partial x} = \frac{\partial c}{\partial u}\frac{\partial u}{\partial x} + \frac{\partial c}{\partial w}\frac{\partial w}{\partial x}$$

Since

$$\frac{\partial c}{\partial u} = w \quad \text{and} \quad \frac{\partial c}{\partial w} = u$$

These become

$$\frac{\partial c}{\partial t} = w\frac{\partial u}{\partial t} + u\frac{\partial w}{\partial t} \quad \text{and} \quad \frac{\partial c}{\partial x} = w\frac{\partial v}{\partial x} + u\frac{\partial w}{\partial x}$$

Now transforming the individual terms of the PDE gives

$$1)\ \frac{\partial c}{\partial x} = w\frac{\partial u}{\partial x} + u\frac{\partial w}{\partial x}$$

Since

$$\frac{\partial u}{\partial x} = \frac{\partial}{\partial x}\exp(\beta_3(x-\beta_3 t/2)/2D) = \frac{\beta_3}{2D}\exp(\beta_3(x-\beta_3 t/2)/2D)$$

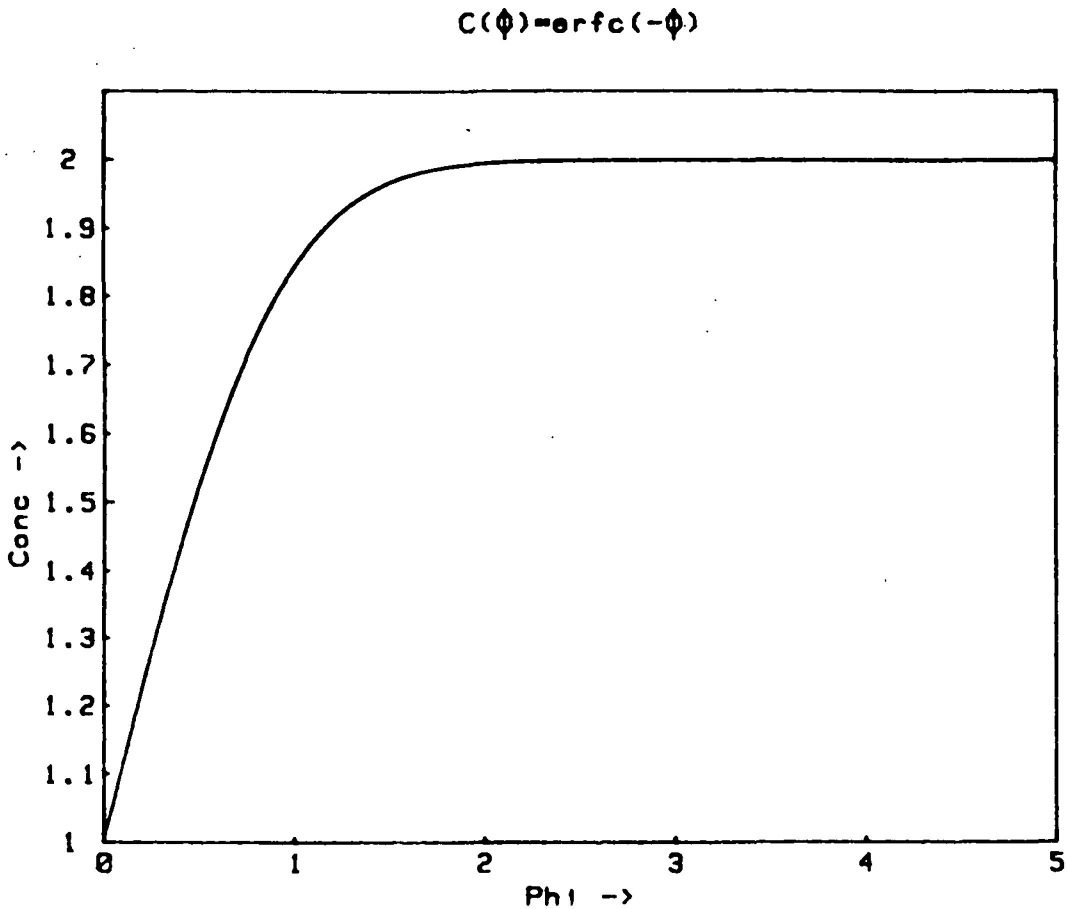

Figure 3. - Plot of elfc $(-\phi)$ versus ϕ.

$$\frac{\partial c}{\partial x} = \exp(\beta_3(x-\beta_3 t/2)/2D) \cdot [\frac{\partial w}{\partial x} + \frac{w\beta_3}{2D}]$$

ii) $$\frac{\partial^2 c}{\partial x^2} = \frac{\partial}{\partial x}(\frac{\partial c}{\partial x}) = \frac{\partial}{\partial x}(\exp(\beta_3(x-\beta_3 t/2)/2D) \cdot [\frac{\partial w}{\partial x} + \frac{w\beta_3}{2D}]$$

$$\frac{\partial^2 c}{\partial x^2} = \exp(\beta_3(x-\beta_3 t/2)/2D) \cdot \frac{\partial^2 w}{\partial x} + \frac{\beta_3}{2D}\frac{\partial w}{\partial x} + \frac{\beta_3}{2D}\frac{\partial w}{\partial x} + \frac{w\beta_3^2}{4D^2}$$

iii) $$\frac{\partial c}{\partial t} = w \cdot \frac{\partial u}{\partial t} + u \cdot \frac{\partial w}{\partial t}$$

Since

$$\frac{\partial u}{\partial t} = \frac{\partial}{\partial t}(\exp(\beta_3(x-\beta_3 t/2)/2D)) = \frac{-\beta_3^2}{4D}\exp(\beta_3(x-\beta_3 t/2)/2D)$$

$$\frac{\partial c}{\partial t} = \exp(\beta_3(x-\beta_3 t/2)/2D) \quad [\frac{\partial w}{\partial t} - w \cdot \frac{\beta^2}{4D}]$$

Since it occurs in all of the terms the exponential may be divided prior to the combination which yields

$$\frac{\partial w}{\partial t} - \frac{w\beta_3^2}{4D} = D\,\{\frac{\partial^2 w}{\partial x^2} + \frac{\beta_3}{D}\frac{\partial w}{\partial x} + \frac{w\beta_3^2}{4D^2}\} - \beta_3\,\{\frac{\partial w}{\partial x} + \frac{w\beta_3}{2D}\} \qquad \text{(C-15)}$$

Multipling through and canceling terms gives

$$\frac{\partial w}{\partial t} = D\,\frac{\partial^2 w}{\partial x^2}$$

transforming the boundary conditions with

$w(x,t) = c(x,t)/\exp(\beta_3(x - (\beta_3 t/2)/2D)$ gives

$$c(o,t) = 1 \quad w(o,t) = \frac{1}{\exp(-\beta_3^{\,2} t/4D)} = \exp(\beta_3^{\,2}/4D)$$

$$c(\infty,t) = 0 \quad w(\infty,t) = o/\infty = 0$$

the initial condition becomes

$$c(x,o) = 0 \quad w(x,o) = o/\exp(\beta x/2D) = 0$$

This new problem may be solved using Laplace transforms.

Transforming the equation[2] gives

$$\frac{\partial w}{\partial t} = D\,\frac{\partial^2 w}{\partial x^2} \rightarrow p\bar{w} = D\,\frac{\partial^2 \bar{w}}{\partial x^2}$$

where $\bar{w}$ is $L[w]$ and p is the Laplace variable. Transforming the boundary condition gives

$$w(o,t) = \exp\frac{\beta_3^2 t}{4D} \rightarrow \bar{w}(o) = \frac{1}{p-\frac{\beta_3^2}{4D}}$$

$$w(\infty,t) = 0 \rightarrow w(\infty) = 0$$

By inspection the solution satisfying these conditions is

$$\bar{w}(x) = \frac{1}{\left(p-\frac{\beta_3^2}{4D}\right)}\exp\left(-\sqrt{\frac{p}{D}}\,x\right)$$

The inverse transformation of this solution, from tables[2], is

$$w(x,t) = \frac{1}{2}\left[\exp\left(\frac{\beta_3^2 t}{4D}\right)\ \exp\left(\frac{-x\beta_3}{2D}\right)\ \mathrm{erfc}\left\{\frac{x}{2\ \ Dt} - \sqrt{\frac{\beta_3^2 t}{4D}}\right\}\right.$$

$$\left. + \exp\left(\frac{x\beta_3}{2D}\right)\ \exp\left\{\frac{x}{2\sqrt{Dt}} + \sqrt{\frac{\beta_3^2 t}{4D}}\right\}\right] \qquad \text{(C-16)}$$

Finally transforming back to the dependent variable $c(x,t)$ gives

$$c(x,t) = \frac{1}{2}\left[\mathrm{erfc}\left(\frac{x}{2\sqrt{Dt}} - \sqrt{\frac{\beta_3^2 t}{4D}}\right) + \exp\left(\frac{x\beta_3}{D}\right)\ \mathrm{erfc}\left(\frac{x}{2\sqrt{Dt}} + \sqrt{\frac{\beta_3^2 t}{4D}}\right)\right]$$

$$\text{(C-17)}$$

This may be written in the dimensionless variables

$$\theta = \frac{x}{2\ \ Dt} \quad \text{and} \quad \varphi = \frac{\beta^2 t}{4D} = \frac{\beta}{2}\ \frac{t}{D}$$

as

$$c(\theta,\varphi) = \frac{1}{2}\,[\mathrm{erfc}(\theta\ \ \varphi) + \exp(4\theta\ \varphi)\mathrm{erfc}(\theta + \varphi)] \qquad \text{(C-18)}$$

Plots of this function versus theta for various values of phi are shown in figures 4 and 5. The behavior of this function is similar to that derived previously. It undergoes a transition from pure erfc, when phi = 0 to very nearly a normalized and displaced erfe as phi gets big. Figure C-6 show a plot of the individual terms of the solution and their sum. It can seem that the term erfc $(\theta - \varphi)$ begins to dominate rapidly with increasing φ while the term exp $(4\theta\ \varphi)$ erfc $(\theta + \varphi)$ gives a gaussian shaped wave which travels on the leading edge of the convective wave.

Conclusions

Solutions to the diffusion equation have been obtained for a semi-infinite slab when constant convection or convection with a time dependency of $t^{1/2}$ exists.

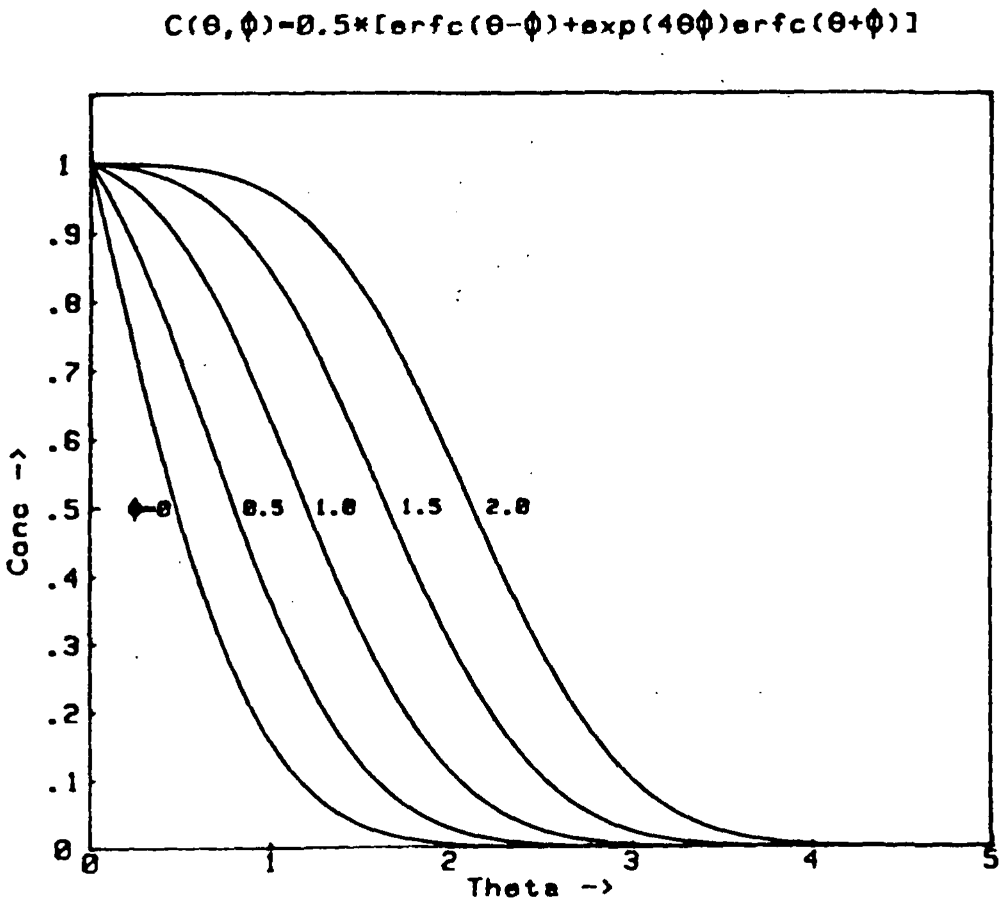

Figure 4. - Plots of the solution to the diffusion equation with constant convection for various ϕ.

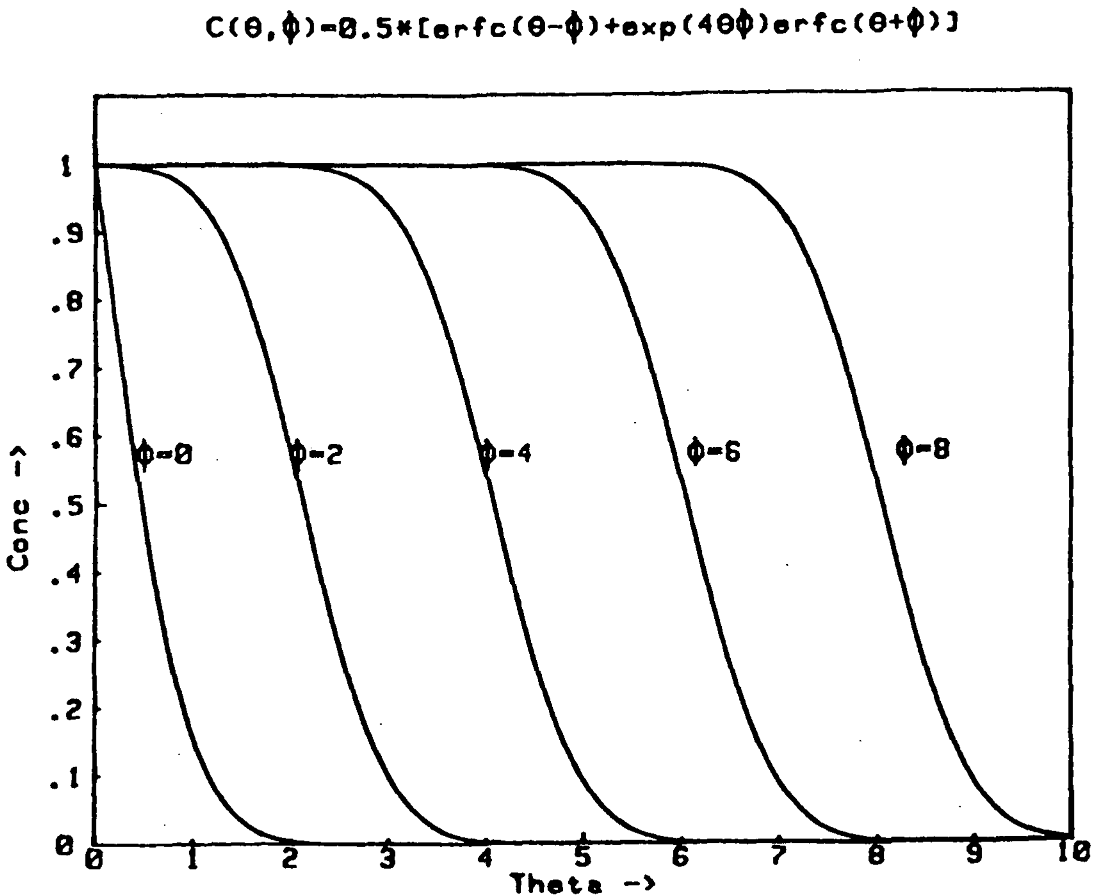

Figure 5. - Plots of the solution to the diffusion equation for constant convection, for various ϕ.

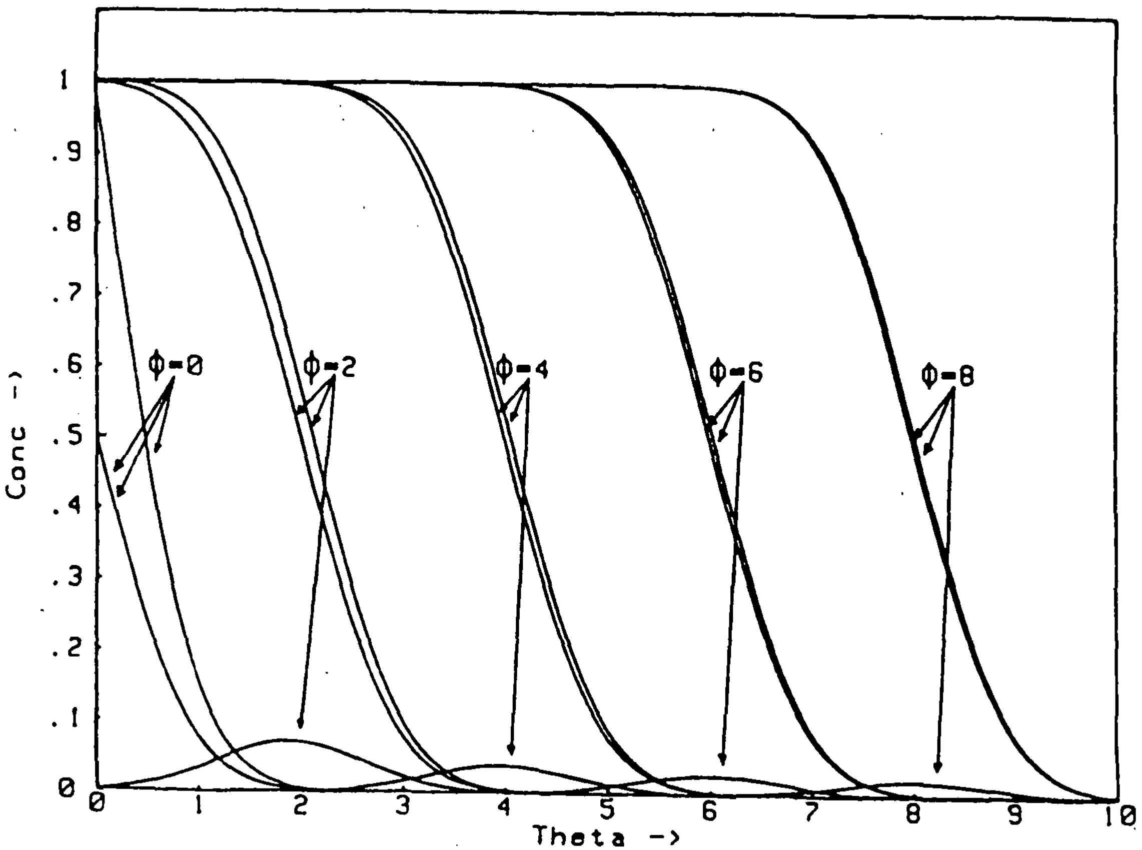

Figure 6. - Plot of the components, and sum, of the solution to the diffusion equation for constant convections.

1. A. R. Cooper, Jr.: "The Effect of the Moving Boundary on Molecular-Diffusion-Controlled Dissolution or Growth Kinetics," Trans. Far. Soc. 58, 2468 (1962).

2. J. S. Crank: The Mathematics of Diffusion 2nd Ed., Clarendon Press, Oxford (1975).

3. S. J. Farlow: Partial Differential Equations for Scientists and Engineers, John Wiley and Sons, New York (1982).

National Aeronautics and
Space Administration

Washington, D.C.
20546

Official Business
Penalty for Private Use, $300

THIRD-CLASS BULK RATE

Postage and Fees Paid
National Aeronautics and
Space Administration
NASA-451

NASA

POSTMASTER: If Undeliverable (Section 158 Postal Manual) Do Not Return